Des signaux cérébraux aux activités cognitives, approches géométriques et apprentissage statistique

Sylvain Chevallier

Université de Versailles Saint-Quentin
Laboratoire d'Ingénierie des Systèmes de Versailles (LISV EA 4048)

Habilitation à diriger des recherches

Discipline : Génie informatique, automatique et traitement du signal

Présentée par :
Sylvain Chevallier

Des signaux cérébraux aux activités cognitives, approches géométriques et apprentissage statistique

Soutenue le 4 décembre 2019 à Vélizy devant le jury :
M. François Cabestaing, Professeur, Université de Lille (rapporteur)
Mme Anne Guérin-Dugué, Professeur, Université de Grenoble (rapporteure)
M. Laurent Perrinet, CR HDR, Institut de Neurosciences de la Timone (rapporteur)
Mme Samia Bouchafa-Bruneau, Professeure, Université d'Evry Val d'Essonne (présidente)
M. François Routhier, Professeur, Université Laval, Québec (examinateur)
M. Eric Monacelli, Professeur, Université de Versailles St Quentin (tuteur)

Résumé

Les progrès en analyse des signaux cérébraux pour un décodage en temps réel ont permis des avancées importantes pour les interfaces cérébrales. Ces interfaces cérébrales ou *brain-computer interfaces* (BCI) permettent de contrôler ou d'échanger des commandes avec un système en nécessitant pas ou peu de capacités physiques. Elles offrent une solution adaptée pour les personnes en situation de handicap. Dans leur forme actuelle, elles requièrent toutefois une bonne capacité de concentration pour fonctionner correctement. Ces BCI ont connu un rapide essor grâce aux méthodes d'apprentissage statistique, mais elles font face à deux verrous scientifiques. Le premier concerne la puissance du signal, qui est très faible, et les bruits environnants qui contaminent les enregistrements de signaux cérébraux, avec des niveaux bien supérieurs à celui du signal d'intérêt. Le second point concerne les variabilités individuelles qui peuvent réduire les algorithmes à des prédictions au niveau de la chance pour 10 à 20% des sujets.

Les travaux présentés dans ce manuscrit abordent les aspects tant expérimentaux que théoriques pour aborder ces deux problèmes. Les approches en traitement du signal utilisées pour travailler sur les signaux cérébraux peuvent dans certains cas s'appliquer sur d'autres types séries temporelles, par exemple pour des applications industrielles sur la détection d'anomalie. Toutes ces approches sont développées avec des outils libres pour une science ouverte et diffusable, en apportant quand c'est possible des contributions aux logiciels libres.

Abstract

Real-time decoding of brain signals has opened new advances for brain interfaces thanks to dedicated signal analysis tools. Those brain-computer interfaces or BCI allow to control or to send commands to numerical systems without relying on physical capability. These interfaces are thus well suited for people with disabilities, but they still require good concentration capabilities. The BCI have attracted a growing interest with the development of dedicated machine learning algorithms. However, two major scientific problems have been identified. First, the signal is very weak while there are multiple noise sources of higher energy. Second, the individual variations could lead the decoding algorithm to approach the chance level for 10 to 20 % of the subjects.

The works presented in this manuscript describe the experimental and theoretical approach proposed to tackle those problems. The signal processing approaches developed for brain signals analysis could be applied to wider class of time series, with possible industrial applications for anomaly detection. All these works are conducted by following the open science principles, relying on and extending open source tools each time it was possible.

Table des matières

Table des matières

Table des figures

1 Curriculum Vitæ

Maître de conférences, 39 ans, français

Coordonnées

Administratives

adresse :	10-12 avenue de l'Europe, 78140 Vélizy
tél. :	01 39 25 49 77 / 06 32 14 09 58
établissement :	LISV, Université de Versailles Saint-Quentin
courriel :	sylvain.chevallier@uvsq.fr
www :	http://sites.google.com/site/sylvchev

Personnelles

adresse :	40 rue de Fontenay, 92330 Sceaux
tél. :	09 80 95 27 69

Situation professionnelle

- Maître de conférences à l'IUT de Vélizy, Université de Versailles Saint-Quentin-en-Yvelines, depuis septembre 2011 (8 ans)
- Chercheur au Laboratoire d'Ingénierie des Systèmes de Versailles (LISV) EA-4048 de Vélizy, dans l'équipe Robotique Interactive
- CRCT accordé par le CNU de 2 semestres en 2018-2019

Formation

2009 Doctorat en informatique, Université Paris-Sud
Mention très honorable
2005 Master 2 recherche en informatique, Université Paris-Sud
Mention très bien
2004 Maîtrise de sciences cognitives, Université Lyon 2
2003 Licence de sciences cognitives, Université Lyon 2
2002 DEUG de sciences de la vie, Université Paris-Sud, Orsay

Expérience professionnelle en enseignement et recherche

2011-auj. Maître de conférences IUT de Vélizy
Université de Versailles Saint-Quentin-en-Yvelines
2011 (6 mois) Post-doctorat, LTCI,
Télécom ParisTech
Apprentissage automatique pour les interfaces cérébrales
2010 (6 mois) Post-doctorat, LRI - équipe TAO
INRIA-Saclay
Réseaux de neurones profonds et interfaces cérébrales
2008-2010 ATER à mi-temps, laboratoire ETIS
Université de Cergy
Émergence d'un biais attentionnel visuel dans l'interaction homme-robot
2005-2008 Bourse MENRT & monitorat, LIMSI
Université Paris-Sud
Implémentation d'un système préattentionnel avec des neurones impulsionnels
sous la direction de Ph. Tarroux et H. Paugam-Moisy

1.1 Encadrement doctoral

Hugo Martin, doctorant CIFRE UVSQ et Bouygues Construction

— Encadrement à 50%, financé par Bouygues, co-encadrement avec Eric Monacelli
— Intitulé de la thèse : "Maquette numérique pour la construction : structurer et visualiser les connaissances métier"
— Publications : [15], [17]
— Soutenue le 7 décembre 2016 (durée : 3 ans et 7 mois)

Emmanuel Kalunga, doctorant en cotutelle UVSQ et Tshwane University of Technology (Afrique du Sud)

— Encadrement à 40%, avec Eric Monacelli, financée sur projets
— Intitulé de la thèse : "Toward User-adapted Brain-Computer Interfaces : Robust Interactions and Machine Learning based on Riemannian Geometry"
— Publications : [1], [4], [12], [16], [18], [22], [23]
— Soutenue le 30 août 2017 (3 ans et 5 mois)

Jinan Charafeddine, doctorante en cotutelle UVSQ et Université Libanaise (Liban)

— Encadrement à 30%, avec Didier Pradon et Samer Alfayad, financement libanais
— Intitulé de la thèse : "Caractérisation et Intégration des signaux musculaires pour le pilotage d'un exosquelette des membres inférieurs lors d'activités locomotrices"
— Publications : [8], [10]
— Soutenue prévue en décembre 2019 (3 ans au 1er septembre)

Amina Alaoui-Belghiti, doctorante CIFRE UVSQ et Nexeya-Hensoldt

— Encadrement à 75%, financé par Nexeya, co-encadrement avec Eric Monacelli
— Intitulé de la thèse : "Analyse et prédiction de défaillances pour les bancs de test : Vers une maintenance prédictive et automatisée"
— Publication : [13]
— 1 an et 2 mois au 1er septembre

1.2 Participation à la vie scientifique

Collaborations et participation à des projets de recherche

Je suis le porteur du projet "Détection de panne pour la maintenance prédictive à partir de signaux temporels récurrents", avec la société Nexeya-Hensoldt depuis septembre 2018. Ce projet finance la thèse CIFRE d'Amina Alaoui-Belghiti et est la première étape pour mettre en place une chaire de recherche avec l'UVSQ.

Je co-anime le projet "Détection anticipée de l'assoupissement des conducteurs" avec Eric Monacelli. Ce projet financé en 2019 par la fondation MAIF [1] est conduit en partenariat avec la société Ellis-Car. L'objectif du projet est d'évaluer la qualité de la détection de l'endormissement au volant dans les conditions les plus réalistes possible.

J'ai participé au projet "Remédiation par neurofeedback des déficits de reconnaissance des émotions faciales" de l'institut iCODE [2] du Campus Paris-Saclay en 2016. Les expériences sont réalisées avec le CIAMS (Université Paris-Sud) et le laboratoire HANDIReSP de l'UVSQ, le LISV assure l'analyse des données. Ce projet a financé une partie du séjour doctoral d'Emmanuel Kalunga en France.

J'ai obtenu deux BQI, projets internes au LISV, en 2011 et en 2015. Ces projets ont permis de financer une extension du post-doc de Zoran Tiganj, une partie du séjour doctoral d'Emmanuel Kalunga, du matériel et des missions.

J'ai été le porteur du projet Cerebraptic financé par la fondation EADS en 2012 sur les interfaces cerveau-machine hybrides. Ce projet m'a permis de

1. https://www.fondation-maif.fr/
2. http://www.icode-institute.fr/

recruter Zoran Tiganj en post-doctorat d'un an et de financer le stage de 6 mois d'Emmanuel Kalunga (TUT, Afrique du Sud) pour son MsC.

J'ai collaboré avec Isabelle Bloch et Joe Wiart (LTCI, Telecom ParisTech) sur les travaux concernant les interfaces cerveau-machine de Yuan Yang, ancien doctorant, maintenant en poste à la Northwestern University, Illinois, États-Unis.

J'ai participé au projet européen SYMBRION[3] en 2010, coordonné par l'Université de Stuttgart (Allemagne) et qui regroupe les universités de Graz, de Vrije, de Karlsruhe, de Bristol, de Tübingen, de Bruxelles ainsi que l'institut de biotechnologie des Flandres (Belgique) et l'INRIA-Saclay.

J'ai participé au projet ANR DEFIS "Apprentissage Statistique pour une Architecture Profonde" (ASAP), coordonné par le LITIS (Université de Rouen, du Havre et INSA) et qui regroupe les équipes LIF de Marseille), LIP6 de l'UPMC et GREYC de Caen en 2010.

J'ai participé au projet ANR MAPS[4] porté l'équipe Cortex de l'INRIA Nancy, qui s'est déroulé sur la période 2007–2010.

Séminaires et présentations

— Séminaire invité lors de la rencontre Encuentro Cientifico Internacional Paris, à l'ENS Ulm en mai 2019 : "Challenges in Brain-Computer Interfaces : Insights from a Riemannian point of view"
— Séminaire invité au GIR de la Tokyo University of Agriculture and Technology (Japon) en mai 2019 : "Riemannian Brain-Computer Interface From invariance to transfer learning"
— Présentation à l'équipe POTIC de l'INRIA Bordeaux en avril 2019 : "Spatial covariance matrices as robust features for BCI"
— Séminaires invités à l'Université Mohammed Ier de Oujda (Maroc) en février 2017 : "Intelligence artificielle et assistances : quels recours et quels besoins ?" et "Robust Riemannian brain-computer interfaces"
— Séminaire invité à l'INMA de l'Université Catholique de Louvain (Seminars in Mathematical Engineering) en février 2016 : "Riemannian geometry applied to EEG-based cerebral interfaces : Challenges and opportunities"

3. http://symbrion.org/tiki-index.php
4. http://maps.loria.fr/

— Présentation à l'University College London, lors du workshop "Virtual Reality in Rehabilitation, Accessibility and Mobility"cadre des UCL Grand Challenges, en mai 2015 : "Assessment of rehabilitation in virtual environment"
— Présentation au GT Réseaux Profonds du Labex DigiCosme en mars 2015 : "Interface cerveau-ordinateur et électroencéphalographie"
— Organisation du workshop "Brain Computer Interface for Rehabilitation", à Vélizy en octobre 2013
— Présentation au workshop Multi-scale dynamics and evolvability of biological networks, organisé dans le cadre du programme joint CNRS – Max Plank Institute à Leipzig : "A spiking neuron network for studying the emergence of collective phenomena in social insect colonies".
— Présentation au workshop Shapes of Brain Dynamics, organisé par R. Doursat et P. Baudot en juin 2010 à l'ISC-PIF : "A spiking neuron network model for the emergence of synchrony in task allocation"
— Présentation à l'équipe TAO du LRI, février 2010 : "SpikeAnts : Task allocation and emergent synchrony in a weakly coupled spiking neuron network"
— Présentation à l'équipe Neurocybernétique de l'ETIS, décembre 2007 : "Modélisation des processus attentionnels avec un réseau de neurones impulsionnels"
— Présentation à l'équipe TURING du LIRIS, juillet 2007 : "Focalisation et suivi attentionnel avec un réseau de neurones impulsionnels"
— Présentation à l'Institut de Neurosciences Cognitives de la Méditerranée dans l'équipe dynamique de la perception visuelle et de l'action, avril 2006 : "Détection de saillances par un réseau de neurones impulsionnels distribué".

Relectures et comités éditoriaux

— Membre du comité éditorial de Frontiers in Applied Mathematics and Statistics
— Relecteur pour les conférences *NIPS*, *AISTATS*, *ICLR*, *ICML*, *ACML* et *IROS*
— Membre du comité scientifique de la conférence internationale ESANN.
— Relecteur pour les journaux *Pattern Recognition Letters*, *Computer Vision*

and Image Understanding, *Neurocomputing* et *Transactions of the Society for Modeling and Simulation*, mes relectures sont accessibles sur Publons[5].
— Rapporteur externe pour un projet européen CHIST-ERA en 2014

Participation à la vie universitaire et à l'animation scientifique

— Membre du conseil d'institut de l'IUT de Vélizy, élu en 2017
— Représentant des personnels au Comité Technique de l'UVSQ depuis 2016
— Membre du conseil du laboratoire du LISV, élu en 2012
— Responsable des séminaires du laboratoire LISV, depuis 2011

Je co-anime le groupe de travail Handiversité[6] qui vise à favoriser l'inclusion des étudiantes et étudiants handicapés dans les filières universitaires dans les établissements du plateau de Saclay. Nous avons construit ce groupe pour répondre au besoin des personnels, chargés de mission ou enseignants, concernés par une meilleure prise en compte du handicap dans les formations. Ce groupe a permis de répondre à des besoins concrets pour des situations individuelles et à la mise en valeur de la politique inclusive dans le schéma directeur de Paris-Saclay. Je suis responsable du comité d'organisation du colloque Handiversité qui regroupent avec les équipes de recherche sur le handicap, les entreprises impliquées et les principales formations du plateau (universités et grandes écoles).

Je contribue au développement des logiciels scientifiques libres dans l'optique de promouvoir une science ouverte, au sens du FAIR (*Findable-Accessible-Interoperable-Reusable*) et des principes défendus par la Commission européenne, qui facilite la reproductibilité des expériences. En particulier, j'ai aidé au développement du *Mother of All BCI Benchmark* (MOABB[7]) qui est un projet soutenu par NeuroTechX et qui permet d'automatiser la récupération des données d'expériences BCI ainsi que la comparaison de modèle d'apprentissage. Je participe également au développement de PyManOpt[8], qui est la version Python de ManOpt, une bibliothèque de code

5. https://publons.com/author/170510/sylvain-chevallier
6. https://www.universite-paris-saclay.fr/fr/handicap
7. https://github.com/NeuroTechX/moabb
8. https://github.com/pymanopt/pymanopt/

pour l'optimisation sur des variétés, initialement développée sur Matlab.

Je suis membre du bureau de l'association Cortico [9], collectif pour la recherche transdisciplinaire sur les interfaces cerveau-ordinateur. Cette association nouvellement créée fait suite au groupe de travail sur les BCI soutenu par l'ITMO. Nous avons organisons tous les ans depuis 2016 des journées jeunes chercheurs et jeunes chercheuses, JJC-ICON, et des colloques, dans les différents centres de recherche français. Ces journées ont eu lieu à Paris en 2016, à Bordeaux en 2017, à Toulouse en 2018, à Lille en 2019 et auront lieu à Grenoble en 2020.

Organisation de colloques et workshop

— Organisateur du workshop de la conférence Graz BCI [10] "Benchmarking BCI classification methods : a hands-on introduction" lors en septembre 2019
— Organisateur du troisième colloque Handiversité de l'Université Paris-Saclay [11], en avril 2018 à EDF-lab Saclay
— Directeur du second colloque Handiversité [12] en avril 2016, dont les actes sont disponibles en version numériquement accessible [13]
— Organisateur du premier colloque Handiversité [14], en novembre 2014
— Organisateur de la journée d'information sur le portail HAL du laboratoire (septembre 2015)
— Organisation de la session spéciale "Deep Learning" de la conférence internationale ESANN 2011, avec L. Arnold, H. Paugam-Moisy et S. Rebecchi.

9. http://www.cortico.fr/
10. https://www.tugraz.at/institute/ine/graz-bci-conferences/8th-graz-bci-conference-2019/satellite-events/
11. https://www.universite-paris-saclay.fr/fr/handiversite2018
12. https://www.universite-paris-saclay.fr/fr/evenement/handiversite-2016-le-handicap-un-vecteur-pour-linnovation
13. https://www.universite-paris-saclay.fr/sites/default/files/les_actes_du_colloque_handiversite_2016.pdf
14. https://www.universite-paris-saclay.fr/fr/evenement/colloque-handiversite

Encadrement d'étudiants

Stagiaires de Master 2

— Encadrement d'Insaf Boguezine, stagiaire de Master 2 RAM Paris-Saclay (avril-août 2019) : "Détection du pré-endormissement en situation de conduite avec des électrodes sèches"
— Encadrement de David Gérard, stagiaire de M2 PCMPS Université Paris-Sud (février-avril 2019) : "Influence des stratégies de réponses sur les activités cérébrales pour des tâches répétitives"
— Encadrement d'Amina Alaoui-Belghiti, stagiaire de Master 2 RAM Paris-Saclay (février-juin 2017) : "Réalisation d'un prototype pour la détection d'hypovigilance par EEG", qui a continué en thèse au laboratoire.
— Encadrement de Mayssa Hammami, stagiaire de Master 2 RAM Paris-Saclay (octobre-mars 2017), "Interface cérébrale pour la détection de difficulté respiratoire", dont le travail a été publié en conférence [11]
— Encadrement d'Ayoub Jebri, stagiaire de Master 2 RAM Paris-Saclay (octobre-juin 2016) : "Évaluation des composantes d'électroencéphalogramme avec des réseaux de neurones profonds"
— Encadrement d'Olga Kamozina, stagiaire de Master 2 Ingénierie des Systèmes Complexes de l'Université de Cergy-Pontoise (septembre-mars 2014) : "Vers la catégorisation de la présence avec un réservoir de neurone"
— Encadrement de Yasaman Mofid, stagiaire de M2 STS Caen (avril-juillet 2013) : "Interactions en réalité virtuelle pour la rééducation"
— Encadrement de Mekhtoub Belaid, stagiaire de Master 2 CSER de l'UVSQ (septembre-février 2013) : "Catégorisation des signatures vibratoires du sol pour l'exploration avec une canne d'aveugle"
— Encadrement d'Emmanuel Kalunga, stagiaire de MSc de Tshwane University of Technology en Afrique du Sud (décembre 2011-juin 2012) : "Extension de l'interface touchless par une interface cérébrale hybride", qui a ensuite continué en thèse au LISV.
— Encadrement d'Hugo Martin, stagiaire de Master 2 CSER de l'UVSQ (septembre-février 2012) : "Apprentissage et reconnaissance des mouvements manuels pour le pilotage d'un exosquelette robotique", qui a continué en thèse au laboratoire.

Stagiaires d'autres niveaux

— Encadrement de Marie-André Faye, stagiaire de M1 Physique UPMC (juin-juillet 2019) : "Influence du biais utilisateur sur la réponse cognitive lors d'une tâche de détection répétitive"
— Encadrement de Yacine Gueye, stagiaire d'IUT RT (juin-août 2019) : "Analyse du signal EEG pour identifier un biais utilisateur dans une tâche de détection répétée"
— Encadrement d'Alphonse Mengue, stagiaire de BTS informatique (juin-juillet) : "Mise en place d'un service de messagerie interne dans un conteneur docker"
— Encadrement de Lamine Sylla, stagiaire IUT RT (avril-juin 2018) : "Intégration et développement d'applications dans docker"
— Encadrement de Joyce Nassar, stagiaire de M1 à l'Université Libanaise (février-avril 2018) : "Extraction automatique de biomarqueurs pour le contrôle d'un exosquelette médical"
— Encadrement de Mohammed Amraoui, stagiaire CESI 2e année (février-mars 2018) : "Réalisation d'un bodyboard adapté et modulaire"
— Encadrement de Elhadji Mady Diouf, stagiaire de M1 E3A (mai-juin 2018) : "Analyses temporelles des ondes cérébrales pour la détection de marqueurs de la théorie de l'esprit chez des patients schizophrènes"
— Encadrement de David Gérard, stagiaire de M1 STAPS (mars-juin 2017) : "Impact de l'imagerie mentale sur la charge cognitive appliquée au tennis"
— Encadrement d'Issam Aggour et Majd Abazid, stagiaire du M1 E3A (mai-juin 2017) : "Visualisation temps réel de signaux temporels avec une Raspberry Pi"
— Encadrement d'Adèle Wagner et Alice Mondjanagni, stagiaires d'IUT Informatique (juillet-août 2016) : "Serious game pour un permis piéton adapté", dont le travail a été présenté aux journées de la mobilité de Vélizy et dont l'application Android est disponible sur le store.
— Encadrement de Marwa Ben Taleb Ali, stagiaire de Master 1 Ensta ParisTech (février-juin 2016) : "Caractérisation des variations temporelles de l'activité cérébrales avec des réseaux de neurones profonds"
— Encadrement de Romain Da Rocha, stagiaire de 2e année ingénieur ISTY (mai-septembre 2015) : "Vectorisation des codes de calculs pour la géométrie Riemanienne"

— Encadrement de Deividas Malcevas, L3 à Alytaus Kolegija en Lituanie (mai-juillet 2015) : "Création d'un jeu sérieux en environnement immersif pour la conduite de fauteuil roulant"
— Encadrement de Franck Roussel, stagiaire IUT Informatique (avril-juin 2014) : "Etude et conception d'une interface pour la réalité augmentée"
— Encadrement de Mindaugas Ardaravicius et Deividas Margelis en L3 à Alytaus Kolegija en Lituanie (avril-juin 2013) : "Distribution des processus de calculs sur des configurations hétérogènes", dont les travaux ont été présentés au congrès national de la recherche des IUT
— Encadrement d'Alexandre Vincendeau, stagiaire IUT informatique (avril-juin 2013) : "Développement d'une interface graphique pour le traitement du signal en Python"
— Encadrement d'Arnaud Kabeya, stagiaire de Master 1 Intelligence Artificielle de l'Université de Cergy-Pontoise (janvier-mai 2010) : "Améliorations et évaluation des mécanismes d'attention visuelle pour le contrôle d'un bras robotique"

Diffusion scientifique

— Exposition de 3 installations interactives art-science co-conçues avec l'artiste Maflohé Passedouet, lors de l'exposition "Entrevoir l'invisible" à la Commanderie des Templiers d'Élancourt d'avril à juillet 2018, puis en avril et mai 2019 à la ferme du Mousseau et à Boston, USA en octobre 2019
— Intervention et accompagnement des élèves de 4e du collège Giacometti pour leur projet sur l'humain augmenté en 2018
— Invitation à la journée d'étude du festival Orphée, sur les arts et le handicap
— Article "Quand la machine se substitue au cerveau" dans le journal de l'UVSQ "Vert & Bleu" de mars 2014.
— Organisation et animation d'une table ronde sur les interfaces cerveau-machine lors de la réunion annuelle du CENRob (Centre d'Expertise Nationale sur les aides Robotiques, labellisé par la Caisse Nationale de la Solidarité pour l'Autonomie) le 4 avril 2013. Cette journée regroupe les principaux acteurs français et internationaux en robotique d'assistance pour le handicap.

— Je présente tous les ans des animations autour des interfaces cérébrales et des activités du laboratoire à la fête de la science, à Vélizy ou à Saint-Quentin en Yvelines
— J'accueille régulièrement des élèves de 3e pour leur stage d'observation : Aurélien Neuhart, Ganem Magroune, Kélian Raoult, Ugo Friederich.

Tâches d'intérêt général

Entre 2013 et 2016, je me suis occupé d'une partie des emplois du temps des départements informatique et réseaux & télécommunications. J'ai également assuré pendant cette période le rôle de directeur des études pour les étudiants de deuxième année du département R&T. Les maquettes du programme pédagogique national sont à implémenter et à répartir sur le contingent des enseignantes et enseignants. Pour chaque département, j'ai donc pris contact avec les enseignantes et enseignants pour adapter l'emploi du temps à leurs contraintes et aux contraintes matérielles de disponibilités des salles. Cette charge comprend également la modification des emplois du temps et la gestion du report des cours, en lien avec les directeurs de département, au cours de l'année. Pour faciliter la gestion du planning, j'ai mis en place une procédure dans le département R&T pour obtenir un squelette relativement fixe au cours d'un semestre.

J'ai participé aux réunions du conseil et j'ai présenté les actions menées sur la prise en charge du handicap au niveau de l'Université Paris-Saclay et de son articulation avec l'IUT de Vélizy. En particulier, je présenterai le travail effectué autour de la formation à l'accessibilité numérique, pour les enseignants et pour les étudiants.

À partir de novembre 2016, j'ai été élu au Comité Technique (CT) de l'Université de Versailles Saint-Quentin. Cette instance relativement peu reconnue est d'une importance première pour le bon fonctionnement démocratique de l'Université, car toutes les décisions présentées au CA doivent d'abord passer devant le CT. Il est alors possible de discuter des orientations tant locales que régionales que souhaite adopter l'Université et de faire évoluer, certaines fois, la position de la direction de l'Université.

Depuis juin 2017, je suis responsable de communication du département réseaux & télécommunications. La tâche est importante, car la visibilité de

cette spécialisation est faible, surtout par rapport au recrutement local du département informatique. Je travaille de concert avec la chargée de communication de l'IUT et les enseignants du département pour remettre à jour les plaquettes de présentation de la formation. Je vais coordonner la mise en place des présentations des étudiants dans leur lycée d'origine. D'une part en automatisant l'envoi d'une lettre aux directeurs d'établissement leur signalant quels étudiants ont été recrutés dans notre IUT et leur proposant une présentation. D'autre part, en incitant et en formant les étudiants pour aller présenter la formation dans leur lycée. Je serais également responsable de la coordination des activités du département pour la journée porte ouverte.

1.3 Publications

Toutes ces publications sont disponibles sur HAL :
https://cv.archives-ouvertes.fr/sylvain-chevallier
ainsi qu'à l'adresse suivante :
https://scholar.google.fr/citations?user=j5Tu_SQAAAAJ

Chapitre de livre

[1] **Sylvain Chevallier**, Emmanuel Kalunga, Quentin Barthélemy, Florian Yger. Riemannian classification for SSVEP based BCI : offline versus online implementations. In *Brain-Computer Interfaces Handbook*, pp. 371-396, 2017.

[2] Taras Kowaliw, Nicolas Bredeche, **Sylvain Chevallier**, René Doursat. Artificial Neurogenesis : An Introduction and Selective Review. In *Growing Adaptive Machines*, pp 1-60, Springer, 2014.

Journaux internationaux

[3] Yuan Yang, **Sylvain Chevallier**, Joe Wiart, Isabelle Bloch. Subject-specific time-frequency selection for multi-class motor imagery-based BCIs using few Laplacian EEG channels. *Biomedical Signal Processing and Control*, 38, 302-311, 2017. [Engineering **Q2**]

[4] Emmanuel K Kalunga, **Sylvain Chevallier**, Quentin Barthélémy, Karim Djouani, Yskandar Hamam, Eric Monacelli. Online SSVEP-based BCI using Riemannian Geometry, *Neurocomputing*, 191, 55-68, 2016. [Computer Science, Artificial Intelligence, **Q1**]

[5] Yuan Yang, Isabelle Bloch, **Sylvain Chevallier**, Joe Wiart. Subject-Specific Channel Selection Using Time Information for Motor Imagery Brain-Computer Interfaces. *Cognitive Computation*, 8(3), 505-518, 2016. [Computer Science, Artificial Intelligence **Q1**]

[6] Yuan Yang, **Sylvain Chevallier**, Joe Wiart, Isabelle Bloch. Time-frequency optimization for discrimination between imagination of right and left hand movements based on two bipolar EEG channels. *EURASIP Journal on Advances in Signal Processing*, 2014 1-38, 2014. [Engineering **Q2**]

[7] Zoran Tiganj, **Sylvain Chevallier**, Eric Monacelli. Influence of extracellular oscillations on neural communication : A computational perspective. *Frontiers in Computational Neuroscience*, 8(9), 2014. [Mathematical & Computational Biology **Q2**]

Conférences internationales avec comité de relecture

[8] Jinan Charafeddine, Mohamad Khalil, Samer Al Fayad, **Sylvain Chevallier** and Didier Pradon. Neuromotor Strategy of Gait Rehabilitation for Lower-Limb Spasticity. *IEEE ICABME*, 2019.

[9] Amina Alaoui-Belghiti, **Sylvain Chevallier**, Eric Monacelli. Unsupervised anomaly detection using optimal transport for predictive maintenance. In *ICANN*, Munich, Allemagne, 2019.

[10] Jinan Charafeddine, **Sylvain Chevallier**, Mohamad Khalil, Didier Pradon, Samer Alfayad. Neuro-Motor Index : Designing an EMG Control Scheme Robust to Lower-Limb Disorder. In *EMBC*, 2019.

[11] **Sylvain Chevallier**, Guillaume Bao, Mayssa Hammami, Fabienne Marlats, Louis Mayaud, Djillali Annane, Frédéric Lofaso, Eric Azabou. Brain-machine interface for mechanical ventilation using respiratory-related evoked potential. In *ICANN*, Rhodes, Grèce, 2018

[12] Emmanuel Kalunga, **Sylvain Chevallier**, Quentin Barthélemy. Transfer learning for SSVEP-based BCI using Riemannian similarities between users. In *EUSIPCO*, Rome, Italie, 2018.

[13] Estelle Massart, **Sylvain Chevallier**. Inductive means and sequences applied to online classification of EEG. In *Geometric Science of Information*, Paris. Springer, 2017.

[14] Amin Zammouri, Abdelaziz Ait Moussa, **Sylvain Chevallier**. Embedded-BCI : assessment of parallelizing computations on an embedded system. In *Last Mile Smart Mobility*, Paris. IEEE, 2016

[15] Hugo Martin, **Sylvain Chevallier**, Eric Monacelli. Smart Interface for New Building Design Process. In *Last Mile Smart Mobility*, Paris. IEEE, 2016

[16] Emmanuel Kalunga, **Sylvain Chevallier**, Quentin Barthélemy, Karim Djouani, Yskandar Hamam, Eric Monacelli. From Euclidean to Riemannian means : Information geometry for SSVEP classification. In *Geometric Science of Information*, pp. 595-604. Palaiseau. 2015.

[17] Hugo Martin, **Sylvain Chevallier**, Eric Monacelli. Adaptive visualization system for construction building information models using saliency. In *Construction Application of VR*, Banff, Canada, 2015

[18] Emmanuel Kalunga, **Sylvain Chevallier**, Quentin Barthélemy. Data augmentation in Riemannian space for Brain-Computer Interfaces. In *ICML Stamlins*, Lille, 2015.

[19] Amin Zammouri, Abdelaziz Ait Moussa, **Sylvain Chevallier**, Eric Monacelli. Intelligent ocular artifacts removal in a non-invasive single channel EEG recording, *IEEE ISCV*. Fez, Morocco, 2015.

[20] **Sylvain Chevallier**, Quentin Barthélémy, Jamal Atif. Subspace metrics for multivariate dictionaries and application to EEG. *IEEE ICASSP*. Florence, Italie, 2014.

[21] **Sylvain Chevallier**, Quentin Barthélémy, Jamal Atif. On the Need for Metrics in Dictionary Learning Assessment. *IEEE Eusipco*. Lisbonne, Portugal, 2014.

[22] Emmanuel Kalunga, **Sylvain Chevallier**, Olivier Rabreau, Eric Monacelli. Hybrid interface : Integrating BCI in Multimodal Human-Machine Interfaces. *IEEE/ASME AIM*, Besançon, 2014

[23] Emmanuel Kalunga, Karim Djouani, Yskandar Hamam, **Sylvain Chevallier**, Eric Monacelli. SSVEP Enhancement Based on Canonical Correlation Analysis to Improve BCI Performances. *IEEE AFRICON*, pp. 1-5, Île Maurice, 2013.

[24] Zoran Tiganj, Mamadou Mboup, **Sylvain Chevallier**, Emmanuel Kalunga. Online frequency band estimation and change-point detection. *ICSCS*, Lille, France, 2012.

[25] Yuan Yang, **Sylvain Chevallier**, Joe Wiart, Isabelle Bloch. Time-frequency selection in two bipolar channels for improving the classification of motor imagery EEG. *IEEE EMBC*, United States, 2012.

[26] Hugo Martin, **Sylvain Chevallier**, Eric Monacelli. Fast calibration of hand movements-based interface for arm exoskeleton control. *ESANN*. Bruges, Belgique, 2012.

[27] Yuan Yang, **Sylvain Chevallier**, Joe Wiart, Isabelle Bloch. Automatic selection of the number of spatial filters for motor-imagery BCI. *ESANN*. Bruges, Belgique, 2012.

[28] Yuan Yang, **Sylvain Chevallier**, Joe Wiart, Isabelle Bloch. A self-paced hybrid BCI based on EEG and EOG. *Workshop TOBI*, Wurzburg, Allemagne, 2012

[29] **Sylvain Chevallier**, Nicolas Bredeche, Hélène Paugam-Moisy, Michèle Sebag. Emergence of Temporal and Spatial Synchronous Behaviors in a Foraging Swarm. *ECAL*, Paris, 2011.

[30] Ludovic Arnold, Sébastien Rebecchi, **Sylvain Chevallier**, Hélène Paugam-Moisy. An introduction to deep learning. In *ESANN*, Bruges, Belgique, 2011.

[31] **Sylvain Chevallier**, Hélène Paugam-Moisy, Michèle Sebag. SpikeAnts, a spiking neuron network modelling the emergence of organization in a complex system. In *NeurIPS*, Vancouver, 2010.

[32] **Sylvain Chevallier**, Nicolas Cuperlier, Philippe Gaussier. Efficient neural models for visual attention. In *ICCVG*, *Lectures Notes in Computer Sciences*, Springer, Varsovie, Pologne, 2010.

Conférences nationales avec comité de relecture

[33] Eric Azabou, Guillaume Bao, **Sylvain Chevallier**, Fabienne Marlats, Bernard Bussel, Louis Mayaud, Hélène Prigent, Michel Petitjean, Fréderic Lofaso. Supra-threshold inspiratory loads elicit respiratory related evoked potentials in healthy subjects. In *Neurophysiologie Clinique*, Lille, 2018.

[34] **Sylvain Chevallier**, Hélène Paugam-Moisy, Michèle Sebag. SpikeAnts : un réseau de neurones impulsionnels pour modéliser l'organisation émergente dans un système complexe. *NeuroComp*, Lyon, France, 2010.

En plus de ces travaux de recherches publiés, plusieurs travaux en cours ont été envoyé à des revues et sont en cours d'évaluation. Je les mentionne tout de même ici car ils attestent d'un travail qui, même s'il n'est pas validé par le processus de publication, montre les approches en cours et les orientations de mes recherches.

Travaux en cours

[35] **Sylvain Chevallier**, Emmanuel Kalunga, Quentin Barthélemy, E. Monacelli. Assessment of Riemannian distances and divergences for SSVEP-based BCI. Neuroinformatics. Submitted, major revision.

[36] Olivier Rabreau, **Sylvain Chevallier**, Luc Chassagne, Eric Monacelli. SenseJoy, a non-invasive solution for assessing user behavior during powered wheelchair driving tasks. Journal of NeuroEngineering and Rehabilitation. Submitted, major revision.

[37] Jinan Charafeddine, **Sylvain Chevallier**, Mohamad Khalil, Didier Pradon and Samer Al-Fayad. Biokinematic Control Strategy for Walking Rehabilitation Exoskeleton based on User Intention. Submitted to International Journal of Modeling and Optimization.

[38] Hugo Martin, **Sylvain Chevallier**, Eric Monacelli. Adaptive visualization for BIM experts : coping with unstructured big data in construction. Submitted to Frontiers in Built Environment. Preprint on arXiv.

1.4 Enseignements

Année universitaire	Heures EqTD
2011-2012	208
2012-2013	222
2013-2014	196
2014-2015	233
2015-2016	265
2016-2017	202
2017-2018	225

Activités d'enseignements

J'ai enseigné dans plusieurs établissements depuis 2005, tout d'abord comme moniteur au département informatique de l'IUT d'Orsay, puis comme ATER à l'Université de Cergy-Pontoise. Depuis 2011, j'enseigne dans les départements d'Informatique et de Réseaux & Télécoms de l'IUT de Vélizy à l'Université de Versailles Saint-Quentin-en-Yvelines. J'interviens également au sein du Master 2 Robotique, Assistance et Mobilité de l'Université Paris-Saclay, de l'Institut des Sciences et Techniques des Yvelines (ISTY) et j'ai fait des interventions à l'École nationale supérieure de l'électronique et de ses applications (ENSEA).

1.5 Conception d'enseignements et pratiques pédagogiques

À l'occasion de la mise à jour du PPN du département informatique en 2013, j'ai repris le module d'introduction à l'administration système. J'ai conçu et réalisé un nouveau cours [15] en coordination avec le cours d'introduction à la programmation, pour amener les étudiantes et les étudiants à être au plus tôt autonomes sur les environnements Linux. Ce module

15. L'environnement de cours est disponible ici : https://e-campus.iut-velizy.uvsq.fr/claroline/course/index.php?cid=INM1101

joue un rôle important pour l'évaluation du semestre : en concertation avec l'équipe enseignante, j'ai mis en place plusieurs contrôles et TP notés qui permettent d'identifier et de repérer les étudiantes et les étudiants à aider avant les vacances de la Toussaint. Pour permettre un suivi plus fin de toute la promotion, j'ai utilisé un outil de participation numérique lors de mes cours magistraux : les étudiantes et étudiants sont invités à répondre anonymement à des questions sur une plateforme en ligne. J'analyse les réponses en amphithéâtre et je peux ainsi repérer les notions qui n'ont pas du tout été intégrées. Suite aux Journées Initiatives Pédagogiques de l'Université Paris-Saclay [16], j'ai commencé à appliquer dans mon cours magistral les propositions faites pour mettre en place la pédagogie renversée. Les évaluations des étudiantes et étudiants en fin de module sur ces innovations étaient plutôt positives, en revanche les conclusions par rapport à l'évolution des notes étaient impossibles à interpréter, car l'équipe enseignante en système a largement changé.

J'ai mis en place l'utilisation d'outil de génération de QCM et de correction automatique [17] et j'ai aidé les utilisateurs au sein du département informatique. Comme l'UVSQ va changer de plateforme pour passer sur Moodle, j'ai travaillé avec le référent de notre site, Jean-Pierre Coulon, pour faire un test pilote dans le module dont je m'occupe. Les étudiants ont pu utiliser la plateforme Moodle et j'ai adapté les évaluations pour qu'elles permettent l'évaluation la plus continue et la plus proche possible des notions vues en TP, pour favoriser les interactions avec les enseignantes et enseignants. Avec Laurent Marsan, directeur des études du département informatique, qui a mis en place l'évaluation par compétences [18] et formé l'équipe enseignante, j'ai travaillé à la mise en place du référentiel de compétence et à la mise en place de groupes pilotes pour ma matière. J'ai pris contact avec l'Institut Villebon-Charpak pour échanger sur les méthodes d'évaluation dans des groupes hétérogènes. Ces discussions ont abouti à l'établissement d'un cahier des charges pour une application de remontée automatique de l'évaluation des compétences. J'ai encadré en 2016 un projet étudiant de l'Institut des Sciences et Techniques des Yvelines (ISTY, école d'ingénieurs informatique de l'UVSQ) sur ce sujet en utilisant des outils de

16. https://www.universite-paris-saclay.fr/fr/evenement/2eme-journee-initiatives-pedagogiques-plaisir-denseigner-et-plaisir-dapprendre
17. http://home.gna.org/auto-qcm/index.fr
18. via la plateforme SACoche, hébergée par l'académie de Versailles pour notre IUT

traitement d'images et une application de remontée d'information. En 2017, j'ai encadré deux étudiants de l'ISTY pour mettre en place un outil de visualisation des connaissances dans Moodle, réalisé en lien avec les collègues de l'IUT d'Orsay, et qui soit connectable avec la plateforme SACoche. Ces projets ont vocation à être pérennisés et diffusés plus largement d'abord dans l'IUT pour une phase d'évaluation, puis avec une licence libre ensuite.

Dans le département réseaux & télécommunications, j'ai créé deux nouveaux cours pour l'administration système. Le premier est un cours en 1ere année sur le déploiement et l'installation d'une distribution GNU/Linux [19]. La spécificité de ce cours et de ces TP est de permettre aux étudiantes et étudiants de comprendre les différentes phases d'installation d'une distribution en les réalisant eux-mêmes. Cette séquence de TP est complexe à mettre en œuvre, car les étudiantes et étudiants sont mis en situation et formatent directement les disques. J'ai donc mis en place une solution de création d'images disque et de restauration pour que les salles puissent être partagées avec d'autres collègues pendant la durée du module.

En 2e année du DUT RT, j'ai mis en place un module pour l'automatisation des tâches d'administration système. J'ai créé les cours et les supports pour ce module, en intégrant le fait que le Python était de plus en plus demandé pour les poursuites d'études et pour l'intégration dans les métiers de l'administration système. J'ai utilisé les *jupyter notebook* qui permettent de mélanger explications, notations mathématiques et code exécutable. Ce support me permet de faire des cours magistraux plus dynamiques et plus interactifs, les étudiantes et les étudiants utilisent ensuite ce support pour faire leur TD et leurs comptes-rendus de TP. Comme le cours est modifié en fonction des interactions avec la classe, la version courante est archivée avec un gestionnaire de version et mise à disposition de tous [20].

J'ai appliqué le même principe pour mes cours en dans le Master 2 RAM de l'Université Paris-Saclay. En plus des supports de cours magistraux, des *jupyter notebooks* permettent de mêler code et explications pour ce cours sur l'apprentissage automatique et la fouille de données [21]. Je me suis appuyé

19. Ce cours est visible sur https://e-campus.iut-velizy.uvsq.fr/claroline/course/index.php?cid=M2102

20. les cours et TP sont disponibles ici : https://e-campus.iut-velizy.uvsq.fr/claroline/course/index.php?cid=RTM3206. La version modifiée avec le groupe est ici : https://github.com/sylvchev/coursIntroPython

21. Les cours sont visibles ici : https://e-campus.iut-velizy.uvsq.fr/claroline/course/

sur une plateforme d'écriture scientifique en ligne (http://authorea.com/) pour expliquer les principes de la formation par la recherche et de la publication scientifique, en sensibilisant les étudiantes et étudiants aux problématiques de l'*open access* et de la reproductibilité des analyses de données. Les master 2 ont pu utiliser cette plateforme pour rendre un devoir analysant des articles choisis et en utilisant les méthodes de traitement de données qui y étaient décrites. L'intérêt de la plateforme est que les étudiants ont pu inclure le code et les données utilisées pour générer les figures qu'ils ont réalisées pour leurs devoirs.

Pour faire le lien avec mes travaux de recherches, l'IUT de Vélizy et le laboratoire LISV ont accepté de me soutenir pour acquérir le matériel nécessaire pour travailler en petit groupe sur les interfaces cérébrales. J'ai utilisé ce matériel pour proposer aux étudiantes et étudiants de l'IUT de Vélizy de travailler sur des projets tutorés : un groupe d'étudiants a travaillé sur la détection de l'attention lors du suivi de cours en ligne, un autre groupe a travaillé sur l'authentification par ondes cérébrales pour déverrouiller un poste de travail. Ce matériel est également utilisé avec le groupe du Master 2 pour un TP d'analyse de données sur les biosignaux et les ondes cérébrales.

Avec le GT Handicap de l'Université Paris-Saclay, nous avons obtenu un financement interne pour former à l'accessibilité numérique le corps enseignant et les groupes d'étudiantes et d'étudiants. J'ai participé aux modules de formation sur l'accessibilité des documents numériques et des applications iOS/Android. Nous réalisons un kit de formation qui sera, à terme, mis à disposition de tout le personnels enseignant de l'Université Paris-Saclay pour intégrer les notions d'accessibilité dans leurs cours. Tous mes supports de cours ont été modifiés pour prendre en compte les recommandations préconisées pendant ces formations et j'interviens auprès des collègues pour les aider à rendre leur cours accessibles.

index.php?cid=RAM et les notebooks ici : https://github.com/sylvchev/coursMLpython

2 Synthèse des travaux

Cette partie présente les travaux effectués après ma thèse, travaux commencés en post-doctorat à l'INRIA et à Télécom ParisTech, puis continués au LISV comme maître de conférences. Les thématiques traitées ont évolué par rapport à mon travail doctoral, qui était positionné au croisement entre la vision pour la robotique et les sciences cognitives.

Dans mes travaux de thèse, je m'étais intéressé à l'utilisation de modèles de neurones spécifiques pour modéliser les prétraitements qui ont cours dans la rétine et les premiers relais corticaux et en proposer une implémentation adaptée aux contraintes de vision en robotique. Les modèles de neurones impulsionnels décrivent l'activité d'un neurone assimilé spatialement à un point et dont la dynamique est simulée avec des équations différentielles (Brette, 2003 ; Gerstner et Kistler, 2002). Leur intérêt principal est de discrétiser l'échange d'information entre les neurones (L. Perrinet et al., 2004), qui communiquent par échange de potentiels d'actions ou *spikes*. L'architecture de traitement que j'ai proposé en thèse permet de réaliser des processus de filtrages spatio-temporels, inspirés par ceux proposés dans la littérature sur la pré-attention visuelle (Hérault, 1999 ; Phuoc et al., 2009 ; Treisman et Gelade, 1980). À la suite de ma thèse, j'ai travaillé au sein de l'équipe Neurocybernétique de l'Université de Cergy-Pontoise, où j'ai implémenté une architecture de pré-attention sur leurs robots et j'ai évalué différentes stratégies de codage de l'information à partir des potentiels d'actions (Chevallier, Cuperlier et al., 2010).

Ce type d'approche, qui avait peu d'opportunités applicatives, a connu un large regain d'intérêt avec la mise sur le marché de caméra de type *Dynamic Vision Sensors* (Gallego et al., 2019). Ces caméras transforment un flux visuel en flux des évènements temporels discret et sont particulièrement utiles pour les cas où le transfert ou le stockage d'information est cher ; au lieu d'envoyer une image complète à chaque trame, seules les variations d'une trame à l'autre sont transmises de façon asynchrone. Le traitement des informations issues de ces capteurs est un sujet de recherche actif, un

large effort est fait sur les possibilités d'utiliser des modèles d'apprentissage automatique ou *machine learning* à partir de la sortie de ces capteurs.

J'ai ensuite rejoint l'équipe TAO de l'INRIA Paris-Saclay puis l'équipe TSI du LTCI de Télécom ParisTech pour travailler comme post-doc sur les interfaces cérébrales. J'ai commencé alors ma collaboration avec Yuan Yang (Yang, Chevallier et al., 2012), qui était en thèse sous la direction d'Isabelle Bloch, collaboration que nous avons continué lors de son post-doc à l'Université de Delft en Hollande (Yang, Bloch et al., 2016) puis à la Northwestern University aux États-Unis (Yang, Chevallier et al., 2017). Ce sont les travaux que je vais présenter dans cette synthèse et qui utilisent l'électroencéphalographie (EEG) pour capturer l'activité cérébrale. La motivation scientifique qui m'anime tend vers le même but, bien que les domaines et les outils théoriques soient très différents, c'est celle de la compréhension du mode de communication des neurones. Avec les interfaces cérébrales, et l'EEG, le niveau n'est plus unitaire – le codage de l'information par un neurone individuel – mais celui de la population. Ce changement de thème de recherche s'est ainsi passé relativement naturellement de mon point de vue, d'autant plus que les sciences cognitives font un retour notable dans les protocoles d'entraînement et d'utilisation des interfaces cérébrales en mettant en lumière l'importance des interactions humaines.

Cette transition a été également facilitée par la réalisation d'un travail qu'on pourrait qualifier de charnière entre les modèles impulsionnels et l'analyse d'activité de population. Lors de mon arrivée au LISV, j'ai pu recruter Zoran Tignaj comme post-doctorant pour quelques mois et nous avons travaillé sur l'interaction entre l'activité d'un neurone et le champ de potentiels local. Ce champ de potentiel local, qui est à l'origine de l'EEG, est la résultante de l'activité électrique d'un groupe de neurones proches et il est le plus souvent assimilé à un épiphénomène sans conséquence locale. En effet, les modèles de neurones théoriques font l'hypothèse que les informations sont uniquement échangées par les canaux de communication inter-neurones [1], ce qui revient à considérer que les modèles de neurones sont isolés électriquement. L'hypothèse selon laquelle deux neurones proches spatialement peuvent avoir une interaction sans avoir de

1. le plus souvent les synapses, dans certains cas spécifiques les *gap junctions* ou les interactions avec d'autres corps cellulaires, type cellules gliales.

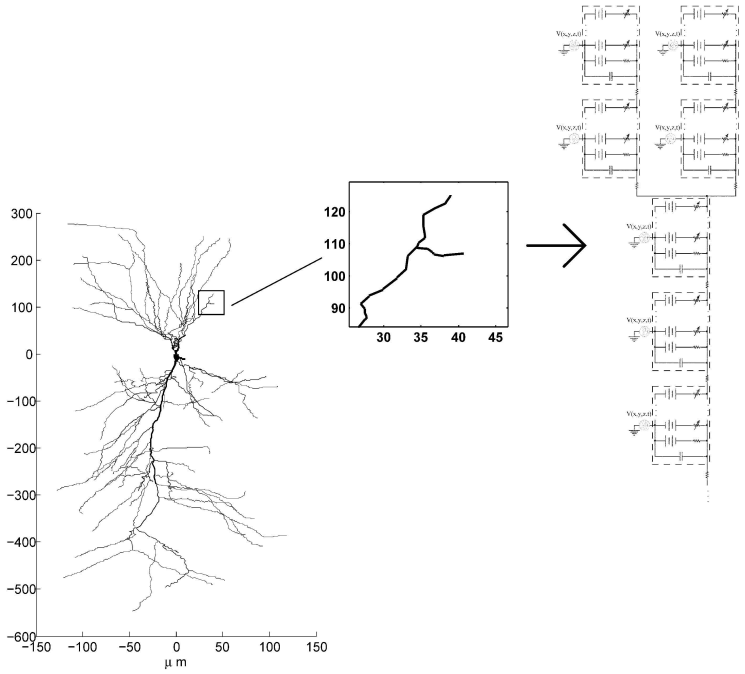

FIGURE 2.1 – Modèle spatial à compartiments multiples d'un neurone hippocampal CA3 avec la prise en compte des oscillations extracellulaires.

liaisons physiques est appelée communication éphaptique (Anastassiou et al., 2011). Ainsi, même si l'effet d'un champ de potentiel local est trop faible pour déclencher l'émission d'un potentiel d'action par un neurone, il peut avoir un effet qui retarde ou facilite l'émission de potentiels d'action. Nous avons conduit une série d'expérimentations sur des neurones de morphologies différentes que nous avons soumis à des champs de potentiels d'intensité comparable ou supérieure à ceux observés *in vivo*. Notre étude montre que pour les types de stimulations observés, seules les oscillations de grande amplitude ont une influence sur l'activité d'un neurone (Tiganj et al., 2014), ce qui correspond aux amplitudes observées lors de stimulus électriques externes comme les stimulations transcrâniennes magnétiques (TMS, (Hallett, 2000)) ou électriques (TES, (Ozen et al., 2010)) ou encore les stimulations profondes (*Deep Brain Stimulation*, (Joucla et Yvert, 2012)).

Le reste de ce manuscrit présente les travaux faits sur les interfaces cérébrales et qui utilisent les signaux EEG comme base de travail. L'EEG

peut être décrit comme la résultante de la somme des potentiels locaux, il n'est donc plus possible d'étudier les variations neuronales individuelles, il faut travailler sur des codages de larges populations, associant les neurones d'aires cérébrales entières. Évidemment, une voie de recherche importante en interface cérébrale concerne les interfaces invasives, où des capteurs sont installés sous la boîte crânienne. Ce type d'approche existe depuis longtemps et a connu un tournant médiatique récent lors de l'annonce par Neuralink, la compagnie d'Elon Musk, d'une nouvelle technologie permettant d'insérer des milliers de microélectrodes et faire des enregistrements simultanés [2]. L'autre type d'approche consiste à enregistrer l'activité de façon non-invasive, en utilisant des mesures de champs de potentiel électrique (EEG) ou hémodynamique (fNIRS), pour caractériser les états cognitifs chez l'être humain afin de mettre en place des interfaces cérébrales.

2.1 Les interfaces cérébrales

Les interfaces cérébrales ou *brain computer interfaces* (BCI) sont développées depuis les années 1970 (Vidal, 1973) et offrent la possibilité d'interagir avec un système, robotique ou virtuel. Leur caractéristique principale est de permettre de s'affranchir des capacités musculaires pour communiquer avec une machine. Les BCI se sont donc tout particulièrement bien intégrées dans le domaine du handicap et de la robotique d'assistance (Babiloni et al., 2007 ; Bekaert et al., 2009).

Après un accroissement rapide de la taille de la communauté scientifique dans les années 2000 (Wolpaw et al., 2002), de nombreuses limitations ont été identifiées et constituent le noyau dur d'un verrou scientifique majeur (Allison et Neuper, 2010). Une première limitation concerne les perturbations induites par les activités musculaires (cou, mâchoires, face), qui rendent très difficile l'utilisation des BCI dans un environnement de vie quotidienne, comme sur un fauteuil roulant électrique ou avec un dispositif d'assistance robotique. En effet, l'amplitude du signal électrique mesuré en électroencéphalographie est de l'ordre du μV alors que les muscles génèrent des signaux d'amplitude mesurable en centaines de μV. Pour réduire ces perturbations d'origine musculaire, la plupart des protocoles nécessitent

2. https://neuralink.com/

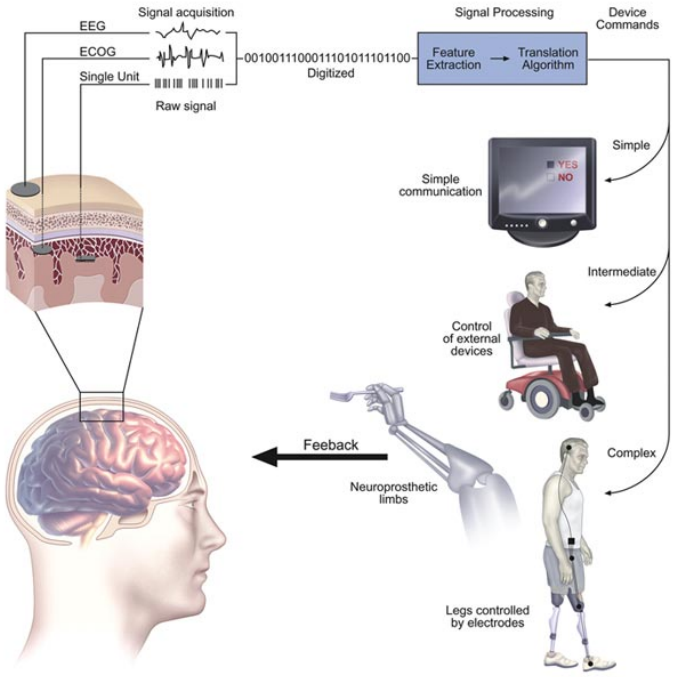

FIGURE 2.2 – Les différentes étapes du traitement de l'information pour une interface cérébrale. [source : CINT, University of Washinghton]

que l'utilisateur soit parfaitement calme, bien installé et ne bouge ni la tête, ni les muscles faciaux. Bien évidemment, ces contraintes ne sont pas compatibles avec une utilisation mobile hors des salles d'expérimentations.

La seconde limitation est plus complexe et encore largement inexpliquée. Pour un utilisateur sur quatre ou sur cinq, les performances des systèmes BCI sont très mauvaises, à tel point que ce phénomène est qualifié d'illettrisme BCI (Vidaurre et Blankertz, 2010). Ce type d'utilisateur ne peut donc pas utiliser certaines BCI et, pour l'instant, aucun facteur simple connu ne permet d'expliquer ce phénomène. De façon plus générale, les BCI nécessitent une complète concentration de l'utilisateur sur la tâche à effectuer, ce qui est rapidement épuisant.

Une partie de la communauté des BCI s'est structurée à partir de 2002

autour d'évaluations, les *BCI Competition*, où le but est de proposer des algorithmes de traitements des signaux électroencéphalographiques (EEG) les plus robustes possible. Ainsi, pour différentes tâches cognitives (imagination motrice, potentiel évoqué, etc.) les données EEG de plusieurs sujets sont enregistrées. Les meilleures approches sont celles qui permettent de discriminer le plus précisément possible les différents états évalués. Par exemple, dans le cas de l'imagination motrice, il faut être capable de différencier lorsque le sujet imagine bouger sa main gauche ou sa main droite.

Les différents états reconnus sont utilisés comme des commandes pour interagir avec un ordinateur ou une machine. Le système fournit en règle générale un retour à l'utilisateur sur la commande qu'il a reconnue. Cependant, en plus des verrous mentionnés précédemment (perturbations musculaires et illettrisme BCI), se rajoute le problème que le système doit fournir une réponse suffisamment rapidement pour maintenir un rythme d'interaction correct avec l'utilisateur. Cette contrainte temporelle limite grandement le choix des méthodes qui peuvent être employées pour traiter les signaux EEG.

Une approche alternative est développée depuis quelques années, qui vise à utiliser les BCI pour faire du suivi ou de la détection d'états cérébraux plutôt que de la commande (Borghini, Astolfi et al., 2014 ; George et Lécuyer, 2010). Il s'agit de travailler à une échelle de temps de l'ordre de la minute, beaucoup plus en adéquation avec les performances des systèmes actuels, pour adapter les interactions homme-machine en fonction de marqueurs cognitifs, par exemple de la charge cognitive, de l'attention, de l'endormissement, etc.

2.2 Apprentissage de dictionnaires parcimonieux

Les interfaces cérébrales nécessitent de pouvoir décoder les enregistrements EEG pour détecter des états cérébraux connus dans un temps court, compatible avec des interactions humaines. Cependant les données EEG sont temporellement complexes et souvent de grande dimension, ce qui limite grandement les approches directement utilisables. Cependant, la propagation des signaux cérébraux contraint fortement leur corrélation spatiale. Ainsi, un signal EEG est décomposable comme étant la somme de différentes composantes et de sources de bruits exogènes. La décomposition parcimo-

nieuse, couplée à l'apprentissage de dictionnaires, permet de séparer les composantes cérébrales des bruits exogènes et a fait ses preuves sur des problèmes de complexité comparable.

Dans sa formulation classique, l'apprentissage de dictionnaire vise à capturer le maximum d'énergie d'un ensemble de signaux d'apprentissage $\{x_j\}_{j=1}^{q}$ avec $x_j \in \mathbb{R}^n$ et à les représenter par une famille de m atomes $D_u = \{u_i\}_{i=1}^{m}$ avec $u_i \in \mathbb{R}^n$ grâce à un ensemble de coefficients parcimonieux $\{a_j\}_{j=1}^{q}$, avec $a_j \in \mathbb{R}^m$ (Tošić et Frossard, 2011). Cette famille D_u, qui est redondante ($m \gg n$), est appelé dictionnaire surcomplet. Les dictionnaires admissibles forment un ensemble convexe, défini comme $\mathcal{D}_u = \{D_u \in \mathbb{R}^{n\times m} : \|u_i\|_2 \leqslant 1,\, i = 1,\dots,m\}$. Le problème d'apprentissage de dictionnaire s'écrit alors :

$$\min_{D_u\in\mathcal{D}_u} \sum_{j=1}^{q} \min_{a_j\in\mathbb{R}^m} \left\| x_j - \sum_{i=1}^{m} a_{i,j}\, u_i \right\|_F^2 \qquad \text{s.t. } \|a_j\|_0 \leqslant K,\ j=1,\dots,q\ , \tag{2.1}$$

où $a_{i,j} \in \mathbb{R}$ sont les coefficients de codage. La pseudo-norme ℓ_0 peut être relaxée par une norme ℓ_1 (Tošić et Frossard, 2011). Ce type de problème est résolu par des algorithmes d'apprentissage de dictionnaire, qui alternent décomposition parcimonieuse et mise à jour des éléments du dictionnaire, en suivant diverses méthodes décrites dans la littérature (Aharon et al., 2006 ; Engan, Aase et al., 2000 ; Engan, Skretting et al., 2007 ; Kreutz-Delgado et al., 2003 ; Mairal et al., 2010).

Plusieurs approches ont été proposées pour manipuler des données multicomposantes, par exemple des données audio-visuelles (Monaci, Jost et al., 2007 ; Monaci, Vandergheynst et al., 2009), des signaux d'électrocardiogrammes (Mailhé et al., 2009) ou d'EEG (Barthélemy, Gouy-Pailler et al., 2013). Dans ce cas, $\{X_j\}_{j=1}^{q}$ est un signal multicomposantes, avec $X_j \in \mathbb{R}^{n\times\rho}$, les dimensions additionnelles ρ étant soit portées par les coefficients pour des approches dites multicanaux, soit par les atomes du dictionnaire pour les approches multivariées, comme c'est illustré sur la figure 2.3.

Dans l'approche multicanaux (Gribonval et al., 2007 ; Rakotomamonjy, 2011), l'hypothèse est que les canaux des signaux peuvent être générés séparément par le même dictionnaire, les coefficients multicanaux codant pour la contribution de leurs atomes communs. Sous l'hypothèse forte

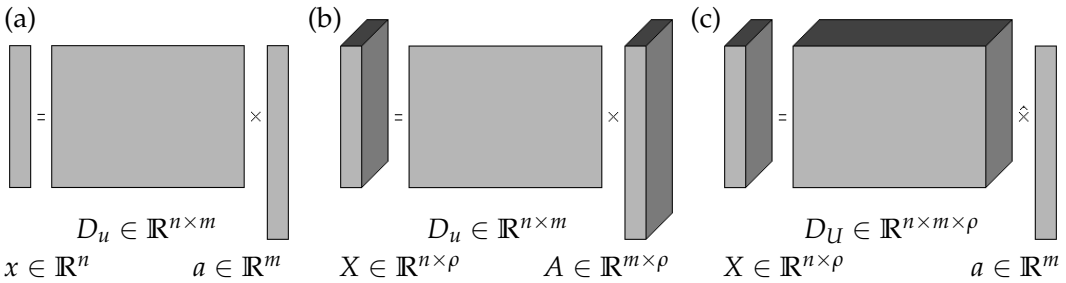

FIGURE 2.3 – Dans sa formulation commune, la décomposition d'un signal sur un dictionnaire d'atomes est représenté en (a). Pour manipuler des signaux multicomposants, il est possible d'utiliser une décomposition multicanaux (b) ou bien multivariée (c).

qu'une décomposition de rang 1 est possible, le problème d'apprentissage de dictionnaire s'écrit :

$$\min_{D_u\in\mathcal{D}_u} \sum_{j=1}^{q} \min_{A_j\in\mathbb{R}^{m\times\rho}} \left\| X_j - \sum_{i=1}^{m} u_i\, A_{i,j} \right\|_F^2 \quad \text{s.t. } \left\|A_j\right\|_x \leqslant K,\ j=1,\dots,q\ , \tag{2.2}$$

où la matrice $A_j \in \mathbb{R}^{m\times\rho}$ contient les coefficients multicanaux. $\|.\|_x$ indique une norme de type $\ell_{2,0}$ ou $\ell_{2,1}$ (Gribonval et al., 2007 ; Rakotomamonjy, 2011) qui permettent d'obtenir une sélection parcimonieuse des atomes et une distribution lissée des ρ coefficients sur la dimension portant les canaux.

Dans un cadre multivarié (Barthélemy, Gouy-Pailler et al., 2013 ; Barthélemy, Larue et al., 2012), les composantes du signal sont reconstruites à partir d'atomes multivariés qui sont combinés à partir d'un unique coefficient. Ce coefficient est donc identique dans toutes les composantes. Cette formulation multivariée de l'apprentissage de dictionnaire permet de préserver la géométrie de l'espace d'entrée en considérant un dictionnaire multivarié $D_U = \{U_i\}_{i=1}^m$ comme une collection de m atomes multivariés $U_i \in \mathbb{R}^{n\times\rho}$. L'ensemble convexe des dictionnaires considérés est $\mathcal{D}_U = \left\{D_U \in \mathbb{R}^{n\times m\times\rho} : \|U_i\|_F \leqslant 1,\ i=1,\dots,m\right\}$. Le problème d'apprentis-

sage de dictionnaire multivarié s'écrit :

$$\min_{D_U \in \mathcal{D}_U} \sum_{j=1}^{q} \min_{a_j \in \mathbb{R}^m} \left\| X_j - \sum_{i=1}^{m} a_{i,j} U_i \right\|_F^2 \quad \text{s.t.} \left\| a_j \right\|_0 \leqslant K,\ j = 1, \ldots, q \ . \tag{2.3}$$

On peut constater qu'après une vectorisation, ce modèle est computationnellement équivalent à un modèle univarié de l'équation (2.1), si l'on fait l'hypothèse que les ρ composantes sont indépendantes. J'ai implémenté une version Python de l'apprentissage de dictionnaire multivarié, qui libre et accessible gratuitement [3].

Il est particulièrement intéressant de noter que la première formulation du problème d'apprentissage de dictionnaire a été formulée par (Olshausen et Field, 1997) pour étudier une possible stratégie employée par les aires visuelles primaires pour coder efficacement la statistique des images naturelles. Cette idée a par la suite été validée expérimentalement sur des enregistrements chez le macaque (Vinje et Gallant, 2000). Si la formulation proposée dans (Olshausen et Field, 1997) est très proche de celle utilisée aujourd'hui, les auteurs proposaient par contre une méthode d'apprentissage complexe et peu stable. Des algorithmes bio-inspirés plus efficaces ont été proposés pour traiter les données audio (Smith et Lewicki, 2005) ou évènementielles (L. Perrinet, 2008 ; L. U. Perrinet, 2019).

L'approche multivariée permet de prendre en compte les interactions entre les composantes dès lors qu'on utilise les variétés matricielles adéquates. Il est particulièrement important de pouvoir comparer des dictionnaires appris dans des conditions différentes, par exemple sur deux sujets différents ou avec deux types de matériels différents sur le même sujet. C'est un problème récurrent pour tous les travaux sur les algorithmes d'apprentissage de dictionnaire, car il n'existe pas de moyen fiable de comparer deux dictionnaires et donc d'évaluer finement les contributions d'un nouvel algorithme (Chevallier, Barthelemy et al., 2014). Avec Jamal Atif et Quentin Barthélemy, nous avons proposé le moyen de construire une métrique ensembliste entre deux dictionnaires en étudiant la distance entre les sous-espaces qu'ils engendrent (Chevallier, Barthélemy et al., 2014). Cette construction est faite en deux étapes, la première consiste a définir la distance entre deux

3. https://github.com/sylvchev/mdla

atomes multivariés en les considérant comme des éléments d'une variété Grassmannienne (Absil et al., 2009). La seconde étape revient alors à utiliser des métriques ensemblistes ou des métriques de transport pour caractériser la distance entre deux collections d'atomes.

La variété $\mathbf{M}$ est l'ensemble des matrices de $\mathbb{R}^{n\times\varrho}$, avec $\varrho \leqslant n$. La variété de Stiefel $\mathbf{St}(\varrho, n)$ est l'ensemble des matrices de rang plein dans $\mathbf{M}$:

$$\mathbf{St}(\varrho, n) := \{U \in \mathbf{M} : \operatorname{rank}(U) = \varrho\} \,. \tag{2.4}$$

L'espace des colonnes $\mathcal{U}$ d'une matrice U dans $\mathbf{St}(\varrho, n)$ définit la base d'un sous-espace de dimension ϱ dans $\mathbb{R}^n$. La variété Grassmannienne $\mathbf{Gr}(\varrho, n)$ est une variété quotient, tel qu'un élément $\mathcal{U}$ de $\mathbf{Gr}(\varrho, n)$ peut également être caractérisé par un sous-espace de dimension ϱ dans $\mathbb{R}^n$. On dit d'une matrice U qu'elle engendre $\mathcal{U}$ si $\operatorname{span}(U) = \mathcal{U}$ et le sous-espace engendré par U est un élément de $\mathbf{Gr}(\varrho, n)$ si et seulement si $U \in \mathbf{St}(\varrho, n)$.

La première étape de notre métrique consiste à définir la distance entre les sous-espaces engendrés par deux atomes d'un dictionnaire multivarié. Il existe plusieurs distances dans la littérature, mais la distance plus communément utilisée est la distance cordale. Cette distance entre deux éléments $\mathcal{U}, \mathcal{W}$ d'une variété Grassmannienne $\mathbf{Gr}(\varrho, n)$ peut être calculée comme (Dhillon et al., 2008) :

$$d_{\mathrm{c}}(\mathcal{U}, \mathcal{W}) = \left(\varrho - \|\underline{U}^T \underline{W}\|_F^2\right)^{\frac{1}{2}} \,, \tag{2.5}$$

où $\underline{U}$ et $\underline{W}$ sont les bases orthonormales associées pour $\mathcal{U}$ et $\mathcal{W}$, telles que $\underline{U}^T\underline{U} = I_\varrho$ et $\operatorname{span}(\underline{U}) = \mathcal{U}$.

Pour construire la deuxième étape, nous allons considérer l'espace métrique $(\mathbb{G}, d_{\mathrm{c}})$ défini par la variété $\mathbf{Gr}(\varrho, n)$ et la distance d_{c}. Soit $\mathbb{U} = \{\mathcal{U}_i\}_{i\in I}$ et $\mathbb{W} = \{\mathcal{W}_j\}_{j\in J}$ deux sous-ensembles de $(\mathbb{G}, d)$, qui correspondent aux sous-espaces engendrés par les atomes de deux dictionnaires. Une première métrique ensembliste est donnée par la distance de Hausdorff, qui est définie comme :

$$d_{\mathrm{H}}(\mathbb{U}, \mathbb{W}) = \max\left(\sup_{\mathcal{U}\in\mathbb{U}} \inf_{\mathcal{W}\in\mathbb{W}} d(\mathcal{U}, \mathcal{W}), \sup_{\mathcal{W}\in\mathbb{W}} \inf_{\mathcal{U}\in\mathbb{U}} d(\mathcal{U}, \mathcal{W})\right). \tag{2.6}$$

Si on définit une mesure π sur l'espace produit $\mathbb{U} \times \mathbb{W}$ où $\mathbb{U}, \mathbb{W} \in \mathbb{G}_U$ avec $\mathbb{G}_U = \{(\mathcal{U}, \pi_\mathcal{U}) : \mathcal{U} \in \mathbb{G}\}$, une seconde métrique entre deux

dictionnaires est donnée par la distance de Wassertein (Villani, 2008) :

$$d_{\mathrm{W}}^{p}(\mathbb{U},\mathbb{W}) = \inf_{\pi\in\mathcal{M}(\pi_{\mathbb{U}},\pi_{\mathbb{W}})} \left(\int_{\mathbb{U}\times\mathbb{W}} d(\mathcal{U},\mathcal{W})^{p} d\pi(\mathcal{U},\mathcal{W}) \right)^{\frac{1}{p}} \tag{2.7}$$

pour $p \geqslant 1$. On peut alors définir la distance entre $D_U = \{U_i\}_{i\in I}$ et $D_W = \{W_j\}_{j\in J}$, deux dictionnaires de dimension $n \times \rho$, comme étant :

$$d_{\mathrm{D}}(D_U, D_W) = d_{\mathrm{W}}^{p}(\mathbb{U},\mathbb{W}) \ , \tag{2.8}$$

où $\mathbb{U} = \{\mathcal{U}_i : \mathcal{U}_i = \mathrm{span}(U_i), i \in I\}$ et $\mathbb{W} = \{\mathcal{W}_j : \mathrm{span}(W_j), j \in J\}$. On s'intéresse donc aux sous-espaces engendrés par les dictionnaires considérés pour bâtir une distance. Cette distance est une pseudo-métrique, car deux dictionnaires distincts peuvent engendrer la même collection de sous-espaces, c'est à dire qu'une distance $d_{\mathrm{D}}(D_U^1, D_U^2) = d_{\mathrm{W}}(\mathbb{U},\mathbb{U}) = 0$ peut exister pour $D_U^1 \neq D_U^2$. Cependant, cela ne pose pas de problèmes en pratique et permet de disposer d'une métrique fiable pour comparer des dictionnaires, comme en attestent les résultats obtenus dans (Chevallier, Barthelemy et al., 2014).

Nous avons également pu évaluer expérimentalement la qualité d'un jeu de données avec ce type de métrique, en l'occurrence celui de la *BCI Competition IV dataset 2a*. Dans ce jeu de données, 9 sujets sont enregistrés sur deux sessions où ils doivent accomplir 4 tâches différentes d'imagerie motrice. J'ai entraîné un dictionnaire pour chaque session et pour chaque tâche, soit 36 dictionnaires au total dont un exemple de noyaux appris est montré sur la figure 2.4. En utilisant un algorithme de clustering alimenté par les distances d_{W}^{p} calculées entre dictionnaires, deux sujets sont systématiquement isolés dans des clusters séparés, il s'agit du sujet qui obtient systématiquement les meilleurs scores en classification et de celui qui obtient les notes les plus basses (Chevallier, Barthélemy et al., 2014). D'autre part, j'ai également appris un dictionnaire pour chaque sujet et pour chaque session (18 au total), il apparait alors que les distances entre les dictionnaires des sujets sont moins grandes que la distance entre les sessions. Ceci indique que pour ce dataset les effets des différences inter-sessions sont plus forts que les différences inter-sujets, ce type de variation est sans doute causé par un changement dans la configuration matérielle ou la calibration des instruments de mesure.

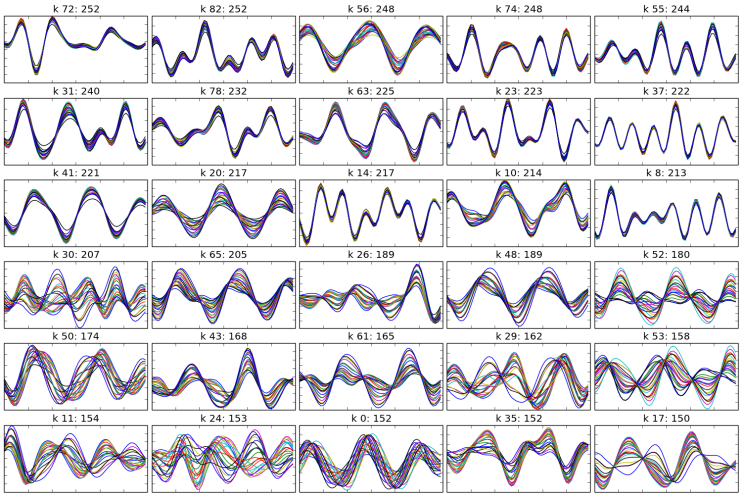

FIGURE 2.4 – Visualisation d'une partie des 90 atomes multivariés d'un dictionnaire appris sur les données de la BCI Competition IV dataset 2a. Au-dessus de chaque atome sont indiqués son identifiant ainsi que le nombre de fois où il est utilisé pour dans la reconstruction des signaux.

La définition d'un espace métrique pour caractériser les variations observées sur des dictionnaires revêt donc un intérêt particulier pour l'évaluation des algorithmes d'apprentissage de dictionnaires, mais ouvre également des possibilités pour évaluer la qualité des données ou la calibration d'un matériel. Dans un effort pour suivre les principes de l'*Open Science*, les expériences et les codes Python utilisés sont partagés librement sur https://github.com/sylvchev/mdla. Ceci inclut à la fois les codes pour l'apprentissage de dictionnaires multivariés invariant par translation et les codes pour le calcul des métriques décrites ci-avant, ainsi que d'autres métriques issues de la littérature.

2.3 Travaux expérimentaux sur la SSVEP

En parallèle de ces travaux théoriques, j'ai également mené une approche plus expérimentale avec Emmanuel Kalunga. Dans ce travail, nous avons exploré les possibilités de définir un système de contrôle hybride pour une orthèse robotique du bras. Le LISV dispose d'une orthèse réalisée avec Thalès dans le cadre d'un projet ANR antérieur et nous avons réutilisé

ce dispositif pour mettre en place une interface cérébrale et évaluer des stratégies de contrôle différentes, comme le montre la figure 2.5.

Nous avons choisi d'utiliser le paradigme de la *Steady-State Visually Evoked Potential*, pour lequel il s'agit de détecter la réponse cérébrale à un stimulus visuel répété (Vialatte et al., 2010). Lorsque le sujet focalise son attention sur un stimulus visuel clignotant, les oscillations induites dans le cortex visuel primaire correspondent à la fréquence du clignotement de ce stimulus. Ce paradigme est connu pour sa robustesse, car les oscillations induites sont d'une amplitude remarquable par rapport aux états de repos et sont corrélées avec la qualité de la focalisation attentionnelle du sujet (Duprès et al., 2014). La SSVEP peut être induite par des LED ou sur un écran d'ordinateur, avec diverses formes de stimulus possible (Gergondet et Kheddar, 2015), toutefois les LEDs induisent une meilleure stimulation que les écrans (Zhu et al., 2010). Nous avons quand même fait quelques tests préliminaires sur écran, avec la difficulté que le choix des fréquences de stimulation est contraint par le taux de rafraîchissement de l'écran. Les moniteurs CRT induisent des oscillations plus facilement détectables que les moniteurs LCD, cela étant sans doute dû à la rémanence de l'écran qui amoindrissait les variations de luminosité de l'écran pour les fréquences que nous avons testé. Pour disposer d'un montage expérimental plus robuste, nous avons donc réalisé une carte électronique avec un contrôleur PIC pour générer les fréquences choisies et alimenter 3 groupes de LEDs.

Nous avons fait un choix conceptuel important pour la mise en place de ce dispositif, le signal de stimulation n'est pas envoyé au boîtier d'enregistrement EEG. Ce choix facilite énormément la mise en place du dispositif expérimental puisqu'il n'est donc pas nécessaire de relier physiquement le boîtier de stimulation au boîtier EEG. Nous voulions en particulier pouvoir proposer une interface cérébrale s'appuyant sur la SSVEP qui puisse fonctionner avec différents objets ; pour rendre un objet "interactif" avec le système BCI, il suffit qu'il émette un signal lumineux à une fréquence prédéterminée, qui lui est propre. L'idée originale était de pouvoir équiper une pièce avec des équipements (TV, chaine hi-fi ...) ou des interrupteurs que le sujet peut activer en focalisant son regard sur le groupe de LED associées. Cependant, ce type d'approche empêche également d'utiliser les informations de phase puisque l'acquisition des EEG n'est pas synchronisée avec le boîtier de stimulation. Cette limitation est assumée, car nous avons cherché à construire un système robuste et fiable plutôt que de travailler

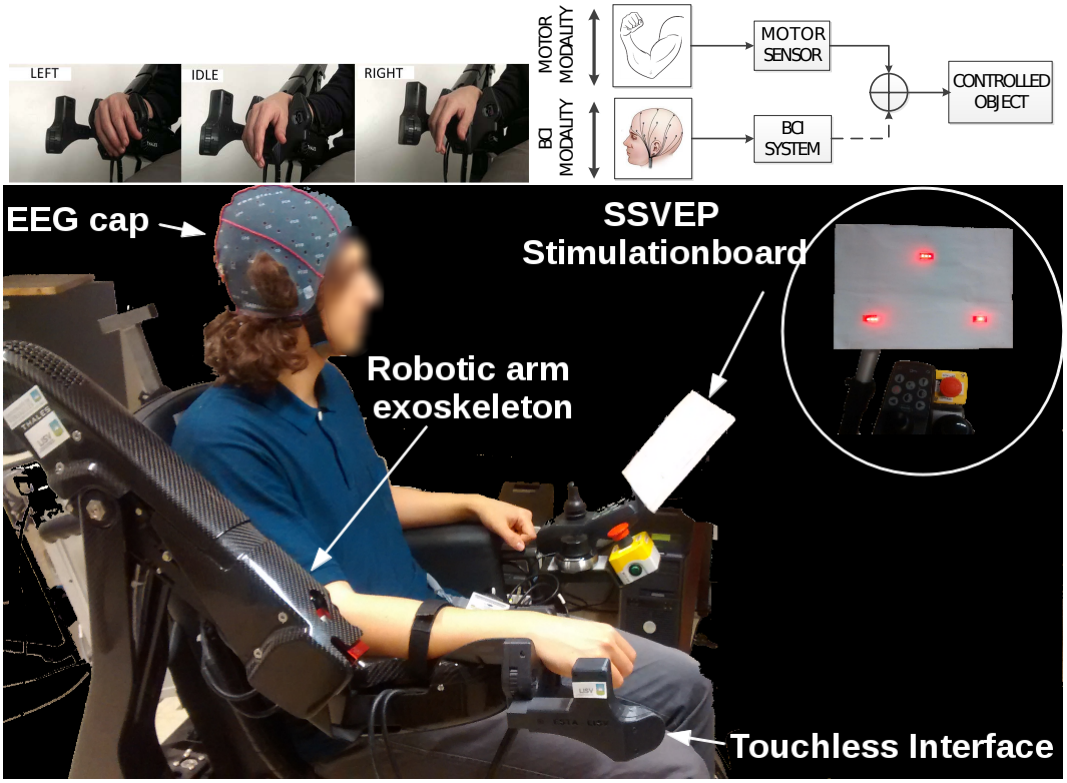

FIGURE 2.5 – Haut gauche : Interface sans contact. Haut droite : architecture de contrôle hybride. Bas : Interface cérébrale utilisant la SSVEP pour contrôler un exosquelette du bras sur un fauteuil électrique. Les stimuli pour la SSVEP sont constitués de 3 groupes de LED qui clignotent à des fréquences différentes.

dans un environnement très contrôlé.

Nous avons exploré différentes stratégies de contrôle avec l'idée que l'interface cérébrale est une solution parmi d'autres et que si un patient dispose d'une certaine liberté en termes de motricité, il préférera utiliser ses capacités motrices pour interagir avec une interface plutôt que d'utiliser systématiquement la BCI (Rouillard et al., 2015). Nous avons donc imaginé un contrôleur hybride qui permette de passer d'un mode de contrôle moteur à un mode de contrôle cérébral. Dans le cadre de l'utilisation d'un exosquelette du bras, j'avais précédemment travaillé avec une interface sans contact développée au sein du laboratoire. Cette interface sans contact utilise des positions de la main, reconnues à partir de capteurs infrarouges,

pour réaliser un contrôle de l'exosquelette, visible en haut à gauche de la figure 2.5. Hugo Martin a réalisé son stage de M2 sur le contrôle de cette interface et il a obtenu de bons résultats (Martin et al., 2012). Le principal problème de cette interface sans contact est qu'il n'est pas possible de saisir un objet et de contrôler en même temps le déplacement du bras. Nous avons donc mis en place une interface de contrôle hybride, qui permet à l'utilisateur de passer d'un mode de contrôle de l'exosquelette à l'autre, la SSVEP étant également utilisée pour faire la bascule (Kalunga, Chevallier, Rabreau et al., 2014).

Les expériences et les données enregistrées ont été traitées, vérifiées et mises en ligne en suivant les recommandations de l'Open Science Foundation et en prenant un peu d'avance sur les nouvelles directives européennes relatives à la mise à disposition des produits de la recherche. J'ai pris soin de mettre en forme les données, de proposer des exemples de codes et d'écrire une documentation pour ces données. Elles sont disponibles sur https://github.com/sylvchev/dataset-ssvep-exoskeleton et des exemples de code sont proposés sur https://gist.github.com/sylvchev/. Ce travail a été utile puisque ces données ont été réutilisées par plusieurs groupes de recherche.

La méthode algorithmique la plus simple pour détecter une oscillation induite par la SSVEP est d'utiliser une transformée de Fourier pour passer en domaine fréquentiel et d'utiliser une méthode détection de pic. Si le pic principal correspond à une des fréquences de stimulations, c'est que l'utilisateur se focalise sur un des stimuli. Cette méthode constitue une baseline mais est trop sensible aux perturbations et aux fausses détections pour être réellement fiables. Les approches utilisant les analyses de corrélations canoniques (CCA) obtiennent de très bons résultats (Lin et al., 2007). La CCA consiste à rechercher un espace de projection qui maximise la cross-covariance de deux groupes de signaux d'entrées tout en minimisant conjointement leur covariance (Kalunga, Djouani et al., 2013). La méthode la plus communément utilisée consiste à trouver un espace canonique entre un signal EEG X et un signal de référence Y_f. Ce signal de référence est construit

de la façon suivante :

$$Y_f = \begin{bmatrix} \sin(2\pi f t) \\ \cos(2\pi f t) \\ \vdots \\ \sin(2\pi N_h f t) \\ \cos(2\pi N_h f t) \end{bmatrix}, \tag{2.9}$$

où N_h est le nombre d'harmoniques, et f est l'une des fréquences de stimulation. L'objectif de la CCA est de maximiser la corrélation σ_f entre $W_X^T X$ et $W_Y^T Y_f$ tel que :

$$\sigma_f = \max_{W_X, W_Y} \frac{W_X^T \Sigma_{XY_f} W_Y}{\sqrt{W_X^T \Sigma_X W_X W_Y^T \Sigma_{Y_f} W_Y}}, \tag{2.10}$$

où Σ_X et Σ_{Y_f} sont les matrices de covariances de X et Y_f, et Σ_{XY_f} est la matrice de cross-covariance de X and Y_f. Pour déterminer quelle est la fréquence $\hat{f}$ sur laquelle le sujet se focalise, une approche efficace (Lin et al., 2007) consiste à prendre :

$$\hat{f} = \arg\max_f \{\sigma_f\} . \tag{2.11}$$

Une autre possibilité consiste à utiliser la CCA comme un filtre adaptatif, dans ce cas le signal filtré est $W_X^T X$. Il faut alors utiliser une méthode de classification sur ce signal filtré (LDA, SVM ou autre). Dans ces deux cas, il est possible d'améliorer les résultats en choisissant correctement les signaux de référence et leur harmonique, mais c'est un choix qui est le plus souvent guidé par les données et il n'y a pas de recommandations générales valables pour toutes les situations.

La *Filter Bank Canonical Correlation Analysis* (FBCCA) a été proposée par (Chen, Y. Wang, Gao et al., 2015) et permet d'améliorer significativement les performances en classification. Le signal d'entrée est décomposé sur $n = 1 \dots N_b$ bandes de fréquences, qui se chevauchent. Des coefficients de corrélation σ_f^n sont calculés pour chaque bande de fréquences n et sont combinés de la façon suivante :

$$\tilde{\sigma}_f = \sum_{n=1}^{N_b} W_n \, (\sigma_f^n)^2 \quad \text{with} \quad W_n = n^{-a} + b \, , \tag{2.12}$$

où a et b sont des constantes qui définissent le poids relatif w_n de chaque bande de fréquences. Une recherche exhaustive est nécessaire pour déterminer les valeurs des hyper-paramètres a, b et N_b qui maximisent les performances en classification. La classification peut être faite dès lors que tous les $\tilde{\sigma}_f$ sont calculés.

Des applications pour épeler des mots en utilisant la SSVEP, proposées par (Nakanishi et al., 2014) et par (Chen, Y. Wang, Nakanishi et al., 2015), ont dépassé largement les scores des études précédentes. Dans ces systèmes, l'utilisateur doit choisir itérativement les lettres pour épeler un mot ; dans leurs travaux (Nakanishi et al., 2014) atteignent une moyenne de 167 bits/min et 270 bits/min pour les travaux de (Chen, Y. Wang, Nakanishi et al., 2015). Ces performances particulièrement élevées sont la résultante de facteurs clés, tout d'abord le protocole de stimulation est conçu pour atteindre des records de performances, en combinant la modulation de phase et une combinaison de fréquence de stimulation. Ensuite, les lettres proposées à l'utilisateur utilisent un schéma prédictif, semblable à celui utilisé pour l'écriture de SMS. Ces performances ne sont possibles que dans un environnement extrêmement contrôlé, avec une synchronisation obligatoire entre le système de capture EEG et l'affichage, pour un système qui est entièrement dédiée et uniquement dédiée à cette tâche.

2.4 Approches Riemanniennes pour la BCI

Avec Emmanuel Kalunga et Quentin Barthélemy, puis plus tard avec Florian Yger, nous avions suivi avec intérêt les développements conduits au laboratoire Gipsa de Grenoble (Congedo, Barachant et Andreev, 2013) et leurs arguments pour l'utilisation de la géométrie Riemanienne pour les interfaces cérébrales. Cette approche repose sur le traitement des matrices de covariance spatiale de l'EEG au lieu de travailler dans le domaine temporel. Un premier constat permet de voir le rôle central joué par les matrices de covariance dans toutes les approches de l'état de l'art en BCI. Pour le paradigme P300 en BCI, qui repose sur la détection d'un potentiel évoqué déclenché par la perception d'un stimulus peu fréquent, la méthode XDAWN (Kristensen et al., 2015 ; Rivet et al., 2009) est la méthode de l'état de l'art pour améliorer la détection du signal avant d'appliquer un algorithme de classification. En imagerie motrice, ce sont les *Common Spatial Patterns* –

ou CSP (Blankertz et al., 2008) et ses variantes (Lotte et Guan, 2011) – qui permettent de capturer au mieux les synchronisations et désynchronisations induites par l'imagination de mouvement. Comme nous l'avons vu pour la SSVEP, c'est la CCA (Chen, Y. Wang, Gao et al., 2015 ; Lin et al., 2007), qui permet de construire un filtre spatial pour rehausser le signal ou faire directement la classification.

Dans le cas de XDAWN, on considère un signal EEG $X \in \mathbb{R}^{c \times n}$ où n est le nombre d'échantillons temporels et c est le nombre de canal (avec $c = \rho$). En notant $E \in \mathbb{R}^{n_t \times c}$ le stimulus à détecter, avec n_t le nombre d'échantillons du stimulus, et en définissant une matrice Toeplitz $D \in \mathbb{R}^{n \times n_t}$ contenant uniquement des 0 sauf pour indiquer la position des stimuli dans le signal EEG, il est possible de modéliser le signal comme résultant du modèle $X^T = DE + N$ avec N une source de bruit exogène. Dans (Rivet et al., 2009), les auteurs proposent de trouver un ensemble de n_f filtres spatiaux $W \in \mathbb{R}^{c \times n_f}$ qui maximisent le rapport signal sur signal plus bruit tel que $\hat{W} = \text{argmax}_W \, g(W)$. Ce rapport est estimé comme :

$$g(W) = \frac{\text{tr}\, W^T \hat{\Sigma}_1 W}{\text{tr}\, W^T \hat{\Sigma}_X W} \tag{2.13}$$

avec $\hat{\Sigma}_1 = \hat{E}^T D^T D \hat{E}$, $\hat{\Sigma}_X = XX^T$ et $\hat{E} = (D^T D)^{-1} D^T X^T$.

Pour utiliser les CSP, les meilleurs résultats sont obtenus lorsque le signal X est filtré avec un filtre passe-bande approprié, puis centré et normalisé. Pour cette approche, il faut estimer les matrices de covariances $\Sigma_1, \Sigma_2 \in \mathbb{R}^{c \times c}$ correspondant à deux conditions expérimentales. L'algorithme du CSP consiste à réaliser une diagonalisation simultanée de $W^T \Sigma_1 W = \Lambda_1$ et $W^T \Sigma_2 W = \Lambda_2$, sous la contrainte que $\Lambda_1 + \Lambda_2 = I$. Une fois les filtres W estimés, il est courant de ne retenir qu'un sous-ensemble W_d de filtres et de les utiliser pour obtenir un signal rehaussé $X_{\text{CSP}} = W_d^T X$. Pour la CCA, nous avons vu qu'il était possible de l'utiliser comme un filtre spatial avec $W_X^T X$. Pour tous ces paradigmes BCI, les algorithmes de l'état de l'art suivent la même approche qui est de trouver un ensemble de filtres spatiaux $W_d \in \mathbb{R}^{c \times d}$ avec $d \leqslant c$ qui rehausse le signal et opère une réduction de dimensionnalité.

Ces approches sont efficaces et ont démontré leur qualité dans de nombreux cas, particulièrement lorsque les données sont très propres. Cela s'entend à la fois au sens où il faut absolument éviter tout bruit dans les

labels, ce qui peut arriver lorsque les sujets ne sont pas très concentrés sur la tâche, et où il faut que les enregistrements soient très bien réalisés, sans électrodes mal positionnées ou bruitées. Ces filtres spatiaux excellent lorsque les expériences sont réalisées dans un cadre très contrôlé et lorsque les enregistrements utilisent un grand nombre d'électrodes. Ils nécessitent que chaque sujet réalise une phase de calibration avant chaque session, en étant particulièrement attentif au bon déroulement de cette phase de calibration puisque la qualité du système en dépend directement. De plus, cette étape de calibration nécessite souvent de faire une sélection de modèles en plus de l'exploration des paramètres, ce qui augmente le risque d'aboutir à surapprentissage.

Il apparaît clairement dans ces méthodes de l'état de l'art que les matrices de covariances $\Sigma \in \mathbb{R}^{c\times c}$ sont au cœur des estimations de ces filtres spatiaux. L'alternative proposée par les approches Riemanniennes (Congedo, Barachant et Bhatia, 2017 ; Yger et al., 2016) consiste a travailler directement avec ces matrices de covariance. Les matrices de covariances sont symétriques et définies positives (SPD) et vivent dans un sous-espace de courbure non nulle. La géométrie riemannienne est bien adaptée pour travailler sur ces représentations, dans laquelle les matrices de covariances sont éléments d'une variété matricielle $\mathcal{M}_c$ matrices SPD de dimension $c \times c$ (Bhatia, 2009) :

$$\mathcal{M}_c = \left\{\Sigma \in \mathbb{R}^{c\times c} \mid \Sigma = \Sigma^T \text{ and } z^T\Sigma z > 0, \forall z \in \mathbb{R}^c \backslash \{0\}\right\} . \tag{2.14}$$

Doté d'une métrique Riemannienne, c'est à dire d'une collection de produits scalaires sur l'espace tangent $T_\Sigma\mathcal{M}$ qui varient de manière lisse en chaque point Σ de la variété, il est possible de calculer la longueur de n'importe quel chemin sur la variété. Le plus court chemin entre deux points Σ_1 et Σ_2 est appelé une géodésique et sa longueur est la distance Riemannienne δ :

$$\delta(\Sigma_1, \Sigma_2) = \left\| \log(\Sigma_1^{-\frac{1}{2}}\Sigma_2\Sigma_1^{-\frac{1}{2}}) \right\|_F \tag{2.15}$$

Cette distance est également appelée distance affine-invariante (Fletcher et Joshi, 2004a ; Moakher, 2005) et une illustration est proposée sur la figure 2.6. La notion de moyenne ou de centre de masse d'un ensemble d'éléments

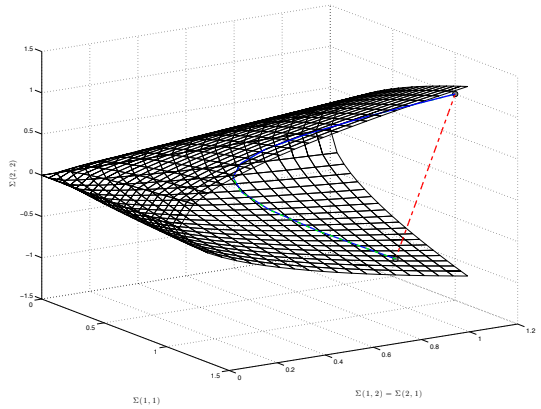

FIGURE 2.6 – Visualisation dans l'espace des matrices de covariances $\Sigma \in \mathbb{R}^{2\times 2}$. La distance Euclidienne (en tirets rouges) ne prend pas en compte la courbure de l'espace alors que la distance affine-invariante (traits pleins bleu) suit la géodésique.

Σ_i est appelée la moyenne de Fréchet. C'est le point $\bar{\Sigma}$ qui minimise la dispersion sur la variété, au sens du carré des distances entre $\bar{\Sigma}$ et les Σ_i :

$$\bar{\Sigma} = \underset{\Sigma}{\operatorname{argmin}} \sum_i \delta^2(\Sigma_i, \Sigma) \tag{2.16}$$

S'il y a 3 éléments Σ_i ou plus, il n'existe pas de solution exacte, mais une approche itérative permet d'obtenir une solution viable expérimentalement.

Un algorithme simple, mais très efficace en pratique est la *Minimum Distance to Riemannian Mean* (MDM). L'idée est illustrée sur la figure 2.7, où l'on dispose d'enregistrements pour deux conditions expérimentales. La première étape consiste à calculer les moyennes de classe, ici $\bar{\Sigma}^{(1)}$ et $\bar{\Sigma}^{(2)}$. Lorsqu'un nouvel enregistrement est présenté, il est attribué à la classe dont le centre est le plus proche. Ce type d'algorithme est très adapté aux traitements *online*, car il peut être initialisé avec des données précédemment enregistrées puis mis à jour itérativement avec les nouveaux enregistrements.

Avec Emmanuel Kalunga et Quentin Barthélemy, nous avons proposé de nouveaux algorithmes qui travaillent directement dans l'espace des matrices de covariances. En particulier, nous avons proposé un algorithme adaptatif qui prend en compte la trajectoire d'un sujet pour améliorer la réactivité du système BCI. La trajectoire d'un sujet fait référence ici à la succession

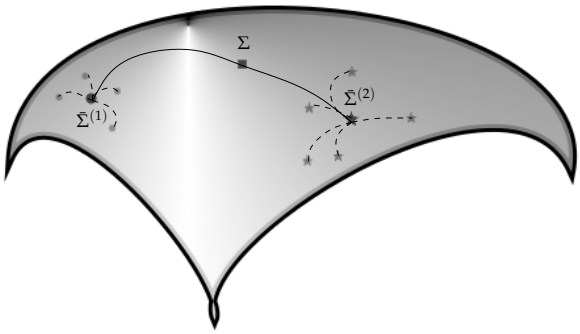

FIGURE 2.7 – Illustration d'un problème de classification à deux classes dans l'espace matrices SPD avec l'algorithme MDM.

de matrices de covariance, estimées à partir des fenêtres temporelles qui se chevauchent. On peut ainsi voir sur la figure 2.8 qu'il y a un délai entre le moment où le sujet regarde un stimulus et le moment où l'algorithme détecte le changement de focalisation du sujet. Ces figures sont obtenues en estimant le centre de masse de l'ensemble des matrices de covariance enregistrées pour un sujet, puis en projetant ces matrices sur le plan tangent situé sur ce point et en réalisant une ACP pour avoir une visualisation en 2D. En estimant un gradient pour cette trajectoire, il est possible de détecter les changements de direction relativement aux centres de classes et d'améliorer la réactivité du système pour des méthodes *online* (Kalunga, Chevallier, Barthélemy et al., 2016).

Les approches Riemannienne on démontré leur robustesse et leur précision, en particulier elles ont été utilisées par Alexandre Barachant pour remporter 5 compétitions en BCI, dont le détail est donné dans (Congedo, Barachant et Bhatia, 2017). Il existe toute une variété d'algorithmes pour réaliser des traitements dépassant la seule classification, qui vont du débruitage (Blum et al., 2019) à la détection d'artefact (Barthélemy et al., 2019). Si les résultats expérimentaux sont clairs, les raisons de leur efficacité demandent encore a être éclaircies. Elles sont particulièrement efficaces pour les enregistrements avec un petit nombre d'électrodes et pour les cas où les données sont bruitées. Ce sont donc des méthodes de choix pour être utilisés dans des conditions réelles et peu contrôlées.

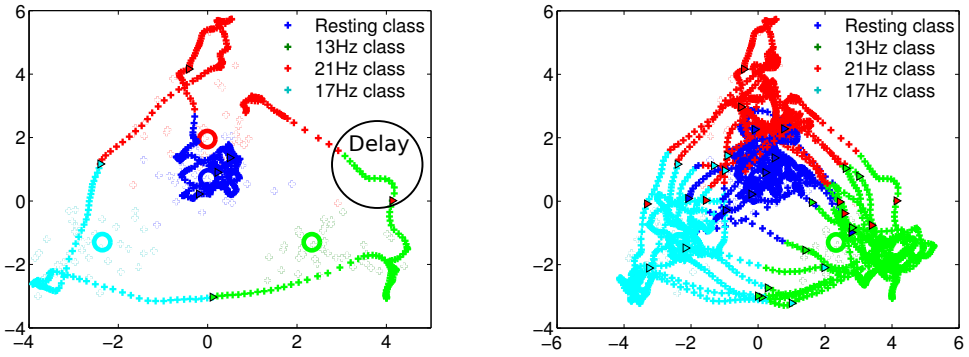

FIGURE 2.8 – Trajectoire d'un sujet dans l'espace des matrices de covariances pour une tâche de SSVEP à 4 classes. Les triangles indiquent le démarrage d'une stimulation.

2.5 Contributions applicatives et industrielles

Mes travaux sur les interfaces cérébrales s'inscrivent dans l'activité de l'équipe "Assistance et Interface" du LISV comme une façon de proposer des interfaces hybrides qui peuvent s'adapter aux capacités et aux choix du sujet. Le LISV dispose de plateformes de réalité virtuelle immersives, avec des retours physiques, adaptés aux personnes en situation de handicap. Les activités du laboratoire sont structurées autour de partenariat fort avec des industriels, sur des sujets sociétaux et environnementaux en lien avec la robotique interactive d'assistance et la caractérisation de systèmes. J'ai ainsi encadré la thèse d'Hugo Martin en CIFRE chez Bouygues Construction International.

Nous avons développé plusieurs projets en partenariat avec Bouygues sur des aspects de recherche et développement ainsi que pour de la formation. Les développements que nous avons réalisés sur les plateformes immersives ont permis de construire une dynamique de recherche commune avec Bouygues. En effet, les métiers de la construction connaissent un tournant majeur avec la numérisation des services. Alors que beaucoup de phases de planification et de gestion sont encore réalisées sur plan papier, il y a une demande croissante des clients et des collectivités pour le déploiement du *Building Information Modeling* ou BIM. La pièce centrale du BIM est une maquette numérique 3D du bâtiment qui contient toutes les informations pour réaliser le projet architectural. Cette maquette regroupe ainsi des

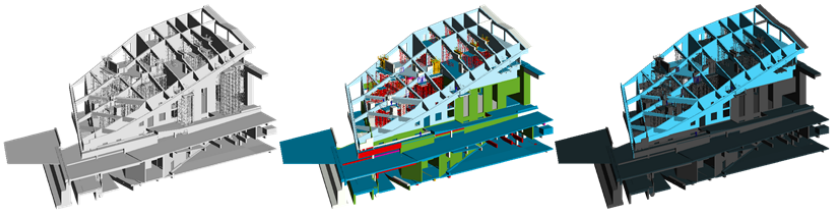

FIGURE 2.9 – Illustration des 3 étapes du processus : à partir d'une maquette numérique brute à droite, les éléments sont automatiquement reconnus et affectés aux différents départements de construction (au centre). À droite, le rendu est modifié dynamiquement pour mettre en valeur les éléments d'un corps de métier.

informations aussi diverses que la position des grues pour le suivi de la construction que les choix de design intérieur pour la génération d'images photoréalistes à destination des clients.

Le principal problème des maquettes vient du fait que tous les corps de métiers utilisent le même modèle pour y intégrer des informations hétérogènes et non-structurées. Nous avons donc travaillé sur deux aspects avec Hugo Martin, d'une part pour la classification automatique des éléments de la maquette BIM afin de disposer d'une information hiérarchisée. D'autre part, nous avons proposé un modèle d'assistance pour la visualisation de la maquette, qui permet à un utilisateur d'accéder à l'information pertinente pour son corps de métiers sans perdre d'informations. Ces deux étapes sont illustrées sur la figure 2.9.

L'affectation automatique des éléments d'une maquette aux différents départements de la construction est rendue complexe du fait de l'internationalisation des équipes et de l'absence de méthodologies commune. Nous avons donc développé un système d'apprentissage qui utilise toutes les informations disponibles, c'est à dire aussi bien les informations géométriques de la maquette (nombre de polygones, taille relative, etc.) que les informations textuelles rentrées dans le modèle (Martin et al., 2016).

À partir d'un corpus de 21 maquettes utilisées en production, dans des équipes avec des locuteurs de 5 langues différentes, Hugo Martin a étiqueté tous les éléments pour les répartir sur 5 départements (Architectes et structures, façades, méthodes, mécaniques/électrique/plomberie, design intérieur). Les informations pour le système d'apprentissage sont extraites

directement à partir du fichier de données brutes [4]. Nous avons conçu un algorithme d'apprentissage ensembliste que nous avons validé avec une approche *"leave-one-model-out"*. Notre approche permet d'étiqueter correctement plus de 80 % des données et cette approche fonctionne également lorsque la langue de la maquette n'appartient pas au corpus.

Une fois les informations contenues dans la maquette correctement labellisées et hiérarchisées, nous avons pu proposer un système de visualisation adaptatif. Pour prendre un cas pratique, si un ingénieur électrique doit travailler sur la maquette BIM, elle contient beaucoup trop d'information et les éléments pertinents de la maquette sont difficiles, voire impossibles à trouver. S'il est tentant d'enlever de l'affichage toutes les informations non pertinentes pour la gestion du réseau électrique, il est important de garder toutes les informations visibles pour éviter par exemple de faire passer un câble électrique au milieu d'une conduite d'eau.

Il faut donc une solution qui permette de conserver toutes les informations à l'écran tout en mettant en avant les informations importantes. J'ai proposé d'utiliser des modèles attentionnels pour détecter les zones saillantes de l'image et, par une méthode itérative, de changer les propriétés de l'affichage pour rendre saillantes les zones importantes de l'image. La maquette numérique disposant d'un moteur de rendu 3D, il est tout à fait possible d'altérer les propriétés de couleur, de contraste, de transparence des objets pour modifier la saillance de l'image (Martin et al., 2015), en prenant en compte les limites des modèles de saillances existants (Ho-Phuoc et al., 2012).

Les images architecturales diffèrent cespendant des images naturelles par la présence très visible de points de fuite. Ces points de fuite concentrent des lignes d'orientations et attirent le regard. Nous avons donc écrit un modèle de détection de point de fuite, que nous avons intégré à un modèle détection de saillance. Ce modèle est appelé itérativement par une procédure qui modifie les propriétés du moteur de rendu.

La résultante est une image sur laquelle les éléments informatifs pour le corps de métier de l'utilisateur sont saillants. Nous avons évalué ce système de visualisation adaptative auprès d'experts et d'ingénieurs en exercice. L'analyse des résultats montre une amélioration significative de la visibilité des éléments pour chaque corps de métiers.

4. https://github.com/HugoMartin78/bim-classifier.git

3 Projets de recherche

La recherche sur les interfaces cérébrales est portée par une communauté active et ce domaine de recherche est situé au carrefour des évolutions technologiques, scientifiques et médicales depuis plusieurs décennies. Chaque nouvelle avancée, que ce soit sur les capteurs, les algorithmes ou la compréhension des mécanismes cognitifs, implique une remise en question des méthodes existantes et est intégrée dans les pratiques expérimentales.

J'ai particulièrement apprécié qu'une partie importante de la communauté travaille à la mise en place et au développement d'outils libres, avec la conviction que ce sujet de recherche est beaucoup trop complexe pour être abordé comme une somme d'expertises locales. Il y a, comme dans certaines communautés de recherche en neurosciences computationnelles, un réel effort pour partager les outils, les pratiques et les données. Cette situation perdure alors que le domaine pourrait facilement céder à une fragmentation des outils et des travaux de recherche, et ce d'autant plus facilement qu'il y a une forte émulation entrepreneuriale et la participation active d'équipementiers médicaux.

Ce caractère interdisciplinaire est particulièrement intéressant lorsqu'on s'intéresse aux verrous existant en BCI. Le premier verrou scientifique est la sensibilité des enregistrements EEG aux bruits exogènes, comme les perturbations électriques, et endogènes, comme les activités musculaires. Bien que les sources de bruits soient différentes, les mêmes problèmes existent avec les acquisitions en imagerie spectroscopique proche infrarouge (ou fNIRS) (Naseer et Hong, 2015). La seconde limitation est la plus difficile à caractériser, il s'agit du phénomène appelé illettrisme BCI (Vidaurre et Blankertz, 2010). Ce terme est trompeur et utilise à mon sens une mauvaise terminologie, car ce n'est pas l'utilisateur qui est illettré en termes de BCI. Ce sont les systèmes BCI qui sont à peine capables d'atteindre des performances supérieures au niveau de la chance, pour certains couples paradigme/sujet. C'est pourquoi le terme d'inefficacité BCI (*BCI-inefficiency*) est sans doute beaucoup plus adéquat, même s'il est plus négatif.

Pour attaquer les limitations précédemment citées des BCI, j'ai développé une expertise dans deux domaines : d'une part dans le traitement du signal cérébral à partir des matrices de covariances et d'autre part dans les modèles de neurones. Les matrices de covariances fournissent une représentation relativement robuste au bruit de mesures. Les bruits de mesures typiques proviennent du positionnement des électrodes et de la calibration du matériel d'acquisition, qui induisent des variations qui affectent significativement les algorithmes de traitement. Ces variations ont une influence réduite lorsque le signal est analysé à partir de ses matrices de covariances. Cette représentation est également bien adaptée pour les analyses discriminantes, permettant de classifier les signaux et leurs états cognitifs sous-jacents.

Cette partie décrit mon projet de recherche qui se décompose en quatre axes que je souhaite développer pour la suite de mon travail autour des interfaces cérébrales. Le premier axe est consacré à l'importance que revêtent les facteurs humains et au positionnement des interfaces cérébrales dans le contexte de l'*Open Science*. J'exposerai ensuite le deuxième axe qui concerne les avancées possibles en BCI Riemannienne, et les possibilités de les rendre plus expressives et d'expliciter plus formellement les raisons de leur succès. Une des évolutions possibles des BCI Riemanniennes est liée au développement de réseaux de neurones profonds (*deep learning*), qui constituent mon troisième axe de travail. Enfin, je présenterai le dernier axe de recherche que je développe sur la détection d'anomalies dans des séries temporelles, commencé dans un contexte applicatif industriel, et qui peut trouver des applications dans les données EEG.

3.1 Des interfaces au service de l'utilisateur

Le problème de l'inefficacité des BCI est sans doute la résultante de facteurs multiples, mais un faisceau d'études vient éclairer une partie de ces facteurs (Lotte et Jeunet, 2015). Les protocoles actuels d'entraînement et de réalisation de tâches cognitives ne tiennent pas forcément compte des facteurs humains (Botte-Lecocq et al., 2014).

Une expérience frappante (Jeunet, Jahanpour et al., 2016) montre qu'en utilisant le protocole le plus répandu pour les expérimentations en imagerie motrice, mais en demandant aux sujets de faire une tâche de contrôle moteur

simple, beaucoup de participants se trompent dans le protocole. Il est en effet très courant de concentrer les efforts sur les objectifs du protocole de recherche plutôt que sur le sujet, et ainsi aboutir à des expériences longues ou complexes du point de vue du sujet. Comme pour n'importe quelle interface, le contexte d'utilisation est important : les relations entre le sujet et l'expérimentateur ou l'expérimentatrice ont une influence qui peut induire stress, regain d'attention ou perte de concentration (Roc et al., 2019). Il est donc important de prendre en compte ces facteurs dans la conception des protocoles de tests.

L'utilisation correcte d'une interface cérébrale requiert une bonne concentration et demande un effort cognitif important. C'est d'ailleurs une des motivations qui m'ont poussé à m'intéresser aux interfaces hybrides. Ces efforts ne peuvent être réalisés à un rythme trop rapide, sous peine de voir le sujet décrocher. La temporalité des interactions est donc d'une importance cruciale, comme cela a pu être constaté dans les domaines de la robotique interactive (Andry et al., 2010) et des interfaces humain-machine en général.

Une interface cérébrale doit être capable d'intégrer un non-choix, c'est-à-dire de laisser au sujet la possibilité de ne pas utiliser le système ou de ne pas répondre, ce qui correspond à un état de repos (Millan, 2004). À minima, l'interface doit intégrer un dispositif pour arrêter ou démarrer l'utilisation des commandes cérébrales de type *brain switch* ou prévoir une interface physique. Il est possible de proposer des systèmes sans état de repos, comme (Chen, Y. Wang, Nakanishi et al., 2015 ; Nakanishi et al., 2014) pour concevoir un SSVEP-speller, mais cela implique que le système est perpétuellement en train d'interagir, même si le sujet fait autre chose. Ce type de travaux évite ainsi de traiter une difficulté importante de la BCI, car s'il est relativement direct de prendre une décision de classification entre plusieurs états de stimulation, la situation est beaucoup plus complexe lorsqu'il faut prendre en compte le cas de non-choix ou de classe de rejet.

Les difficultés sont de deux ordres, d'une part phénoménologique et d'autre part de modélisation. Premièrement, il est plus difficile d'entraîner un classifieur sur des signaux comportant des données relatives à une tâche (imagerie motrice, P300, SSVEP) et des données non spécifiques, caractéristique de l'état de repos (Várkuti et al., 2013). La classe de rejet regroupe sous une même étiquette pour le classifieur des situations qui peuvent être très différentes, pour un même sujet et d'un sujet à l'autre. La seconde difficulté a trait au choix et au paramétrage du modèle, l'ajout

d'une classe de rejet suppose en effet que le classifieur dispose d'un seuil de confiance pour ses prédictions et qu'il est capable de proposer une non-réponse. Ce type de classifieur est plus complexe à paramétrer et plus difficile à entraîner (Friedman et al., 2001). Le fait de prendre en compte le rythme des interactions souhaité par le sujet et de lui laisser la possibilité d'avoir le contrôle sur le système revêt une une importance majeure. Les interfaces cérébrales s'inscrivent à la croisée de plusieurs domaines de recherche, constituant une approche pluridisciplinaire qui mêle interface humain-machine, traitement du signal, neuroscience, psychologie cognitive. S'il est tentant de mettre l'accent sur l'un ou l'autre des aspects de cette recherche, cela ne peut pas se faire au détriment de l'utilisateur.

En relation avec ces considérations, je souhaite privilégier pour mes travaux une approche expérimentale qui s'inscrive dans la lignée des interfaces cérébrales passives ou implicite (George et Lécuyer, 2010 ; Zander et Kothe, 2011). Il n'est ainsi plus question de demander à l'utilisateur d'essayer de contrôler son activité cérébrale pour interagir avec le système. Le système essaie de détecter des états cognitifs à partir des EEG pour proposer des adaptations du système, comme c'est le cas par exemple pour l'informatique affective (*affective computing*, (Molina et al., 2009)). Ces interfaces fonctionnent sur des temps caractéristiques beaucoup plus longs que les interfaces réactives, travaillant globalement à l'échelle de la minute. Ceci permet d'accumuler beaucoup plus de mesures avant de prendre une décision, il est ainsi possible d'écarter les échantillons contaminés par des artefacts et de faire des estimations plus précises et plus fiables des propriétés du signal. Les retours utilisateurs sont donc moins fréquents, ce qui permet également d'accumuler les informations de décision et d'augmenter la fiabilité des retours.

3.2 Une recherche inscrite dans l'Open Science

S'il est souvent difficile de s'entendre sur une terminologie précise au sein d'une discipline scientifique, la tâche est d'autant plus ardue lorsque l'objet de l'étude est pluridisciplinaire. C'est évidemment un enjeu majeur pour les interfaces cérébrales. Je me suis intéressé aux aspects de traitement du signal et d'apprentissage, dans le sens *machine learning*, pour les BCI. J'ai pu constater dans la littérature une variété d'approches, tant

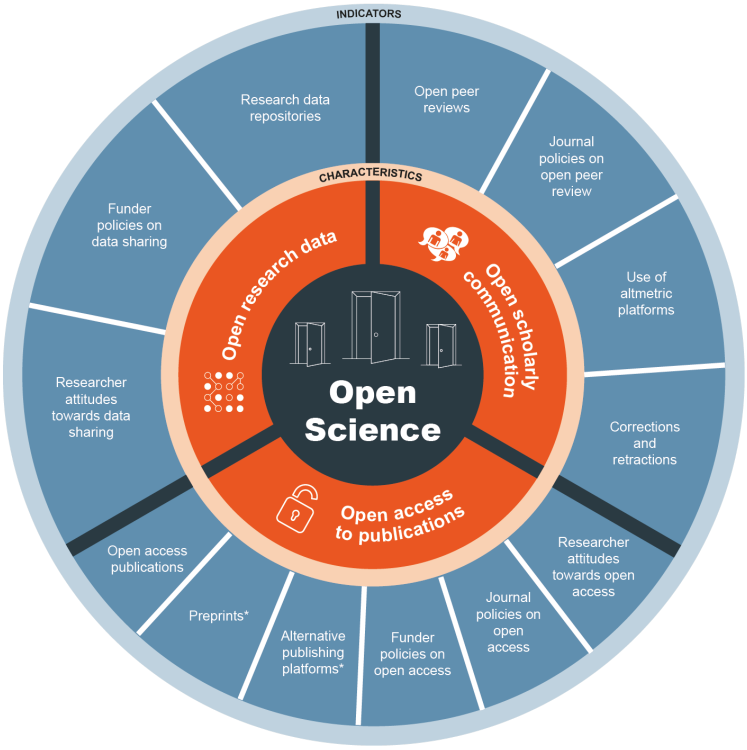

FIGURE 3.1 – Vision de la science ouverte (*open science*) défendue par le conseil de la recherche européenne.

dans la description des modèles d'apprentissage que dans les modalités d'évaluation, qui ne permet pas une comparaison objective et une analyse objective de méthodes proposées. Bien évidemment, ce phénomène est plus global et touche beaucoup de disciplines scientifiques (Baker, 2016). Les disciplines informatiques posent des questions spécifiques sur la pérennité des codes, sur la réplicabilité des expériences avant même de traiter de leur reproductibilité. Les outils – bibliothèques, environnements d'exécution, d'exploitation – sont souvent intimement liés avec les approches proposées, l'article de (Blankertz et al., 2008) sur les CSP indique par exemple que leur méthode tient une seule ligne de Matlab.

Le conseil de la recherche européenne est moteur dans la promotion de la science ouverte [1], ou *open science*, et insiste entre autres sur la mise en

1. https://ec.europa.eu/research/openscience/pdf/ospp_combined_

place d'outils pour faciliter la reproductibilité des expériences [2] (Wilkinson et al., 2016). Des initiatives indépendantes comme ReScience [3] (Rougier et al., 2017) peuvent jouer un rôle important dans la conservation et la diffusion de modèle de référence. Dans le cadre des BCI, une initiative vise à proposer un outil pour faciliter l'évaluation et la comparaison de modèle d'apprentissage, ainsi que de faciliter la diffusion des données (Jayaram et Barachant, 2018). J'ai étendu le code existant pour gérer le paradigme SSVEP et j'ai implémenté certains des classifieurs de référence. Je souhaite bien évidemment poursuivre ces travaux et proposer des formations sous forme de workshop ou d'atelier de code.

La suite de ce document détaille les axes de travail plus formel que je souhaite développer dans la suite de mes travaux. Ces axes sont structurés autour de la construction de représentations adaptées pour étudier l'activité cérébrale à partir des analyses des covariances spatiales et temporelles. Ces représentations invariantes peuvent être utilisées pour la conception de modèles neuronaux ou bien pour l'optimisation de l'architecture de réseaux.

3.3 Construction d'espaces de représentation adaptés

Le deuxième axe de mon projet de recherche s'organise autour du développement d'algorithmes pour analyser les signaux caractéristiques dans l'activité cérébrale, à partir de l'étude de leur covariance. Les variabilités des signaux cérébraux, qu'elles soient d'origine électronique ou dues à des perturbations endogènes, génèrent des représentations invariantes lorsqu'on considère ces matrices de covariance avec des métriques adaptées. Parmi les métriques existantes pour les matrices symétriques définies positives, j'ai présenté la distance affine-invariante dans l'équation (2.15) au chapitre précédent. D'autres distances existent, comme la distance log-euclidienne, la log-déterminante, la métrique de Wasserstein, les α-β-divergences ou la distance de Bhattacharyya.

recommendations.pdf

2. https://ec.europa.eu/info/research-and-innovation/strategy/goals-research-and-innovation-policy/open-science/open-science-monitor/about-open-science-monitor_en

3. http://rescience.github.io/

TABLE 3.1 – Distances, divergences et moyennes dans la littérature pour les matrices SDP.

	Distance/Divergence	Mean
Arithmetic	$d_{\mathrm{E}} = \|\Sigma_1 - \Sigma_2\|_F$	$\bar{\Sigma}_{\mathrm{E}} = \frac{1}{I}\sum_{i=1}^{I}\Sigma_i$
Harmonic	$d_{\mathrm{H}} = \|\Sigma_1^{-1} - \Sigma_2^{-1}\|_F$	$\bar{\Sigma}_{\mathrm{H}} = \left(\frac{1}{I}\sum_{i=1}^{I}\Sigma_i^{-1}\right)^{-1}$
Log-Euclidean	$d_{\mathrm{LE}} = \|\mathrm{Log}(\Sigma_1) - \mathrm{Log}(\Sigma_2)\|_F$	$\bar{\Sigma}_{\mathrm{LE}} = \mathrm{Exp}\left(\frac{1}{I}\sum_{i=1}^{I}\mathrm{Log}(\Sigma_i)\right)$
Affine-invariant	$d_{\mathrm{AIR}} = \|\mathrm{Log}(\Sigma_1^{-1}\Sigma_2)\|_F$	Algorithm 3 in (Fletcher et Joshi, 2004b)
Kullback-Leibler	$D_{\mathrm{KL}} = \frac{1}{2}\left(\log\frac{\det(\Sigma_2)}{\det(\Sigma_1)} + \mathrm{tr}(\Sigma_2^{-1}\Sigma_1) - C\right)$	Algorithm 1 in (Chebbi et Moakher, 2012)
Jeffreys	$D_{\mathrm{J}} = \frac{1}{2}\left(\mathrm{tr}(\Sigma_2^{-1}\Sigma_1) + \mathrm{tr}(\Sigma_1^{-1}\Sigma_2)\right) - C$	Lemma 17.4.4 in (Moakher et Batchelor, 2006)
S-divergence	$D_{\mathrm{S}} = \log\det(\frac{\Sigma_1+\Sigma_2}{2}) - \frac{1}{2}\log\det(\Sigma_1\Sigma_2)$	Eq. (17-20) in (Cherian et al., 2011)
α-divergence	D_{LD}^{α} from (Chebbi et Moakher, 2012)	Algorithm 1 in (Chebbi et Moakher, 2012)
Wasserstein	$d_{\mathrm{W}} = \left(\mathrm{tr}\left(\Sigma_1 + \Sigma_2 - 2\left(\Sigma_1^{1/2}\Sigma_2\Sigma_1^{1/2}\right)^{1/2}\right)\right)^{1/2}$	Eq. (19) in (Álvarez-Esteban et al., 2016)

	References
Harmonic	(Lim et Pálfia, 2012)
Log-Euclidean	(Arsigny et al., 2007)
Affine-invariant	(Fletcher et Joshi, 2004b ; Moakher, 2005)
Kullback-Leibler	(Chebbi et Moakher, 2012 ; Kang et al., 2009)
Jeffreys	(Moakher et Batchelor, 2006)
S-divergence	(Cherian et al., 2011 ; Sra, 2016)
α-divergence	(Chebbi et Moakher, 2012)
Wasserstein	(Agueh et Carlier, 2011 ; Álvarez-Esteban et al., 2016)

Ces métriques sont dotées des propriétés et d'invariances différentes, un travail bibliographique est nécessaire pour proposer une comparaison complète et cohérente de leur intérêt vis-à-vis des signaux cérébraux. Le but est d'aboutir à une meilleure compréhension des invariants caractéristiques de fonctions cognitives (préparation motrice, décision, attention, etc.), à partir de signaux enregistrés à un niveau macroscopique (EEG, MEG, IRMf, etc.) ou mesoscopique (ECoG, SEEG, LFP, etc). La confrontation avec d'autres niveaux d'enregistrement peut permettre, par l'analyse des différences, de mieux caractériser les spécificités du signal EEG et ainsi focaliser les efforts de recherches sur les aspects les plus pertinents.

J'ai pu commencer ce travail de recherche bibliographique et le résultat actuel est visible dans les tableaux 3.1 et 3.2. C'est une première étape qui permet de proposer une implémentation de référence de ces distances.

Table 3.2 – Propriétés des distances et divergences.

Distance/Divergence	Strictly positive eigenvalues	Invariances
Arithmetic	×	Rotation
Harmonic	×	Rotation
Log-Euclidean	✓	Rotation, inversion, Lie group bi-invariance, similarity
Affine-invariant	✓	Rotation, inversion, similarity, affine transform
Kullback-Leibler	✓	Rotation, affine transform
Jeffreys	✓	Rotation, inversion, affine transform
S-divergence	✓	Rotation, inversion, affine transform
α-divergence	✓	Dual-invariance under inversion, affine transform
Wasserstein	✓	Rotation, affine transform

Une première version est déjà disponible et je vais proposer une nouvelle implémentation pour permettre une meilleure intégration aux bibliothèques de codes existantes[4]. Dans la suite de ce travail, je souhaite caractériser les invariances les plus importantes du point de vue du traitement du signal EEG. Ces travaux sont menés en collaboration avec Florian Yger, Quentin Barthélemy et Emmanuel Kalunga.

Au niveau macroscopique, les premières études sur ce sujet tendent à montrer qu'il est possible de construire des représentations robustes, caractéristiques de certains processus cognitifs, indépendamment du sujet. De telles représentations, insensibles aux variations inter-individuelles, permettent d'envisager la mise en place d'indicateurs qualitativement plus précis sur les séquences d'activations réalisés lors de tâches cognitives (Jeunet, Lotte et al., 2018). Les premiers résultats en imagerie motrice confirment ces hypothèses et les approches s'appuyant sur la géométrie des matrices de covariances ont remporté plusieurs compétitions internationales, en EEG et en MEG.

L'utilisation de métriques adaptées peut permettre d'étudier le déroulement temporel précis des activations cérébrales. Une meilleure compréhension des séquences d'activations peut permettre de différencier finement des réponses obtenues lors de tâches similaires. Appliquée à la prise de décision, la capacité d'étudier les différences entre plusieurs tâches proches peut apporter un éclairage plus précis sur les changements intervenant dans les réseaux mis en jeu. L'hypothèse que je souhaite développer est que l'étude des covariances spatiales, avec une fonction de distance adéquate, permet de

4. pyriemann et scikit-learn

travailler implicitement dans un espace des sources optimal. Même s'il n'est pas possible d'expliciter les réseaux mis en jeux, il est possible de comparer l'évolution d'un processus cognitif pour en déduire les changements dans le traitement de l'information. Ce type de réponse peut permettre d'alimenter la conception des modèles ou d'affiner les stratégies d'adaptation en ligne.

Il sera particulièrement intéressant de pouvoir éprouver la robustesse des représentations construites à partir des matrices de covariances en fonction des différents réseaux activés lors d'une tâche. Réciproquement, l'utilisation de représentations relativement fines temporellement peut permettre d'améliorer la détection et la caractérisation des réseaux spécifiques à une tâche.

3.4 Architecture neuronale et apprentissage profond

J'ai étudié les modèles de neurones impulsionnels pour la modélisation de l'attention visuelle pendant ma thèse et pour la prise de décision lors de mes travaux en postdoctorat à l'INRIA. Ces modèles sont particulièrement intéressants dans le cadre des réseaux récurrents et de leur utilisation comme *reservoir computing* (Lukoševičius et al., 2012). Dans ce type de paradigme, des entrées séquentielles sont projetées dans un réseau récurrent qui va permettre la prise en compte des dépendances à différentes échelles temporelles via les boucles d'interactions. L'analyse de l'activité d'une petite partie du réseau permet d'identifier des séquences spécifiques en utilisant des classifieurs faibles.

Ce type d'approche est encore utilisé pour modéliser des séries chaotiques ou donne de bons résultats pour prédire des séries temporelles qui sont réputées pour leur court horizon prédictif. Les récentes avancées en géométrie de l'information (Y. Ollivier, 2015) permettent d'envisager de mettre en place des mécanismes d'adaptation dans ces réseaux "réservoirs". Ce travail est d'une utilité limitée pour les réseaux de type *Long Short Term Memory* (LSTM) qui sont de très loin les réseaux récurrents les plus utilisés à l'heure actuelle. Il est cependant particulièrement adapté pour les réseaux de type réservoir et peut permettre de réaliser des apprentissages en ligne efficaces (Tallec et Yann Ollivier, 2017).

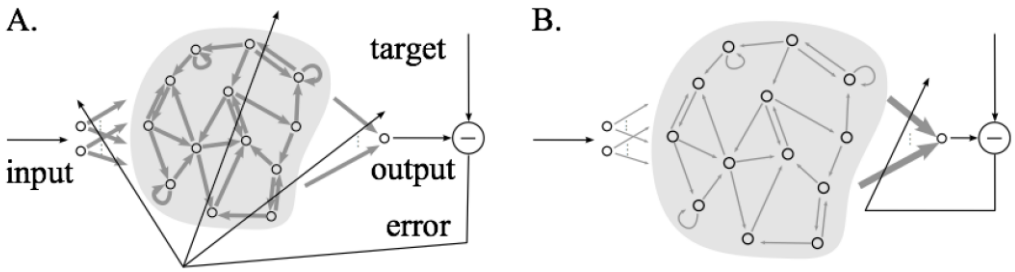

FIGURE 3.2 – Différence entre les réseaux récurrents et les réseaux de type réservoir, dans lesquels l'apprentissage est restreint à une couche d'interprétation externe.

Il est envisageable de faire évoluer des réseaux récurrents sans adapter la structure du réseau à chaque problème. Ceci permet d'envisager la mise en place d'une architecture composée de plusieurs réseaux récurrents, où chaque réseau se spécialise dans une tâche. Ce type d'architecture peut apprendre à détecter des dépendances temporelles fines et reste suffisamment légère pour être calculable. Elle pourrait être en particulier assez précise pour permettre des applications pour la compensation du handicap, soit au niveau de la perception sensorielle (Maglione et al., 2014) ou à la compensation de fonctions motrices (Borghini, Aricò et al., 2016).

Une deuxième piste à explorer consiste à étudier les possibilités de génération de données dans l'espace des matrices de covariance. Pour faire suite à des premiers résultats expérimentaux prometteurs (Kalunga, Chevallier et Barthélemy, 2015), je souhaite explorer les possibilités de générer de nouveaux points dans l'espace d'apprentissage disponible pour un sujet. Les retombées sont doubles : tout d'abord, il est possible d'augmenter le nombre d'exemples d'apprentissage disponible pour entraîner les classifieurs. Cette approche est particulièrement utile dans le cas des réseaux de neurones profonds, car elle permet d'améliorer la finesse de la frontière de décision (Perez et J. Wang, 2017). Les premiers résultats semblent indiquer que cette approche est particulièrement efficace dans le cas d'illettrisme BCI, les résultats des classifieurs augmentant significativement pour les sujets avec les scores les plus bas.

Ensuite, il est possible de compenser les données manquantes ou les situations déséquilibrées. Certains processus cognitifs sont complexes à mesurer et à produire, par exemple le potentiel d'erreur, qui est généré lorsqu'un

système commandé par un utilisateur ne répond pas à son attente. Il est donc fréquent d'avoir des données d'entraînement dans lesquels certaines situations sont sous-représentées (Spüler et al., 2012). La génération de données apporte un moyen simple de rétablir l'équilibre dans les données d'entraînement et permet de tirer un meilleur parti des algorithmes d'apprentissage.

Je travaille actuellement avec Violette Gautheret, étudiante en thèse au Gipsa, et Marco Congedo sur cette problématique. Dans l'approche que nous mettons en place, les données acquises dans des conditions différentes sont projetées dans un espace de représentation commun. Le but est de proposer une approche qui permette de faire du *transfer learning* et d'utiliser ainsi les données d'un sujet ou d'une condition expérimentale pour améliorer les résultats en classification d'un autre sujet.

La troisième approche que je souhaite développer, centrée là encore sur la recherche de représentations adaptées pour les signaux EEG. Un nouveau schéma d'apprentissage pour les réseaux de neurones profonds, inspirés des théories sur l'adaptation de domaine, permet de construire des représentations robustes et discriminantes de signaux. Appliqué aux signaux cérébraux, l'idée est de construire une séquence de filtres pour obtenir une représentation dépendante du sujet, mais ne dépendant pas des sessions d'enregistrements, et donc des variations temporelles intra-individuelles. La représentation du signal ainsi construite peut être interprétée comme une "normalisation" qui permet à la fois de préserver les relations spatio-temporelles fines du signal et offre une représentation suffisamment discriminante du signal pour qu'il puisse être utilisé dans des applications d'interfaces cérébrales.

De façon plus formelle, la représentation doit permettre une compression avec perte du signal, de telle sorte que les différentes sessions d'enregistrements soient issues de la même distribution, ou de distributions les plus similaires possible. Cette formulation fait référence à l'adaptation de domaine, qui s'intéresse aux possibilités de transférer un modèle appris sur les données d'un domaine *source* vers un domaine d'application *cible*. Une des principales motivations pour l'adaptation de domaine est de réduire les efforts d'étiquetage manuel des données, qui est un problème difficile et coûteux pour les signaux cérébraux.

3.5 Détection d'anomalies

Avec Amina Alaoui-Belghiti, actuellement en fin de première année de thèse CIFRE chez Nexeya-Hensoldt, nous avons travaillé sur la détection d'anomalie. L'entreprise qui l'emploie est en effet intéressée pour mettre en place de solutions de maintenance prédictive. Au contraire de la maintenance préventive, qui est réalisée de façon systématique à partir d'une expertise du domaine, la maintenance prédictive implique de suivre le fonctionnement d'un appareil industriel et de déclencher des opérations de maintenance si son comportement évolue.

Ce projet recoupe en plusieurs points les approches que nous développons au LISV, car l'idée est de disposer d'un système léger qui permette une évaluation continue et non-invasive. Ce type de problématique est traité dans l'équipe pour le suivi, la caractérisation et l'évaluation de l'interaction entre une personne en situation de handicap et une aide technique. À partir du relevé de mesures, le système doit être capable de détecter les variations s'écartant d'une situation normale, que ce soit pour les faire remonter au thérapeute dans le cas d'une personne ou à l'expert dans le cas d'une machine. La situation de référence étant une période définie par le thérapeute, qui correspond le plus souvent au moment où il est présent, ou alors, dans le cas d'un système industriel, la période qui suit directement l'étalonnage de l'appareil par un expert.

Dans cette catégorie de problème appelé *positive unlabeled learning*, le système ne dispose donc que de données non étiquetées et qui sont considérées comme positives, car issues d'une période de référence. Il faut distinguer cette situation de celle nécessitant d'utiliser des algorithmes de détection d'artefacts (*outlier detection*). Pour cette dernière, le système dispose d'une base d'exemples bruités, contenant aussi bien des données utiles que corrompues, et là encore sans étiquettes associées aux exemples.

Ce type de détection peut s'inspirer des approches menées pour quantifier la dissimilarité (J. Ma et Perkins, 2003 ; Manolova et Guérin-Dugué, 2013) ou des distances par rapport au plus proches voisins (H. Ma et al., 2013). Nous avons choisi d'utiliser des métriques de transport pour proposer des approches plus formelles, qui bénéficient des réçentes avancées sur leur versants computationels (Peyré, Cuturi et al., 2019) Nous travaillons sur une méthode de détection d'anomalie dans le domaine fréquentiel, qui mesure les écarts par rapport aux échantillons de référence en utilisant

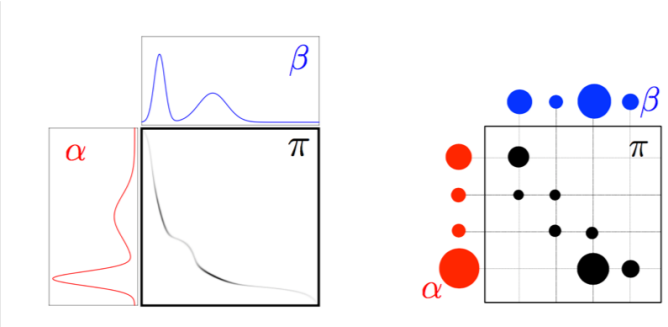

FIGURE 3.3 – Illustration du transport optimal appliqué à une distribution unimodale

des métriques de transport, du type de celle illustrée sur la figure 3.3. L'idée est de proposer une approche qui dispose d'une certaine souplesse, supportée par le terme de couplage, pour éviter les détections intempestives. Je souhaite reformuler les algorithmes existants de détection d'anomalies dans le cadre du transport optimal pour construire des algorithmes sur les bases solides d'une métrique.

J'ai associé dans ce travail l'équipe d'Eric Azabou, MCU-PH à l'hôpital de Garches, pour évaluer possibilité d'application de ces méthodes de détection d'anomalies dans le cadre de la recherche médicale. L'équipe développe des méthodes innovantes de stimulation du nerf vague pour soigner spondyloarthrites et d'autres types d'inflammations. Avec Guillaume Bao, ingénieur de recherche dans ce service, nous mettons en place une méthode automatique d'alerte du personnel médical en cas de changements dans les profils de réponses cérébrales aux stimulations.

Bibliographie

Absil, P.-A., Mahony, R. & Sepulchre, R. (2009). *Optimization algorithms on matrix manifolds*. Princeton University Press.

Agueh, M. & Carlier, G. (2011). Barycenters in the Wasserstein space. *SIAM Journal on Mathematical Analysis*, *43*(2), 904-924.

Aharon, M., Elad, M. & Bruckstein, A. (2006). K-SVD : An Algorithm for Designing Overcomplete Dictionaries for Sparse Representation. *IEEE Trans. Signal Processing*, *54*, 4311-4322.

Allison, B. Z. & Neuper, C. (2010). Could Anyone Use a BCI? In D. S. Tan & A. Nijholt (Éd.), *Brain-Computer Interfaces* (Chap. 3, p. 35-54). Human-Computer Interaction Series. Springer London.

Álvarez-Esteban, P., del Barrio, E., Cuesta-Albertos, J. & Matrán, C. (2016). A fixed-point approach to barycenters in Wasserstein space. *Journal of Mathematical Analysis and Applications*, *441*, 744-762.

Anastassiou, C. A., Perin, R., Markram, H. & Koch, C. (2011). Ephaptic coupling of cortical neurons. *Nature Neuroscience*, *14*(2), 217-223.

Andry, P., Blanchard, A. & Gaussier, P. (2010). Using the rhythm of nonverbal human–robot interaction as a signal for learning. *IEEE Transactions on Autonomous Mental Development*, *3*(1), 30-42.

Arsigny, V., Fillard, P., Pennec, X. & Ayache, N. (2007). Geometric means in a novel vector space structure on symmetric positive-definite matrices. *SIAM Journal on Matrix Analysis and Applications*, *29*(1), 328-347.

Babiloni, F., Cichocki, A. & Gao, S. (2007). Brain-computer interfaces : towards practical implementations and potential applications. *Computational Intelligence and Neuroscience*, *2007*.

Baker, M. (2016). 1,500 scientists lift the lid on reproducibility. *Nature News*, *533*(7604), 452.

Barthélemy, Q., Gouy-Pailler, C., Isaac, Y., Souloumiac, A., Larue, A. & Mars, J. (2013). Multivariate Temporal Dictionary Learning for EEG. *Journal of Neuroscience Methods*, *215*, 19-28.

Barthélemy, Q., Larue, A., Mayoue, A., Mercier, D. & Mars, J. (2012). Shift & 2D Rotation Invariant Sparse Coding for Multivariate Signals. *IEEE Trans. Signal Processing*, *60*, 1597-1611.

Barthélemy, Q., Mayaud, L., Ojeda, D. & Congedo, M. (2019). The Riemannian potato field : a tool for online signal quality index of EEG. *IEEE Transactions on Neural Systems and Rehabilitation Engineering*, *27*(2), 244-255.

Bekaert, M.-H., Botte-Lecoq, C., Cabestaing, F. & Rakotomamonjy, A. (2009). Les interfaces cerveau-machine pour la palliation du handicap moteur sévère. *STH*.

Bhatia, R. (2009). *Positive definite matrices*. Princeton university press.

Blankertz, B., Tomioka, R., Lemm, S., Kawanabe, M. & Muller, K. R. (2008). Optimizing Spatial filters for Robust EEG Single-Trial Analysis. *Signal Processing Magazine, IEEE*, *25*(1), 41-56.

Blum, S., Jacobsen, N., Bleichner, M. G. & Debener, S. (2019). A Riemannian modification of Artifact Subspace Reconstruction for EEG artifact handling. *Frontiers in human neuroscience*, *13*, 141.

Borghini, G., Aricò, P., Graziani, I., Salinari, S., Sun, Y., Taya, F., ... Babiloni, F. (2016). Quantitative assessment of the training improvement in a motor-cognitive task by using EEG, ECG and EOG signals. *Brain topography*, *29*(1), 149-161.

Borghini, G., Astolfi, L., Vecchiato, G., Mattia, D. & Babiloni, F. (2014). Measuring neurophysiological signals in aircraft pilots and car drivers for the assessment of mental workload, fatigue and drowsiness. *Neuroscience & Biobehavioral Reviews*, *44*, 58-75.

Botte-Lecocq, C., Bekaert, M.-H., Vannobel, J.-M., Leclercq, S. & Cabestaing, F. (2014). Considering human factors in BCI experiments : A global approach.

Brette, R. (2003). *Modèles Impulsionnels de Réseaux de Neurones Biologiques* (Thèse de Doctorat, École Doctorale Cerveau-Cognition-Comportement).

Chebbi, Z. & Moakher, M. (2012). Means of Hermitian positive-definite matrices based on the log-determinant α-divergence function. *Linear Algebra and its Applications*, *436*(7), 1872-1889.

Chen, X., Wang, Y., Gao, S., Jung, T. & Gao, S. (2015). Filter bank canonical correlation analysis for implementing a high-speed SSVEP-based brain–computer interface. *Journal of neural engineering*.

Chen, X., Wang, Y., Nakanishi, M., Gao, X., Jung, T. & Gao, S. (2015). High-speed spelling with a noninvasive brain–computer interface. *Proceedings of the National Academy of Sciences*, *112*(44), E6058-E6067.

Cherian, A., Sra, S., Banerjee, A. & Papanikolopoulos, N. (2011). Efficient similarity search for covariance matrices via the Jensen-Bregman LogDet divergence. In *2011 International Conference on Computer Vision* (p. 2399-2406). IEEE.

Chevallier, S., Barthelemy, Q. & Atif, J. (2014). On the need for metrics in dictionary learning assessment. In *EUSIPCO* (p. 1427-1431). IEEE.

Chevallier, S., Barthélemy, Q. & Atif, J. (2014). Subspace metrics for multivariate dictionaries and application to EEG. In *ICASSP* (p. 7178-7182). IEEE.

Chevallier, S., Cuperlier, N. & Gaussier, P. (2010). Efficient neural models for visual attention. In *International Conference on Computer Vision and Graphics* (p. 257-264). Springer.

Congedo, M., Barachant, A. & Andreev, A. (2013). A New Generation of Brain-Computer Interface Based on Riemannian Geometry. *arXiv preprint arXiv :1310.8115*.

Congedo, M., Barachant, A. & Bhatia, R. (2017). Riemannian geometry for EEG-based brain-computer interfaces ; a primer and a review. *Brain-Computer Interfaces*, *4*(3), 155-174.

Dhillon, I., Heath Jr., R., Strohmer, T. & Tropp, J. (2008). Constructing Packings in Grassmannian Manifolds via Alternating Projection. *Experimental Mathematics*, *17*(1), 9-35.

Duprès, A., Cabestaing, F. & Rouillard, J. (2014). SSVEP-based BCIs : study of classifier stability over time and effects of human learning on classification accuracy.

Engan, K., Aase, S. & Husøy, J. (2000). Multi-frame compression : theory and design. *Signal Processing*, *80*, 2121-2140.

Engan, K., Skretting, K. & Husøy, J. (2007). Family of iterative LS-based dictionary learning algorithms, ILS-DLA, for sparse signal representation. *Digit. Signal Process. 17*, 32-49.

Fletcher & Joshi, S. (2004a). Principal Geodesic Analysis on Symmetric Spaces : Statistics of Diffusion Tensors. In *Computer Vision and Mathematical Methods in Medical and Biomedical Image Analysis* (T. 3117, p. 87-98). LNCS. Springer.

Fletcher & Joshi, S. (2004b). Principal Geodesic Analysis on Symmetric Spaces : Statistics of Diffusion Tensors. In *Computer Vision and Mathematical Methods in Medical and Biomedical Image Analysis* (T. 3117, p. 87-98). LNCS. Springer.

Friedman, J., Hastie, T. & Tibshirani, R. (2001). *The elements of statistical learning*. Springer.

Gallego, G., Delbruck, T., Orchard, G., Bartolozzi, C., Taba, B., Censi, A., ... Daniilidis, K. et al. (2019). Event-based vision : A survey. *arXiv preprint arXiv :1904.08405*.

George, L. & Lécuyer, A. (2010). An overview of research on "passive" brain-computer interfaces for implicit human-computer interaction. In *ICABB*.

Gergondet, P. & Kheddar, A. (2015). SSVEP stimuli design for object-centric BCI. *Brain-Computer Interfaces*, *2*(1), 11-28.

Gerstner, W. & Kistler, W. (2002). *Spiking Neuron Models : Single Neurons, Population, Plasticity*. New York, NY, USA : Cambridge University Press.

Gribonval, R., Rauhut, H., Schnass, K. & Vandergheynst, P. (2007). *Atoms of all channels, unite ! Average case analysis of multi-channel sparse recovery using greedy algorithms* (rapp. tech. N° PI-1848). IRISA.

Hallett, M. (2000). Transcranial magnetic stimulation and the human brain. *Nature*, (406), 147-150.

Hérault, J. (1999). Rétine et cortex visuel : formalisation et application au traitement des images. Hermès.

Jayaram, V. & Barachant, A. (2018). MOABB : trustworthy algorithm benchmarking for BCIs. *Journal of neural engineering*, *15*(6), 066011.

Jeunet, C., Jahanpour, E. & Lotte, F. (2016). Why standard brain-computer interface (BCI) training protocols should be changed : an experimental study. *Journal of neural engineering*, *13*(3), 036024.

Jeunet, C., Lotte, F., Batail, J.-M., Philip, P. & Franchi, J.-A. M. (2018). Using recent BCI literature to deepen our understanding of clinical neurofeedback : A short review. *Neuroscience*, *378*, 225-233.

Joucla, S. & Yvert, B. (2012). Modeling extracellular electrical neural stimulation : From basic understanding to MEA-based applications. *Journal of Physiology, Paris*, *106*(3-4), 146-58.

Kalunga, E. K., Chevallier, S. & Barthélemy, Q. (2015). Data augmentation in Riemannian space for Brain-Computer Interfaces. In *ICML workshop Stamlins*.

Kalunga, E. K., Chevallier, S., Barthélemy, Q., Djouani, K., Monacelli, E. & Hamam, Y. (2016). Online SSVEP-based BCI using Riemannian geometry. *Neurocomputing*, *191*, 55-68.

Kalunga, E. K., Chevallier, S., Rabreau, O. & Monacelli, E. (2014). Hybrid interface : Integrating BCI in multimodal human-machine interfaces. In *AIM* (p. 530-535). IEEE.

Kalunga, E. K., Djouani, K., Hamam, Y., Chevallier, S. & Monacelli, E. (2013). SSVEP enhancement based on Canonical Correlation Analysis to improve BCI performances. In *AFRICON, 2013* (p. 1-5).

Kang, H., Nam, Y. & Choi, S. (2009). Composite common spatial pattern for subject-to-subject transfer. *Signal Processing Letters, IEEE*, *16*(8), 683-686.

Kreutz-Delgado, K., Murray, J., Rao, B., Engan, K., Lee, T. & Sejnowski, T. (2003). Dictionary Learning Algorithms for Sparse Representation. *Neural Comput. 15*, 349-396.

Kristensen, E., Guerin-Dugué, A. & Rivet, B. (2015). Comparison between Adjar and Xdawn algorithms to estimate eye-fixation related potentials distorted by overlapping. In *IEEE/EMBS NER* (p. 976-979).

Lim, Y. & Pálfia, M. (2012). Matrix power means and the Karcher mean. *Journal of Functional Analysis*, *262*(4), 1498-1514.

Lin, Z., Zhang, C., Wu, W. & Gao, X. (2007). Frequency recognition based on canonical correlation analysis for SSVEP-based BCIs. *IEEE Transactions on Biomedical Engineering*, *53*(12), 2610-2614.

Lotte, F. & Guan, C. (2011). Regularizing Common Spatial Patterns to Improve BCI Designs : Unified Theory and New Algorithms. *Biomedical Engineering, IEEE Transactions on*, *58*(2), 355-362.

Lotte, F. & Jeunet, C. (2015). Towards improved BCI based on human learning principles. In *Winter Conf. on BCI* (p. 1-4). IEEE.

Lukoševičius, M., Jaeger, H. & Schrauwen, B. (2012). Reservoir computing trends. *KI-Künstliche Intelligenz*, *26*(4), 365-371.

Ma, H., Hu, Y. & Shi, H. (2013). Fault detection and identification based on the neighborhood standardized local outlier factor method. *Industrial & Engineering Chemistry Research*, *52*(6), 2389-2402.

Ma, J. & Perkins, S. (2003). Time-series novelty detection using one-class support vector machines. In *IJCNN* (T. 3, p. 1741-1745).

Maglione, A. G., Vecchiato, G., Leone, C. A., Grassia, R., Mosca, F., Colosimo, A., ... Babiloni, F. (2014). Different perception of musical stimuli in patients with monolateral and bilateral cochlear implants. *Computational and mathematical methods in medicine*, *2014*.

Mailhé, B., Gribonval, R., Bimbot, F., Lemay, M., Vandergheynst, P. & Vesin, J. (2009). Dictionary learning for the sparse modelling of atrial fibrillation in ECG signals. In *IEEE ICASSP* (p. 465-468).

Mairal, J., Bach, F., Ponce, J. & Sapiro, G. (2010). Online Learning for Matrix Factorization and Sparse Coding. *J. Mach. Learn. Res. 11*, 19-60.

Manolova, A. & Guérin-Dugué, A. (2013). A new metric for dissimilarity data classification based on Support Vector Machines optimization. In *ESANN*.

Martin, H., Chevallier, S. & Monacelli, E. (2012). Fast calibration of hand movement-based interface for arm exoskeleton control. In *European Symposium on Artificial Neural Networks (ESANN)* (p. 573-578).

Martin, H., Chevallier, S. & Monacelli, E. (2015). Adaptive visualisation system for construction building information models using saliency. In *15th International Conference on Construction Applications of Virtual Reality* (p. 317-326).

Martin, H., Chevallier, S. & Monacelli, E. (2016). Adaptive visualization for BIM experts : coping with unstructured big data in construction. *arXiv preprint arXiv :1603.02028*.

Millan, J. R. (2004). On the need for on-line learning in brain-computer interfaces. In *IEEE IJCNN* (T. 4, p. 2877-2882).

Moakher, M. (2005). A differential geometric approach to the geometric mean of symmetric positive-definite matrices. *SIAM Journal on Matrix Analysis and Applications*, *26*(3), 735-747.

Moakher, M. & Batchelor, P. G. (2006). Symmetric Positive-Definite Matrices : From Geometry to Applications and Visualization. In *Visualization and Processing of Tensor Fields* (Chap. 17, p. 285-298).

Molina, G. G., Tsoneva, T. & Nijholt, A. (2009). Emotional brain-computer interfaces. In *ICACII* (p. 1-9). IEEE.

Monaci, G., Jost, P., Vandergheynst, P., Mailhé, B., Lesage, S. & Gribonval, R. (2007). Learning multimodal dictionaries. *IEEE Trans. Image Processing*, *16*, 2272-2283.

Monaci, G., Vandergheynst, P. & Sommer, F. (2009). Learning Bimodal Structure in Audio-Visual Data. *IEEE Trans. Neural Networks*, *20*, 1898-1910.

Nakanishi, M., Wang, Y., Wang, Y., Mitsukura, Y. & Jung, T. (2014). High-speed brain speller using steady-state visual evoked potentials. *International journal of neural systems*, *24*(06), 1450019.

Naseer, N. & Hong, K.-S. (2015). fNIRS-based brain-computer interfaces : a review. *Frontiers in human neuroscience*, *9*, 3.

Ollivier, Y. [Y.]. (2015). Riemannian metrics for neural networks II : recurrent networks and learning symbolic data sequences. *Information and Inference*, *4*(2), 154-193.

Olshausen, B. & Field, D. (1997). Sparse coding with an overcomplete basis set : a strategy employed by V1 ? *Vision Research*, *37*, 3311-3325.

Ozen, S., Sirota, A., Belluscio, M. A., Anastassiou, C. A., Stark, E., Koch, C. & Buzsáki, G. (2010). Transcranial electric stimulation entrains cortical neuronal populations in rats. *Journal of Neuroscience*, *30*(34), 11476-11485.

Perez, L. & Wang, J. (2017). The effectiveness of data augmentation in image classification using deep learning. *arXiv preprint arXiv :1712.04621*.

Perrinet, L. (2008). Sparse Spike Coding : applications of Neuroscience to the processing of natural images. In *SPIE Photonics Europe*.

Perrinet, L. U. (2019). An Adaptive Homeostatic Algorithm for the Unsupervised Learning of Visual Features. *Vision*, *3*(3), 47.

Perrinet, L., Samuelides, M. & Thorpe, S. (2004). Coding static natural images using spiking event times : do neurons cooperate ? *IEEE Transactions on neural networks*, *15*(5), 1164-1175.

Peyré, G., Cuturi, M. et al. (2019). Computational optimal transport. *Foundations and Trends in Machine Learning*, *11*(5-6), 355-607.

Phuoc, T. H., Guérin-Dugué, A. & Guyader, N. (2009). A computational saliency model integrating saccade programming. In *International Conference on Bio-inspired Systems and Signal Processing* (p. 57-64).

Ho-Phuoc, T., Guyader, N., Landragin, F. & Guérin-Dugué, A. (2012). When viewing natural scenes, do abnormal colors impact on spatial or temporal parameters of eye movements ? *Journal of Vision*, *12*(2), 4-4.

Rakotomamonjy, A. (2011). Surveying and comparing simultaneous sparse approximation (or group-lasso) algorithms. *Signal Process. 91*, 1505-1526.

Rivet, B., Souloumiac, A., Attina, V. & Gibert, G. (2009). xDAWN Algorithm to Enhance Evoked Potentials : Application to Brain-Computer Interface. *Biomedical Engineering, IEEE Transactions on*, *56*(8), 2035-2043.

Roc, A., Pillette, L., N'Kaoua, B. & Lotte, F. (2019). Would Motor-Imagery based BCI user training benefit from more women experimenters ? *arXiv preprint arXiv :1905.05587*.

Rougier, N. P., Hinsen, K., Alexandre, F., Arildsen, T., Barba, L. A., Benureau, F. C., ... Davison, A. P. et al. (2017). Sustainable computational science : the ReScience initiative. *PeerJ Computer Science*, *3*, e142.

Rouillard, J., Duprès, A., Cabestaing, F., Leclercq, S., Bekaert, M.-H., Piau, C., ... Lecocq, C. (2015). Hybrid BCI coupling EEG and EMG for severe motor disabilities. *Procedia Manufacturing*, *3*, 29-36.

Smith, E. & Lewicki, M. S. (2005). Efficient coding of time-relative structure using spikes. *Neural Computation*, *17*(1), 19-45.

Spüler, M., Rosenstiel, W. & Bogdan, M. (2012). Online adaptation of a c-VEP brain-computer interface (BCI) based on error-related potentials and unsupervised learning. *PloS one*, *7*(12), e51077.

Sra, S. (2016). Positive definite matrices and the S-divergence. *Proceedings of the American Mathematical Society*, *144*(7), 2787-2797.

Tallec, C. & Ollivier, Y. [Yann]. (2017). Unbiased online recurrent optimization. *arXiv preprint arXiv :1702.05043*.

Tiganj, Z., Chevallier, S. & Monacelli, E. (2014). Influence of extracellular oscillations on neural communication : a computational perspective. *Frontiers in computational neuroscience*, *8*, 9.

Tošić, I. & Frossard, P. (2011). Dictionary Learning. *IEEE Signal Processing Magazine*, *28*, 27-38.

Treisman, A. & Gelade, G. (1980). A feature-integration theory of attention. *Cognitive Psychology*, *12*(1), 97-136.

Várkuti, B., Guan, C., Pan, Y., Phua, K. S., Ang, K. K., Kuah, C. W. K., ... Sitaram, R. (2013). Resting state changes in functional connectivity correlate with movement recovery for BCI and robot-assisted upper-extremity training after stroke. *Neurorehabilitation and neural repair*, *27*(1), 53-62.

Vialatte, F., Maurice, M., Dauwels, J. & Cichocki, A. (2010). Steady-state visually evoked potentials : focus on essential paradigms and future perspectives. *Progress in neurobiology*, *90*(4), 418-438.

Vidal, J. J. (1973). Toward direct brain-computer communication. *Annual review of biophysics and bioengineering*, *2*(1), 157-180.

Vidaurre, C. & Blankertz, B. (2010). Towards a cure for BCI illiteracy. *Brain topography*, *23*(2), 194-198.

Villani, C. (2008). *Optimal transport : old and new*. Springer Science & Business Media.

Vinje, W. E. & Gallant, J. L. (2000). Sparse coding and decorrelation in primary visual cortex during natural vision. *Science*, *287*(5456), 1273-1276.

Wilkinson, M. D., Dumontier, M., Aalbersberg, I. J., Appleton, G., Axton, M., Baak, A., ... Bourne, P. E. et al. (2016). The FAIR Guiding Principles for scientific data management and stewardship. *Scientific data*, *3*.

Wolpaw, J., Birbaumer, N., McFarland, D. J., Pfurtscheller, G. & Vaughan, T. M. (2002). Brain–computer interfaces for communication and control. *Clinical Neurophysiology*, *113*(6), 767-791.

Yang, Y., Bloch, I., Chevallier, S. & Wiart, J. (2016). Subject-specific channel selection using time information for motor imagery brain–computer interfaces. *Cognitive Computation*, *8*(3), 505-518.

Yang, Y., Chevallier, S., Wiart, J. & Bloch, I. (2012). Time-frequency Selection in Two Bipolar Channels for Improving the Classification of Motor Imagery EEG. In *IEEE EMBC* (p. 2744-2747).

Yang, Y., Chevallier, S., Wiart, J. & Bloch, I. (2017). Subject-specific time-frequency selection for multi-class motor imagery-based BCIs using few Laplacian EEG channels. *Biomedical Signal Processing and Control*, *38*, 302-311.

Yger, F., Berar, M. & Lotte, F. (2016). Riemannian approaches in brain-computer interfaces : a review. *IEEE Transactions on Neural Systems and Rehabilitation Engineering*, *25*(10), 1753-1762.

Zander, T. O. & Kothe, C. (2011). Towards passive brain–computer interfaces : applying brain–computer interface technology to human–machine systems in general. *Journal of neural engineering*, *8*(2), 025005.

Zhu, D., Bieger, J., Molina, G. G. & Aarts, R. M. (2010). A survey of stimulation methods used in SSVEP-based BCIs. *Intell. Neuroscience*, *2010*, 1-12.

Appendix

Sélection de publications

1. Zoran Tiganj, Sylvain Chevallier, Eric Monacelli. Influence of extracellular oscillations on neural communication : A computational perspective. *Frontiers in Computational Neuroscience*, 8(9), 2014
2. Sylvain Chevallier, Quentin Barthélémy, Jamal Atif. Subspace metrics for multivariate dictionaries and application to EEG. *IEEE International Conference on Acoustics, Speech, and Signal Processing (ICASSP)*. Florence, Italie, 2014
3. Emmanuel K Kalunga, Sylvain Chevallier, Quentin Barthélémy, Karim Djouani, Yskandar Hamam, Eric Monacelli. Online SSVEP-based BCI using Riemannian Geometry, *Neurocomputing*, 191, pp. 55-68, 2016
4. Yuan Yang, Sylvain Chevallier, Joe Wiart, Isabelle Bloch. Subject-specific time-frequency selection for multi-class motor imagery-based BCIs using few Laplacian EEG channels. *Biomedical Signal Processing and Control*, 38, pp. 302-311, 2017
5. Emmanuel Kalunga, Sylvain Chevallier, Quentin Barthélemy. Transfer learning for SSVEP-based BCI using Riemannian similarities between users. In *EUSIPCO*, Rome, Italie, 2018.

frontiers in
COMPUTATIONAL NEUROSCIENCE

ORIGINAL RESEARCH ARTICLE
published: 07 February 2014
doi: 10.3389/fncom.2014.00009

Influence of extracellular oscillations on neural communication: a computational perspective

Zoran Tiganj*, Sylvain Chevallier and Eric Monacelli

LISV, Université de Versailles Saint-Quentin-en-Yvelines, Vélizy-Villacoublay, France

Edited by:
Terrence J. Sejnowski, The Salk Institute for Biological Studies, USA

Reviewed by:
G. B. Ermentrout, University of Pittsburgh, USA
Benjamin Torben-Nielsen, Hebrew University of Jerusalem, Israel

****Correspondence:***
Zoran Tiganj, Theoretical Cognitive Neuroscience Lab, Department of Psychological and Brain Sciences, Center for Memory and Brain, Boston University, 2 Cummington Street, Boston, MA 02215, USA
e-mail: zorant@bu.edu

Neural communication generates oscillations of electric potential in the extracellular medium. In feedback, these oscillations affect the electrochemical processes within the neurons, influencing the timing and the number of action potentials. It is unclear whether this influence should be considered only as noise or it has some functional role in neural communication. Through computer simulations we investigated the effect of various sinusoidal extracellular oscillations on the timing and number of action potentials. Each simulation is based on a multicompartment model of a single neuron, which is stimulated through spatially distributed synaptic activations. A thorough analysis is conducted on a large number of simulations with different models of CA3 and CA1 pyramidal neurons which are modeled using realistic morphologies and active ion conductances. We demonstrated that the influence of the weak extracellular oscillations, which are commonly present in the brain, is rather stochastic and modest. We found that the stronger fields, which are spontaneously present in the brain only in some particular cases (e.g., during seizures) or that can be induced externally, could significantly modulate spike timings.

Keywords: extracellular oscillations, local field potentials, ephaptic coupling, nonsynaptic communication, multi-compartment model, NEURON simulation environment, pyramidal neurons

1. INTRODUCTION

Ion exchange between neurons and the surrounding extracellular medium is essential for neural communication. In the extracellular medium, this exchange causes oscillations of electric potential, commonly referred to as Local Field Potentials (LFPs) (Ebersole and Milton, 2003; Buzsáki et al., 2012). The LFPs often exhibit significant levels of temporal and spatial coherence and are linked with a number of cognitive phenomena (see Ward, 2003; Buzsáki and Draguhn, 2004; Uhlhaas et al., 2010; Wang, 2010 for reviews). For instance, theta and gamma oscillations, particularly in the hippocampus, are often linked with memory formation and retrieval (Schack et al., 2002; Sederberg et al., 2003; Osipova et al., 2006; Nyhus and Curran, 2010), while attention is associated with a reduced alpha rhythm and increased gamma rhythm (Thut et al., 2006; Lisman and Buzsáki, 2008; Capotosto et al., 2009; Deco and Thiele, 2009; Schroeder and Lakatos, 2009). Different rhythms are related with processing in early sensory systems (Koepsell et al., 2010) and in speech generation and processing (Peelle and Davis, 2012). Furthermore, it has recently been proposed that some neurons code information by firing with respect to the phase of the ongoing oscillations (Fries et al., 2007; Montemurro et al., 2008; Kayser et al., 2009).

The extracellular oscillations are commonly considered to be an epiphenomena, a sporadic consequence of neural dynamics. Contrary to this hypothesis, it has been speculated that the periodic oscillations in the extracellular medium in some cases have a functional role, that they support the neural communication. This alternative hypothesis, based on *ephaptic transmission*, assumes that the neurons might not communicate only by exchanging information through their synaptic connections, but additionally through the extracellular medium (Fröhlich and McCormick, 2010; Weiss and Faber, 2010; Anastassiou et al., 2011). Even though the LFPs are generally too weak to trigger an action potential, they can still affect the spike number and timing (Parra and Bikson, 2004; Radman et al., 2007; Anastassiou et al., 2010).

If the hypotheses about the functional role of the extracellular oscillations are proven right, it will provide new insights for understanding the neural code, indicating mechanisms that can contribute to the widely observed synchrony of the neural activity. This finding could have impact on theoretical and clinical research, including neuropharmacology and neuroprostetics. Additionally, it would be beneficial for developing new approaches in computational models of the brain, and more generally, models of artificial neural networks, since the existing models (e.g., Izhikevich, 2006; Markram, 2006) do not address the ephaptic transmission.

The main motivations for the proposed study are to deepen the understanding of this prospective mode of neural communication and to investigate whether the externally induced electrical fields (e.g., through Transcranial Magnetic Stimulation (TMS) (Barker et al., 1985; Hallett, 2000; Walsh and Cowey, 2000; Allen et al., 2007), Transcranial Electrical Stimulation (TEC) (Deans et al., 2007; Kirov et al., 2009; Ozen et al., 2010; Reato et al., 2010) and Deep Brain Stimulation (DBS) (Benabid et al., 2009; Joucla and Yvert, 2012) might promote the ephaptic coupling. Modifying the ephaptic coupling could alter synchrony of the neural assemblies and potentially help to correct pathological network dynamics.

Through a computational study, we investigated what changes in the timing and number of action potentials can be induced by the temporal and spatial oscillations of the extracellular potential. Our study is conducted at a single neuron level and is done through several simulation setups, hard to implement experimentally. Contrary to the common experimental protocols, where the stimulation is done by current injection into the soma (see for example Anastassiou et al., 2011), we used PostSynaptic Potentials (PSPs) which are applied at different spatial locations of the dendrites. We generated a sufficient number of PSPs for the neuron to exhibit different firing patterns. Moreover, we analyzed the influence of extracellular oscillations with respect to the spatial part of the dendritic tree receiving most of the inputs. We modeled the dendrites with active ion conductances and considered different dendritic morphologies. Since the considered neuronal model is multi-compartmental, we computed the strength of the extracellular oscillations for each compartment separately, so that it depends on the spatial location of the compartment.

Focusing on models of the CA1 and the CA3 neurons, we investigated the influence of the extracellular oscillations at a single neuron level depending on:

1. Properties of the active ion conductances, i.e., we used different sets of active ion channels.
2. Spatial distribution of the dendritic inputs, i.e., we altered the locations of the synaptic inputs between the basal and apical branches.
3. Morphological properties, i.e., we used different shapes of the dendritic tree.

For each of these three cases, we examined the following properties of the extracellular oscillations (as shown in **Figure 1**): the temporal and spatial frequencies, the amplitude, and the phase. In this study, we always addressed the influence of the oscillations on an individual neuron, not on neural assemblies. Through randomly delivered PSPs the membrane potential was set to fluctuate around the threshold level, with a certain probability of crossing it. We studied how the above properties of the extracellular oscillations influence the number and the timing of generated spikes.

We did not investigate directly the influence of the spontaneous LFPs or the artificially induced oscillations, but the influence of the extracellular oscillations on a more general level, regardless of their origin. The link between this general level and the spontaneous LFPs of a particular temporal and spatial properties can still be made and will be discussed here.

It is important to mention that the proposed study is difficult to perform experimentally, either *in vivo* or *in vitro*. It is particularly difficult to produce repetitive stimulation with the PSPs of controlled amplitude, timing and spatial distribution. Since such repetitive stimulation is essential for our investigation, we find it suitable to approach the problem through a computational study. Complex interactions of nonlinear ionic currents within branched dendritic trees can be described through a set of equations, based on the Hodgkin–Huxley model, which cannot be solved analytically. We used the simulator NEURON (Hines and Carnevale, 1997) to numerically solve the equations (Mainen and Sejnowski, 1998). This study is not a replacement for *in vivo* or *in vitro* experiments, but rather a complementary approach that can help in focusing future research.

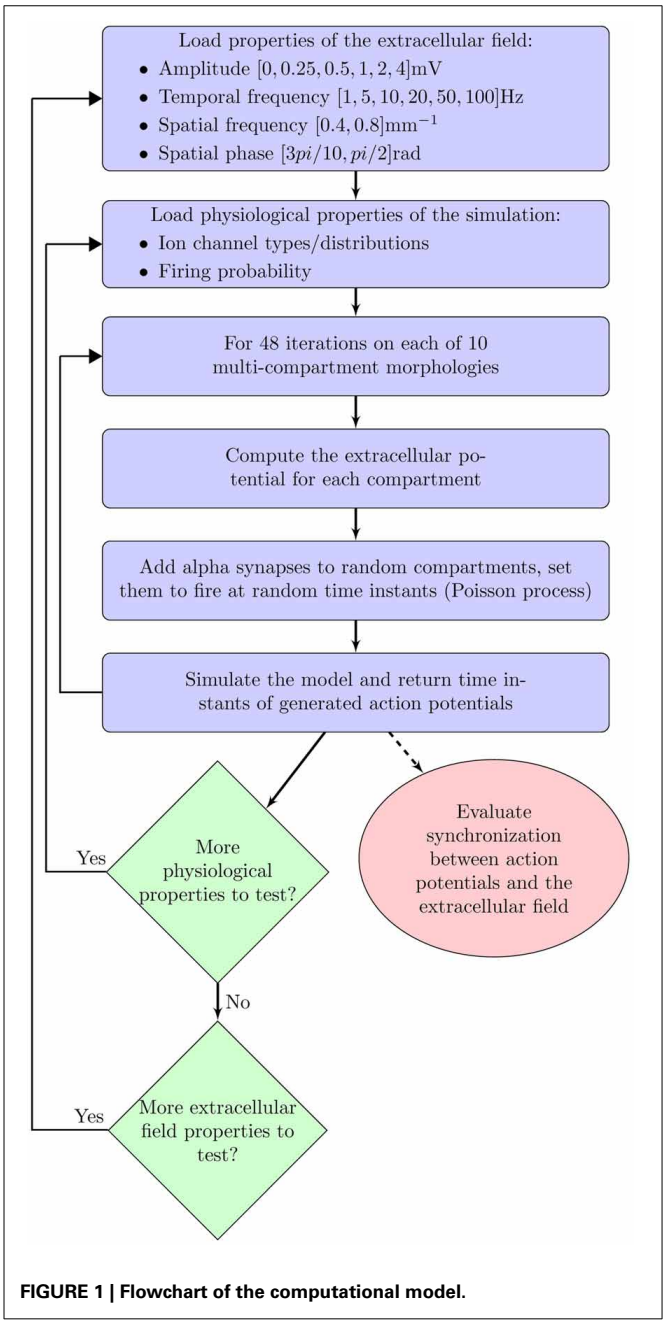

FIGURE 1 | Flowchart of the computational model.

Common use of the Hodgkin–Huxley model assumes that the extracellular medium is equipotential and it is typically considered as an electrical ground. Here we assume that the electric potential in the extracellular space varies through time and space. If we consider the neural membrane to consist of the ohmic conductance (active and passive) and the capacitance, the above assumption implies that the voltage on the conductance and capacitance is not simply equal to the intracellular membrane potential, which is the case in the Hodgkin–Huxley model.

Instead, it is set to be equal to the difference between the intracellular membrane potential and the instantaneous amplitude of the extracellular oscillations.

The paper is organized as follows. Parameters of the model are closely analyzed in the following section. In particular, we describe the neural morphologies and give details on the properties of the ion channels in the model. We also describe the model of PSPs and the extracellular oscillations. In section 3 we present the results of the simulations: first, when the stimulation is done with the current injection, and then when it is done with the PSPs. The results illustrate the importance of the amplitude, the temporal and spatial frequency and the spatial phase of the extracellular oscillations. Finally, the results are discussed in section 4.

2. MATERIALS AND METHODS

This section provides details on the computational models that are used to obtain the results presented in the paper. The models are implemented in neural simulator NEURON (Hines and Carnevale, 1997) that we run on a Linux-based cluster, consisting of 75 dual-core computers. We used multi-compartment models for two different neuron types: the CA1 and the CA3 rat hippocampal pyramidal neurons. The time step of the simulation was 25μs. The stability of the models with respect to the time step was tested by verifying that for smaller times steps the influence of the extracellular oscillations does not change significantly. To account for the artifacts caused by the initial conditions we added an extra period of 100 ms at the beginning of each simulation (not displayed in the results) that allowed the membrane potential to grow from the initial −65 mV to the value controlled only by the PSPs.

2.1. MORPHOLOGY

Each neuron in our model consists of the dendritic tree, the soma and the short axon. The length of the axon was determined experimentally (100μm), in a such way that simulating longer axon did not quantitatively change the results. For each of the two neuron types, we investigated five different morphologies of the dendritic tree. The morphologies of the CA3[1] are taken from Samsonovich and Ascoli (2003) and those of the CA1 cells[2] are taken from Pyapali et al. (1998).

All the morphology files are given in SWC format. In this format, each segment is described as a cylinder and is associated with a type (soma, axon, basal, or apical dendrite), a spatial position of the end point, a diameter, and the information about which segment is connected to the given one on the path to the soma. Thus, from such files we were able to precisely reconstruct 3D shapes of the given morphologies. Each morphology file describes a branched dendritic tree, with the number of compartments spanning from 151 to 503. The size of the compartments was computed using the `d_lambda` rule proposed by Carnevale and Hines (2006).

[1]We used morphologies named: `cell_a`, `cell_c`, `cell_m`, `cell_t`, and `cell_v`; they are available for download on http://krasnow1.gmu.edu/cn3/L-Neuron/database/.

[2]We used morphologies named: `n121CNG`, `n129CNG`, `n141CNG`, `n142CNG`, and `n145CNG`; they are available for download on http://www.neuromorpho.org.

2.2. PROPERTIES OF THE ACTIVE ION CONDUCTANCES

To study how the influence of the extracellular oscillations on the spike number and timing depends on the active ion conductances in the soma and the dendrites, two different sets of active ion conductances were used, one corresponding to the CA1 and the other to the CA3 pyramidal neurons. Notice that adding active conductances in the dendrites was necessary for the PSPs to propagate in a significant amount from the apical dendrites to the soma. In such way the PSPs could contribute to the generation of the dendritic as well as the somatic spikes (Kim et al., 2012). Properties of the ion channels used in the simulations have been described in Migliore et al. (2005) for the CA1 neurons and in Hemond et al. (2008) for the CA3 neurons[3]:

- CA1: Uniform passive properties were $\tau_m = 28$ ms (membrane time constant), $R_m = 28\,\mathrm{k\Omega cm^2}$ (radial resistance of the membrane), $R_a = 150\,\Omega$cm (axial resistance of the membrane), while the active properties included sodium, DR-, and A-type potassium conductances and a hyperpolarization-activated I_h current. The kinetics for all the channels and the spatial distribution of the channels were identical to those in Migliore et al. (2005).
- CA3: Passive: $\tau_m = 35$ ms, $R_m = 25\,\Omega\mathrm{cm^2}$, $R_a = 150\,\Omega$cm. The set of active channel properties included sodium conductances, a repertoire of potassium conductances: delayed rectifier, M-current, fast-inactivating A-type, and slowly-inactivating D-type current, three voltage-gated Ca^{2+} conductances (Ca_V N-, L-, and T-type), two calcium-dependent potassium conductances (KC and KAHP), and I_h current.

These two sets give rather different profiles of ion conductances. While for the CA1 neurons only the main conductances involved in the action potential generation and regulation were included, for the CA3 neurons we included a much broader set of ion conductances.

2.3. MODEL OF POSTSYNAPTIC POTENTIALS

The spatial location of each synapse and their corresponding PSPs times were determined randomly for each simulation. We repeated each simulation for several different properties of the extracellular field, e.g., we varied the amplitude of the extracellular field. To study the influence of the extracellular oscillations, we kept the spatial locations and the PSPs times fixed for each different property of the extracellular field.

To emphasize spatiotemporal summation of the PSPs, we balanced the contributions from different synapses by pacing them only onto dendritic compartments thinner than 0.35μ m. The probability of a synapse being placed onto any compartment thinner than 0.35μ m was set to be equal, unless otherwise specified. The exact spatial location within the compartment was also determined randomly, with equal probability that the synapse will be placed onto any of the sections within the compartment. One

[3]Both models are available in ModelDB on the following addresses: http://senselab.med.yale.edu/modeldb/showmodel.asp?model=101629 and http://senselab.med.yale.edu/modeldb/showmodel.asp?model=55035.

example of synaptic locations generated in such way is given in **Figure 2A**.

Temporal profile of the PSPs was modeled as a Poisson process. The number of the PSPs per second was adjusted so that the neuron exhibits a firing rate F within a desired range. We define three ranges of the firing rate: low for $F \leqslant 5$ Hz, medium for $5 < F < 15$ Hz and high for $F \geqslant 15$ Hz. To achieve these firing rates we altered the of the PSPs to be between 200 and 7000 Hz.

The synaptic conductance is modeled for $t \geqslant t_{\text{onset}}$ as an alpha function:

$$g = g_{\max} \frac{t - t_{\text{onset}}}{\tau} e^{-\frac{1}{\tau}(t - t_{\text{onset}} - \tau)}, \quad (1)$$

while for $t < t_{\text{onset}}$, $g = 0$. The parameters within the alpha function were the same for all the synapses: $\tau = 0.1$ ms, $g_{\max} = 1\mu$S.

2.4. MODEL OF THE EXTRACELLULAR OSCILLATIONS

The voltage oscillations were simulated in the extracellular medium by adding a voltage source to each compartment[4], as illustrated on **Figure 2B**. We modeled the oscillations as a temporal and spatial fluctuation. The change across space was only occurring along the somatodendritic axis, which we denote as the x axis. The other two axes of the Cartesian coordinate system are denoted as y and z. Consequently, at any time, the amplitude of the extracellular oscillations was different for different spatial points along the somatodendritic axis, but the same for any spatial point along the other two axis (y and z). This is depicted on a 2D plane in **Figure 3**. Shape of the oscillations is described by a simple sinusoidal function $V_e(x, y, z, t)$. Then, the extracellular potential at the spatial point (x, y, z) and at the time t writes as follows:

$$V_e(x, y, z, t) = V_o \sin(2\pi f_t t) \sin(2\pi f_s x + \phi_s) \quad (2)$$

where V_o is the amplitude of the oscillations, f_t is the temporal frequency, f_s is the spatial frequency and ϕ_s is the spatial phase.

In the context of the Hodgkin–Huxley model, the equation for the current I_k going through the kth ion channel is:

$$I_k = g_k(V_i - V_e - V_k) \quad (3)$$

where V_i is the intracellular potential, V_k is the reversal potential of the kth ion channel and g_k is the channel conductance.

To have better understanding of the influence of the extracellular oscillations on neural activity, the simulations were repeated for different values of V_o, f_t, f_s and ϕ_s.

The amplitude of the extracellular oscillations depends on many factors, from the animal species, to the regions of the brain and the cognitive states (Buzsáki et al., 2012). In the band below 100 Hz, the amplitude rarely exceeds 1 mV (Anastassiou et al., 2010; Brette and Destexhe, 2011; Buzsáki et al., 2012). We performed the simulations for the following set of amplitudes V_o: 0.25, 0.5, 1, 2 and 4 mV. This wide range of values allowed us to investigate the significance of the amplitude in a rather general

[4]Within the simulator NEURON, we used mechanism `extracellular` to drive the voltage oscillations into each compartment.

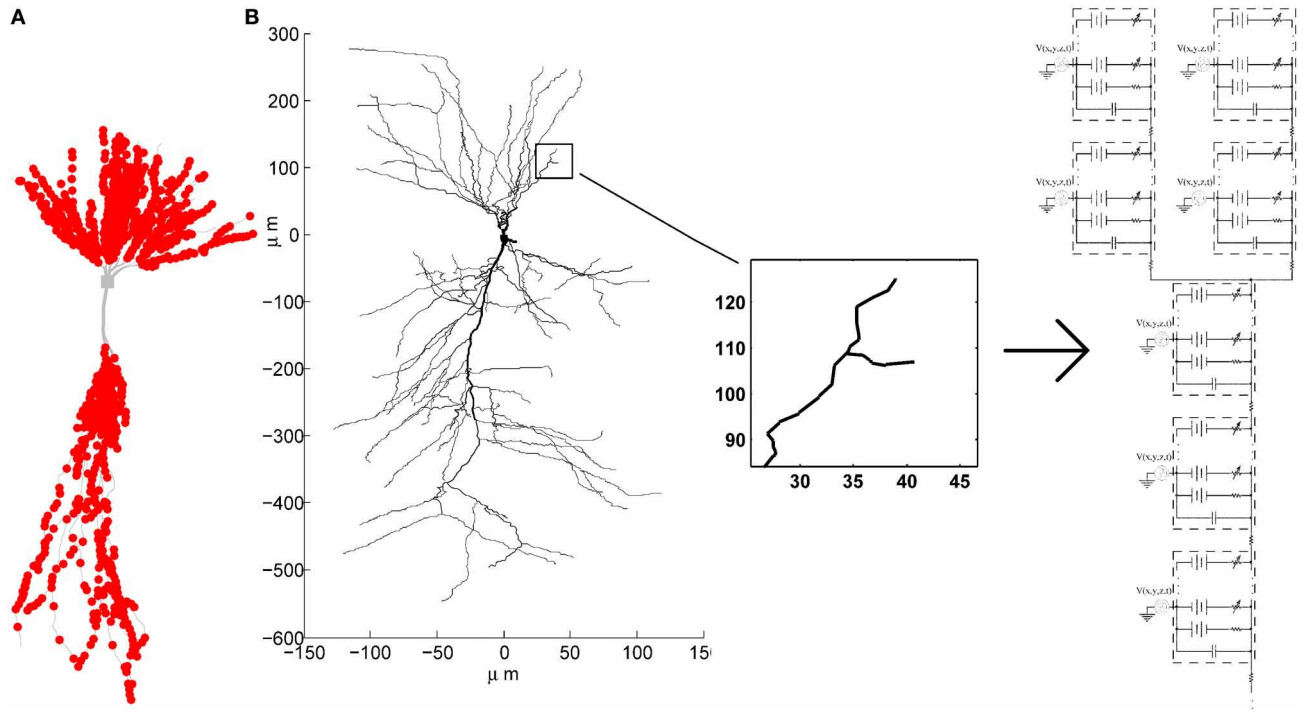

FIGURE 2 | (A) Example of synaptic locations (red dots) on one of the CA3 neuron morphologies. **(B)** Multi-compartment model of a CA3 neuron with active conductances and the extracellular oscillations added to each compartment.

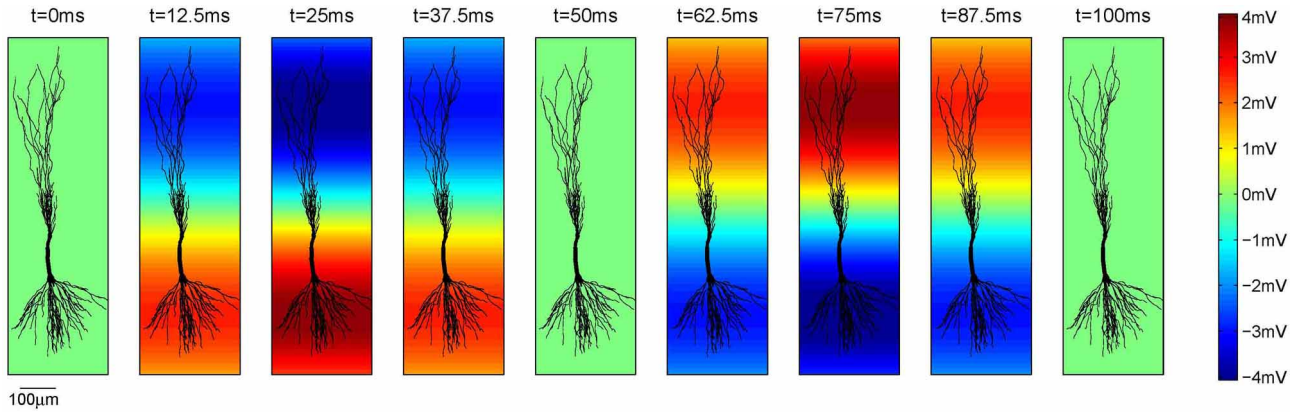

FIGURE 3 | The amplitude of the extracellular oscillations across one full temporal cycle of 100 ms, i.e., $f_t = 10$ Hz. In this example $V_o = 4$ mV, $f_s = 0.8\,\text{mm}^{-1}$ and $\phi_s = \frac{3\pi}{10}$ rad. The parameter ϕ_s is expressed at the bottom of the plots as the reference.

context, including the spontaneous and the artificially induced oscillations.

The extracellular oscillations that exhibit a significant spatial extent commonly have temporal frequencies below 100 Hz, although there are notable exceptions, such as the hippocampal sharp waves (Buzsáki, 1986). Even though the high amplitude oscillations are known to occur in several particular bands, e.g., theta waves (Kahana et al., 2001), we performed the simulations for a relatively broad set of frequency values: 1, 5, 10, 20, 50, and 100 Hz. These values have been chosen to investigate whether the values observed in reality are in some sense optimal for high or low influence on neural activity.

Regarding the spatial frequency, sources and sinks were located at the opposite sides of the dendritic tree, e.g., if the sources were located around the apical dendrites, then the sinks were located around the basal dendrites and vice versa. Therefore, we set $f_s = 0.8\,\text{mm}^{-1}$ as illustrated in **Figure 3**. The influence of the extracellular oscillations when sinks and sources were more distant from each other was also investigated by setting the spatial frequency $f_s = 0.4\,\text{mm}^{-1}$. In this case, to ensure the consistency of the results, the strength of the electrical field was kept constant: when the distance between the sink and the source was doubled, the amplitude of the extracellular oscillations was also doubled. The spatial distributions of the oscillations for both cases are shown in **Figure 4A**.

The spatial phase of the oscillations was set so that the peak amplitude was reached around the middle of the basal dendrites and around the upper end of the apical dendrites, as these areas often contain the largest number of branches. The exact value of the phase was $\phi_s = \frac{3\pi}{10}$ rad, as shown on the left hand side plot in **Figure 4B**. Additionally, we investigated a case when the peak amplitude was reached around the soma. In that case $\phi_s = \frac{\pi}{2}$ rad was used (see the right hand side plot in **Figure 4B**).

3. RESULTS

In this section we first present the results of a simulation conducted with current injection as the stimulus input. We then present the results from a set of simulations in which the PSPs, instead of current injection, were used to stimulate the neuron.

3.1. STIMULATION WITH CURRENT INJECTION

As an initial validation of the models used in this study we performed a simulation that is similar to the experimental protocol described in Anastassiou et al. (2011). The goal of the simulation was to analyze the influence of extracellular oscillations on spike timing during current injection into soma. The results are displayed in **Figure 5**.

For the CA3 neuron model, the injection of a 0.35 nA constant current into the soma led to a tonic spiking, such that each action potential was fired periodically, approximately every 75 ms. Adding the extracellular oscillations affected this periodicity, degrading the period stability. The time shift of the spikes increases with the amplitude of the oscillations. However, the increase is not linear, due to the complex nonlinear dynamics of the voltage-gated ion channels in the soma and in the dendritic tree.

The results displayed in **Figure 5** are qualitatively similar to those reported in the experiments presented in Anastassiou et al. (2011). This type of simulation demonstrates that the extracellular oscillations can affect the timing of action potentials. Nevertheless, the influence of the low amplitude oscillations, which are observable in different cortical structures, seems to be rather modest. The temporal shift of the firing instants is very small, e.g., the influence of $V_o = 0.25$ mV oscillations results in 0.5 ms change in the timing of the action potential shown in the zoomed part on the top of **Figure 5**.

3.2. STIMULATION WITH POSTSYNAPTIC POTENTIALS

Current injection into the soma gives an illustration of the influence of extracellular oscillations on the timing of action potentials. However, this is not a very realistic setup and. Stimulation mediated by the PSPs is more biologically realistic. The PSPs properties were set as described in section 2.3 and the results of the simulation are presented for different properties of the extracellular oscillations according to the parameters presented in section 2.4.

3.2.1. Influence of the amplitude of the extracellular oscillations

The simulations were first performed to explore the influence of the amplitude of the extracellular oscillations on the spike

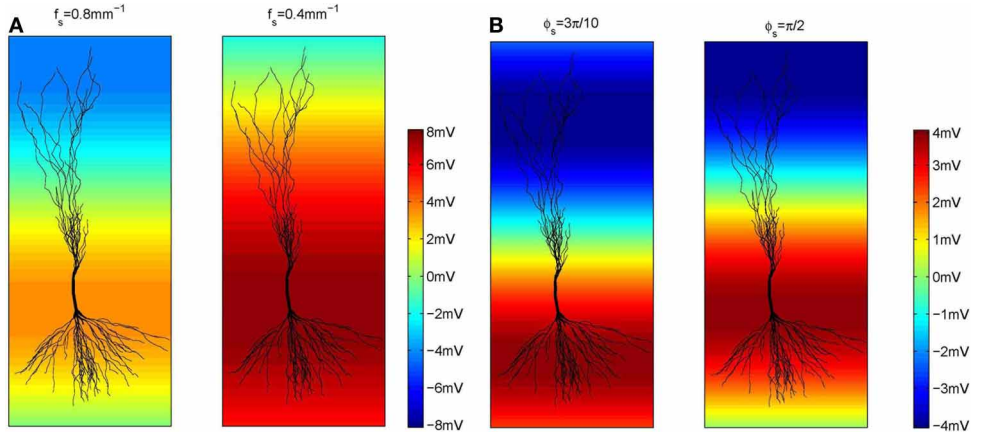

FIGURE 4 | (A) The amplitude of the extracellular oscillations for two spatial frequencies, $f_s = 0.8\,\text{mm}$ (the left side plot) and $0.4\,\text{mm}^{-1}$ (the right side plot). **(B)** The amplitude of the extracellular oscillations for two spatial phases, $\phi_s = \frac{3\pi}{10}$ rad (left side plot) and $\frac{\pi}{2}$ rad (right side plot).

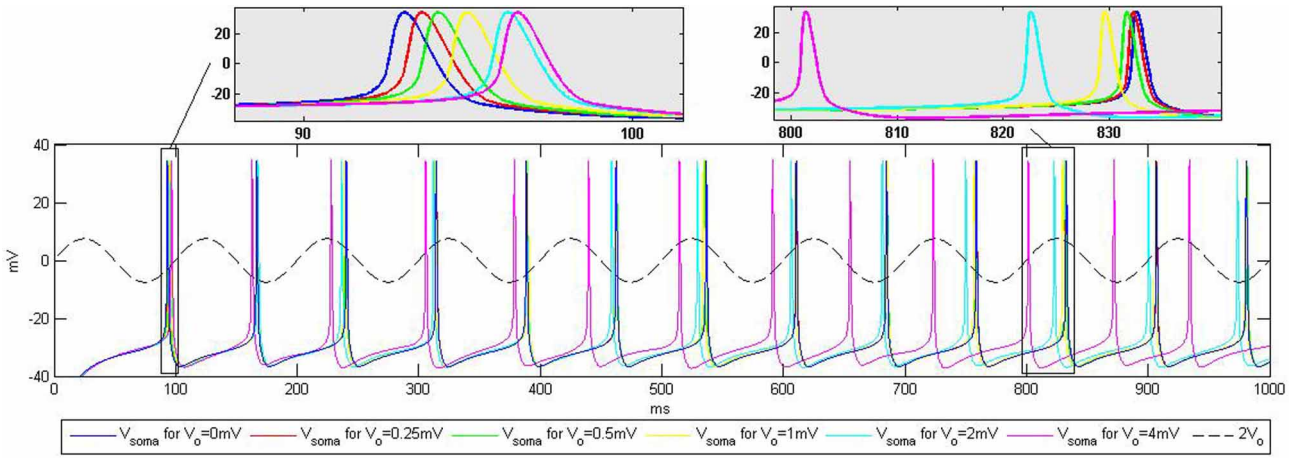

FIGURE 5 | Influence of the extracellular oscillations on the timing of the action potentials during current injection into the soma. The top boxes highlight the influence of the extracellular oscillations on the spike timing. The baseline (no extracellular oscillations) is displayed in blue. The dashed line represents the extracellular oscillations. We display the maximum amplitude used in the simulations, $V_o = 4\,\text{mV}$, scaled up by the factor of two for better visibility.

number and timing. The temporal frequency was set to 10 Hz, the spatial frequency to $0.8\,\text{mm}^{-1}$ and the spatial phase to $\frac{-3\pi}{10}$ rad. The plots on the top of **Figure 6** show the membrane potential at the soma of a CA3 neuron for different values of the amplitude of the oscillations. Hereafter we will refer to *baseline* as the evolution of the soma potential evoked by the PSPs in absence of the extracellular oscillations, i.e., it corresponds to the simulations with $V_o = 0\,\text{mV}$. The baseline is shown in blue in **Figure 6**. In this example, the PSPs frequency was tuned so that the firing rate F stays below 5 Hz. The zooms of the four different parts of the plot illustrate the small changes of the membrane potential, as well as the small time shifts in the spike timing, both due to the influence of the extracellular oscillations.

The bottom plot in **Figure 6** further illustrates how the membrane potential depends on the amplitude of the extracellular oscillations. The plot shows the membrane potential at the soma in the presence of 4 mV extracellular oscillations subtracted from the membrane potential at the soma with no extracellular oscillations (black line). To illustrate the phase relationship, on the same plot we also displayed the extracellular oscillations (blue line). The phase and amplitude of the difference of the two membrane potentials follow those of the extracellular oscillations, but due to a large nonlinearity of the voltage-gated channels, large fluctuations of the amplitude occur frequently.

To have a better understanding of the correlation between the extracellular oscillations and the resulting changes in the timing and the number of action potentials, we performed an ensemble of simulations: simulations on 5 CA1 and 5 CA3 models were repeated 48 times (called *iterations*), resulting in a total number of 480 simulations. As described in section 2.3, in each of the 480 simulations the time onsets of the PSPs and the spatial locations of

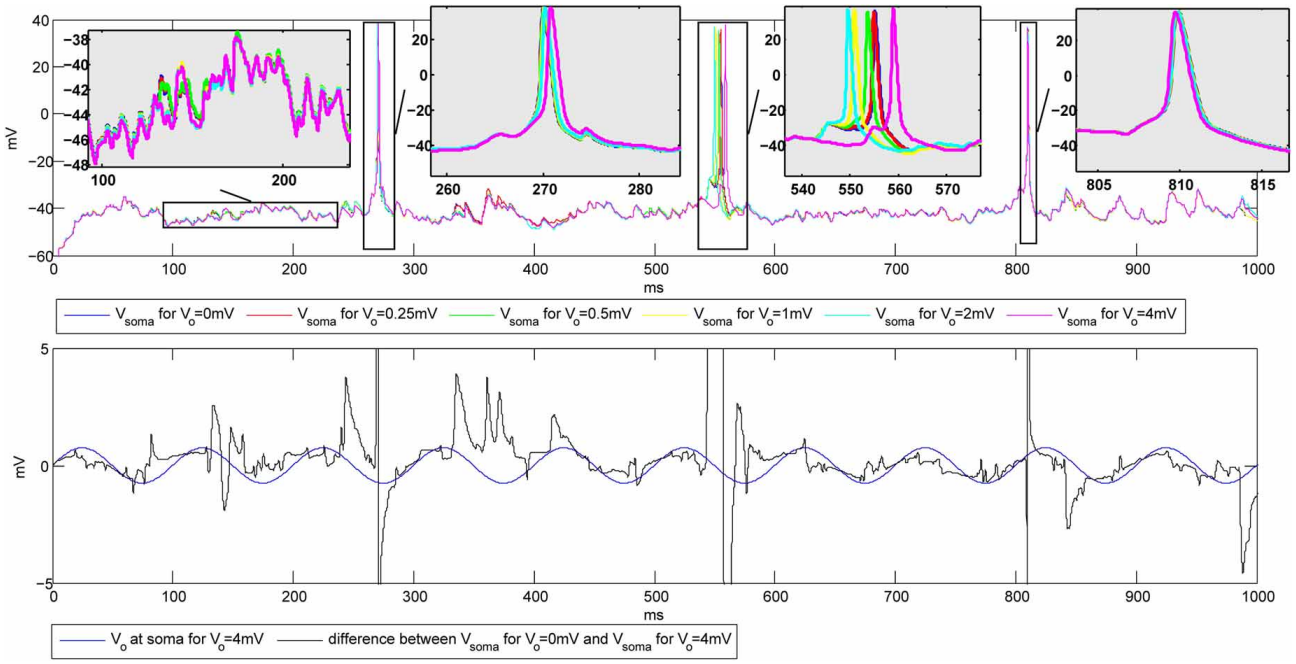

FIGURE 6 | Top: Influence of the extracellular oscillations on the timing of the action potentials during the stimulation with PSPs. Bottom: The extracellular oscillations at the soma ($V_o =$ 4 mV) and the difference between the membrane potential of the soma without and with the extracellular oscillations of 4 mV amplitude. The vertical lines on the **bottom** plot that exceed the plot boundaries results from action potentials visible on the **top** plot.

the synapses were randomly chosen. **Figure 7A** displays the raster plots obtained for the medium firing rate, $5 < F < 15$ Hz, of the CA3 neuron models (5 cell morphologies, each used for 48 iterations, resulting in 240 simulations). Differences in the timing and the numbers of action potentials are evident, but they are difficult to quantify directly from the raster plots.

To provide a meaningful visualization of the changes caused by the extracellular oscillations, several processing steps were made. First, we created a peristimulus time histogram: the spikes were binned, that is, the time axis was divided into 10 ms bins and the spikes were gathered to obtain a spike count per bin. Then, the spike count of each bin was subtracted from the corresponding baseline spike count. The next step was to generate cumulative results, where all the bins corresponding to the same phase of the oscillations were summed. For example, when 10 Hz sinusoidal oscillations were applied during a 1 s long simulation, the spike counts at different phases of the oscillations were summed. The resulting graphs for basal and apical stimulations of the CA3 and the CA1 neural models, together with the plot of the phase of the oscillations at the soma, are shown in **Figure 7B**. Comprehensive figures of all the intermediate steps are provided in supplementary material.

The stimulations of the basal dendrites, on either the CA1 or the CA3 neurons, yielded a significant negative correlation for the high amplitude oscillations, $V_o \geqslant 1$ mV. On the contrary, the correlation was positive for the apical dendrites, with a smaller absolute value than the correlation observed for the basal dendrites. These trends, anti-correlation for the basal dendrites and correlation for the apical, are evident in **Figure 7C** where the cross-correlations between the bins and the phase of the oscillations for three different firing rates F are plotted.

The negative correlation during the stimulation of the basal dendrites is caused by the fact that an increase of the extracellular oscillations induces a decrease in the difference between the intracellular and the extracellular potential as written in Equation (3). Thus, the positive half-wave (with respect to the phase of the oscillations at the soma) of the extracellular oscillations drives the membrane potential away from the firing threshold, resulting in the negative correlation and vice versa.

The opposite signs of the correlation coefficients for the stimulation of the basal and the apical dendrites is a direct consequence of the asymmetrical morphology of the pyramidal neurons. As shown in **Figure 3**, for the spatial frequency of $f_s = 0.8\,\mathrm{mm}^{-1}$, when the positive half-wave of the extracellular oscillations is around the soma, the negative half-wave will be around the apical dendrites. The negative half-wave of the oscillations facilitates the spike emission, raising the membrane potential toward the firing threshold. When the overall positive correlation is observed, it indicates that the distal oscillations have a higher influence than those around the soma. This is observed when the neuron is stimulated in the apical part of the dendritic tree, as shown on right hand side plot in **Figure 7C**.

To explain the difference between the absolute values of the correlation coefficients, which are higher for the stimulations of the basal dendrites, we speculate that the difference is influenced by the morphology of the pyramidal neurons: the apical dendrites are widely spread and the basal dendrites are gathered around the soma. Only a small part of the apical tree was affected by the peak

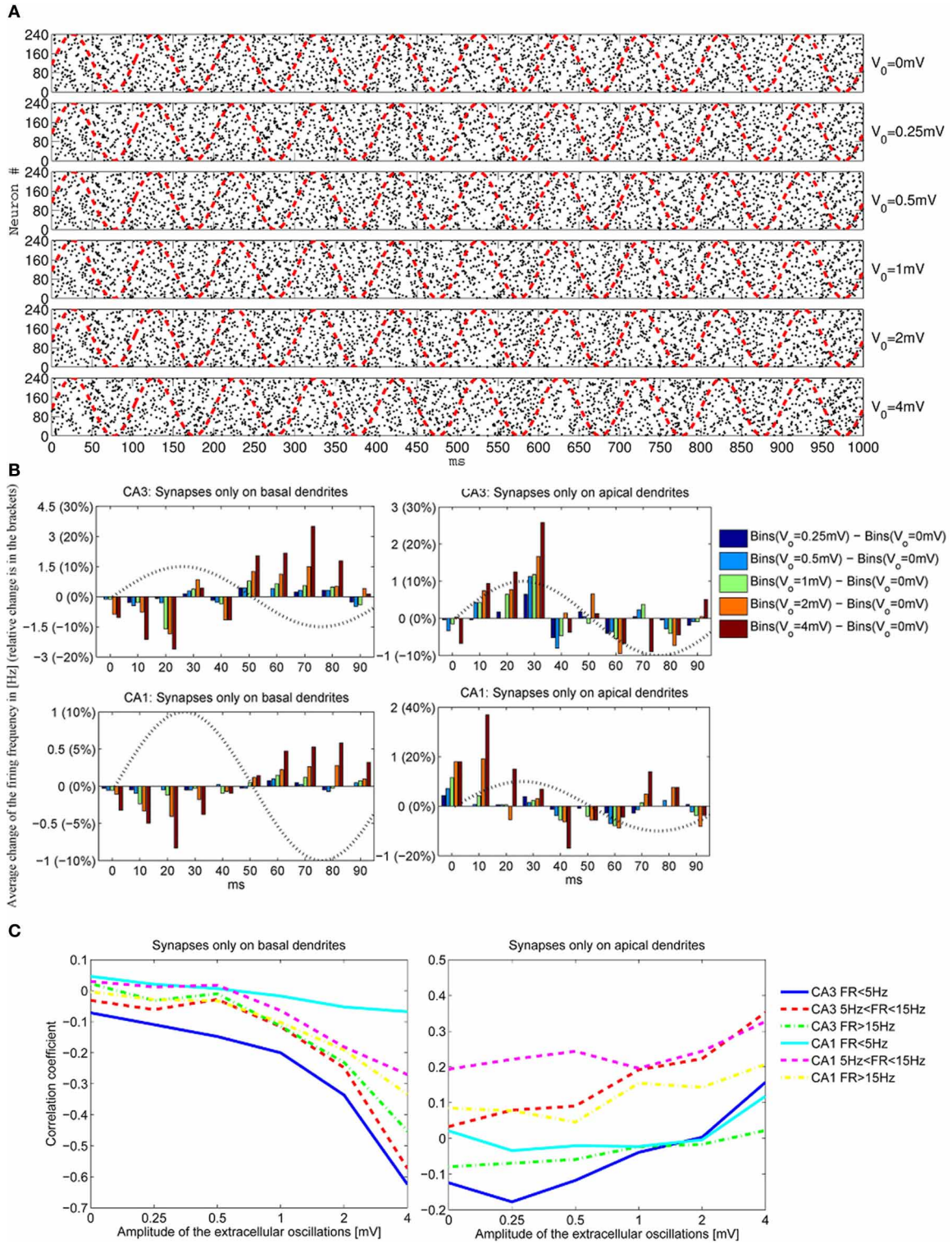

FIGURE 7 | (A) The raster plots showing firing times of CA3 neurons for different amplitudes of the extracellular oscillations, $V_o = 0$, 0.25, 0.5, 1, 2 and 4 mV, across 48 iterations for 5 morphologies, resulting in 240 spike trains. The phase of the extracellular oscillations is given with red dashed lines. **(B)** The average (across all 240 iterations) difference between the firing frequencies with and without the extracellular oscillations. Additionally, an observation of 1 s for each iteration is cumulated and averaged in a single period of the extracellular oscillations (100 ms). All the plots are shown for the medium firing rate, i.e., $5 < F < 15$ Hz. The sin wave, indicating the phase of the extracellular oscillations, is plotted with a dotted line and with a dimensionless amplitude. **(C)** Correlation coefficients between bins of 1 ms and the phase of the extracellular oscillations for the CA3 and the CA1 neurons for different firing rates F.

of the oscillations, while most of the basal dendrites are affected by the peak. Furthermore, the soma and a nonnegligible part of the apical tree proximal to the soma were stimulated by oscillations with the phase opposite to the oscillations taking place in the distal apical dendrites.

The firing rate plays also a role in the sensitivity of the membrane potential to the influence of the extracellular oscillations. For CA3 models, it appears that when the basal dendrites were stimulated the largest change of the correlation coefficients is observed for low firing rate, then for medium and eventually for high firing rate. This result is inverted for the CA1 neurons, as illustrated in **Figure 7B**, suggesting that the link between the firing rate and the sensitivity to the extracellular oscillations highly depends on the properties of the ion channels. In our simulations the difference might come from the calcium and potassium conductances, since they differ in the two models.

After observing how timing of the action potentials is influenced by the extracellular oscillations, we investigated the overall change in the number of action potentials as a function of the extracellular oscillations. This indicator is given in **Figure 8A**. The overall number of action potentials is computed separately for the positive and the negative period of the extracellular oscillations. The number of action potentials for the positive period is shown with red dashed lines and for the negative period with blue dot-dashed lines.

For the stimulation of the basal dendrites, both the CA3 and the CA1 neurons exhibit a decrease in the number of action potentials during the positive period and an increase during the negative period. The change is larger for the CA3 than for the CA1 neurons, suggesting that the dynamical properties of the ion channels are important for this kind of analysis. The effects are inverted for the apical dendrites and the variations are smaller than for the basal dendrites: during the positive period there is an increase in the number of action potentials, while during the negative period it decreases or does not show a significant change. This is in accordance with the previous observations where the proximal and distal contributions from the apical dendrites are balancing each other out. The average number of action potentials during both the positive and the negative period is shown with the solid black line. The average number slightly increases with the increase of the amplitude of the extracellular oscillations.

The last indicator we explored assesses the influence of the extracellular oscillations on the precise timing of action potentials. **Figure 8B** displays the mean timing and its standard deviation. The mean timing tends to stay near the center of the half period, which is 25 ms for the positive half-wave and 75 ms for the negative. In cases where the mean value was initially biased, i.e., significantly different from 25 or 75 ms without the extracellular oscillations, the extracellular oscillations bring the mean value closer to the middle of the half period. This is evident in the results of the stimulation of the apical dendrites in **Figure 8B**. This result is expected since 25 and 75 ms correspond to the peak of the amplitude of the extracellular oscillations.

3.2.2. Influence of the temporal frequency of the extracellular oscillations

To investigate the influence of the temporal frequency of the extracellular oscillations, we conducted simulations with $V_o = 4$ mV and the following set of the temporal frequencies $f_t = 1$, 5, 10, 20, 50, and 100 Hz. The results are shown in **Figure 9A** and displayed as histograms representing the difference in the number of action potentials caused by the oscillations. **Figure 9A** is given for the stimulation of the CA1 basal dendrites, and the figures that display the results of the stimulation of the CA1 apical dendrites and the CA3 basal and apical dendrites are given in the supplemental. The results are cumulated over a single period of oscillations. The phase of the oscillations at the soma is indicated with dashed red lines. The stimulation with the PSPs was set so that the firing frequency was in the medium firing range interval, i.e., $5 < F < 15$ Hz. Spatial phase of the oscillations was $\frac{3\pi}{10}$ rad.

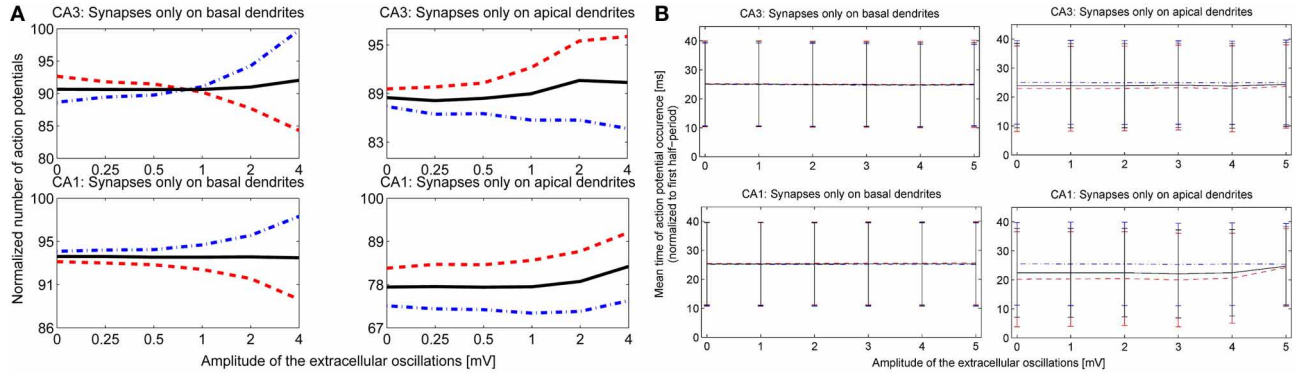

FIGURE 8 | (A) The number of action potentials as a function of the amplitude of the extracellular oscillations, with the frequency of 10 Hz and for the medium firing rate ($5 < F < 15$ Hz). The results for the CA3 neuron models are shown in the first row and for the CA1 in the second row. The curves are obtained from results of 240 simulations (48 iterations for 5 morphologies) with 1 s duration. The results during the positive period w.r.t. the potential at the soma, are shown with red dashed lines, and during the negative period with blue dot-dashed lines and the average number of the action potentials is shown with solid black lines. **(B)** The mean timing of the action potentials with the standard deviations. The *x*-axis denotes the amplitude of the 10 Hz extracellular oscillations. To facilitate the visual comparison, we subtracted 50 ms from the negative half-wave mean timing (blue dash-dotted lines).

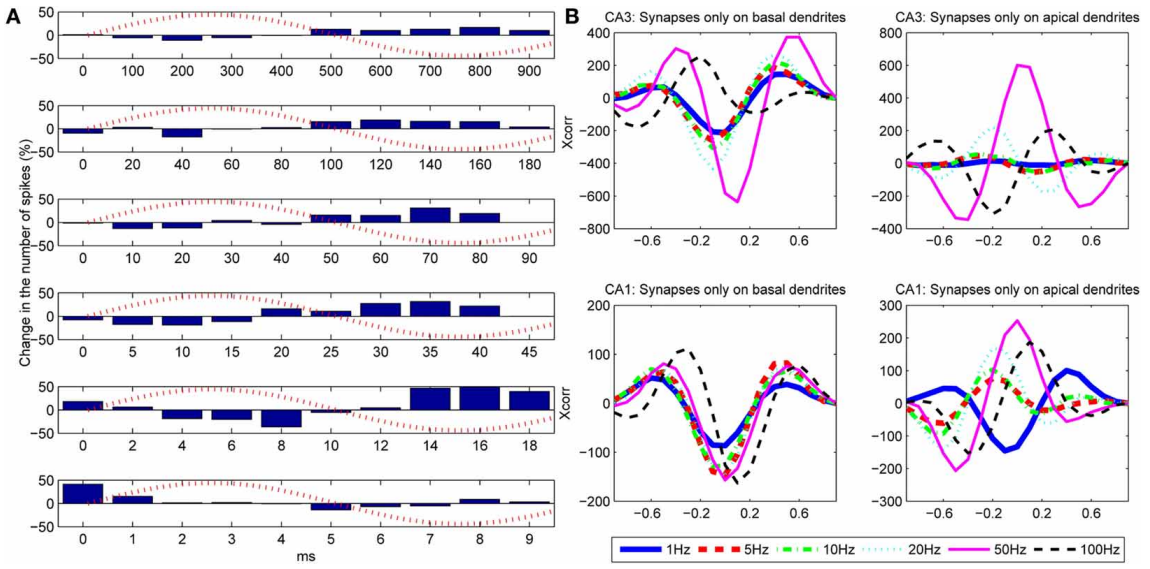

FIGURE 9 | (A) Influence of the frequency of the extracellular oscillations on the number of action potentials for the stimulation of the basal dendrites of the CA3 neuron model. From top to bottom the plots correspond to the following frequencies: $f_t = 1$, 5, 10, 20, 50 and 100 Hz. The bins are created by cumulating the results over 1 s of simulation. **(B)** Cross-correlation between the difference of the bins (cumulated over a single period of the extracellular oscillations) and the extracellular oscillations. The cross-correlation is computed for six different frequencies of the extracellular oscillations.

To evaluate the correlation between the change in the number of action potentials and the frequency of the extracellular oscillations, we computed the cross-correlation coefficient for each frequency of the oscillations. The results for the basal and the apical stimulation of the CA1 and the CA3 neurons are given in **Figure 9B**. The stimulation of the basal dendrites led to anti-correlation with the phase of the oscillations at the soma, which tends to be larger for higher frequencies, except for 100 Hz where it gets out of the phase. When the apical dendrites were stimulated, the relative change in the number of action potentials is still of the same order as when the basal dendrites were stimulated, but the level of correlation with the oscillations at the soma significantly varies for different frequencies. This suggests that the oscillations have important influence, not only at the soma, but at the dendrites as well.

3.2.3. *Influence of the spatial frequency and the spatial phase of the extracellular oscillations*

We performed a sensitivity analysis of the neural activity to the spatial frequency and the spatial phase of the extracellular oscillations. The methodology detailed in section 3.2.1 was applied with a different spatial frequency, $f_s = 0.4\,\text{mm}^{-1}$ instead of $0.8\,\text{mm}^{-1}$ as shown in **Figure 4A**, and with a different spatial phase, $\phi_s = \frac{\pi}{2}$ rad instead of $\frac{3\pi}{10}$ rad as shown in **Figure 4B**. The cross-correlation coefficients, computed as for **Figure 7C**, are shown in **Figure 10A**. The resulting number of action potentials is shown in **Figure 10B** for $f_s = 0.8\,\text{mm}^{-1}$ and $\phi_s = \frac{\pi}{2}$ rad and in **Figure 10C** for $f_s = 0.4\,\text{mm}^{-1}$ and $\phi_s = \frac{\pi}{2}$ rad. Even though the results are different for each parameter, especially for the higher amplitudes of the extracellular oscillations, the difference often appears to be rather stochastic, reflecting the highly nonlinear processing defined by the activation and inactivation functions of the active ion channels.

When $\phi_s = \frac{\pi}{2}$ rad, the peak of the extracellular oscillations is around the soma, while for $\phi_s = \frac{3\pi}{10}$ rad the peak occurs in the basal part of the dendritic tree (see **Figure 4**). The lack of significant difference between the two cases indicates that the influence of the extracellular oscillations at the soma is not more important than the influence at the dendritic tree. This suggests that for an accurate modeling of the nonsynaptic communication, the active properties of the dendritic tree should not be neglected.

The results for the apical dendrites show a great diversity, resulting mainly from the fact that the apical dendrites occupy a larger volume than the basal dendrites, thus the locations of the PSPs inputs are more spread for the apical dendrites. Also, variations across morphologies were more significant for the apical dendrites than for the basal ones, in particular for the CA1 neurons which have highly branched apical part of their dendritic tree along the entire somatodendritic axis (Spruston, 2008). This could account for the variability of the results when the stimulation is given through the apical dendrites.

4. DISCUSSION

Studies that investigate how the LFPs influence timing and number of action potentials are commonly based on stimulating neurons by injection of a constant current into the soma (Parra and Bikson, 2004; Radman et al., 2007; Anastassiou et al., 2010, 2011). In this paper, we show that the neural models with active conductances and dendrites stimulated by spatially distributed alpha function-shaped excitatory PSPs (EPSPs) have highly stochastic firing dynamics, which can to some degree be influenced by the parameters of the extracellular oscillations.

The weak extracellular oscillations studied in this paper correspond to those existing spontaneously in the brain. The strength of the extracellular oscillations in the mammalian brain is

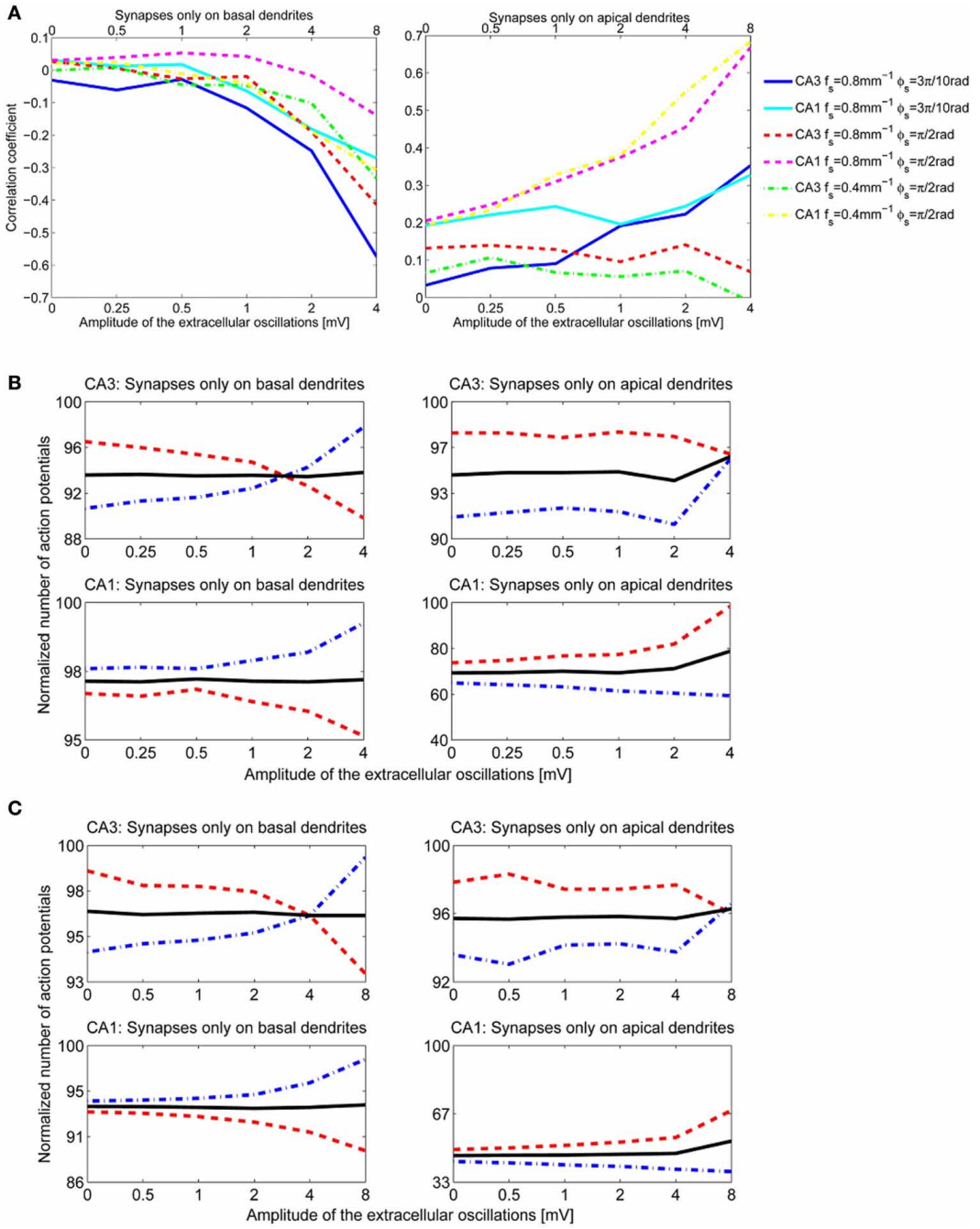

FIGURE 10 | (A) The correlation coefficients between the bins of 1 ms width and the phase of the extracellular oscillations. Extracellular oscillations with several different spatial properties for the CA3 and the CA1 neuron models are used. **(B)** The number of action potentials as a function of the amplitude when $f_s = 0.8\,\text{mm}^{-1}$ and $\phi_s = \frac{\pi}{2}$ rad. **(C)** The number of action potentials as a function of the amplitude when $f_s = 0.4\,\text{mm}^{-1}$ and $\phi_s = \frac{\pi}{2}$ rad.

commonly considered to go up to 3 mV mm^{-1}. This corresponds to 1 mV oscillations in the present study. Our results suggest that these weak oscillations have a modest influence on the timing of the action potentials. Larger fields, above 6 mV mm^{-1} (which correspond to 2 and 4 mV oscillations in our study) have a significant influence on the timing. Such strong fields are seldom observed in the brain, e.g., during the hippocampal sharp waves (Buzsáki, 1986; Sullivan et al., 2011). Another source of strong oscillations could be external stimulations, for example techniques such as TES, TMS or DBS. These methods could cause significant and coherent changes in the neural activity. We speculate that inducing a synchronous neural activity in the brain using strong extracellular electric fields could help to restore the normal neural activity.

It is important to emphasize that it has been shown that small correlations, which could be induced by the extracellular oscillations, can be amplified through network interactions and lead to increase in synchronization among the neurons (Parra and Bikson, 2004; Radman et al., 2007). The neuronal synchrony has been suggested to have a computational purpose, in particular to help maintain neural rhythmic activity (Weiss and Faber, 2010).

Recent findings suggest that the extracellular oscillations of the magnitude spontaneously present in the brain usually change the membrane potential only by 1–2 mV (Radman et al., 2007; Anastassiou et al., 2010; Buzsáki et al., 2012). This is rather small with respect to the depolarization required to reach the firing threshold level from the resting potential, which is usually about 15 mV. Nevertheless, since neurons are constantly bombarded with synaptic inputs of various amplitudes, their membrane potentials are generally significantly different from the resting potential and stay in a balanced state often close to the threshold level (Wilson, 2008). When the membrane potential is close to the firing threshold, the extracellular oscillations might affect neural firing more strongly. Our results suggest that the changes in the overall firing rate are rather small, generally below 5% even for the oscillations of 4 mV amplitude. The weaker fields usually do not cause an overall change greater than 1%, see **Figures 8A**, **10B,C**.

Changes in the firing rates show that, for a given simulation setup, the influence of the extracellular oscillations is more significant when the synaptic inputs are received through the basal than through the apical dendrites. We speculate that this is due to the spatial properties of the extracellular oscillations. The phase of the oscillations is the same along the entire basal part of the dendritic tree, as well as along the soma. On the contrary, the phase of the oscillations along the apical part of the tree is the opposite to that around the soma, thus the resulting influence of the oscillations when synaptic inputs are on the apical tree gets balanced out.

We also observed that the correlation of the firing times with the phase of the extracellular oscillations for the CA3 neuron models is stronger than for the CA1 models. This emphasizes the importance of the ion channels which have a nonlinear dependence on the voltage and alter significantly the influence of the oscillations. The presented study did not investigate all the possible scenarios through which the extracellular oscillations could have a functional role. For instance, one possible functional role could be in gating some particular (hypothetical) ion channels that could be sensitive primarily to some properties of the extracellular oscillations (e.g., voltage or slope). Such ion channels could transfer this stochastic influence of the extracellular oscillations on the membrane potential into a more structured one, which could alter the neural activity in some functional way. In our study, the CA3 model, which contained more potassium and calcium channels, was generally influenced by the extracellular oscillations in a more coherent way.

The functional role of the spontaneous LFPs is an open question, but we have shown that even if the mean firing rate is not affected, the spontaneous LFPs could influence spike timings for up to several milliseconds. This could affect the neural synchronization and thus the entire network dynamics. This is important in the context of development of biologically inspired artificial neural networks. A way to test whether an artificial neural network behaves in the same way as a biological one could be to evaluate its robustness to small changes in the spike timing.

It has been observed that the amplitude of extracellular oscillations is larger for smaller brains, i.e., it decreases from rat to cat, and from cat to primate (Buzsáki et al., 2012). One possible explanation for this is that, due to the brain size, bodies of the pyramidal neurons are vertically the best aligned in the rat brain, then in the cat brain, and in the human brain. Since studies, including this one, suggest that the amplitude of the oscillations is crucial for their coherent influence on firing properties, a decrease in the amplitude in larger brains can be an argument against the functional role of the oscillations.

SUPPLEMENTARY MATERIAL

The Supplementary Material for this article can be found online at: http://www.frontiersin.org/journal/10.3389/fncom.2014.00009/abstract

Figure S1 | Spikes from Figure 9 in the main part of the paper binned into 10 ms time bins (only first 300 out of 1000 ms are shown). Bins corresponding with different amplitudes of the extracellular oscillations are color coded. Phase of the extracellular oscillations at the soma is indicated with dashed black line.

Figure S2 | Difference of the time bins from Figure S1.

Figure S3 | Influence of the frequency of the extracellular oscillations on the number of action potentials for the stimulation of the apical dendrites of CA3 neuron model. This figure is produced in analogous way as **Figure 9A** in the main part of the paper. **(A)** The stimulation of the CA1 apical dendrites. **(B)** The stimulation of the CA3 basal dendrites. **(C)** The stimulation of the CA3 apical dendrites.

REFERENCES

Allen, E. A., Pasley, B. N., Duong, T., and Freeman, R. D. (2007). Transcranial magnetic stimulation elicits coupled neural and hemodynamic consequences. *Science* 317, 1918–1921. doi: 10.1126/science.1146426

Anastassiou, C. A., Montgomery, S. M., Barahona, M., Buzsáki, G., and Koch, C. (2010). The effect of spatially inhomogeneous extracellular electric fields on neurons. *J. Neurosci.* 30, 1925–1936. doi: 10.1523/JNEUROSCI.3635-09.2010

Anastassiou, C. A., Perin, R., Markram, H., and Koch, C. (2011). Ephaptic coupling of cortical neurons. *Nat. Neurosci.* 14, 217–223. doi: 10.1038/nn.2727

Barker, A. T., Jalinous, R., and Freeston, I. L. (1985). Non-invasive magnetic stimulation of human motor cortex. *Lancet* 1, 1106–1107. doi: 10.1016/S0140-6736(85)92413-4

Benabid, A. L., Chabardes, S., Mitrofanis, J., and Pollak, P. (2009). Deep brain stimulation of the subthalamic nucleus for the treatment of Parkinson's disease. *Lancet Neurol.* 8, 67–81. doi: 10.1016/S1474-4422(08)70291-6

Brette, R., and Destexhe, A. (2011). *Handbook of Neural Activity Measurement*. Cambridge: Cambridge University Press.

Buzsáki, G. (1986). Hippocampal sharp waves: their origin and significance. *Brain Res.* 398, 242–252. doi: 10.1016/0006-8993(86)91483-6

Buzsáki, G., Anastassiou, C. A., and Koch, C. (2012). The origin of extracellular fields and currents – EEG, ECoG, LFP and spikes. *Nat. Rev. Neurosci.* 13, 407–420. doi: 10.1038/nrn3241

Buzsáki, G., and Draguhn, A. (2004). Neuronal oscillations in cortical networks. *Science* 304, 1926–1929. doi: 10.1126/science.1099745

Capotosto, P., Babiloni, C., Romani, G. L., and Corbetta, M. (2009). Frontoparietal cortex controls spatial attention through modulation of anticipatory alpha rhythms. *J. Neurosci.* 29, 5863–5872. doi: 10.1523/JNEUROSCI.0539-09.2009

Carnevale, N. T., and Hines, M. L. (2006). *The NEURON Book*. Cambridge: Cambridge University Press. doi: 10.1017/CBO9780511541612

Deans, J. K., Powell, A. D., and Jefferys, J. G. (2007). Sensitivity of coherent oscillations in rat hippocampus to AC electric fields. *J. Physiol.* 583, 555–565. doi: 10.1113/jphysiol.2007.137711

Deco, G., and Thiele, A. (2009). Attention: oscillations and neuropharmacology. *Eur. J. Neurosci.* 30, 347–354. doi: 10.1111/j.1460-9568.2009.06833.x

Ebersole, J. S., and Milton, J. (2003). "The electroencephalogram (EEG): a measure of neural synchrony," in *Epilepsy as a Dynamic Disease* (Berlin; Heidelberg: Springer), 51–68. doi: 10.1007/978-3-662-05048-4_5

Fries, P., Nikolic, D., and Singer, W. (2007). The gamma cycle. *Trends Neurosci.* 30, 309–316. doi: 10.1016/j.tins.2007.05.005

Fröhlich, F., and McCormick, D. A. (2010). Endogenous electric fields may guide neocortical network activity. *Neuron* 67, 129–143. doi: 10.1016/j.neuron.2010.06.005

Hallett, M. (2000). Transcranial magnetic stimulation and the human brain. *Nature* 406, 147–150. doi: 10.1038/35018000

Hemond, P., Epstein, D., Boley, A., Migliore, M., Ascoli, G. A., and Jaffe, D. B. (2008). Distinct classes of pyramidal cells exhibit mutually exclusive firing patterns in hippocampal area CA3b. *Hippocampus* 18, 411–424. doi: 10.1002/hipo.20404

Hines, M. L., and Carnevale, N. T. (1997). The NEURON simulation environment. *Neural Comput.* 9, 1179–1209. doi: 10.1162/neco.1997.9.6.1179

Izhikevich, E. M. (2006). *Dynamical Systems in Neuroscience: The Geometry of Excitability and Bursting*. Cambridge: The MIT Press.

Joucla, S., and Yvert, B. (2012). Modeling extracellular electrical neural stimulation: from basic understanding to mea-based applications. *J. Physiol.* 106, 146–158. doi: 10.1016/j.jphysparis.2011.10.003

Kahana, M. J., Seelig, D., and Madsen, J. R. (2001). Theta returns. *Curr. Opin. Neurobiol.* 11, 739–744. doi: 10.1016/S0959-4388(01)00278-1

Kayser, C., Montemurro, M. A., Logothetis, N. K., and Panzeri, S. (2009). Spike-phase coding boosts and stabilizes information carried by spatial and temporal spike patterns. *Neuron* 61, 597–608. doi: 10.1016/j.neuron.2009.01.008

Kim, S., Guzman, S. J., H., H., and Jonas, P. (2012). Active dendrites support efficient initiation of dendritic spikes in hippocampal ca3 pyramidal neurons. *Nat. Neurosci.* 15, 600–606. doi: 10.1038/nn.3060

Kirov, R., Weiss, C., Siebner, H. R., Born, J., and Marshall, L. (2009). Slow oscillation electrical brain stimulation during waking promotes EEG theta activity and memory encoding. *Proc. Natl. Acad. Sci. U.S.A.* 106, 15460–15465. doi: 10.1073/pnas.0904438106

Koepsell, K., Wang, X., Hirsch, J. A., and Sommer, F. T. (2010). Exploring the function of neural oscillations in early sensory systems. *Front. Neurosci.* 4:53. doi: 10.3389/neuro.01.010.2010

Lisman, J., and Buzsáki, G. (2008). A neural coding scheme formed by the combined function of gamma and theta oscillations. *Schizophr. Bull.* 34, 974–980. doi: 10.1093/schbul/sbn060

Mainen, Z. F., and Sejnowski, T. J. (1998). "Modeling active dendritic processes in pyramidal neurons," in *Methods in Neuronal Modeling, 2nd Edn.*, eds C. Koch and I. Segev (Cambridge: MIT Press), 170–209.

Markram, H. (2006). The blue brain project. *Nat. Rev. Neurosci.* 9, 153–160. doi: 10.1038/nrn1848

Migliore, M., Ferrante, M., and Ascoli, G. A. (2005). Signal propagation in oblique dendrites of ca1 pyramidal cells. *J. Neurophysiol.* 94, 4145–4155. doi: 10.1152/jn.00521.2005

Montemurro, M. A., Rasch, M. J., Murayama, Y., Logothetis, N. K., and Panzeri, S. (2008). Phase-of-firing coding of natural visual stimuli in primary visual cortex. *Curr. Biol.* 18, 375–380. doi: 10.1016/j.cub.2008.02.023

Nyhus, E., and Curran, T. (2010). Functional role of gamma and theta oscillations in episodic memory. *Neurosci. Biobehav. Rev.* 34, 1023–1035. doi: 10.1016/j.neubiorev.2009.12.014

Osipova, D., Takashima, A., Oostenveld, R., Fernandez, G., Maris, E., and Jensen, O. (2006). Theta and gamma oscillations predict encoding and retrieval of declarative memory. *J. Neurosci.* 26, 7523–7531. doi: 10.1523/JNEUROSCI.1948-06.2006

Ozen, S., Sirota, A., Belluscio, M. A., Anastassiou, C. A., Stark, E., Koch, C., et al. (2010). Transcranial electric stimulation entrains cortical neuronal populations in rats. *J. Neurosci.* 30, 11476–11485. doi: 10.1523/JNEUROSCI.5252-09.2010

Parra, L. C., and Bikson, M. (2004). Model of the effect of extracellular fields on spike time coherence. *Conf. Proc. IEEE Eng. Med. Biol. Soc.* 6, 4584–4587. doi: 10.1109/IEMBS.2004.1404271

Peelle, J. E., and Davis, M. H. (2012). Neural oscillations carry speech rhythm through to comprehension. *Front. Psychol.* 3:320. doi: 10.3389/fpsyg.2012.00320

Pyapali, G., Sik, A., Penttonen, M., Buzsaki, G., and Turner, D. (1998). Dendritic properties of hippocampal ca1 pyramidal neurons in the rat: intracellular staining *in vivo* and *in vitro*. *J. Comp. Neurol.* 391, 335–352. doi: 10.1002/(SICI)1096-9861(19980216)391:3<335::AID-CNE4>3.0.CO;2-2

Radman, T., Su, Y., An, J. H., Parra, L. C., and Bikson, M. (2007). Spike timing amplifies the effect of electric fields on neurons: implications for endogenous field effects. *J. Neurosci.* 27, 3030–3036. doi: 10.1523/JNEUROSCI.0095-07.2007

Reato, D., Rahman, A., Bikson, M., and Parra, L. C. (2010). Low-intensity electrical stimulation affects network dynamics by modulating population rate and spike timing. *J. Neurosci.* 30, 15067–15079. doi: 10.1523/JNEUROSCI.2059-10.2010

Samsonovich, A. V., and Ascoli, G. A. (2003). Statistical morphological analysis of hippocampal principal neurons indicates cell-specific repulsion of dendrites from their own cell. *J. Neurosci. Res.* 71, 173–187. doi: 10.1002/jnr.10475

Schack, B., Vath, N., Petsche, H., Geissler, H. G., and Möller, E. (2002). Phase-coupling of theta-gamma EEG rhythms during short-term memory processing. *Int. J. Psychophysiol.* 44, 143–163. doi: 10.1016/S0167-8760(01)00199-4

Schroeder, C. E., and Lakatos, P. (2009). Low-frequency neuronal oscillations as instruments of sensory selection. *Trends Neurosci.* 32, 9–18. doi: 10.1016/j.tins.2008.09.012

Sederberg, P. B., Kahana, M. J., Howard, M. W., Donner, E. J., and Madsen, J. R. (2003). Theta and gamma oscillations during encoding predict subsequent recall. *J. Neurosci.* 23, 10809–10814.

Spruston, N. (2008). Pyramidal neurons: dendritic structure and synaptic integration. *Nat. Rev. Neurosci.* 9, 206–221. doi: 10.1038/nrn2286

Sullivan, D., Csicsvari, J., Mizuseki, K., Montgomery, S., Diba, K., and Buzsáki, G. (2011). Relationships between hippocampal sharp waves, ripples, and fast gamma oscillation: influence of dentate and entorhinal cortical activity. *J. Neurosci.* 31, 8605–8616. doi: 10.1523/JNEUROSCI.0294-11.2011

Thut, G., Nietzel, A., Brandt, S. A., and Pascual-Leone, A. (2006). alpha-band electroencephalographic activity over occipital cortex indexes visuospatial attention bias and predicts visual target detection. *J. Neurosci.* 26, 9494–9502. doi: 10.1523/JNEUROSCI.0875-06.2006

Uhlhaas, P., Roux, F., Rodriguez, E., Rotarska-Jagiela, A., and Singer, W. (2010). Neural synchrony and the development of cortical networks. *Trends Cogn. Sci.* 14, 72–80. doi: 10.1016/j.tics.2009.12.002

Walsh, V., and Cowey, A. (2000). Transcranial magnetic stimulation and cognitive neuroscience. *Nat. Rev. Neurosci.* 1, 73–79. doi: 10.1038/35036239

Wang, X.-J. J. (2010). Neurophysiological and computational principles of cortical rhythms in cognition. *Physiol. Rev.* 90, 1195–1268. doi: 10.1152/physrev.00035.2008

Ward, L. M. (2003). Synchronous neural oscillations and cognitive processes. *Trends Cogn. Sci.* 7, 553–559. doi: 10.1016/j.tics.2003.10.012

Weiss, S. A., and Faber, D. S. (2010). Field effects in the CNS play functional roles. *Front. Neural Circuits* 4:15. doi: 10.3389/fncir.2010.00015

Wilson, C. (2008). Up and down states. *Scholarpedia* 3, 1410. doi: 10.4249/scholarpedia.1410

Conflict of Interest Statement: The authors declare that the research was conducted in the absence of any commercial or financial relationships that could be construed as a potential conflict of interest.

Received: 03 July 2013; accepted: 16 January 2014; published online: 07 February 2014.
Citation: Tiganj Z, Chevallier S and Monacelli E (2014) Influence of extracellular oscillations on neural communication: a computational perspective. Front. Comput. Neurosci. ***8****:9. doi: 10.3389/fncom.2014.00009*
This article was submitted to the journal Frontiers in Computational Neuroscience.

SUBSPACE METRICS FOR MULTIVARIATE DICTIONARIES AND APPLICATION TO EEG

Sylvain Chevallier[⋆] *Quentin Barthélemy*[†] *Jamal Atif*[‡]

[⋆] LISV, University of Versailles [†] Mensia Technologies [‡] LRI, University Paris-Sud

ABSTRACT

Overcomplete representations and dictionary learning algorithms are attracting a growing interest in the machine learning community. This paper addresses the emerging problem of comparing multivariate overcomplete dictionaries. Despite a recurrent need to rely on a distance for learning or assessing multivariate overcomplete dictionaries, no metrics in their underlying spaces have yet been proposed. Henceforth we propose to study overcomplete representations from the perspective of matrix manifolds. We consider distances between multivariate dictionaries as distances between their spans which reveal to be elements of a Grassmannian manifold. We introduce set-metrics defined on Grassmannian spaces and study their properties both theoretically and numerically. Thanks to the introduced metrics, experimental convergences of dictionary learning algorithms are assessed on synthetic datasets. Set-metrics are embedded in a clustering algorithm for a qualitative analysis of real EEG signals for Brain-Computer Interfaces (BCI). The obtained clusters of subjects are associated with subject performances. This is a major methodological advance to understand the BCI-inefficiency phenomenon and to predict the ability of a user to interact with a BCI.

Index Terms— Dictionary Learning, Metrics, Frames, Grassmannian Manifolds, Multivariate Dataset

1. INTRODUCTION

Dictionary learning approaches and sparse approximations attracted a lot of attention in several application fields, achieving often state of the art results. Within this context, the contribution of this paper is of double nature. The first one is to be found on the theoretical machine learning side. We introduce metrics in the space of multivariate dictionaries; a topic that has not been tackled yet despite its importance. The second contribution is applicative. Indeed, the introduced metrics are embedded in a clustering algorithm to tackle the very challenging problem of Brain-Compute Interfaces.

Despite the profusion of research papers dealing with overcomplete representations, aside from some noticeable exceptions [1, 2], few results have been reported on how the constructed representations should be compared. Thus, to qualitatively assess a specific dictionary learning algorithm, one has to indirectly evaluate it through a benchmark based on a task performance [3, 4, 5]. Meanwhile, one can find in the literature some hints for dictionaries comparison with the aim of learning assessment [6, 7, 2, 8], but they fall short to define a true metric. However, a related topic has been studied in non-harmonic analysis. In [1], the question of comparing frames is addressed by considering a mapping from the frame space to a continuous functional space. The constructed functions allow then for the definition of an equivalence class, a partial order and a distance. Nonetheless this distance is not invariant to linear transforms, a desirable property in several application fields. Furthermore, its extension to the multivariate case is not straightforward since one should define a new mapping from the space of multivariate frames to an unknown continuous functional space.

In this paper, we introduce metrics exhibiting strong properties, among them the invariance to linear transforms. We propose to study overcomplete representations from the perspective of matrix manifolds. The proposed metrics are built in two stages: first we consider distance between two multivariate atoms as a distance between their spans, which reveal to be elements of a Grassmannian manifold. Then, the collection of spans are then compared by considering transportation distances, e.g. Wasserstein distance.

From the BCI standpoint, one challenging problem is the inter-individual variability. A large proportion of BCI users ($\approx$ 15 to 30%) leads to very poor results [9, 10] even with state of the art algorithms. This phenomenon is known as "BCI-inefficiency" or "BCI-illiteracy". A major difficulty of EEG signal processing is that many artifacts and noise sources (electrical, muscular, etc) corrupt the signal, lowering the SNR of brain signals, while several brain sources are continuously active and mixed in the recording electrodes. The linear transform invariance property of the proposed metric is highly desirable: the metric is insensitive to changes in the electrode positions. We aim at tackling this problem by embedding the proposed metrics in a hierarchical clustering algorithm. The obtained clusters of subjects are then associated with the user's ability to interact with the BCI.

The paper is organized as follows. Section 2 introduces some formal definitions. In Section 3 we define set-metrics on dictionaries. Section 4 provides experimental validations. On synthetic datasets, the convergence of dictionary learning algorithm (DLA) is shown with set-metrics. On BCI Competition datasets, set-metrics are embedded in a clustering algorithm to characterize BCI-inefficient subjects. Section 5 concludes this paper and points out some future research directions.

2. PRELIMINARIES

We consider an n-dimensional real vector space $\mathcal{V}$ (Euclidean n-space). The vectors of $\mathcal{V}$ will be denoted by u, w, the matrices by U, W, and the transpose as $(\cdot)^T$. The inner product induces the ℓ_2 norm $\|u\|_2^2 = \langle u, u \rangle$. The pseudo-norm $\|u\|_0$ is defined as the number of nonzero elements in the vector u. The Frobenius norm is defined as $\|U\|_F^2 = \mathrm{trace}(U^T U)$ and its associated inner product as $\langle U, W \rangle_F = \mathrm{trace}(W^T U)$. Elements U, W have respective spans: $\mathrm{span}(U) = \mathcal{U}$ and $\mathrm{span}(W) = \mathcal{W}$, with $\dim(\mathcal{U}) = \dim(\mathcal{W}) = \varrho$. The indexed families of matrices will be denoted as $\mathbf{U} = \{U_i\}_{i \in I}$ and $\mathbf{W} = \{W_j\}_{j \in J}$ respectively. Indexed families of subspaces will be denoted by $\mathbb{U} = \{\mathcal{U}_i\}_{i \in I}$ and $\mathbb{W} = \{\mathcal{W}_j\}_{j \in J}$ respectively.

S. Chevallier is supported by the Cerebraptic project of EADS Foundation.

978-1-4799-2893-4/14/$31.00 ©2014 IEEE

2.1. Dictionary learning problem

In its classical formulation, the dictionary learning problem aims at capturing most of the energy of a set of training signals $Y = [y_1, \ldots, y_q]$ with $y_j \in \mathbb{R}^n$ and representing it through a collection $U = [u_1, \ldots, u_m]$ in $\mathbb{R}^{n\times m}$ thanks to a set of sparse coefficients $A = [a_1, \ldots, a_q]$ in $\mathbb{R}^{m\times q}$. This collection U, which is redundant ($m \gg n$), is called overcomplete dictionary. The admissible set of dictionaries is convex and is defined as $\mathcal{D}_U = \{U \in \mathbb{R}^{n\times m} : \|u_i\|_2 \leqslant 1,\ i = 1, \ldots, m\}$. Formally, the dictionary learning problem writes as:

$$\min_{U\in\mathcal{D}_U, A\in\mathbb{R}^{m\times q}} \|Y - UA\|_F^2 \quad \text{s.t. } \|a_j\|_0 \leqslant K,\ j = 1, \ldots, q\,. \quad (1)$$

This problem is tackled by dictionary learning algorithms (DLAs), in which energy representative patterns of the dataset are iteratively selected by a sparse approximation step, and then updated by a dictionary update step (see for instance [6, 3, 11, 12]).

2.2. Multivariate dictionary learning problem

Several DLA approaches have been proposed to handle multivariate signals $\mathbf{Y} = [Y_1, \ldots, Y_q]$, with $Y_i \in \mathbb{R}^{n\times\rho}$, the additional dimension ρ being either supported by the coefficients (multichannel approach, [13, 14, 15]) or by the dictionary atoms (multivariate approach, [16]).

The multivariate reformulation of the dictionary learning problem, called M-DLA hereafter, allows to preserve the input space geometry by considering a multivariate dictionary $\mathbf{U}$ as a collection of m multivariate atoms U_i. The considered convex set of dictionaries is defined as $\mathcal{D}_M = \left\{\{U_i\}_{i=1}^m \in \mathbb{R}^{n\times\rho} : \|U_i\|_F \leqslant 1,\ i = 1, \ldots, m\right\}$. The dictionary learning problem thus writes:

$$\min_{\mathbf{U}\in\mathcal{D}_M} \sum_{j=1}^{q} \min_{a_j\in\mathbb{R}^m} \left\| Y_j - \sum_{i=1}^{m} a_{i,j}\, U_i \right\|_F^2 \quad \text{s.t. } \|a_j\|_0 \leqslant K, j = 1, \ldots, q. \quad (2)$$

where $a_{i,j} \in \mathbb{R}$, $a_j \in \mathbb{R}^m$ are the coding coefficients. The sparse decomposition is achieved using a greedy approach [17, 16]. Remark that after vectorization, this model is computationally equivalent to the univariate model of Equation (1), under the hypothesis that the ρ components are independent. The multivariate approach allows the dictionary learning algorithm to take into account existing interactions between components, such as rotations or unconstrained linear transformations (case studied in this paper).

2.3. Grassmannian manifolds and their metrics

The Grassmannian $\mathbf{Gr}(\varrho, n)$ is the set of all ϱ-dimensional linear subspaces of $\mathcal{V}$. The notion of principal angles is central when characterizing the distance between subspaces and hence for metrics on the Grassmannians. Principal angles $0 \leqslant \theta_1 \leqslant \ldots \leqslant \theta_\varrho \leqslant \frac{\pi}{2}$ between two subspaces $\mathcal{U}$ and $\mathcal{W}$ rely on the singular value decomposition of the bases $A = \{a_i\}_{i\in I}$ spanning $\mathcal{U}$ and $B = \{b_i\}_{i\in J}$ spanning $\mathcal{W}$, with I and J two indexing sets:

$$A^T B = \underline{Y}\,\Sigma\underline{Z}^T = \underline{Y}\,(\cos\boldsymbol{\theta})\underline{Z}^T\,, \quad (3)$$

where $\underline{Y} = [y_1, \ldots, y_\varrho]$ and $\underline{Z} = [z_1, \ldots, z_\varrho]$ are orthonormal bases. We denote by $\boldsymbol{\theta}$ the ϱ-vector formed by the principal angles θ_k, $k = 1, \ldots, \varrho$. Here $\cos\boldsymbol{\theta}$ is the diagonal matrix formed by $\cos\theta_1, \ldots, \cos\theta_\varrho$ along the diagonal. It is also known as principal correlations or canonical correlations [18].

Let $\mathcal{U}, \mathcal{W}$ be two elements of a Grassmannian manifold $\mathbf{Gr}(\varrho, n)$ and let $\{\theta_1, \ldots, \theta_\varrho\}$ be their associated principal angles. The chordal distance is probably the most known Grassmannian metric [19, 20]. A detailed and complete study of other Grassmannian metrics could be found in [21] or in [22]. The chordal distance is defined as:

$$d_c(\mathcal{U}, \mathcal{W}) = \|\sin\boldsymbol{\theta}\|_2 = \left(\sum_{k=1}^{\varrho} \sin^2\theta_k\right)^{\frac{1}{2}} = \left(\varrho - \|\underline{U}^T\underline{W}\|_F^2\right)^{\frac{1}{2}}, \quad (4)$$

where $\underline{U}$ and $\underline{W}$ are the orthonormal bases for $\mathcal{U}$ and $\mathcal{W}$, that is $\underline{U}^T\underline{U} = I_\varrho$ and $\text{span}\,(\underline{U}) = \mathcal{U}$.

3. METRICS FOR MULTIVARIATE DICTIONARIES

In this section, we will exploit the chordal metric described in the previous paragraph to act on subsets of a Grassmannian manifold as a ground distance. This ground distance has a key role for the definition of a metric between sets of points in a Grassmannian space.

The Grassmannian manifold $\mathbf{Gr}(\varrho, n)$ together with a distance d, such as the chordal distance, defines a metric space, or pseudo-metric space depending on the properties of the underlying distance. We will denote it in the sequel as $(\mathbb{G}, d)$, and when there is no confusion as $\mathbb{G}$. A result from [23] states that $\mathbf{Gr}(\varrho, n)$ is a Hausdorff, compact, connected smooth manifold of dimension $\varrho(n - \varrho)$. This result is of prime importance since one can define a Borel measure, denoted π, on Grassmannian spaces and consequently a transportation metric.

3.1. Wasserstein distance

Let us denote by $\mathcal{C}(\mathbb{G})$ any collection on $\mathbb{G}$ and by $\mathbb{G}_W = \{(\mathcal{U}, \pi_\mathcal{U}) : \mathcal{U} \in \mathbb{G}\}$ where $\pi_\mathcal{U}$ is a Borel measure. A measure π on the product space $\mathbb{U} \times \mathbb{W}$, with $\mathbb{U}, \mathbb{W} \in \mathbb{G}_W$, is a coupling of $\pi_\mathbb{U}$ and $\pi_\mathbb{W}$ if:

$$\pi(\bar{\mathbb{U}} \times \mathbb{W}) = \pi_\mathbb{U}(\bar{\mathbb{U}}), \quad \pi(\mathbb{U} \times \bar{\mathbb{W}}) = \pi_\mathbb{W}(\bar{\mathbb{W}}) \quad (5)$$

for all Borel sets $\bar{\mathbb{U}} \subset \mathbb{U}$, $\bar{\mathbb{W}} \subset \mathbb{W}$. We denote by $\mathcal{M}(\pi_\mathbb{U}, \pi_\mathbb{W})$ the set of all couplings of $\pi_\mathbb{U}$ and $\pi_\mathbb{W}$.

We could then define the Wasserstein distance, given $p \geqslant 1$, $\mathbb{U}$, $\mathbb{W} \in \mathbb{G}_W$ and a coupling π, as:

$$d_W^p(\mathbb{U}, \mathbb{W}) = \inf_{\pi\in\mathcal{M}(\pi_\mathbb{U}, \pi_\mathbb{W})} \left(\int_{\mathbb{U}\times\mathbb{W}} d(\mathcal{U}, \mathcal{W})^p d\pi(\mathcal{U}, \mathcal{W})\right)^{\frac{1}{p}} \quad (6)$$

This distance is also called the Wasserstein-Kantorovich-Rubinstein [24, Chap. 6].

3.2. Set-Metrics for dictionaries

Metric in Equation (6) is defined on Grassmannian spaces. Then $(\mathbb{G}, d)$ is a separable metric space allowing to compute a distance between the collection of subspaces spanned by a dictionary and the collection of subspaces spanned by another. The distance between two dictionaries in the dictionary space, that is $\mathcal{V}$, is defined as follows.

Let $\mathbf{U} = \{U_i\}_{i\in I}$ and $\mathbf{W} = \{W_j\}_{j\in J}$ be two dictionaries of the $n \times \rho$ vector space $\mathcal{V}$. We define a distance between these two dictionaries as:

$$d_D(\mathbf{U}, \mathbf{W}) = d_{W,p}(\mathbb{U}, \mathbb{W})\,, \quad (7)$$

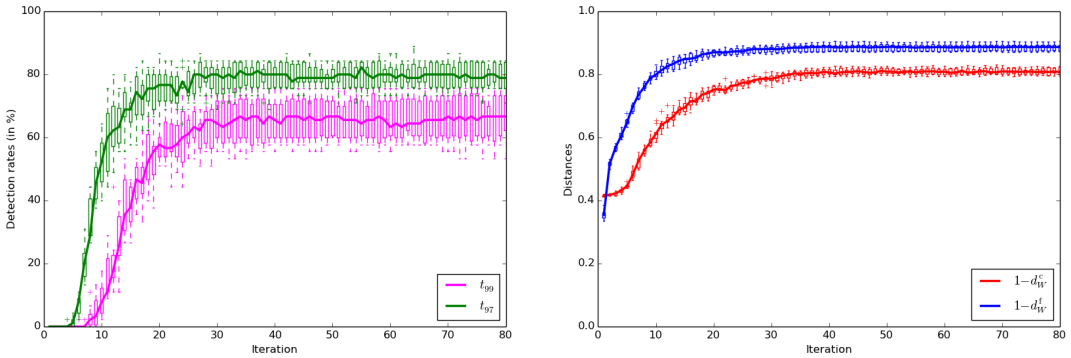

Fig. 1. Left: Detection rates with a threshold of 0.99 and 0.97 as a function of the learning iteration. Right: Wasserstein set-metrics for M-DLA using chordal ($1 - d_{\mathrm{W}}^{\mathrm{c}}$) and Frobenius-based distance ($1 - d_{\mathrm{W}}^{\mathrm{f}}$).

where $\mathbb{U} = \{\mathcal{U}_i : \mathcal{U}_i = \mathrm{span}(U_i), i \in I\}$ and $\mathbb{W} = \{\mathcal{W}_j : \mathrm{span}(W_j), j \in J\}$. In the following, we will denote $d_{W,p}$ as d_W to simplify the notation.

From this definition, we can state the following: Let $\mathcal{C}(\mathcal{V})$ be any collection on $\mathcal{V}$. Then the following holds:

- d_D is pseudo-metric and hence $(\mathcal{C}(\mathcal{V}), d_D)$ is pseudo-metric space,
- d_D is invariant by linear combinations.

The proof is a direct consequence of Equation (7) since d_D is defined as a distance between subspaces.

The dictionary distance d_D is defined as the distance between their subspaces, that is d_D is acting in the dictionary space $\mathcal{V}$ whereas the distance d_W is acting in the Grassmannian space $\mathbb{G}$. As an element $\mathcal{U}$ of $\mathbb{G}$ is a subspace, there exists an infinite number of elements U in $\mathcal{V}$ spanning $\mathcal{U}$. Thus two distinct dictionaries $\mathbf{U}_1 \neq \mathbf{U}_2$, that is two collections $\{U_i^1\}_{i\in I}$ and $\{U_i^2\}_{i\in I}$ of elements in $\mathcal{V}$, could span the same collection of subspaces $\mathbb{U} = \{\mathcal{U}_i\}_{i\in I}$ in $\mathbb{G}$. In other words, a distance $d_D(\mathbf{U}_1, \mathbf{U}_2) = d_W(\mathbb{U}, \mathbb{U}) = 0$ could exist for two separate dictionaries $\mathbf{U}_1 \neq \mathbf{U}_2$. As the separability axiom does not hold, d_D is a pseudo-metric and the separability axiom is relaxed to the identity axiom: $d(x, x) = 0, \forall x \in X$.

4. EXPERIMENTS

This section demonstrates that set-metrics are able to capture the convergence of DLA on synthetic dataset. On real EEG-based dataset, from BCI Competition IV [25], set-metrics are embedded in a hierarchical clustering algorithm to investigate the BCI-inefficiency phenomenon.

4.1. Convergence evaluation in a dictionary recovering task

This section is devoted to demonstrate why relying on metrics allows to improve the assessment of dictionary learning algorithms. More precisely, a set of experiments is conducted to reproduce state-of-the-art results on synthetic datasets and to show how the different proposed metrics behave compared to the commonly used indicators.

Dictionaries criteria and metrics: A first measure to compare dictionaries is the known as *detection rate*. Given two dictionaries $\mathbf{U}$ and $\hat{\mathbf{U}}$, corresponding respectively to a collection of m atoms U_i and m atoms $\hat{U}_i$, a common methodology [26] is to match an atom $\hat{U}_i$ w.r.t. its corresponding atom U_i if their correlation value ν_i is above a chosen threshold s. The correlation is expressed as $\nu_i = |\langle U_i, \hat{U}_i \rangle| \geqslant s$. The detection rate is defined as the percentage of the U_i atoms in $\mathbf{U}$ matched with atoms of $\hat{\mathbf{U}}$.

The set-metric defined in Equation (7) provides a principled way of comparing dictionaries. In the following experiments, the Wasserstein is parametrized with $p = 1$ and the measures are uniform on the whole support, see Equation (6), it is also known as Earth Mover's distance or Mallows distance and many efficient implementations are available [27, 28]. The Wasserstein distance is applied with two different ground distances. The first one relies on the chordal distance, described in Equation (4), and is denoted $d_{\mathrm{W}}^{\mathrm{c}}$. The second one, denoted $d_{\mathrm{W}}^{\mathrm{f}}$, relies on a Frobenius distance and is defined as $(d^{\mathrm{f}}(U_i, \hat{U}_j))^2 = \| \hat{U}_j - U_i \|_F^2 = 2(1 - \langle U_i, \hat{U}_j \rangle)$, assuming that $\|U_i\|_F = \|\hat{U}_j\|_F = 1$. The distance d^{f} is related to the detection rate ν_i, but without the sign invariance: $\hat{U}_j$ is not considered recovered if it is close to $-U_i$. This distance is not invariant to linear transforms.

Experimental protocol: A dictionary $\mathbf{U}$ of $m = 135$ normalized multivariate atoms with $\rho = 10$ is created from white uniform noise. The atom length is $n = 20$ samples. A training dataset $\mathbf{Y}_{\mathrm{train}}$ is generated by combining atoms of $\mathbf{U}$. $\mathbf{Y}_{\mathrm{train}}$ contains $q = 2000$ training signals of length n. Each training signal is generated as the sum of three atoms, the coefficients and the atom indices being randomly drawn. A dictionary $\hat{\mathbf{U}}$ with at least m atoms is built from $\mathbf{Y}_{\mathrm{train}}$ using M-DLA [16] described in (2). The quality of the DLA is assessed by measuring the proportion of atoms in $\mathbf{U}$ recovered in $\hat{\mathbf{U}}$. Here, $\hat{\mathbf{U}}$ is initialized with random signals from $\mathbf{Y}_{\mathrm{train}}$ and 80 iterations of DLA are performed (sparse approximation and dictionary update).

Results: The results are presented in Fig. 1: the set-metrics and detection rates are computed at each iteration. It appears clearly that the dictionary has almost converged after only 15 to 20 iterations. It is thus interesting to investigate how the detection rates and the set-metrics capture the evolution of the dictionary $\hat{\mathbf{U}}$ during these first iterations. The detection rates completely fail to detect any modification ongoing in $\hat{\mathbf{U}}$ before 5 or 8 iterations. Then, they abruptly increase between iterations 5 and 20. The detection rates are converging toward 67% for $s = 0.99$ and 72% for $s = 0.97$ but display important variations. These variations are a direct consequence of the thresholding occurring in the detection rates.

All the set-metrics start with positive values because they detect

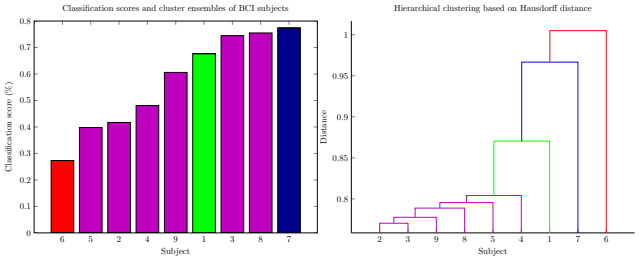

Fig. 2. Left: Performance of the subjects from the BCI Competition IV-2a with state of the art algorithm from [29], color indicates cluster ensembles obtained with consensus clustering on learned dictionaries. Right: Hierarchical clustering on the same dataset.

that $\hat{\mathbf{U}}$ is initialized with training signals. They provide a smoother and more accurate evaluation of the convergence. The $d_{\mathrm{W}}^{\mathrm{f}}$ metric provides the smoother results of all distances and the $d_{\mathrm{W}}^{\mathrm{c}}$ is sensible enough to capture modification of $\hat{\mathbf{U}}$ after the 20^{th} iteration.

Contrary to detection rates based indicators that provide oscillating values, one can note the regularity of the values provided by the set-metrics. This demonstrates their efficiency in the context of dictionary learning.

4.2. Clustering on EEG-based BCI

Experimental protocol: The aim here is to rely on set-metrics embedded in a clustering algorithm to investigate user-specific characteristics in BCI tasks. The individual variability of BCI subjects is still largely unharnessed: from 15 to 30% of BCI users obtain very poor results [9, 10] with the state of the art algorithms. This phenomenon is referred to as "BCI-illiteracy" or "BCI-inefficiency". We claim here that the comparison of subjects through computing the distances between their associated learned dictionaries could help to characterize the BCI-inefficiency.

Multivariate dictionaries are learned with M-DLA [16] using the datasets from BCI Competition IV set 2a [25]. This is a motor imagery experiment, where 9 subjects have been instructed to imagine four tasks (imagination of left hand, right hand, tongue or feet movements) during two sessions. Each session consists of 288 trials (72 trials for each task) and a trial is 3 seconds recording of $\rho = 22$ electrodes sampled at 250 Hz. For a given subject, a dictionary is learned for each task using the first session dataset, with a sparsity parameter $K = 1$. Thus for all nine subjects, $9 \times 4 = 36$ dictionaries are learned.

Relation between subject clusters and BCI-inefficiency: A distance matrix G^t between subjects is computed for each task t using the Wasserstein set-metric based on the chordal distance $d_{\mathrm{W}}^{\mathrm{c}}$. For a given task, the distances $d_{\mathrm{W}}^{\mathrm{c}}(\mathbf{U}_i, \mathbf{U}_j)$ between dictionaries of subjects i and j are converted to Gaussian similarities: $s_{ij}^t = \exp\left(-(d_{\mathrm{W}}^{\mathrm{c}}(\mathbf{U}_i, \mathbf{U}_j))^2/2\right)$. Subject's clusters are gathered using affinity propagation [30] on G^t. The preference value of subjects for affinity propagation is set to the median value of G^t.

The subject's clusters obtained for each task are combined using cluster ensembles techniques [31]. Hence, a partition of the subjects in C clusters is obtained by maximizing the shared mutual information of all tasks. The results show that the subjects are aggregated in $C = 3$ or 4 stable cluster ensembles. This clustering is stable since increasing the C value results in empty clusters. These clusters are represented with different colors on the left-hand side of Fig. 2. The histograms in Fig. 2 report the subject performances based on Filter Bank CSP [29], the state-of-the-art algorithm. The subjects are sorted according to their performance, the best performing subject is on the right-hand side. Using $C = 3$ cluster ensembles, the subject with the highest performance is always alone in a cluster. The same holds for the subject with the worst performance.

To highlight the relation between clusters of subjects, a hierarchical clustering is shown on the right-hand side of Fig. 2. This hierarchy is built using the distance matrix G^t of only one task, the one computed from feet imaginary motion[1]. The obtained dendrogram is shown on the right-hand side of Fig. 2. One can note that subjects 2, 3, 9, 8, 5 and 4 belong to the same cluster and that each one of the subjects 1, 7 and 6 constitute three separate clusters.

On this BCI dataset, most of the subjects share a common profile except for the two extreme cases of the most BCI-inefficient and BCI-efficient subjects. Set-metrics based on multivariate dictionaries offer new opportunities to qualitatively assess datasets used in competitions and challenges. We hope that our approach could help the community to propose more consistent and more complete benchmarks or evaluations.

5. CONCLUSION

This contribution relies on advances from algebraic geometry and matrix manifolds to define suited metrics for multivariate dictionaries. It is the first attempt with respect to this emerging field. The distance between dictionaries is computed as the distance between their subspaces, yielding pseudo-metrics which are invariant to linear transformations, a very desirable property when dealing with multivariate dictionaries.

The interest of the described metrics has been shown through its direct application on two examples: a synthetic dataset and real dataset of EEG-based BCI. The proposed metrics allow to estimate empirically the convergence of a dictionary learning algorithm with a precision outperforming the classical measurements based on detection rates. On the BCI dataset, we have shown how these metrics applied on multivariate dictionaries learned from EEG data can help assessing the "BCI-inefficiency" of subjects. The chordal distance endows the set metric with an invariance to linear transforms, a desirable property for analyzing EEG brain signals as the set metric is thus not affected by variations in electrods positions. Thus, the proposed hierarchical clustering approach allows to gain new neurophysiological insight on the user's ability to interact with BCI systems.

Future work will be devoted to the extensive analysis of BCI datasets, using various clustering approaches based on the introduced set-metrics. From a theoretical perspective, an ongoing work concentrates on the embedding of these set-metrics in dictionary learning algorithms.

6. REFERENCES

[1] R. Balan, "Equivalence Relations and Distances between Hilbert Frames," *Proceedings of the American Mathematical Society*, vol. 127, no. 8, pp. 2353–2366, 1999.

[2] K. Skretting and K. Engan, "Learned dictionaries for sparse image representation: properties and results," in *SPIE Conference*, San Diego, USA, 2011, vol. 8138.

[1] Hierarchical clustering requires a distance matrix. Cluster ensembles using all tasks provide only a partition, thus the hierarchy is built using only one task.

[3] K. Engan, S.O. Aase, and J.H. Husøy, "Multi-frame compression: theory and design," *Signal Processing*, vol. 80, pp. 2121–2140, 2000.

[4] R. Grosse, R. Raina, H. Kwong, and A.Y. Ng, "Shift-invariant sparse coding for audio classification," in *Proc. Conf. on Uncertainty in Artificial Intelligence (UAI)*, Corvallis, USA, 2007, pp. 149–158.

[5] J. Mairal, F. Bach, J. Ponce, G. Sapiro, and A. Zisserman, "Non-local sparse models for image restoration," in *IEEE ICCV*, Kyoto, Japan, 2009, pp. 2272–2279.

[6] M. Aharon, M. Elad, and A.M. Bruckstein, "K-SVD: An algorithm for designing overcomplete dictionaries for sparse representation," *IEEE Trans. Signal Processing*, vol. 54, pp. 4311–4322, 2006.

[7] A. Aldroubi, "Portraits of Frames," *Proceedings of the American Mathematical Society*, vol. 123, no. 6, pp. 1661–1668, 1995.

[8] D. Vainsencher, S. Mannor, and A.M. Bruckstein, "The sample complexity of dictionary learning," *Journal of Machine Learning Research*, vol. 12, pp. 3259–3281, 2011.

[9] E.M. Hammer, S. Halder, B. Blankertz, C. Sannelli, T. Dickhaus, S. Kleih, K.-R. Müller, and A. Kübler, "Psychological predictors of SMR-BCI performance," *Biological Psychology*, vol. 89, no. 1, pp. 80–86, 2012.

[10] C. Vidaurre and B. Blankertz, "Towards a cure for BCI illiteracy," *Brain Topography*, vol. 23, no. 2, pp. 194–198., 2010.

[11] K. Engan, K. Skretting, and J.H. Husøy, "Family of iterative LS-based dictionary learning algorithms, ILS-DLA, for sparse signal representation," *Digital Signal Processing*, vol. 17, pp. 32–49, 2007.

[12] J. Mairal, F. Bach, J. Ponce, and G. Sapiro, "Online learning for matrix factorization and sparse coding," *Journal of Machine Learning Research*, vol. 11, pp. 19–60, 2010.

[13] J.A. Tropp, "Algorithms for simultaneous sparse approximation; Part II: Convex relaxation," *Signal Processing*, vol. 86, pp. 589–602, 2006.

[14] R. Gribonval, H. Rauhut, K. Schnass, and P. Vandergheynst, "Atoms of all channels, unite! Average case analysis of multichannel sparse recovery using greedy algorithms," Tech. Rep. PI-1848, IRISA, 2007.

[15] A. Rakotomamonjy, "Surveying and comparing simultaneous sparse approximation (or group-lasso) algorithms," *Signal Processing*, vol. 91, pp. 1505–1526, 2011.

[16] Q. Barthélemy, C. Gouy-Pailler, Y. Isaac, A. Souloumiac, A. Larue, and J.I. Mars, "Multivariate temporal dictionary learning for EEG," *Journal of Neuroscience Methods*, vol. 215, pp. 19–28, 2013.

[17] Q. Barthélemy, A. Larue, A. Mayoue, D. Mercier, and J.I. Mars, "Shift & 2D rotation invariant sparse coding for multivariate signals," *IEEE Trans. Signal Processing*, vol. 60, pp. 1597–1611, 2012.

[18] G.H. Golub and H. Zha, "The canonical correlations of matrix pairs and their numerical computation," in *Linear Algebra for Signal Processing*, A. Bojanczyk and G. Cybenko, Eds., vol. 69 of *The IMA Volumes in Mathematics and its Applications*, pp. 27–49. Springer, 1995.

[19] G.H. Golub and C.F. van Loan, *Matrix Computations*, The Johns Hopkins University Press, 3rd edition, 1996.

[20] J.H. Conway, R.H. Hardin, and N.J.A. Sloane, "Packing lines, planes, etc.: Packings in Grassmannian spaces," *Experimental Mathematics*, vol. 5, no. 2, pp. 139–159, 1996.

[21] I.S. Dhillon, R.W. Heath Jr., T. Strohmer, and J.A. Tropp, "Constructing Packings in Grassmannian Manifolds via Alternating Projection," *Experimental Mathematics*, vol. 17, no. 1, pp. 9–35, 2008.

[22] A. Edelman, T.A. Arias, and S.T. Smith, "The Geometry of Algorithms with Orthogonality Constraints," *SIAM J. Matrix Anal. Appl.*, vol. 20, no. 2, pp. 303–353, 1999.

[23] J.W. Milnor and J.D. Stasheff, *Characteristic Classes. (AM-76)*, vol. 76, Princeton University Press, 1974.

[24] C. Villani, *Optimal transport: old and new*, vol. 338 of *Grundlehren der mathematischen Wissenschaften*, Springer, 2009.

[25] M. Tangermann, K.-R. Müller, A. Aertsen, N. Birbaumer, C. Braun, C. Brunner, R. Leeb, C. Mehring, K.J. Miller, G. Müller-Putz, G. Nolte, G. Pfurtscheller, H. Preissl, G. Schalk, A. Schlögl, C. Vidaurre, S. Waldert, and B. Blankertz, "Review of the BCI Competition IV," *Frontiers in Neuroscience*, vol. 6, no. 55, 2012.

[26] M. Aharon, *Overcomplete Dictionaries for Sparse Representation of Signals*, Ph.D. thesis, Technion - Israel Institute of Technology, 2006.

[27] Y. Rubner, C. Tomasi, and L. J. Guibas, "A metric for distributions with applications to image databases," in *International Conference on Computer Vision (ICCV)*. 1998, pp. 59–66, IEEE.

[28] O. Pele and M. Werman, "Fast and robust earth mover's distances," in *International Conference on Computer Vision (ICCV)*. 2009, pp. 460–467, IEEE.

[29] K.K. Ang, Z.Y. Chin, C. Wang, C. Guan, and H. Zhang, "Filter bank common spatial pattern algorithm on BCI competition IV datasets 2a and 2b.," *Frontiers in Neuroscience*, vol. 6, pp. 1–9, 2012.

[30] B.J. Frey and D. Dueck, "Clustering by passing messages between data points," *Science*, vol. 315, pp. 972–976, 2007.

[31] A. Strehl and J. Ghosh, "Cluster ensembles — a knowledge reuse framework for combining multiple partitions," *Journal of Machine Learning Research*, vol. 3, pp. 583–617, 2003.

Neurocomputing 191 (2016) 55–68

Contents lists available at ScienceDirect

Neurocomputing

journal homepage: www.elsevier.com/locate/neucom

Online SSVEP-based BCI using Riemannian geometry

Emmanuel K. Kalunga [a,b], Sylvain Chevallier [b,*], Quentin Barthélemy [c], Karim Djouani [a], Eric Monacelli [b], Yskandar Hamam [a]

[a] Department of Electrical Engineering and the French South African Institute of Technology, Tshwane University of Technology, Pretoria 0001, South Africa
[b] Laboratoire d'Ingénierie des Systèmes de Versailles, Université de Versailles Saint-Quentin, 78140 Velizy, France
[c] Mensia Technologies, S.A. ICM, Hôpital de la Pitié-Salpêtrière, 75013 Paris, France

ARTICLE INFO

Article history:
Received 10 April 2015
Received in revised form
17 December 2015
Accepted 8 January 2016
Communicated by S. Fiori
Available online 17 February 2016

Keywords:
Riemannian geometry
Online
Asynchronous
Brain–Computer Interfaces
Steady State Visually Evoked Potentials

ABSTRACT

Challenges for the next generation of Brain Computer Interfaces (BCI) are to mitigate the common sources of variability (electronic, electrical, biological) and to develop online and adaptive systems following the evolution of the subject's brain waves. Studying electroencephalographic (EEG) signals from their associated covariance matrices allows the construction of a representation which is invariant to extrinsic perturbations. As covariance matrices should be estimated, this paper first presents a thorough study of all estimators conducted on real EEG recording. Working in Euclidean space with covariance matrices is known to be error-prone, one might take advantage of algorithmic advances in Riemannian geometry and matrix manifold to implement methods for Symmetric Positive-Definite (SPD) matrices. Nonetheless, existing classification algorithms in Riemannian spaces are designed for offline analysis. We propose a novel algorithm for online and asynchronous processing of brain signals, borrowing principles from semi-unsupervised approaches and following a dynamic stopping scheme to provide a prediction as soon as possible. The assessment is conducted on real EEG recording: this is the first study on Steady-State Visually Evoked Potential (SSVEP) experimentations to exploit online classification based on Riemannian geometry. The proposed online algorithm is evaluated and compared with state-of-the-art SSVEP methods, which are based on Canonical Correlation Analysis (CCA). It is shown to improve both the classification accuracy and the information transfer rate in the online and asynchronous setup.

1. Introduction

Human–machine interactions without relying on muscular capabilities is possible with Brain–Computer Interfaces (BCI) [1] They are the focus of a large scientific interest [2–4], especially those based on electroencephalography (EEG) [5]. From a large literature based on the BCI competition datasets [6–8], one can identify the two most challenging BCI problems: on the one hand, the inter-individual variability plagues the models and leads to BCI-inefficiency effect [9–11], on the other hand, the intra-individual changes calls for the development of online algorithms and adaptive systems following the evolution of the subject's brain waves [12–14]. To alleviate these variations, several signal processing and machine learning techniques have been proposed, such as filtering, regularization or clustering [15,16] without the emergence of an obvious "best candidate" methodology.

A common vision is shared by all the most successful approaches to reduce signal variabilities: they are applied on covariance matrices instead of working in the input signal space. Common Spatial Pattern (CSP) [17–19], which is the most known preprocessing technique in 2-class BCI, try to maximize the covariance of one class while minimizing the covariance of the other. Similarly, Principal Components Analysis (PCA) [6,7], also applied for spatial filtering in BCI, is based on the estimation of covariance matrices. Canonical Correlation Analysis (CCA) is another example of a technique relying on covariance estimates successfully applied on EEG for spatial filtering [15,20]. Covariance matrices are also found in classifiers such as the Linear Discriminant Analysis (LDA), which is largely used in BCI. In all cases, they are handled as elements of an Euclidean space. However, being Symmetric and Positive-Definite (SPD), covariance matrices lie on a subset of the Euclidean space, with reduced dimensionality and specific properties, the *Riemannian manifold*. Considering covariance matrices in their original space would reduce the search area for an optimization problem [21,22]. As Riemannian manifolds inherently define a metric, the distance between SPD matrices takes into account the space where they lie on; approximating it to an Euclidean space introduces inaccuracies and results in ill-conditioned matrices.

* Corresponding author.

http://dx.doi.org/10.1016/j.neucom.2016.01.007
0925-2312/

Recently, studies have been done to consider covariance matrices obtained from multichannel brain signals in their original space [23–25]. Covariance matrices are the input features of the BCI system and the classifier algorithms rely on Riemannian metric for partitioning the feature space. The authors propose building specific covariance matrices in order to emphasize the spatial and frequential information of the multichannel brain signals [25]. The outcome of this approach is a simple processing tool chain, which achieves state-of-the-art classification performances.

This paper introduces an online version of the *minimum distance to Riemannian mean* (MDRM) algorithm [23], with an application to Steady-State Visually Evoked Potential (SSVEP) signals. In SSVEP, the subjects concentrate on stimuli blinking at fixed frequencies. Depending on the focus of their attention, brain waves will arise with the same phase and frequency as the stimulus chosen by the subject. The signals are recorded in an application of assistive robotics,[1] with a shared control scheme relying on an SSVEP-based BCI and a 3D touchless interface based on IR-sensors to operate an arm exoskeleton [26]. The long term objective is to equip a home environment with assistive technologies, including BCI, as proposed in [27,28]. In this context, it is important to design an online system, i.e. that adapt continuously to the user's brain signals, and asynchronous, i.e. that could be activated "on demand".

Our online implementation[2] is similar to the unsupervised or semi-unsupervised learning scheme proposed in [29,30]; that has the potential of shortening (or even removing) the calibration phase. We apply a similar approach to the dynamic stopping criterion used in [31] to increase the speed of the BCI system. This approach allows to dynamically determine the trial length and ensure robustness in classification results. Our MDRM approach outperforms state-of-the-art algorithms in the offline setup. Moreover, these state-of-the-art algorithms, that are based on CCA, are inherently limited as they could not handle resting state. They must rely on an external command to be turn on or off, and are thus only suitable to lab environment.

When working with covariance matrices, a crucial point is to correctly estimate the covariance when the number of samples is small or heavily corrupted by noise. Several approaches have been proposed to build the covariance matrices, relying on normalization or regularization of the sample covariances. To assess the quality of the covariance matrices obtained from EEG samples, a comparative study of these estimators is conducted.

Hence, the contributions of this works are:

- a comprehensive review of the literature on Riemannian geometry applied to EEG and time-series,
- a thorough analysis of the covariance estimators and their impact on tools derived from information geometry,
- first online application of a Riemannian classification algorithm on SSVEP-based BCI,
- introduction of a novel algorithm for online and asynchronous BCI, including a resting state class, yielding better performance than state-of-the-art SSVEP algorithms. No phase synchronization is required for the SSVEP.

The paper is divided as follows: Section 2 reviews the state of the art in SSVEP-based BCI and the applications of Riemannian geometry in machine learning for BCI. Section 3 presents concepts of Riemannian geometry relevant to this work and estimators of covariance. In Section 4, the proposed classification algorithm for online SSVEP is introduced and the experimental results are presented in Section 5 for offline and online setups as well as without and with a resting state class.

2. State of the art

2.1. Steady-state visually evoked potential

Sensory evoked potentials often oppose Event Related Potential (ERP) and Steady-State Response (SSR) [32]. This distinction originates from the idea that the SSR may be generated by neural oscillations elicited by the repeated stimulations [33] whereas the ERP is the transient response to an event occurring at sufficiently long time interval to allow the system to return to its initial state [34]. We will focus on the visual SSR, called SSVEP and its application to BCI.

The SSVEP-based BCI is often employed as a dependent BCI [35], that is, some residual muscular capabilities are required to move the eye toward the blinking stimulus as opposed to independent BCI, such as Motor Imagery (MI), where the communication does not rely on any motor capability. It has been shown that SSVEP could be used as an independent BCI [36,37] as the brain oscillations are strongly related to the focus of attention. Using covert attention, i.e. shifting the focus of attention without moving the eyes, subjects can generate different SSVEP responses.

BCI have highly variable subject-specific performances. 20–30% of the subjects cannot operate correctly brain interfaces. This phenomenon is referred to as BCI illiteracy [9–11]. It affects SSVEP-based BCI and it is correlated with age and gender, male subjects being more afflicted than female ones [38]. Offline BCI, that is approaches where the learning algorithms are trained on a large dataset of subject's EEG recording, are also afflicted which indicate that a source of variability at the subject level is not handled correctly by the existing approaches. BCI illiteracy is also afflicting online approaches, where the algorithms are adapted to the subject's EEG as the experiment goes by.

Visual stimulus plays a crucial role, affecting the BCI performance, and should be designed carefully. An in-depth review of the literature [39] shows that LED stimuli provide better results than those obtained on computer screen. A cognitive study [40] indicates that any stimulation between 2 and 50 Hz induces visible oscillations in the visual cortex. Another study shows that a peak in signal to noise ratio is visible at around 15 Hz [41]. Common values employed in SSVEP studies are between 12 and 25 Hz, as they induce oscillations with higher amplitudes [39]. One should note that safety of the subject should be taken into account as some frequency ranges of the stimulation train could trigger epileptic seizure [42].

The phase of the stimulation signal can also be modulated, enhancing the BCI performance by boosting the Information Transfer Rate (ITR) [43,44]. An important constraint in that case is that the experimental setup requires a synchronization between the display and the recording system, to ensure the correct estimation of the stimulus' phase. Better alternatives are available when considering systems with such constraints: code-modulated VEP (c-VEP) has yield the highest ITR in BCI [45,46]. In c-VEP, the sole difference is that the stimulus flickering is based on pseudorandom sequences instead of the fixed frequencies of SSVEP. All these successful approaches in SSVEP and c-VEP rely on CCA. Given two sets of signals, CCA aims at finding the projection space that maximizes their cross-covariance while jointly minimizing their covariance [20,15,44]. The common methodology is to find the canonical space between the multichannel EEG trial on the one hand and reference signals, usually sine and cosine of target frequencies and harmonics, on the other hand.

[1] This dataset is freely available from https://github.com/sylvchev/dataset-ssvep-exoskeleton.

[2] The open source code is available on https://github.com/emmanuelkalunga/Online-SSVEP.

This study is part of our efforts to conceive a smart and adapted environment for people with disabilities, with a standing point similar to [27,28]. In our case, the device generating flickering stimulus should not be connected to the EEG processing system, to allow, for example, the design of "smart switches" distributed in the home environment in further studies. Hence, we could not rely on phase-dependent setups, such as c-VEP or phase-modulated SSVEP.

Another requirement of our system is to be self-paced, a property also called asynchronous, to provide the user with the ability to use the system "on demand", i.e. when needed. As pointed out by [47], it is thus necessary to provide a "no-control" state to cope with situation where the user does not want to produce any command. Several methods could be considered, such as including a reject threshold in the system, as in [47], or directly provide the system with a reject class, see for example [48]. This "no-control" state or "resting" state is not always included in the existing studies, see for example [27,20,44]. The high ITR obtained with these systems are thus confined to the lab environment and could not be directly applied to realistic assistive scenarios.

2.2. Riemannian geometry in BCI

Information geometry provides useful tools for various machine learning and optimization problems. In machine learning, SPD matrices have been used in various applications where features and data are only considered in the Euclidean space. Indeed, covariance matrices lie in the space of SPD matrices which is a subset of the Euclidean space when considered with the scalar product. But the same space of SPD matrices, endowed with a differential structure, induces a Riemannian manifold.

Riemannian geometry can improve machine learning algorithms, taking explicitly into consideration the underlying structure of the considered space. Three kinds of approaches in the literature use the geometry of data in machine learning. The first one relies on the mapping of the Riemannian manifold onto an Euclidean vector space. One such mapping, called logarithmic mapping, exists between the manifold and its tangent space, which is an Euclidean space, and has been used in classification task for BCI [24]. Some kernels have been applied successfully to this end: Stein kernel, Log-Euclidean kernels as well as their normalized versions [49]. The main idea is to map the input data to a high dimensional feature space, providing a rich and hopefully linearly separable representation. The so-called kernel trick is to provide a kernel function, which computes an inner product in the feature space directly from points lying in the input space, defining a Reproducing Kernel Hilbert Space (RKHS). The family of kernels defined on the Riemannian manifold allows the implementation of extensions of all kernel-based methods, such as SVM, kernel-PCA or kernel k-means [50]. Apart from the kernel approaches, once the data are mapped onto a vector space, any machine learning algorithm working in Euclidean space, such as LDA, could be applied [23].

A second kind of machine learning approach exploits the underlying geometry of the data. Instead of mapping the data to an Euclidean space, either a tangent space or an RKHS, the algorithms are adapted to Riemannian space. For instance, sparse coding algorithm has been adapted to Riemannian manifold, using the geodesic distance to estimate the data point and its sparse estimate [51]. Similarly nonlinear dimensionality reduction techniques have been adapted to Riemannian manifold, such as Laplacian Eigenmaps (LE), Locally Linear Embedding (LLE), and Hessian LLE. This adaptation was used to cluster data using their probability density functions (pdf) [52] or covariance matrices [53] as features. Another example is the adaptation of interpolation and filtering of data to Riemannian space performed in [54], where an affine-invariant Riemannian metric is also proposed to offer a geodesically complete manifold i.e. a manifold with no edge and no singular point that can be reached in finite time.

In the last kind of approach, instead of adapting existing algorithm from Euclidean to Riemannian geometry, new algorithms are developed directly for Riemannian manifolds. The *minimum distance to Riemannian mean* (MDRM) relies on a Riemannian metric to implement a multi-class classifier and have been applied on EEG. New EEG trials are assigned to the class whose average covariance matrix is the closest to the trial covariance matrix [23]. The MDRM classification can be preceded by a filtering of covariance matrices, like in [55] where covariance matrices are filtered with LDA component in the tangent space, then brought back to the Riemannian space for classification with MDRM. Another example is the *Riemannian Potato* [56], an unsupervised and adaptive artifact detection method, providing an online adaptive EEG filtering (i.e. outliers removal). Incoming signals are rejected if their covariance matrix lies beyond a predefined z-score, computed from a sliding window. With the same objective of achieving robustness to noise that affects covariance matrices, Riemannian geometry is used to solve divergence functions of pdfs [57]. This allows to reformulate the CSP as the maximization of the divergence between the distributions of data from two different classes corresponding to two cognitive states [58,59]. Using the *beta divergence* the obtained CSP is robust to outliers in sample covariance matrices and this algorithm is successfully applied to EEG filtering for BCI. Riemannian metrics are also used for EEG channel selection [60] and the selection of the most discriminatory spatial filters in CSP [61].

In MI experiment, the subject is asked to imagine a movement (usually hand, feet or tongue), generating Event-Related Synchronization and Desynchronization (ERD/ERS) in pre-motor brain area. Riemannian BCI is well suited for MI experiment as the spatial information linked with synchronization is directly embedded in covariance matrices obtained from multichannel recordings. However, for BCI that rely on Evoked Potential such as SSVEP or Event Related Potential (ERP), as P300, both frequential and temporal information are needed; the spatial covariance matrix does not contain these information. To apply Riemannian geometry to SSVEP and ERP, the sample covariance matrices can be defined from a rearrangement of the recorded data. The rearrangement is done such that the temporal or frequency information are captured [25]. With similar motivations, [62,63] defined a new Riemannian distance between SPD matrices that would take into account a weighting factor on matrices. They use this new distance as a dissimilarity between weighted matrices of power spectral density to classify EEG into different sleep state by k-nearest neighbors.

3. Covariance matrices and their geometry

This section presents some formal definitions for the information geometry concepts used in this paper. The link with the covariance matrices is explicated in Section 3.2, along with the covariance estimators proposed in the literature.

3.1. Riemannian manifold

An m-dimensional *manifold* $\mathcal{M}$ is a Hausdorff space for which every point has a neighborhood that is homeomorphic to an open subset of $\mathbb{R}^m$ [64]. When a tangent space is defined at each point, $\mathcal{M}$ is called a differential manifold. A *geodesic* γ is the shortest smooth curve between two points, Σ_1 and Σ_2. The tangent space $T_\Sigma\mathcal{M}$ at point Σ is the vector space spanned by the tangent vectors of all geodesics on $\mathcal{M}$ passing through Σ. A *Riemannian* manifold is

a manifold endowed with an inner product defined on the tangent space, which varies smoothly from point to point.

For the rest of this paper, we will restrict to the analysis of the manifold $\mathcal{M}_C$ of the $C \times C$ symmetric positive definite matrices, defined as:

$$\mathcal{M}_C = \left\{ \Sigma \in \mathbb{R}^{C\times C} : \Sigma = \Sigma^\top \text{ and } x^\top \Sigma x > 0, \forall x \in \mathbb{R}^C \backslash 0 \right\}.$$

The tangent space $T_\Sigma \mathcal{M}_C$ is identified to the Euclidean space of symmetric matrices:

$$\mathcal{S}_C = \left\{ \Theta \in \mathbb{R}^{C\times C} : \Theta = \Theta^\top \right\}.$$

The dimension of the manifold $\mathcal{M}_C$, and its tangent space $T_\Sigma \mathcal{M}_C$, is $m = C(C+1)/2$.

The mapping from a point Θ_i of the tangent space to the manifold is called the exponential mapping $\mathrm{Exp}_\Sigma(\Theta_i)$: $T_\Sigma \mathcal{M}_C \rightarrow \mathcal{M}_C$ and is defined as:

$$\mathrm{Exp}_\Sigma(\Theta_i) = \Sigma^{\frac{1}{2}} \mathrm{Exp}(\Sigma^{-\frac{1}{2}} \Theta_i \Sigma^{-\frac{1}{2}}) \Sigma^{\frac{1}{2}}. \quad (1)$$

Its inverse mapping, from the manifold to the tangent space is the logarithmic mapping $\mathrm{Log}_\Sigma(\Sigma_i)$: $\mathcal{M}_C \rightarrow T_\Sigma \mathcal{M}_C$ and is defined as:

$$\mathrm{Log}_\Sigma(\Sigma_i) = \Sigma^{\frac{1}{2}} \mathrm{Log}(\Sigma^{-\frac{1}{2}} \Sigma_i \Sigma^{-\frac{1}{2}}) \Sigma^{\frac{1}{2}}. \quad (2)$$

$\mathrm{Exp}(\cdot)$ and $\mathrm{Log}(\cdot)$ are the matrix exponential and matrix logarithm, respectively. The computation of these operators is straightforward for SPD matrices of $\mathcal{M}_C$. They are obtained from their eigenvalue decomposition (EVD):

$$\Sigma = U\, \mathrm{diag}(\lambda_1, \ldots, \lambda_C) U^\top,$$
$$\mathrm{Exp}(\Sigma) = U\, \mathrm{diag}(\log(\lambda_1), \ldots, \log(\lambda_C)) U^\top,$$
$$\mathrm{Log}(\Sigma) = U\, \mathrm{diag}(\exp(\lambda_1), \ldots, \exp(\lambda_C)) U^\top,$$

where $\lambda_1, \ldots, \lambda_C$ are the eigenvalues and U the matrix of eigenvectors of Σ. As any SPD matrix can be diagonalized with strictly positive eigenvalues, $\mathrm{Log}(\cdot)$ is always defined. Similarly the square root $\Sigma^{\frac{1}{2}}$ is obtained as:

$$\Sigma^{\frac{1}{2}} = U\, \mathrm{diag}(\lambda_1^{\frac{1}{2}}, \ldots, \lambda_C^{\frac{1}{2}}) U^\top,$$

and is unique. The same goes for $\Sigma^{-\frac{1}{2}}$.

The tangent vector of the geodesic $\gamma(t)$ between Σ_1 and Σ_2, where $\gamma(0) = \Sigma_1$ and $\gamma(1) = \Sigma_2$ is defined as $v = \overrightarrow{\Sigma_1 \Sigma_2} = \mathrm{Log}_{\Sigma_1}(\Sigma_2)$. A Riemannian distance between Σ_1 and Σ_2 can thus be defined as [65]:

$$\delta(\Sigma_1, \Sigma_2) = \| \mathrm{Log}(\Sigma_1^{-1} \Sigma_2) \|_F = \left[\sum_{c=1}^{C} \log^2 \lambda_c \right]^{1/2}, \quad (3)$$

where λ_c, $c = 1, \ldots, C$, are the eigenvalues of $\Sigma_1^{-1} \Sigma_2$. From Eq. (3), the geometric mean of I points Σ_i on the manifold, $i = 1, \ldots, I$, can be defined as the point that minimizes the sum of squared distances to all Σ_i:

$$\mu(\Sigma_1, \ldots, \Sigma_I) = \arg\min_{\Sigma \in \mathcal{M}_C} \sum_{i=1}^{I} \delta^2(\Sigma_i, \Sigma). \quad (4)$$

This mean has no closed form, and can be computed iteratively [66].

3.2. Covariance matrix estimation

Let $x_n \in \mathbb{R}^C$, $n = 1, \ldots, N$, denotes a sample of a multichannel EEG trial recorded on C electrodes. N is the trial length. Let $X \in \mathbb{R}^{C\times N}$ be the EEG trial such as $X = [x_1, \ldots, x_N]$. Under the hypothesis that all N samples x_n are randomly drawn from a distribution, it follows that $\boldsymbol{x}$ is a variable of random vectors and its expected vector is $\omega = E\{\boldsymbol{x}\}$ [67]. The covariance matrix of the random variable $\boldsymbol{x}$ is defined by $\Sigma = E\{(\boldsymbol{x} - \omega)(\boldsymbol{x} - \omega)^\top\}$ and is unknown, thus an estimate $\hat{\Sigma}$ should be computed. The choice of the appropriate estimator is crucial to verify that the obtained covariance matrices fulfill the following properties: they should be accurate, SPD, and well-conditioned. The last property requires that the ratio between the maximum and minimum singular value is not too large. Moreover, to ensure the computational stability of the algorithm, the estimator should provide full-rank matrices, and its inversion should not amplify estimation errors.

3.2.1. Sample covariance matrix estimator

The most usual estimator is the empirical *sample covariance matrix* (SCM), defined as:

$$\hat{\Sigma}_{\mathrm{scm}} = \frac{1}{N-1} \sum_{n=1}^{N} (x_n - \overline{x})(x_n - \overline{x})^\top = \frac{1}{N-1} X \left(\mathbf{I}_N - \frac{1}{N} \mathbf{1}_N \mathbf{1}_N^\top \right) X^\top, \quad (5)$$

where $\overline{x} \in \mathbb{R}^C$ is the sample mean vector $\overline{x} = \frac{1}{N} \sum_{n=1}^{N} x_n$. In the matrix notation, $\mathbf{I}_N$ is the $N \times N$ identity matrix and $\mathbf{1}_N$ is the vector $[1, \ldots, 1]$. The SCM is often normalized [67] as:

$$\hat{\Sigma}_{\mathrm{nscm}} = \frac{C}{N} \sum_{n=1}^{N} \frac{(x_n - \overline{x})(x_n - \overline{x})^\top}{\sigma_{x_n}^2}, \quad (6)$$

with the inter-channel variance at time $n$defined as $\sigma_{x_n}^2 = (x_n - \overline{x})^\top (x_n - \overline{x})$. Other normalization techniques could be used.

This estimation is fast and computationally simple. However when $C \approx N$, the SCM is not a good estimator of the true covariance. In the case $C > N$, the SCM is not even full rank.

3.2.2. Shrinkage covariance matrix estimators

To overcome the shortcomings of SCM, the shrinkage estimators have been developed as a weighted combination of the SCM and a target covariance matrix, which is often chosen to be close to the identity matrix, i.e. resulting from almost independent variables of unit variance.

$$\hat{\Sigma}_{\mathrm{shrink}} = \kappa \Gamma + (1 - \kappa) \hat{\Sigma}_{\mathrm{scm}}, \quad (7)$$

where $0 \leq \kappa < 1$. This estimator provides a regularized covariance that outperforms the empirical $\hat{\Sigma}_{\mathrm{scm}}$ for small sample size, that is $C \approx N$. The shrinkage estimator has the same eigenvectors as the SCM, but the extreme eigenvalues are modified i.e. the estimator is shrunk or elongated toward the average.

The different shrinkage estimators differ in their definition of the target covariance matrix Γ. Ledoit and Wolf [68] ($\hat{\Sigma}_{\mathrm{shrink\_ledoit}}$ in Fig. 1) have proposed $\Gamma = \nu \mathbf{I}_C$, with $\nu = \mathrm{Tr}(\hat{\Sigma}_{\mathrm{scm}})$. Blankertz [69] ($\hat{\Sigma}_{\mathrm{shrink\_blank}}$) defines Γalso as $\nu \mathbf{I}_C$ but with $\nu = \frac{\mathrm{Tr}(\hat{\Sigma}_{\mathrm{scm}})}{C}$. Schäfer ($\hat{\Sigma}_{\mathrm{shrink\_schaf}}$) proposes several ways of defining Γdepending on the observed $\hat{\Sigma}_{\mathrm{scm}}$ [70].

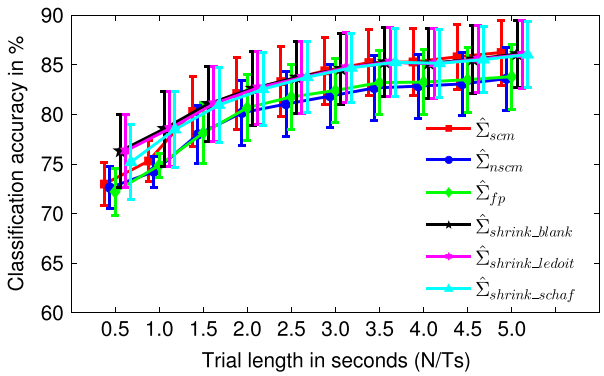

Fig. 1. Comparison of covariance estimators in terms of classification accuracy obtained with MDRM with increasing EEG trial length. For each trial length, the average accuracy across all subjects and across all replications is shown. Bars indicate the error of the mean, i.e. standard deviation divided by the square root of $n-1$, n = number of samples.

3.2.3. Fixed point covariance matrix estimator

The Fixed Point Covariance Matrix [71] is based on the maximum likelihood estimator $\hat{\ell}$ which is a solution to the following equation:

$$\hat{\Sigma}_{\text{fp}} = \hat{\ell} = \frac{C}{N}\sum_{n=1}^{N}\left(\frac{(x_n-\overline{x})(x_n-\overline{x})^{\top}}{(x_n-\overline{x})^{\top}\hat{\ell}^{-1}(x_n-\overline{x})}\right). \tag{8}$$

As there is no closed form expression to Eq. (8), it can be written as a function of $\hat{\ell} : g(\hat{\ell}) = \hat{\Sigma}_{\text{fp}}$. g admits a single *fixed point* $\hat{\ell}^*$, where $g(\hat{\ell}^*) = \hat{\ell}^*$, which is a solution to Eq. (8). Using $\hat{\ell}_0 := \hat{\Sigma}_{\text{nscm}}$ as the initial value of $\hat{\ell}$, it is solved recursively as $\hat{\ell}_t \underset{t\to\infty}{\longrightarrow} \hat{\ell}^*$.

4. Online adaptation of the Riemannian classifier

Concerning Riemannian classification of SSVEP, the offline methodology is explained in [25]. In this paper, we propose an online classifier for SSVEP, composed of an offline training phase and an online and asynchronous test phase. This analysis is performed for each subject independently.

4.1. Offline Riemannian classification

The proposed classifier relies on the Minimum Distance to Riemannian Mean (MDRM) introduced in [55] and extended in [25,72] for possible offline applications on SSVEP signals. Let us consider an experimental SSVEP setup with F stimulus blinking at F different frequencies. It is a multiclass classification with $K = F + 1$ classes: one class per stimulus and one resting state class. The covariance matrices are estimated from a modified version of the input signal X:

$$X \in \mathbb{R}^{C\times N} \to \begin{bmatrix} X_{\text{freq}_1} \\ \vdots \\ X_{\text{freq}_F} \end{bmatrix} \in \mathbb{R}^{FC\times N}, \tag{9}$$

where X_{freq_f} is the input signal X band-pass filtered around frequency freq_f, $f = 1,\ldots,F$. Thus the resulting covariance matrix $\hat{\Sigma}$ belongs to $\mathcal{M}_{FC}$. Henceforth, all EEG signals will be considered as filtered and modified by Eq. (9).

From I labelled training trials $\{X_i\}_{i=1}^{I}$ recorded per subject, K centers of class $\Sigma_\mu^{(k)}$ are estimated using Algorithm 1. When an unlabelled test trial Y is given, it is classified as belonging to the class whose center $\Sigma_\mu^{(k)}$ is the closest to the trial's covariance matrix (Algorithm 2, step 2).

Algorithm 1. Offline estimation of Riemannian centers of classes.

Inputs: $X_i \in \mathbb{R}^{FC\times N}$, for $i = 1,\ldots,I$, a set of labelled trials.
Inputs: $\mathcal{I}(k)$, a set of indices of trials belonging to class k.
Output: $\Sigma_\mu^{(k)}$, $k = 1,\ldots,K$, centers of classes.

1: Compute covariance matrices $\hat{\Sigma}_i$ of X_i
2: **for** $k=1$ **to** K **do**
3: $\Sigma_\mu^{(k)} = \mu(\hat{\Sigma}_i : i \in \mathcal{I}(k))$, Eq. (4)
4: **end**
5: **return** $\Sigma_\mu^{(k)}$

Algorithm 2. Minimum distance to Riemannian mean.

Inputs: $\Sigma_\mu^{(k)}$, K centers of classes from Algorithm 1.
Input: $Y \in \mathbb{R}^{FC\times N}$, an unlabelled test trial.
Output: k^*, the predicted label of Y.

1: Compute covariance matrix $\hat{\Sigma}$ of Y
2: $k^* = \arg\min_k \delta(\hat{\Sigma}, \Sigma_\mu^{(k)})$
3: **return** k^*

4.2. Curve-based online classification

In offline synchronous BCI paradigm, cue onset are used as reference for the localization of a brain response, e.g. an evoked potential. Nonetheless most of the BCI applications are online and asynchronous; cue onsets are not known, thus designing online version of BCI algorithms is not a trivial task. The approach introduced here identifies a period (i.e. time interval) in the online EEG $\chi \in \mathbb{R}^{FC\times\mathcal{N}}$, where $\mathcal{N}$ is the number of recorded samples, associated with a high probability (above threshold) of observing an SSVEP at a specific frequency, as illustrated in Algorithm 3.

Algorithm 3. Curve-based online classification.

Inputs: hyper-parameters $w, \Delta n, D$, and ϑ.
Inputs: $\Sigma_\mu^{(k)}$, $k = 1,\ldots,K$, centers of classes from Algorithm 1 (offline training).
Inputs: Online EEG recording $\chi(n)$.
Output: $\tilde{k}(n)$, online predicted class.

1: $d = 1$
2: **for** $n = w$ **to** $\mathcal{N}$ **step** Δn
3: Epoch X_d, Eq. (10), and classify it with Algorithm 2
4: **if** $d \geq D$
5: Find the most recurrent class in $\mathcal{K} = k^*_{j\in\mathcal{J}(d)}$: $\overline{k} = \arg\max_k \rho(k)$, Eq. (11)
6: **if** $\rho(\overline{k}) > \vartheta$
7: Compute $\tilde{\delta}_{\overline{k}}$, Eq. (12)
8: **if** $\tilde{\delta}_{\overline{k}} < 0$
9: **return** $\tilde{k} = \overline{k}$
10: **end**
11: **end**
12: **end**
13: $d = d+1$
14: **end**

To locate this interval, we focus on the last D recorded EEG overlapping epochs $\{X_j \in \mathbb{R}^{FC\times w}\}_{j\in\mathcal{J}(d)}$, with the set of indices $\mathcal{J}(d) = d-D+1,\ldots,d-1,d$; where d is the index of the current epoch X_d in the online recording $\chi(n)$. Epochs have size w, and the interval between two consecutive epochs is Δn, with $w > \Delta n$:

$$X_d = \chi(n-w,\ldots,n). \tag{10}$$

To obtain the first D epochs $X_{j\in\mathcal{J}(d)}$, at least $w+(D-1)\Delta n$ samples of χ should be recorded (step 4).

The classification outputs $k^*_{j\in\mathcal{J}(d)}$ obtained in step 3 by applying Algorithm 2 on $X_{j\in\mathcal{J}(d)}$ are stored in a vector $\mathcal{K}$, which always contains the latest D classification outputs. The class that occurs the most in $\mathcal{K}$ (step 5), with an occurrence probability $\rho(k)$ above a defined threshold ϑ, is considered to be the class, denoted $\overline{k}$, of the ongoing EEG recording $\chi(n)$. The vector ρ is defined as:

$$\rho(k) = \frac{\#\{k^*_{j\in\mathcal{J}(d)} = k\}}{D}, \quad \text{for } k = 1,\ldots,K, \tag{11}$$

with $\overline{k} = \arg\max_k \rho(k)$; then $\rho(\overline{k})$ is compared to the threshold ϑ. If ϑ is not reached within the last D epochs, the classification output is held back, and the sliding process continues until ϑ is reached. In the last D epochs, once a class $\overline{k}$ has been identified, a curve direction criterion is introduced to enforce the robustness of the result. For class $\overline{k}$ to be validated, this criterion requires that the direction taken by the displacement of covariance matrices

$\hat{\Sigma}_{j\in\mathcal{J}(d)}$ be toward the center of class $\Sigma_\mu^{(\bar{k})}$. Hence $\tilde{\delta}_{\bar{k}}$, the sum of gradients (i.e. differentials) of the curve made by distances from $\hat{\Sigma}_{j\in\mathcal{J}(d)}$ to $\Sigma_\mu^{(\bar{k})}$ should be negative (step 8):

$$\tilde{\delta}_{\bar{k}} = \sum_{j\in\mathcal{J}(d)} \frac{\Delta\delta_{\bar{k}}(j)}{\Delta j} = \sum_{j=d-D+2}^{d} \delta_{\bar{k}}(j) - \delta_{\bar{k}}(j-1) < 0 \quad \text{with}$$

$$\delta_{\bar{k}}(j) = \frac{\delta(\hat{\Sigma}_j, \Sigma_\mu^{(\bar{k})})}{\sum_{k=1}^{K} \delta(\hat{\Sigma}_j, \Sigma_\mu^{(k)})}. \tag{12}$$

The occurrence criterion is inspired by the dynamic stopping of [31]; there is no fixed trial length for classification. The occurrence criterion ensures that the detected user intention is unaffected by any short time disturbances due to noise or subject's inattention, as presented in Algorithm 3. This approach offers a good compromise to obtain robust results within a short and flexible time.

The curve direction criterion solves both the problems of latency in the EEG synchronization and of the delays inserted by the EEG epochs processing. Indeed, some EEG epochs gather signals from different classes and might be wrongfully classified if the decision is solely based on the distance with the center of the class. This situation and the effect of the curve direction criterion are well shown in Section 5.4. Ensuring that the covariance matrices are displaced toward the center of the detected class provides a guarantee that it matches with the current EEG state. Inversely, if the direction of the curve is moving away from the center of the detected class, it might indicate that there has been a change in the EEG state that has not been detected.

Algorithm 3 has 4 hyperparameters: $w, \Delta n, D$, and ϑ. The values of w, D, and ϑ are set through cross validation and are given in Section 5.4. Although a large window size w is expected to increase the classification accuracy, it increases the response time, thus reducing the time resolution, and extends the overlap between different EEG states. The step size Δn should be set to a minimum value to allow a maximum number of overlapping epochs (D) within a short time. However, it should be large enough to avoid too many calculations within a time interval with small or inexistent changes in EEG states. If the number of epoch D is too small, the classification will be sensitive to non-intentional and abrupt changes in the EEG. A too large D will increase the momentum and reinforce the influence of the past EEG signals. It should also be mentioned that both the occurrence and the curve direction criteria cannot have a significant impact if the value of D is too small. The probability threshold parameter ϑ acts like a rejection parameter: high ϑ values correspond to a high rejection rate.

4.3. Outliers removal with Riemannian potato

Outliers in the training data might affect the Riemannian mean of classes in the MDRM classification scheme. To alleviate this effect, an approach called the Riemannian potato, introduced in [56], is exploited. In this approach, all trials are represented by their covariance matrices Σ_i. A reference covariance matrix is estimated, e.g. Riemannian mean of all trials Σ_μ. The Riemannian distances δ_i between each Σ_i and Σ_μ are computed. Any trial that lies too far, i.e. beyond a certain threshold, from the reference matrix Σ_μ in terms of Riemannian distance is rejected. In [56], the distance z-score thresholding is defined as:

$$z(\delta_i) = \frac{\delta_i - \mu}{\sigma} > z_{th} \tag{13}$$

where μ and σ are respectively the mean and standard deviation of distances $\{\delta_i\}_{i=1}^{I}$. In other words, any trial Σ_i whose z-score $z(\delta_i)$ is larger than the threshold $z_{th} = 2.5$ is rejected.

In this work, we propose a slightly different application of the Riemannian potato where the outliers are removed per class. Hence for K class, K Riemannian potatoes are defined $\left\{\Sigma_\mu^k, \mu^k, \sigma^k\right\}_{k=1}^{K}$. Since Riemannian distances to geometric mean do not have a Gaussian distribution, we make use of the geometric mean for μ, the geometric standard deviation for σ and the geometric z-score. They are defined as follows [72]:

$$\mu^k = \exp\left(\frac{1}{I}\sum_i \ln(\delta_i^k)\right)$$

$$\sigma^k = \exp\left(\sqrt{\frac{1}{I}\sum_i \left(\ln\left(\delta_i^k/\mu^k\right)\right)^2}\right)$$

$$z(\delta_i^k) = \frac{\ln\left(\delta_i^k/\mu^k\right)}{\ln(\sigma^k)}. \tag{14}$$

Through cross-validation, the z-score threshold is set to $z_{th} = 2.2$.

Moreover, outliers are removed iteratively. Each time outliers are rejected, a new center of class is computed and used as reference for the next iteration. Iterations continue until convergence, i.e. no more outlier found.

5. Experimental validation

Covariance matrix estimators, Algorithms 2 and 3 are applied to SSVEP signals for offline and online analysis. This section presents the analysis and results obtained.

5.1. Data description

The signals are recorded from 12 subjects during an SSVEP experiment. EEG are measured on $C = 8$ channels: O_Z, O_1, O_2, PO_Z, PO_3, PO_4, PO_7, and PO_8. The ground and the reference electrodes were placed respectively on F_Z and the right hear mastoid respectively. The acquisition rate is $T_s = 256$ Hz on a gTec MobiLab Amp (gTec, Graz, Austria). The subjects are presented with $F = 3$ visual target stimuli blinking respectively at freq = 13 Hz, 17 Hz and 21 Hz. It is a $K = 4$ classes BCI setup made of the $F = 3$ stimulus classes and one resting class (no-SSVEP). In a session, which lasts 5 min, 32 trials are recorded: 8 for each visual stimulus and 8 for the resting class. The number of sessions recorded per subject varies from 2 to 5. Thus the longest EEG recorded for a single subject is 25 min or 160 trials. The trial length is 6 s, that is $N = 6 \times T_s = 1536$ samples. Since data are rearranged as detailed in (9), trials $X \in \mathbb{R}^{FC\times N}$, where $FC = 24$ corresponding to 8 channel times 3 stimulus frequencies. For each subject, a test set is made of 32 trials whereas the remaining trials (which might vary from 32 to 128) make up for the training set.

5.2. Covariance estimators comparison

In this section, the effectiveness of covariance matrix estimators is evaluated for SSVEP signals. The evaluation is done in terms of classification accuracy and integrated discrimination improvement (IDI), obtained by each estimator (see Section 3.2) with respect to SCM estimator while using the offline MDRM classifier. The different conditioning of covariance matrices are also investigated.

A bootstrapping with 1000 replications is performed to assess the performances of each estimator. Estimators are compared on 10 trial lengths $t \in \{0.5, 1.0, \ldots, 5.0\}$ s, as these are known to affect the estimators performance. Here $N \in \{128, 256, \ldots, 1280\}$ is computed as $N = t \times T_s$.

Fig. 1 shows the classification accuracies of each estimator computed across all subjects. Even if the error bars show an

important inter-subject variability, the increase in the accuracy can be attributed to the fact that the relevant patterns in EEG accumulate with the trial length, producing better estimation of the covariance matrices. This is known to be particularly true for the SCM estimator and it could be seen in Fig. 1. It appears that shrinkage estimators (especially Ledoit and Schäfer) are less affected by the reduction of epoch sizes than the other estimators. This is a direct consequence of the regularization between the sample covariance matrices and the targeted (expected) covariance matrix of independent variables.

For computational purposes, it is important to look at the matrix conditioning. Fig. 2 shows the ratio $\mathcal{C}$ between the largest and smallest eigenvalues: in well-conditioned matrices, $\mathcal{C}$ is small. Shrinkage estimators offer better conditioned matrices whereas the SCM, NSCM, and Fixed Point matrices are ill-conditioned below 2 s of trial length, and may result in singular matrices.

In Fig. 2b, the Integrated Discrimination Improvement (IDI), as defined in [73], is computed for the different estimators and trial lengths. The SCM is used as a reference for improvement, as this is the most popular estimator in the literature. Negative IDI means a deterioration in the method discrimination ability. It is clear that shrinkage estimators increase the discrimination power of the classifier. However, despite being more complex than the SCM, the

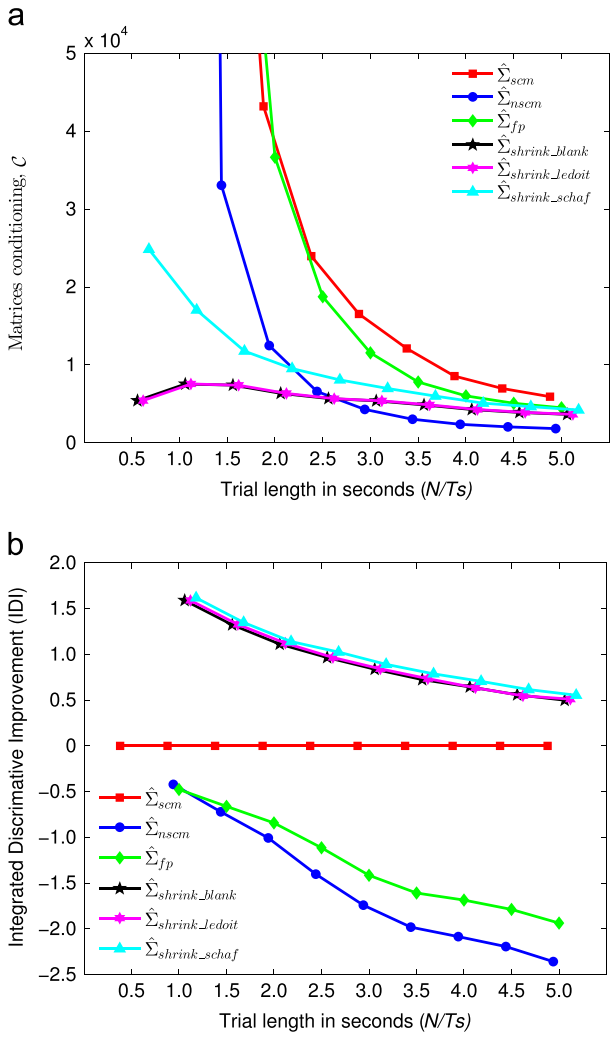

Fig. 2. (a) Covariance matrices condition expressed as the ratio $\mathcal{C}$ between largest and smallest eigenvalues for the different covariance estimators. The comparison is done for increasing EEG trial length. (b) Integrated discrimination improvement brought to the classification task by various estimators along varying trail length. The indicated IDI values are multiplied by 10^2. $\hat{\Sigma}_{\mathrm{scm}}$ is used as a baseline.

NSCM and the Fixed Point estimators decrease the discrimination ability of classifiers. From Figs. 1 and 2b, it is apparent that the difference in performance between the SCM and shrinkage estimators reduces as the trial length increases. The simplicity of the SCM plays a favorable role: it is an attractive method for longer trials. The p-values under the hypothesis that there is no improvement (i.e. IDI$=0$) from one estimator to another are all inferior to 10^{-47}, ($p<10^{-3}$ indicating a statistically significant discriminatory improvement); hence the improvement is significant. It should be noted that the estimation of covariance matrices is a trade-off between the quality of the estimate and the computation time required; this should be considered for real-time processing.

5.3. Effect of outliers on center estimations

Outliers can affect the offline training of the K centers of class $\Sigma_{\mu}^{(k)}$ by Algorithm 1, which is crucial for the evaluation phase and online application. Fig. 3 shows representations of training covariance matrices Σ_i in the tangent space (Θ_i), projected at the mean of all training trials, for the subjects with the lowest (Fig. 3a and b) and the highest (Fig. 3c and d) BCI performance. To obtain this visualization, the first two principal components of a PCA applied on $\{\Theta_i\}_{i=1}^{I}$ are selected. In Fig. 3b and d, the Riemannian potato presented in Section 4.3 is applied; outliers in each class are removed. The interest of using a Riemannian potato is well seen in Fig. 3a and b. In Fig. 3a, the outliers are so distant from the rest of the class matrices that the center of class is stretched away. Applying a Riemannian potato removes the outliers, and the center of class is better estimated (Fig. 3b).

When training trials are not noisy, their covariance matrices are compact around their Riemannian mean. In this case the removal of outliers by the Riemannian potato does not influence, at least not significantly, the Riemannian mean. This is the case in Fig. 3c and d. Thus, applying the Riemannian potato is crucial for noisy data and will have a limited effect on clean data. The impact of the Riemannian potato on the classification accuracy is discussed in Section 5.4.

5.4. Classification results and analysis

In this section, the performance of the proposed method is presented. First, the performance of the MDRM approach in an offline setup is analyzed, then the results of the online algorithm are presented. In the offline analysis, the relevance of identifying the latency between cue onset and SSVEP response is shown. The results of the MDRM approach are compared to two state-of-the-art methods [20,44]. The online evaluation is divided into two parts: in the first one the algorithm discriminates between $K=F=3$ SSVEP classes (i.e. 13, 17 and 21 Hz) and in the second one is applied on $K=4$ classes, i.e. the $F=3$ SSVEP class and the resting class.

5.4.1. Offline analysis

A close inspection of the filtered signals shows that almost all signals are synchronized with the trial frequency 2 s after cue onset $\tau_0=0$, as shown in Fig. 4. This delay is mainly due to protocol design and user specific cognitive processes. The protocol is aimed to provide an asynchronous setup close to real application. The user are not required to look at a fixation point or to directly gaze toward the target, as in [74,44], during inter-trial periods. This is a tentative explanation for the higher delay observed in our study and it is consistent with literature observations [75,76]. In fact, before τ_0+2 s, for some users the signal could still be synchronized with the previous trial frequencies. An important

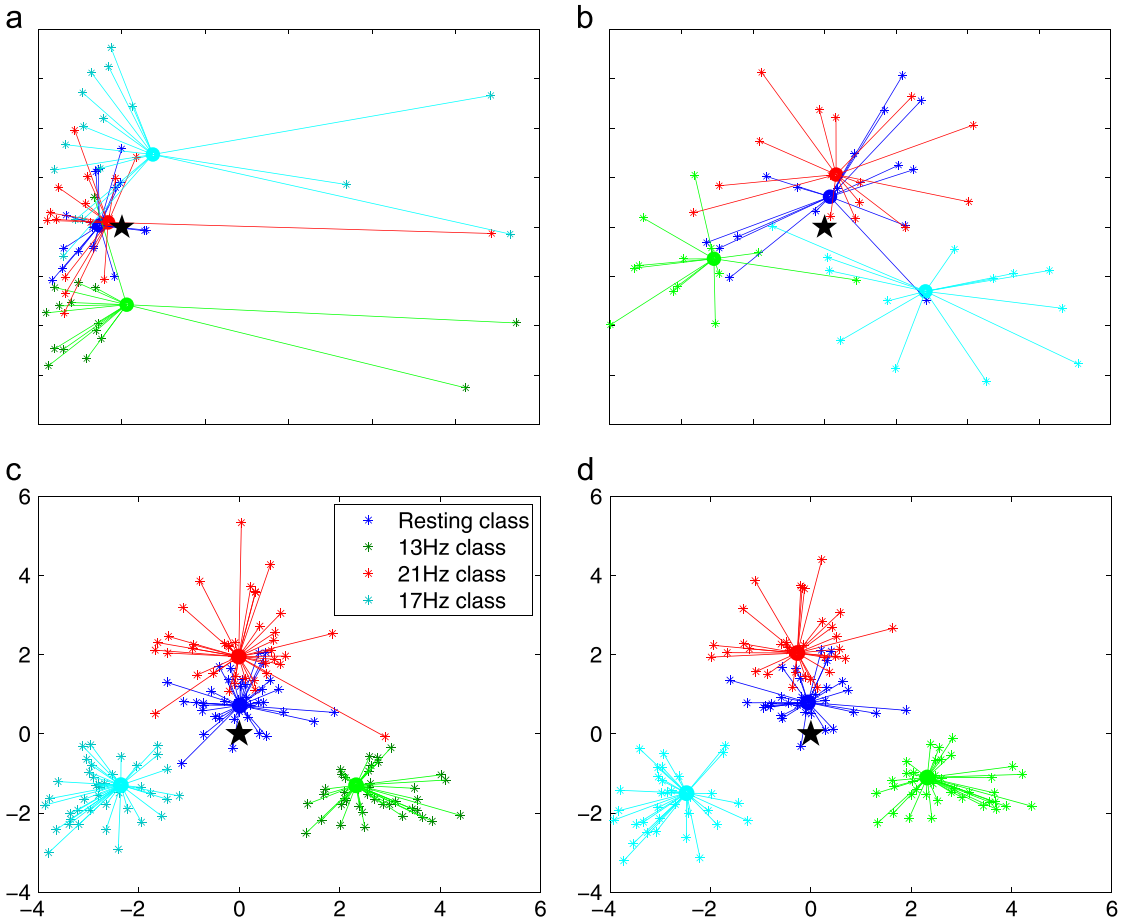

Fig. 3. Scatter plot of covariance matrices for all trials mapped on the tangent space. The distance between each trial covariance matrix Σ_i and its Riemannian mean class $\Sigma_\mu^{(k)}$ is shown as connection line. The black/thick star represents the Riemannian mean of all trials. Matrices of resting class, 13Hz class, 21Hz class, and 17Hz class are represented with starts in black, grey, dark grey, and light grey respectively. Subject with lowest BCI performance, (3a) before and (3b) after Riemannian potato filtering. Subject with highest BCI performance, (3c) before and (3d) after Riemannian potato filtering.

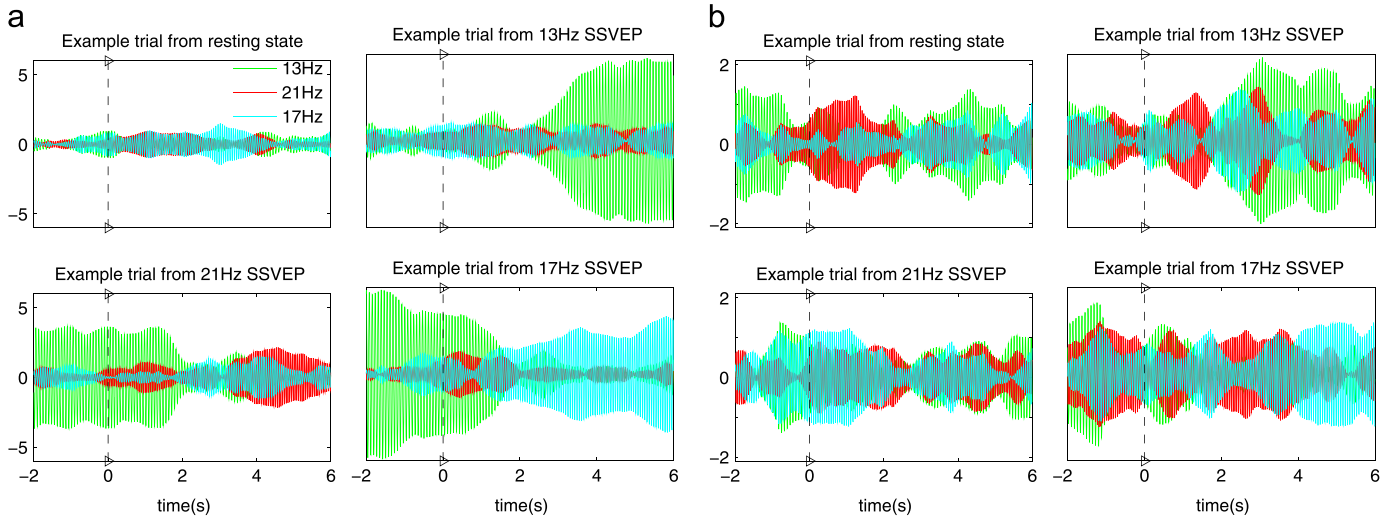

Fig. 4. Signal amplitude at each stimulus frequency, showing synchronization of EEG with respect to time (seconds). The raw signal of the trial measured on Oz is band filtered using a Butterworth of order 8 at each stimulus frequency and the resulting signals are shown in blue (light grey), green (grey), and red (dark grey) for the same signal filtered respectively at 13, 17, and 21 Hz. The cue onset τ_0 at time 0 on the x-axis is shown with a vertical discontinued line. 4 trials are shown, one for each class. Signals are from the subjects with the highest (4a) and with the lowest BCI performance (4b). (For interpretation of the references to color in this figure caption, the reader is referred to the web version of this paper.)

increase in average classification accuracy (almost 10%) could be obtained by taking the trial from 2 s after cue onset. It is therefore crucial to consider the latency between the cue onset of trial and the actual synchronization of SSVEP at stimulus frequency. Thus in the offline synchronous processing, the confident window for classification is set 2 s after the cue onset (τ_0+2).

Table 1 shows the offline classification accuracies for each subject obtained by the application of the *MDRM* as described in

Table 1
Offline performance in terms of accuracy and ITR. Five methods are compared: (1) CCA approach introduced by Lin et al. [20], (2) CCA approach introduced by Nakanishi et al. [44], (3) MDRM described in Section 4.1 (Algorithm 2), (4) MDRM where processed epochs are taken 2 s from the beginning of the trial, and (5) MDRM-Potato, where outliers are removed using the Riemannian potato approach described in Section 4.3.

	Offline algorithms									
	Lin et al. [20]		Nakanishi et al. [44]		MDRM (τ_0)		MDRM		MDRM-Potato	
	acc (%)	itr (bpm)	acc (%)	itr (bpm)	acc (%)	itr (bpm)	acc (%)	itr (bpm)	acc (%)	itr (bpm)
S1	91.7	16.3	84.7	12.2	67.6	3.5	84.7	12.2	84.5	12.1
S2	45.8	0.7	47.9	1.0	66.0	3.2	79.4	9.7	79.3	9.6
S3	100.0	23.8	93.0	17.2	90.2	10.3	99.3	22.7	99.3	22.7
S4	97.9	21.3	96.6	20.0	78.3	6.1	89.7	15.0	89.7	15.0
S5	83.3	11.5	82.2	11.0	76.0	5.5	89.5	14.9	89.4	14.9
S6	77.1	8.7	76.2	8.3	72.2	4.5	87.2	13.6	87.2	13.6
S7	98.6	22.0	96.7	20.1	90.0	10.2	99.8	23.5	99.8	23.4
S8	97.9	21.3	65.5	4.7	90.4	10.3	99.7	23.2	99.7	23.2
S9	91.7	16.3	77.9	9.0	64.0	2.8	85.8	12.8	85.7	12.7
S10	80.2	10.0	76.9	8.6	79.2	6.4	93.1	17.3	93.0	17.2
S11	89.6	15.0	82.7	11.2	54.8	1.4	78.2	9.2	78.2	9.1
S12	95.8	19.4	93.8	17.8	82.3	7.4	98.6	22.0	98.6	22.0
Mean	**87.5 ± 15.1**	**15.5 ± 6.8**	**81.2 ± 14.1**	**11.8 ± 6.0**	**75.9 ± 11.4**	**6.0 ± 3.1**	**90.4 ± 7.8**	**16.3 ± 5.3**	**90.4 ± 7.8**	**16.3 ± 5.3**

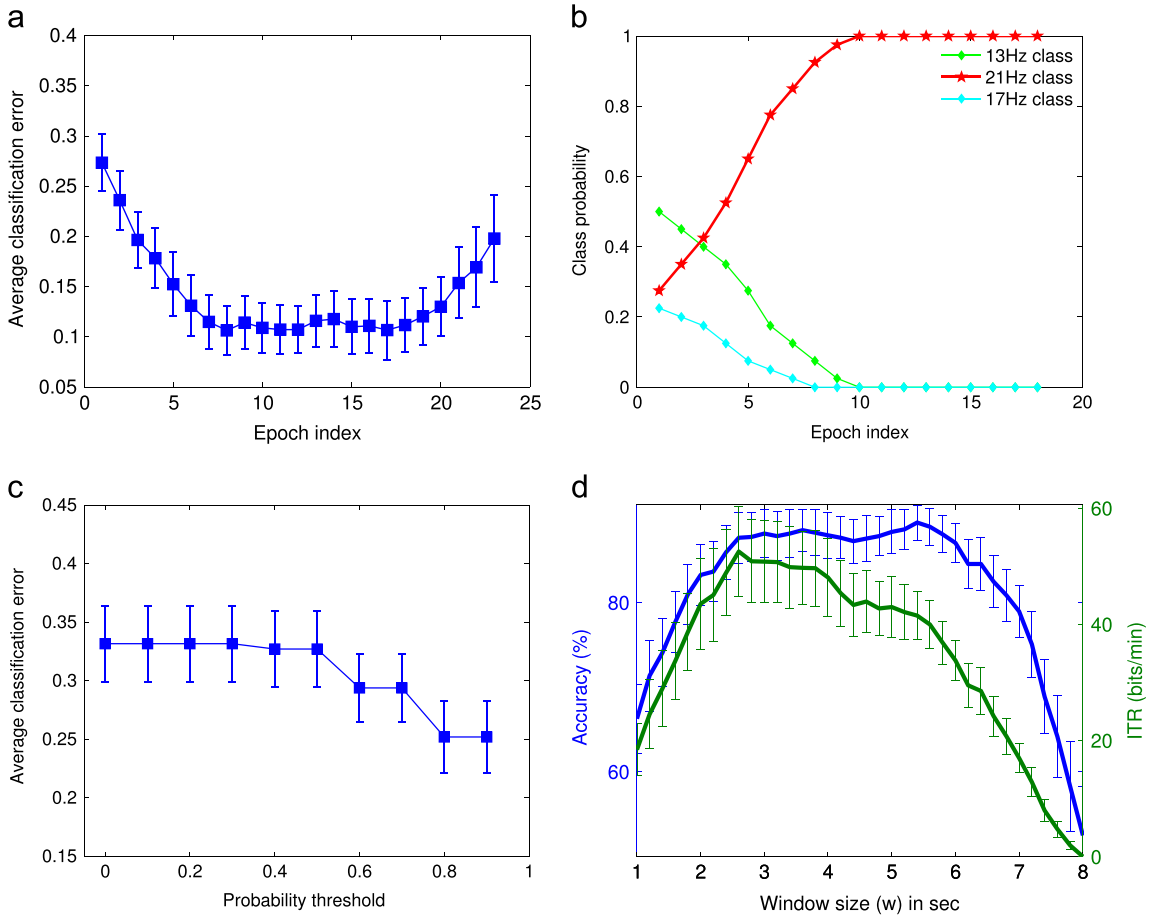

Fig. 5. Evaluation of the online algorithm parameters. 5a shows the decrease of the average classification error over all subjects during the successive epochs after the beginning of the trial. 5b is an example taken from the subject with the best performance showing how the probability of the actual class varies with epoch position from beginning of trial. The groundtruth class probability is represented with a thick-and-star line, while other classes probability lines are thin-and-diamond. 5c shows the variation of the average classification error for different probability threshold ($0 \leq \vartheta < 1$) and its influence on the classifier output (Algorithm 3 step 6). 5d shows how the average online performance varies with respect to the epoch size (w). It shows both the classification accuracy (left y-axis, black curve) and the ITR (right y-axis, grey curve). In 5a, 5c, and 5d, the bars represent the error of the mean i.e. standard deviation divided by the square root of $n-1$, n = number of samples.

Algorithm 2, with the epochs taken at τ_0+2. Column MDRM (τ_0) shows the results obtained when the epochs are taken from cue onset. The Riemannian potato technique presented in Section 4.3 was applied for outliers removal (*MDRM-Potato*). The performance of the MDRM approach is compared to two CCA-based state-of-the-art methods proposed by Lin et al. [20] and Nakanishi et al.

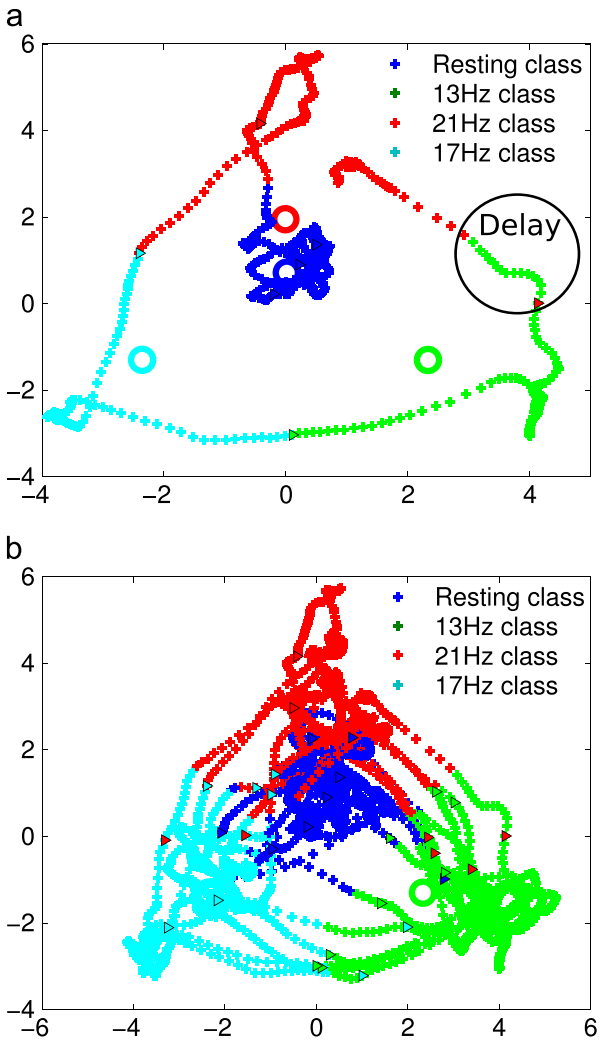

Fig. 6. Covariance matrices trajectory during a 4-class SSVEP online recording. The circles represent class centers. The triangles mark the beginning in the experiment of a new trial whose class is indicated by the triangle's color. Matrices of resting class, 13Hz class, 21Hz class, and 17Hz class are represented in black, grey, dark grey, and light grey respectively. 6a shows the first 7 trials. The first 3 trials are from the resting class, the remaining are respectively class 13 Hz, 17 Hz, and 21 Hz. 6b shows the entire recording. Data are taken from the subject with the highest BCI performance.

[44] respectively. In the implementation of these methods, the epochs are also taken from τ_0+2.

The MDRM approach outperforms both CCA-based method with an average classification accuracy of $90.4 \pm 7.8\%$ and ITR of 16.3 ± 5.3 bits/min. Lin et al. rank second with $87.5 \pm 15.1\%$ and 15.5 ± 6.8 bits/min. The method proposed by Nakanishi et al., which could be expected to achieve better results as reported in [44], only ranks third. This is mainly due to the fact that this method requires information on the phase of the stimuli. In fact, Nakanishi et al. use the average of all training trials belonging to a unique class as reference signal in the CCA. When SSVEP trials belonging to a unique trial are not in-phase, which is the case in the current work, averaging them will cancel the signal.

Within the MDRM approach, it is shown that taking into account the latency between the cue onset and the SSVEP response significantly increases the classification performances: accuracy and ITR rises from $75.9 \pm 11.4\%$ and 6.0 ± 3.1 bits/min to $90.4 \pm 7.8\%$ and 16.3 ± 5.3 bits/min. In turn removing outliers with the Riemannian potato does not bring significant change. This could be attributed to the fact that the recording have been conducted in controlled environment, with small or little external noise.

5.4.2. *Online analysis without resting class*

In an online asynchronous experiment, there is no cue onset, and the delay before SSVEP synchronization might differ from one trial to another and from one subject to another. To locate the trust EEG region for the classification, D and ϑ are set respectively to 5 and 0.7 through cross-validation. The performance of this online setup are analyzed and Fig. 5 shows the results. From the analysis shown in Fig. 5d, the epoch size is set to $w = 2.6$ s. The step size is set to $\Delta n = 0.2$ s, that is a new epoch is classified every 0.2 s.

In Fig. 5a, the classification error is plotted against the epoch index. It shows that the error decreases as epochs move from the beginning of the trial. The error increases in the last epochs of the trial, corresponding to the end of the SSVEP task. Fig. 5b details the evolution of the probability for each class as epochs index increases. It appears clearly that the class of the EEG trial (thick-and-star line) has the largest probability only a few epochs after the beginning of the trial. Moreover, one can see that this is an increasing trend over the whole trial. Thus by setting an appropriate probability threshold ϑ, the actual class can be identified with enough confidence. Fig. 5c shows the influence of the probability threshold ϑ on the classification error. The error is reduced when the probability threshold ϑ is increased. Fig. 5d shows how

Table 2
Classification performances (accuracy in %, delay before valid and confident classification in seconds, and ITR in bits/min) achieved using the online algorithm. The first column indicates the subjects. The following three columns show the results obtained without the curve direction criterion (Algorithm 3 up to 6): by stopping at step 6, $\bar{k}$ is taken to be the valid class. The next three columns contain the results of the complete online algorithm. The last three columns report the results obtain when outliers are removed in the training phase using the Riemannian potato technique described in Section 4.3.

	Online ($\rho(\bar{k}) > \vartheta$)			Online (full Algorithm 3)			Online-Potato		
	acc (%)	delay (s)	itr (bpm)	acc (%)	delay (s)	itr (bpm)	acc (%)	delay (s)	itr (bpm)
S1	68.8	0.8	26.3	77.1	1.1	27.9	77.1	1.1	27.9
S2	64.6	0.7	21.6	77.1	1.2	26.8	77.1	1.2	26.8
S3	81.2	0.7	54.3	95.8	1.0	73.0	95.8	1.0	73.0
S4	83.3	0.8	53.2	91.7	1.0	58.6	95.8	1.0	69.2
S5	72.9	0.7	37.1	83.3	1.0	42.5	83.3	1.0	42.5
S6	66.7	0.7	24.5	72.9	1.1	24.3	72.9	1.1	24.3
S7	93.1	0.7	89.6	98.6	0.9	87.0	98.6	0.9	86.8
S8	87.5	0.6	76.2	100.0	0.9	95.9	100.0	0.9	95.9
S9	60.4	0.7	15.7	77.1	1.2	27.6	77.1	1.2	27.6
S10	64.6	0.7	21.5	87.5	1.1	45.3	87.5	1.1	45.3
S11	54.2	0.7	9.9	87.5	1.3	38.9	87.5	1.3	38.9
S12	52.5	0.7	8.0	99.2	1.2	71.7	99.2	1.2	71.8
Mean	**70.8 ± 13**	**0.7 ± 0.0**	**36.5 ± 26.3**	**87.3 ± 9.8**	**1.1 ± 0.1**	**51.6 ± 25.1**	**87.7 ± 10**	**1.1 ± 0.1**	**52.5 ± 25.5**

Table 3
This table summarizes the performance achieved with the online algorithm with resting class identification, as in Table 2.

	Online ($\rho(\overline{k}) > \vartheta$)			Online (full Algorithm3)			Online-Potato		
	acc (%)	delay (s)	itr (bpm)	acc (%)	delay (s)	itr (bpm)	acc (%)	delay (s)	itr (bpm)
S1	67.2	0.7	37.6	71.4	1.1	32.4	71.4	1.1	32.4
S2	78.1	0.7	59.0	75.0	1.0	39.2	75.0	1.0	39.2
S3	89.1	0.8	85.2	89.1	1.0	67.6	89.1	1.0	67.6
S4	75.0	0.7	52.2	75.0	0.9	42.9	75.0	0.9	43.4
S5	71.9	0.7	46.7	70.3	1.1	31.0	70.3	1.1	31.0
S6	87.5	0.8	80.2	87.3	1.1	58.7	87.3	1.1	58.7
S7	84.4	0.7	76.3	85.4	1.0	62.5	88.5	1.0	69.1
S8	85.9	0.8	76.4	89.1	1.0	68.1	89.1	1.0	68.1
S9	67.2	0.7	37.2	75.0	1.0	39.6	76.6	1.1	40.3
S10	62.5	0.7	30.3	69.5	1.0	32.0	69.5	1.0	32.0
S11	59.4	0.8	23.5	68.8	1.1	29.1	68.8	1.1	29.1
S12	69.4	0.7	44.8	93.8	1.0	79.4	93.8	1.0	79.9
Mean	**74.8** $\pm$ **10.2**	**0.7** $\pm$ **0.0**	**54.1** $\pm$ **21.0**	**79.1** $\pm$ **9.1**	**1.0** $\pm$ **0.1**	**48.6** $\pm$ **17.6**	**79.5** $\pm$ **9.3**	**1.0** $\pm$ **0.1**	**49.2** $\pm$ **18.2**

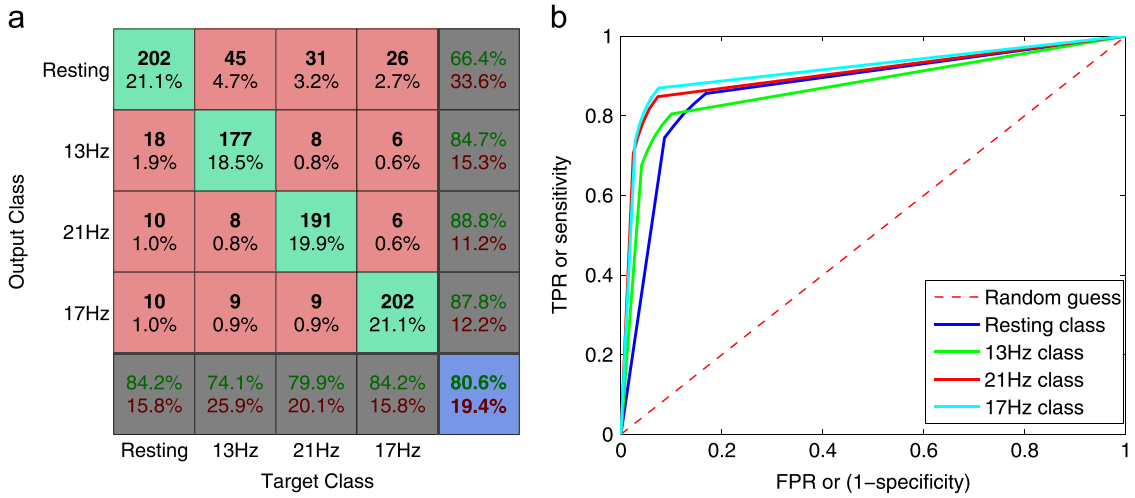

Fig. 7. (a) Confusion matrix for K=4 classes with Online-Potato. (b): ROC curve indicating the influence of the ϑ parameter.

the average online performance varies with respect to the epoch size (w). Both the classification accuracy and the ITR are shown. With short w values, the epoch size does not capture enough feature for a correct classification, and with long w, the epoch loses temporal resolution. The ITR increases with the classification rate but drops sensibly after a peak value.

The observation of Fig. 6 provides a visualization of the principle guiding the online implementation of Eq. (12). This figure shows the trajectory on the tangent space taken by covariance matrices during a 4-class SSVEP experiment, and how they are classified epoch by epoch. It can be seen (encircled in Fig. 6a) that a change in the SSVEP stimulus might not be detected instantaneously by the classifier. The trials are erroneously attributed with confidence to the previous class. The proposed online algorithm, described in Algorithm 3, mitigates this issue and increases the classification accuracy as shown in Table 2. The "Online ($\rho(\overline{k}) > \vartheta$)" column shows the results of the online algorithm without the curve direction criterion (i.e., without steps 6–11), and "Online (full Algorithm 3)" shows the improvement brought by this criterion. The performances are in terms of average classification accuracy (acc (%)), average time taken into the trial before classification (delay (s)), and the ITR (itr (bits/min)).

The curve direction criterion increases the rejection of epochs that could be wrongly classified, it thus significantly increases the classification accuracy of the online algorithm (70.8 $\pm$ 13% to 87.3 $\pm$ 9.8%), while increasing the delay (0.7–1.1 s) before classification. When compared to the state-of-the-art offline MDRM, the online curve-based classification yields better results in terms of ITR as the delay before classification is much shorter in the latter than the trial length used in the former; classification outputs are reached faster with the online algorithm. Moreover, the online algorithm can be applied in both synchronous and asynchronous paradigms, whereas the offline algorithms are limited to synchronous paradigms which provide strongly limited user interaction.

Last, the impact of the Riemannian potato is analyzed. A bootstrapping with 50 replications was performed on the offline data to assess the effect of applying the Riemannian potato. The results show that for most subjects the results are unchanged when the Riemannian potato is applied: due to the fact that data are recorded in a controlled environment, most of them are thus clean. It does however improve the results of few subjects. It was then applied in the training phase of the online application, and a similar observation is made. We can conclude that the Riemannian potato can be used as a safety guard to ensure that the Riemannian mean used in the MDRM classification scheme is not affected by outliers, especially for BCI used in less controlled environment.

5.4.3. *Online analysis with resting class*

Using the MDRM approach it is possible to identify the resting class. In fact, covariance matrices of signal recorded during resting periods can be characterized with their own Riemannian mean. As such, they can be identified as any other class using the MDRM

approach. The state-of-the-art methods, Lin et al. [20] and Nakanishi et al. [44], are both based on CCA where a reference signal is needed. These methods do not handle resting class, since there is no reference signal for them. In this section, the performance of the proposed approach including the identification of the resting class is presented. Table 3 summarizes the classifier performance in the same format as Table 2, in terms of classification accuracy, delay before valid classification and ITR. Like in Table 2, the best performance is achieved by the complete online algorithm preceded with outliers removal with the Riemannian potatoes (i.e. *Online-Potato*). The identification of the resting class induces a drop of the overall classification accuracy by 8.2%, and a drop of ITR from 52.5 ± 25.5 to 49.2 ± 18.2.

The effect of the resting class is seen with more details in Fig. 7. Fig. 7a shows the classification confusion matrix. There are few misclassifications between SSVEP classes compared to the misclassifications between the resting class and any SSVEP class: the largest percentages are located in the first row and the first column, apart from the diagonal block. Fig. 7b displays a ROC curve showing how the classifier performs in discriminating each class versus the others depending on the value of the ϑ parameter. On this ROC curve, the performance of the *Online−Potato* algorithm are indicated in terms of False Positive Rate (FPR) and True Positive Rate (TPR).

Confirming the observation from the confusion matrix, the ROC curve indicates that the resting is the most prone to false positive. Despite the drop in performance, the identification of resting class is crucial for online BCI setup, allowing the subject to use the system at his own pace.

6. Conclusion

This work investigated the efficiency of Riemannian geometry when dealing with covariance matrices as classification features. A novel algorithm based on MDRM, enhanced by class probability and the curve direction in the space of covariance EEG signals, was introduced and applied on an SSVEP classification task for a 4-class brain computer interface. Existing covariance matrix estimators were investigated and their robustness was assessed on multichannel SSVEP signals to ensure that the obtained matrices are accurate estimates of data covariance, are well conditioned, and verify the positive-definiteness property. The Schäfer shrinkage estimator was found to be the best as it yielded the highest classification accuracy with the MDRM algorithm.

The MDRM approach is first analyzed in a offline classification setup. To prevent the effect of noisy signals on the MDRM approach, outliers in the training set of are removed using a modified version of the *Riemannian potato*. This approach is compared to two CCA-based state-of-the-art methods. The results show that offline MDRM achieves better classification performances than any of the CCA-based methods.

In the online setup, the proposed online algorithm enhances the stability of the BCI system, balancing between classification speed and prediction accuracy. The evaluation of the classification confidence over several epochs mitigates the short term perturbations in the experimental conditions and the attentional variations of the subject. The curve direction overcomes the misclassification of EEG trials that are still synchronized with past stimuli frequencies at classification time.

Unlike the CCA-based state-of-the-art methods considered in this work, the proposed online algorithm is capable of identifying the resting periods during an online EEG recording. These resting periods are considered as an additional class in the classification task.

All these contributions help to pave the way towards BCI used in non-controlled, assistive environment.

Acknowledgement

The authors would like to thank Louis Mayaud from Mensia Technologies for his contribution in discussions that led to the completion of this work.

References

[1] J.R. Wolpaw, N. Birbaumer, D.J. McFarland, G. Pfurtscheller, T.M. Vaughan, Brain–computer interfaces for communication and control, Clin. Neurophysiol. 113 (6) (2002) 767–791.
[2] J.J. Vidal, Toward direct brain–computer communication, Annu. Rev. Biophys. Bioeng. 2 (1) (1973) 157–180.
[3] J.D. Bayliss, D.H. Ballard, Single trial P3 epoch recognition in a virtual environment, Neurocomputing 32–33 (2000) 637–642.
[4] W. Tu, S. Sun, A subject transfer framework for EEG classification, Neurocomputing 82 (2012) 109–116.
[5] E. Niedermeyer, F. Lopes da Silva, Electroencephalography: Basic Principles, Clinical Applications, and Related Fields, 5th Ed., Lippincott Williams & Wilkins, 2004.
[6] B. Blankertz, K.-R.R. Müller, G. Curio, T.M. Vaughan, G. Schalk, J.R. Wolpaw, A. Schlögl, C. Neuper, G. Pfurtscheller, T. Hinterberger, M. Schröder, N. Birbaumer, The BCI competition 2003: progress and perspectives in detection and discrimination of EEG single trials, IEEE Trans. Biomed. Eng. 51 (6) (2004) 1044–1051.
[7] B. Blankertz, K.R. Muller, D.J. Krusienski, G. Schalk, J.R. Wolpaw, A. Schlogl, G. Pfurtscheller, J. Millan, M. Schroder, N. Birbaumer, The BCI competition III: validating alternative approaches to actual BCI problems, IEEE Trans. Neural Syst. Rehabil. Eng. 14 (2) (2006) 153–159.
[8] M. Tangermann, K.-R. Müller, A. Aertsen, N. Birbaumer, C. Braun, C. Brunner, R. Leeb, C. Mehring, K.J. Miller, G. Mueller-Putz, G. Nolte, G. Pfurtscheller, H. Preissl, G. Schalk, A. Schlögl, C. Vidaurre, S. Waldert, B. Blankertz, Review of the BCI Competition IV, Front. Neurosci. 6 (55). http://dx.doi.org/10.3389/fnins.2012.00055.
[9] T. Dickhaus, C. Sannelli, K.-R. Müller, G. Curio, B. Blankertz, Predicting BCI performance to study BCI illiteracy, BMC Neurosci. 10 (Suppl 1) (2009) 1–2.
[10] B.Z. Allison, C. Neuper, Could anyone use a BCI? in: D.S. Nijholt (Eds.), Brain–Computer Interfaces, Human–Computer Interaction Series, Springer, London, 2010, pp. 35–54 (Chapter 3).
[11] C. Vidaurre, B. Blankertz, Towards a cure for BCI illiteracy, Brain Topogr. 23 (2) (2010) 194–198.
[12] B. Obermaier, C. Guger, C. Neuper, G. Pfurtscheller, Hidden Markov models for online classification of single trial EEG data, Pattern Recognit. Lett. 22 (12) (2001) 1299–1309.
[13] A. Lenhardt, M. Kaper, H. Ritter, An adaptive P300-based online brain computer interface, IEEE Trans. Neural Syst. Rehabil. Eng. 16 (2) (2008) 121–130.
[14] L.F. Nicolas-Alonso, R. Corralejo, J. Gomez-Pilar, D. Álvarez, R. Hornero, Adaptive semi-supervised classification to reduce intersession non-stationarity in multiclass motor imagery-based brain–computer interfaces, Neurocomputing 2016. http://dx.doi.org/10.1016/j.neucom.2015.02.005.
[15] E. Kalunga, K. Djouani, Y. Hamam, S. Chevallier, E. Monacelli, SSVEP enhancement based on Canonical Correlation Analysis to improve bci performances, in: IEEE, Africon 2013, pp. 1–5.
[16] H. Lu, H.-L. Eng, C. Guan, K. Plataniotis, A. Venetsanopoulos, Regularized common spatial pattern with aggregation for EEG classification in small-sample setting, IEEE Trans. Biomed. Eng. 57 (12) (2010) 2936–2946.
[17] B. Blankertz, R. Tomioka, S. Lemm, M. Kawanabe, K.R. Muller, Optimizing spatial filters for robust EEG single-trial analysis, IEEE Signal Process. Mag. 25 (1) (2008) 41–56.
[18] F. Lotte, C. Guan, Regularizing common spatial patterns to improve BCI designs: unified theory and new algorithms, IEEE Trans. Biomed. Eng. 58 (2) (2011) 355–362.
[19] Y. Yang, S. Chevallier, J. Wiart, I. Bloch, Automatic selection of the number of spatial filters for motor-imagery BCI, in: European Symposium on Artificial Neural Networks (ESANN), 2012, pp. 109–114.
[20] Z. Lin, C. Zhang, W. Wu, X. Gao, Frequency recognition based on canonical correlation analysis for SSVEP-based BCIs, IEEE Trans. Biomed. Eng. 53 (12) (2006) 2610–2614.
[21] P.-A. Absil, R. Mahony, R. Sepulchre, Optimization Algorithms on Matrix Manifolds, Princeton University Press, Princeton, 2009.
[22] R. Bhatia, Positive Definite Matrices, Princeton University Press, Princeton, 2009.
[23] A. Barachant, S. Bonnet, M. Congedo, C. Jutten, Multiclass brain–computer interface classification by Riemannian geometry, IEEE Trans. Biomed. Eng. 59 (4) (2012) 920–928.
[24] A. Barachant, S. Bonnet, M. Congedo, C. Jutten, Classification of covariance matrices using a Riemannian-based kernel for BCI applications, Neurocomputing 112 (2013) 172–178.
[25] M. Congedo, A. Barachant, A. Andreev, A new generation of brain–computer interface based on Riemannian geometry, arXiv preprint arXiv:1310.8115.
[26] E.K. Kalunga, S. Chevallier, O. Rabreau, E. Monacelli, Hybrid interface: integrating BCI in multimodal human–machine interfaces, in: IEEE/ASME

International Conference on Advanced Intelligent Mechatronics (AIM), 2014, pp. 530–535.
[27] X. Gao, D. Xu, M. Cheng, S. Gao, A BCI-based environmental controller for the motion-disabled, IEEE Trans. Neural Syst. Rehabil. Eng. 11 (2) (2003) 137–140.
[28] G. Edlinger, C. Holzner, C. Guger, A hybrid Brain–Computer interface for smart home control, in: J.A. Jacko (Ed.), Human–Computer Interaction. Interaction Techniques and Environments, Lecture Notes in Computer Science, vol. 6762, Springer, Berlin, Heidelberg, 2011, pp. 417–426.
[29] R.C. Panicker, S. Puthusserypady, Y. Sun, Adaptation in P300 brain–computer interfaces: a two-classifier cotraining approach, IEEE Trans. Biomed. Eng. 57 (12) (2010) 2927–2935.
[30] F. Schettini, F. Aloise, P. Aricò, S. Salinari, D. Mattia, F. Cincotti, Self-calibration algorithm in an asynchronous P300-based brain–computer interface, J. Neural Eng. 11 (3) (2014) 035004.
[31] H. Verschore, P.-J. Kindermans, D. Verstraeten, B. Schrauwen, Dynamic stopping improves the speed and accuracy of a P300 speller, in: Artificial Neural Networks and Machine Learning–ICANN 2012, Toronto, Canada, Springer, 2012, pp. 661–668.
[32] D. Regan, Comparison of transient and steady-state methods, Ann. N.Y. Acad. Sci. 388 (1) (1982) 45–71.
[33] T. Takahashi, K.H. Chiappa, Activation methods, Electroencephalography. in: Basic Principles, Clinical Applications, and Related Fields, 5th ed., Lippincott Williams & Wilkins, 2004, pp. 241–262.
[34] E. Niedermeyer, F.L. da Silva, Electroencephalography: Basic Principles, Clinical Applications, and Related Fields, 5th ed., 2004.
[35] J. Wolpaw, N. Birbaumer, D.J. McFarland, G. Pfurtscheller, T.M. Vaughan, Brain–computer interfaces for communication and control, Clin. Neurophysiol. 113 (6) (2002) 767–791.
[36] S.T. Morgan, J.C. Hansen, S.A. Hillyard, Selective attention to stimulus location modulates the steady-state visual evoked potential, Proc. Natl. Acad. Sci. USA 93 (10) (1996) 4770–4774.
[37] M.M. Müller, S. Andersen, N.J. Trujillo, P. Valdés-Sosa, P. Malinowski, S.A. Hillyard, Feature-selective attention enhances color signals in early visual areas of the human brain, Proc. Natl. Acad. Sci. USA 103 (38) (2006) 14250–14254.
[38] B. Allison, T. Lüth, D. Valbuena, A. Teymourian, I. Volosyak, A. Gräser, BCI demographics: how many (and what kinds of) people can use an SSVEP BCI?, IEEE Trans. Neural Syst. Rehabil. Eng. 18 (2) (2010) 107–116.
[39] D. Zhu, J. Bieger, G.G. Molina, R.M. Aarts, A survey of stimulation methods used in SSVEP-based BCIs, Intell. Neurosci. (2010), http://dx.doi.org/10.1155/2010/702357.
[40] C.S. Herrmann, Human EEG responses to 1100 hz flicker: resonance phenomena in visual cortex and their potential correlation to cognitive phenomena, Exp. Brain Res. 137 (2001) 346–353.
[41] M.A. Pastor, J. Artieda, J. Arbizu, M. Valencia, J.C. Masdeu, Human cerebral activation during steady-state visual-evoked responses, J. Neurosci. 23 (37) (2003) 11621–11627.
[42] R.S. Fisher, G. Harding, G. Erba, G.L. Barkley, A. Wilkins, Photic- and pattern-induced seizures: a review for the epilepsy foundation of america working group, Epilepsia 46 (9) (2005) 1426–1441.
[43] J. Pan, X. Gao, F. Duan, Z. Yan, S. Gao, Enhancing the classification accuracy of steady-state visual evoked potential-based brain–computer interfaces using phase constrained canonical correlation analysis, J. Neural Eng. 8 (3) (2011) 036027. 〈http://iopscience.iop.org/article/10.1088/1741-2560/8/3/036027/meta〉.
[44] M. Nakanishi, Y. Wang, Y.-T. Wang, Y. Mitsukura, T.-P. Jung, A high-speed brain speller using steady-state visual evoked potentials, Int. J. Neural Syst. 24 (06) (2014) 1450019.
[45] M. Spüler, W. Rosenstiel, M. Bogdan, Online adaptation of a c-VEP brain–computer interface (BCI) based on error-related potentials and unsupervised learning, PLoS ONE 7 (12) (2012) e51077. 〈http://journals.plos.org/plosone/article?id=10.1371/journal.pone.0051077〉.
[46] G. Bin, X. Gao, Y. Wang, Y. Li, B. Hong, S. Gao, A high-speed BCI based on code modulation VEP, J. Neural Eng. 8 (2) (2011) 025015. 〈http://iopscience.iop.org/article/10.1088/1741-2560/8/2/025015/meta〉.
[47] H. Cecotti, A self-paced and calibration-less SSVEP-based brain–computer interface speller, IEEE Trans. Neural Syst. Rehabil. Eng. 18 (2) (2010) 127–133.
[48] S. Parini, L. Maggi, A.C. Turconi, G. Andreoni, A robust and self-paced BCI system based on a four class SSVEP paradigm: algorithms and protocols for a high-transfer-rate direct brain communication, Intell. Neurosci. (2009), http://dx.doi.org/10.1155/2009/864564.
[49] F. Yger, A review of kernels on covariance matrices for BCI applications, in: IEEE International Workshop on Machine Learning for Signal Processing (MLSP), 2013, pp. 1–6.
[50] S. Jayasumana, R. Hartley, M. Salzmann, H. Li, M. Harandi, Kernel methods on the Riemannian manifold of symmetric positive definite matrices, in: IEEE Conference on Computer Vision and Pattern Recognition (CVPR), 2013, pp. 73–80.
[51] Y. Xie, J. Ho, B. Vemuri, On a nonlinear generalization of sparse coding and dictionary learning, in: International Conference on Machine Learning (ICML), 2013, p. 1480.
[52] A. Goh, R. Vidal, Unsupervised Riemannian clustering of probability density functions, in: Machine Learning and Knowledge Discovery in Databases, Springer, 2008, pp. 377–392.
[53] A. Goh, R. Vidal, Clustering and dimensionality reduction on Riemannian manifolds, in: IEEE Conference on Computer Vision and Pattern Recognition (CVPR), 2008, pp. 1–7.
[54] X. Pennec, P. Fillard, N. Ayache, A Riemannian framework for tensor computing, Int. J. Comput. Vis. 66 (1) (2006) 41–66.
[55] A. Barachant, S. Bonnet, M. Congedo, C. Jutten, Riemannian geometry applied to BCI classification, in: Latent Variable Analysis and Signal Separation, Springer, 2010, pp. 629–636.
[56] A. Barachant, A. Andreev, M. Congedo, et al., The Riemannian potato: an automatic and adaptive artifact detection method for online experiments using Riemannian geometry, in: Proceedings of TOBI Workshop IV, 2013, pp. 19–20.
[57] S.-I. Amari, α-divergence is unique, belonging to both f-divergence and Bregman divergence classes, IEEE Trans. Inf. Theory 55 (11) (2009) 4925–4931.
[58] W. Samek, D. Blythe, K.-R. Müller, M. Kawanabe, Robust spatial filtering with beta divergence, in: Advances in NeuralInformation Processing Systems (NIPS), 2013, pp. 1007–1015.
[59] W. Samek, K.-R. Muller, Information geometry meets BCI spatial filtering using divergences, in: International Winter Workshop on Brain–Computer Interface, Seoul, Korea, IEEE, 2014, pp. 1–4.
[60] A. Barachant, S. Bonnet, Channel selection procedure using Riemannian distance for BCI applications, in: International IEEE/EMBS Conference on Neural Engineering (NER), 2011, pp. 348–351.
[61] A. Barachant, S. Bonnet, M. Congedo, C. Jutten, Common spatial pattern revisited by Riemannian geometry, in: IEEE International Workshop on Multimedia Signal Processing (MMSP), 2010, Saint Malo, France, pp. 472–476.
[62] Y. Li, K.M. Wong, H. De Bruin, EEG signal classification based on a Riemannian distance measure, in: Science and Technology for Humanity (TIC-STH), 2009 IEEE Toronto International Conference, IEEE, 2009, Toronto, Canada pp. 268–273.
[63] Y. Li, K. Wong, H. De Bruin, Electroencephalogram signals classification for sleepstate decision: a Riemannian geometry approach, IET Signal Process. 6 (4) (2012) 288–299.
[64] J. Jost, Riemannian Geometry and Geometric Analysis, vol. 62011, Springer, New-York, NY, USA, 2011.
[65] M. Moakher, A differential geometric approach to the geometric mean of symmetric positive-definite matrices, SIAM J. Matrix Anal. Appl. 26 (3) (2005) 735–747.
[66] P.T. Fletcher, C. Lu, S.M. Pizer, S. Joshi, Principal geodesic analysis for the study of nonlinear statistics of shape, IEEE Trans. Med. Imag. 23 (8) (2004) 995–1005.
[67] K. Fukunaga, Introduction to Statistical Pattern Recognition, Academic Press, San Diego, CA, USA, 1990.
[68] O. Ledoit, M. Wolf, A well-conditioned estimator for large-dimensional covariance matrices, J. Multivar. Anal. 88 (2) (2004) 365–411.
[69] B. Blankertz, S. Lemm, M. Treder, S. Haufe, K.-R. Müller, Single-trial analysis and classification of ERP components: a tutorial, NeuroImage 56 (2) (2011) 814–825.
[70] J. Schäfer, K. Strimmer, A shrinkage approach to large-scale covariance matrix estimation and implications for functional genomics, Stat. Appl. Genet. Mol. Biol. 4 (1). http://dx.doi.org/10.2202/1544-6115.1175.
[71] F. Pascal, P. Forster, J.P. Ovarlez, P. Arzabal, Theoretical analysis of an improved covariance matrix estimator in non-gaussian noise, in: IEEE International Conference on Acoustics, Speech, and Signal Processing (ICASSP), vol. 4, 2005.
[72] M. Congedo, EEG source analysis, Habilitation á diriger des recherches, Université de Grenoble, October 2013.
[73] M.J. Pencina, R.B. D'Agostino, R.S. Vasan, Evaluating the added predictive ability of a new marker: from area under the ROC curve to reclassification and beyond, Stat. Med. 27 (2) (2008) 157–172.
[74] Y. Kimura, T. Tanaka, H. Higashi, N. Morikawa, SSVEP-based brain–computer interfaces using FSK-modulated visual stimuli, IEEE Trans. Biomed. Eng. 60 (10) (2013) 2831–2838.
[75] F.-B. Vialatte, M. Maurice, J. Dauwels, A. Cichocki, Steady-state visually evoked potentials: focus on essential paradigms and future perspectives, Prog. Neurobiol. 90 (4) (2010) 418–438.
[76] H. Bakardjian, T. Tanaka, A. Cichocki, Optimization of SSVEP brain responses with application to eight-command brain–computer interface, Neurosci. Lett. 469 (1) (2010) 34–38.

Emmanuel K. Kalunga is a Ph.D. candidate, in his second year, in the joint doctorate program between the Tshwane University of Technology (South Africa) and Université de Versailles Saint-Quentin, France. On completion of his Baccalaureus Technologiae (Cum Laude) in 2010 at the Tshwane University, Emmanuel was awarded the Mandela Rhodes Scholarship and pursued a double Masters degree (Mtech/Msc) in Control, Image and Signal processing at the same university on the topic "Development of brain computer interface (BCI) based intention detection approach for persons with limited neuro-muscular control". He graduated Cum Laude in September 2013 after spending a year of internship at the Laboratoire d'ingénierie des systémes de Versailles (France). Since January 2014, Emmanuel is enrolled for his PhD on the topic of "Pattern recognition techniques for implicit brain computer interfaces", under the supervision of Karim Djouani, Eric Monacelli, Sylvain Chevallier, and Yskandar Hamam.

Sylvain Chevallier obtained his Ph.D. in computer science at the LIMSICNRS, with a speciality in cognitive science as he was interested in visual attention process for robotics. He spent 2 years in the neurocybernetic team of ETIS-CNRS where he worked on biologically inspired decision processes and visual perception. He joined afterwards INRIA Saclay to study deep neural network and brain computer interface. He pursued this post-doctoral research theme within Telecom ParisTech laboratory. In 2011, he was hired as an assistant professor in Université de Versailles to work on rehabilitation robotics. He is interested in neural communication and brain-like bioinspired methods for assistive technologies. He is focusing on brain–computer interfaces using shared control and passive approaches.

Quentin Barthélemy received the Engineering degree and the M.Res. in signal and images analysis and processing (with distinction) from Grenoble Institut National Polytechnique (Grenoble INP), France, both in 2009; and the Ph.D. degree in signal processing from Grenoble University and CEA-LIST (Alternative Energies and Atomic Energy Commission), France, in 2013. His Ph.D. dissertation deals with sparse representations for multivariate signals, including invariances as shift, rotation and affine transformation. He joined Mensia Technologies at the Institut du Cerveau et de la Moelle Epiniére, Paris, France, in 2013, to develop signal processing and machine learning methods for real-time EEG analysis. His research interests are sparse representation, time-frequency analysis, source separation and Riemannian geometry.

Karim Djouani is a professor, scientist and technical group supervisor of soft computing, telecommunication, networking systems and Robotics. Since January 2011 he is Full professor at University Paris Est-Creteil (UPEC), France and Tshwane University of Technology, Pretoria, South Africa. From July 2008 to December 2010, he was seconded by the French Ministry of Higher Education to the French South African Institute of Technology (F'SATI) at Tshwane University of Technology (TUT), Pretoria, South Africa. He was also national and European projects manager at the LISSI Lab.His current works focus on the development of novel and highly efficient algorithms for reasoning systems with uncertainty as well as optimization, for distributed systems, networked control systems, wireless ad-hoc network, wireless and mobile communication, and wireless sensors networks as well as Robotics. He has authored/co-authored over 150 articles in archival journals and conference proceedings as well as five chapters in edited books.

Eric Monacelli is an HDR Associate Professor at Versailles University (UVSQ), working in the LISV laboratory. He is working on the development of analysis methods and experimental devices adapted to the assistance of specific end users. His research projects incorporate issues of man–machine interface, robotics, assistive technologies and ambient intelligence systems.

Yskandar Hamam graduated as a Bachelor of the American University of Beirut (AUB) in 1966. He obtained his M.Sc. in 1970 and Ph.D. in 1972 from the University of Manchester Institute of Science and Technology. He also obtained his “Diplôme d'Habilitation á Diriger des Recherches” (equivalent to D.Sc.) from the “Université des Sciences et Technologies de Lille” in 1998. He conducted research activities and lectured in England, Brazil, Lebanon, Belgium and France. He was the head of the Control department and dean of faculty at ESIEE, France. He was an active member in modelling and simulation societies and was the president of EUROSIM. He was the Scientific Director of the French South African Institute of Technology (F'SATI) at TUT in South Africa from 2007 to 2012. He is currently professor at the Department of Electrical Engineering of TUT. He has authored/co-authored about 300 papers in archival journals and conference proceedings as well as book contributions. He is a senior member of the IEEE.

Biomedical Signal Processing and Control 38 (2017) 302–311

Contents lists available at ScienceDirect

Biomedical Signal Processing and Control

journal homepage: www.elsevier.com/locate/bspc

Subject-specific time-frequency selection for multi-class motor imagery-based BCIs using few Laplacian EEG channels☆

Yuan Yang[a,c,d,*], Sylvain Chevallier[b], Joe Wiart[a,c], Isabelle Bloch[a,c]

[a] LTCI, CNRS, Télécom ParisTech, Université Paris-Saclay, Paris, France
[b] Université de Versailles St-Quentin, Vélizy, France
[c] Whist Lab, Paris, France
[d] Department of Biomechanical Engineering, Delft University of Technology, Delft, The Netherlands

ARTICLE INFO

Article history:
Received 6 February 2017
Received in revised form 9 June 2017
Accepted 30 June 2017

Keywords:
FDA-type F-score
Time-frequency selection
Multi-class classification
Brain–computer interfaces
Motor imagery

ABSTRACT

The essential task of a motor imagery brain–computer interface (BCI) is to extract the motor imagery-related features from electroencephalogram (EEG) signals for classifying motor intentions. However, the optimal frequency band and time segment for extracting such features differ from subject to subject. In this work, we aim to improve the multi-class classification and to reduce the required EEG channel in motor imagery-based BCI by subject-specific time-frequency selection. Our method is based on a criterion namely Fisher discriminant analysis-type F-score to simultaneously select the optimal frequency band and time segment for multi-class classification. The proposed method uses only few Laplacian EEG channels (C3, Cz and C4) located around the sensorimotor area for classification. Applied to a standard multi-class BCI dataset (BCI competition III dataset IIIa), our method leads to better classification performance and smaller standard deviation across subjects compared to the state-of-art methods. Moreover, adding artifacts contaminated trials to the training dataset does not necessarily deteriorate our classification results, indicating that our method is tolerant to artifacts.

1. Introduction

Brain–computer interfaces measure specific brain activities (e.g. attention level, motor imagery) and then decode them to build a direct interaction between brains and computers [1]. Existing BCIs can be controlled by various types of signals from the brain, such as electroencephalography (EEG) and fMRI. As it is inexpensive, portable and non-invasive, EEG seems to be the most promising brain signals for BCI [2]. Numerous BCI systems has been proposed using EEG signals, such as P300 BCI [3,4], SSVEP BCI [5,6], motor imagery BCI [7] as well as hybrid BCI using more than one type of signal [8,9].

EEG oscillations at μ and β bands measured around sensorimotor cortex are known as sensorimotor rhythms and associated with body movements or motor imagery [10]. Motor imagery (MI)-based BCI is one typical EEG-based BCI, which predicts the subject's motor intentions through classifying sensorimotor rhythms. Several factors indicate that MI-based BCI is quite promising for motor rehabilitation [11] and general public applications. On the one hand, this type of BCI employs the signals from the sensorimotor cortex, which are directly linked to the motor output pathway in the brain. MI-based BCI realizes motor tasks without involving the spinal cord and the periphery, and therefore can be used to help patients with spinal cord injury [12] and lock-in syndrome [13]. On the other hand, MI-based BCI can be driven by voluntary brain activities without any cues from conditioning protocols, so that the control can be independent and self-paced [14]. This advantage makes MI-based BCI also suitable for virtual reality and neuro-games [15–17].

However, individual differences of sensorimotor rhythms (frequency bands, time windows) and poor signal-to-noise ratio (SNR) impair the inter-subject robustness of MI-based BCI. Although data driven spatial filtering algorithms, such as common spatial pattern (CSP) [18,19] and independent component analysis [20], can greatly improve the SNR of sensorimotor rhythms, they usually require a large number of EEG channels. Multi-channel EEG recording reduces the portability of daily use BCI and therefore constitutes a main drawback for end users [21,22].

☆ This paper is based on Yuan Yang's Ph.D. work in Télécom ParisTech. Yuan Yang has finished his PhD in Télécom ParisTech and been with Department of Biomechanical Engineering, Delft University of Technology, Delft, the Netherlands since November 2013.

* Corresponding author.
E-mail address: Y.Yang-2@tudelft.nl (Y. Yang).

http://dx.doi.org/10.1016/j.bspc.2017.06.016
1746-8094/

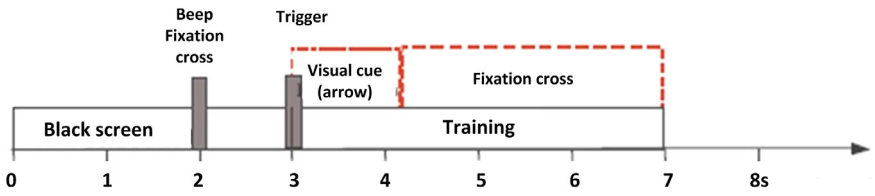

Fig. 1. Timing of the experimental paradigm for BCI competition III dataset IIIa [34].

Thus, many methods have been developed to reduce the number of channels in MI-based BCI by using machine learning techniques to select an optimal channel subset [21–27]. Due to individual differences between subjects, the estimated optimal subsets of channels usually vary with subjects. A high-density EEG recording may still be needed for finding an optimal subset for each individual. Hence, those methods did not really improve the portability and practicability of BCI. A few studies aimed to address this problem by using transfer learning frameworks to provide task-specific methods, so as to seek the channel subset that could be shared among all subjects for a particular MI task [28]. However, their classification performances are usually not as good as those obtained by subject-specific channel selection approaches. Moreover, task-specific methods are difficult to apply to the multi-class BCI, since the optimal channel subset is for a specific MI task (e.g. hand MI).

To address this challenge, we have proposed an alternative solution to increase inter-subject robustness of MI-based BCI using few EEG channels [29,30]. Instead of using machine learning techniques to select the optimal subset of channels, we simply used a few EEG channels located around the sensorimotor cortex. By selecting optimal time-frequency areas to extract subject-specific band power (BP) features, our preliminary study yielded better classification performances using fewer channels than the state-of-art methods in decoding hand MI [29,30]. Similar strategies have also been used in some other recent studies. For example, Yang and colleagues proposed a subject-based Fisher wavelet packet decomposition method using a few EEG channels to improve classification accuracy and inter-subject robustness of MI-based BCI [31]. Luo and colleagues developed a dynamic frequency feature selection method based on three bipolar channels for a similar purpose [32]. Liang and colleagues proposed a Hilbert-Huang transform based algorithm to extract the subject-specific time-frequency area for the hand MI discrimination based on two Laplacian channels [17]. All these studies focused on the two-class BCIs mainly for decoding the hand MI tasks, though multi-class BCIs can be more useful in daily applications. The optimal time-frequency areas for extracting the features could be different for different MI tasks. Increasing the number of classes will increase the inter-subject difference of optimal time-frequency areas as well as the dimensionality of features. All these eventually impair the inter-subject robustness.

In this work we focused on multi-class BCI to address this challenge. We proposed a novel method to select the optimal time-frequency areas for extracting subject-specific features, in order to improve the multi-class BCI performance using few EEG channels. The proposed method is based on a criterion called FDA-type F-score to simultaneously select both frequency band and time segment for extracting optimal BP features. FDA-type F-score is a simplified measure based on Fisher discriminant analysis (FDA) for measuring the discriminative power of a group of features. In our previous studies, we have successfully applied this criterion to seek the optimal channel subset for two-class BCIs [21] and to select the best kinematic feature group for two-class motor recognition [33]. Based on our preliminary work for two-class cases, here we extended the application of FDA-type F-score to multi-class cases using a one-versus-rest strategy. We evaluated our method in a standard multi-class BCI dataset (BCI competition III dataset IIIa [34]) to classify four classes of MI tasks (left hand, right hand, foot and tongue). This dataset has 60 channels EEG. Thus, it is suitable to test the effectiveness of our methods in improving multi-class classification when using a reduced number of EEG channels, and to compare with the state-of-the-art methods using full 60 channels or reduced channels. Meanwhile, part of this data has artifacts, so this dataset is also useful for evaluating the robustness of our methods to artifacts.

Table 1
Numbers of training and testing trials in BCI competition III dataset IIIa [34].

Subject	Training trials			Testing trials
	Clean trials	AC trials	Total	
k3	149	31	180	180
k6	92	28	120	120
l1	84	36	120	120

We used only three Laplacian channels C3, Cz and C4 (according to the standard 10/20 EEG recording system) out of 60 EEG channels. These channels are around the sensorimotor cortex, providing a better signal-to-noise ratio than the other channels, and are thus more important in decoding MI tasks [10,35]. The results are compared with those obtained by using other feature extraction methods based on all 60 channels [34,36–41], as well as using BP features extracted from the broad band (8–30 Hz) and full length (from the start to the end of motor imagery) EEG signals at the same three Laplacian channels. Furthermore, we also test our method with different amounts of artifacts contaminated trials to evaluate its robustness to artifacts.

2. Materials and methods

2.1. Experimental dataset

The BCI competition III dataset IIIa [34] was used in this study. This dataset is provided by Laboratory of Brain–Computer Interfaces, Graz University of Technology. It contains four classes of 4-s MI tasks: left hand, right hand, foot and tongue. The timing of experimental paradigm is shown in Fig. 1. In each trial, the subjects sat quietly for the first two seconds. Then, a "beep" was given, with a cross presented at the center of the screen, to indicate the beginning of the trial. A visual cue in form of an arrow pointing either to left, right, up or down (corresponding to left hand, right hand, both feet and tongue) was given at 3 s and stayed on the screen for one second. The subjects were required to imagine the corresponding movement during four seconds after the cue on-set. The cues indicating different motor imagery tasks were displayed in a randomized order.

The dataset was recorded from three subjects (denoted "k3", "k6", "l1") using 60 channels EEG. There are 180 training vs. 180 testing trials for Subject "k3", and 120 training vs. 120 testing trials for Subjects "k6" and "l1". The dataset providers have marked out the training trials contaminated with artifacts by the data property "HDR.ArtifactSelection". The numbers of training and testing trials for each subject are listed in Table 1, including the number of artifacts contaminated (AC) trials in the training data. Trials with

artifacts were marked out by the dataset provider. According to the data description provided in the BCI competition website (http://www.bbci.de/competition/iii/), the source derivation based on the center and the four nearest neighbor electrodes [59] was calculated for visually identifying the muscle and ocular artefacts. Artifacts in boundary electrodes were not considered. Our method used central electrodes only. Thus, the artifacts marked by the data provider are sufficient for testing our methods.

2.2. FDA-type F-score

FDA-type F-score is a simplified criterion based on Fisher discriminant analysis (FDA) for estimating the discriminative power of a group of features (a feature vector) [22]. We defined this measure first for two-class (e.g. Class "L" vs "R") cases:

$$F = \frac{\left\|\vec{\mu}^{L} - \vec{\mu}^{R}\right\|_2^2}{tr(\Sigma^{L}) + tr(\Sigma^{R})} \tag{1}$$

where $\vec{\mu}$ denotes the mean of the feature vector, $\|\cdot\|_2$ the $L2$-norm (Euclidean norm), Σ the covariance matrix of the feature vector and $tr(\cdot)$ the trace of a matrix. Thus, FDA-type F-score relies on the Euclidean distance between class centers to evaluate the difference between classes, and employs the trace of the covariance matrix to estimate the variance within one class. FDA-type F-score, as a simplified measure, avoids estimating a projection direction in multi-dimensional FDA, and has been successfully used in two-class BCI and motor recognition studies for channel and feature selection [21,22,33,42].

2.3. Subject-specific time-frequency optimization for multi-class EEG classification

In this study, we used three EEG channels, i.e. C3, Cz and C4, nearby the sensorimotor cortex. To improve the SNR of EEG signals, a small-distant Laplacian transformation [43] was applied as a spatial high-pass filter to each channel, in order to reduce the signal correlation and common noise caused by the head volume conduction. The EEG signals at C3, Cz and C4 were decomposed into a series of overlapping time-frequency areas $(\omega_m \times \tau_n)$, $m \in \{1, \ldots, M\}, n \in \{1, \ldots, N\}$, with successive frequency bands $\omega_m = [f_m, f_m + F - 1], f_{m+1} = f_m + F_s$ (F is the frequency bandwidth, F_s is the step in the frequency domain) and overlapping time intervals $\tau_n = [t_n, t_n + T - 1], t_{n+1} = t_n + T_s$ (T is the time interval width, T_s is the step in the time domain). The details of the parameter setting in this preprocessing step are provided in Section 2.4

We used FDA-type F-score to estimate the optimal time-frequency areas for extracting the subject-specific BP features. According to Eq. (1), in the optimal time-frequency area, the populations of features from different classes should have the largest FDA-type F-score distance. This concept can be extended to multi-class cases using the one-versus-rest (OVR) strategy, which is often used in multi-class classification [44]. Let us denote by $\mathcal{C}$ the set of all classes, and $\mathcal{C}\backslash\{O\}$ for all classes except class O. If we can consider $\mathcal{C}\backslash\{O\}$ as a large class, the multi-class problem can be transferred to a two-class problem, so as to compute the OVR-based F-score:

$$\hat{F} = \frac{\left\|\vec{\mu}^{O} - \vec{\mu}^{\mathcal{C}\backslash\{O\}}\right\|_2^2}{tr(\Sigma^{O}) + tr(\Sigma^{\mathcal{C}\backslash\{O\}})} \tag{2}$$

where $\vec{\mu}$ denotes the mean of the feature vector, $\|\cdot\|_2$ the Euclidean norm, Σ the covariance matrix of the feature vector and $tr(\cdot)$ the trace of a matrix.

The feature vector, $[BP_{C3}, BP_{Cz}, BP_{C4}]$, contains the BP features (BP) from three Laplacian channels C3, Cz and C4, so the OVR-based F-score is calculated by:

$$\hat{F} = \frac{(\bar{BP}^{O}_{C3} - \bar{BP}^{\mathcal{C}\backslash\{O\}}_{C3})^2 + (\bar{BP}^{O}_{Cz} - \bar{BP}^{\mathcal{C}\backslash\{O\}}_{Cz})^2 + (\bar{BP}^{O}_{C4} - \bar{BP}^{\mathcal{C}\backslash\{O\}}_{C4})^2}{(\bar{S}^{O}_{C3} + \bar{S}^{O}_{Cz} + \bar{S}^{O}_{C4}) + (\bar{S}^{\mathcal{C}\backslash\{O\}}_{C3} + \bar{S}^{\mathcal{C}\backslash\{O\}}_{Cz} + \bar{S}^{\mathcal{C}\backslash\{O\}}_{C4})} \tag{3}$$

with:

$$\bar{BP} = \frac{1}{K}\sum_{k=1}^{K} BP(k) \tag{4}$$

$$\bar{S} = \frac{1}{K-1}\sum_{k=1}^{K} (BP(k) - \bar{BP})^2 \tag{5}$$

where K is the number of trials.

Before calculating the F-score, we applied the logarithm on BP features to make their distributions approximately normal [45]. In probability theory, a random vector is considered to be multivariate normally distributed if all linear combinations of its components obey univariate (one-dimensional) normal distributions [46]. Thus, the feature vector, $[BP_{C3}, BP_{Cz}, BP_{C4}]$, should be multivariate normally distributed. In practice, Mardia's test can be used to check whether a given dataset obeys the multivariate normal distribution with a given significance level of 0.05 [47].

For each class, we calculated $\hat{F}(\omega_m, \tau_n)$ at each time-frequency area $(\omega_m \times \tau_n)$ using Eq. (3), in order to measure its discriminative power for separating the class against all the others. The optimal time-frequency area (ω^*, τ^*) for separating each class was estimated by searching the maximum value of $\hat{F}(\omega_m, \tau_n)$ among all $M \times N$ time-frequency areas (M is the total number of frequency bands, N is the total amount of time intervals):

$$\hat{F}(\omega^*, \tau^*) = \max\left\{\hat{F}(\omega_m, \tau_n) \mid m \in \{1, 2\ldots, M\}, n \in \{1, 2\ldots, N\}\right\} \tag{6}$$

Without loss of generality, Fig. 2 presents the scheme of multi-class F-score based time-frequency selection (MFTFS) for a four-class problem. The optimal time-frequency area for separating one class from all the others can be considered as the characteristic time-frequency area for the class, since it contains information that makes the class different from all the others. Let us assume that the characteristic time-frequency areas for I different classes are $(\omega^*, \tau^*)_i$, $(i = 1, \ldots, I)$. BP features, $BP_{C3}, BP_{Cz}, BP_{C4}$, are extracted from the characteristic time-frequency area $(\omega^*, \tau^*)_i$ of each class i in Laplacian channels C3, Cz and C4, so called the class-relevant feature vector. Considering the selected characteristic time-frequency areas for some classes may be the same in practice, we only use the set of feature vectors from all different (ω^*, τ^*) for classification. This step can be achieved by:

$$\mathcal{A} = UNIQUE(\{(\omega^*, \tau^*)_i \mid i \in 1\ldots, I\}) \tag{7}$$

where $\mathcal{A}$ is the set of all different time-frequency areas (ω^*, τ^*), the operator $UNIQUE$ eliminates possible time-frequency area repetitions in the set of $\{(\omega^*, \tau^*)_i \mid i \in 1\ldots, I\}$. Then, the feature vector $[BP_{C3}, BP_{Cz}, BP_{C4}]$ is extracted from each time-frequency area in $\mathcal{A} = \{(\omega^*, \tau^*)_i \mid i \in 1\ldots, K, 1 \le K \le I\}$ for classification.

2.4. Data processing, method evaluation and comparison

Fig. 3 indicates how the EEG signal is decomposed into a series of overlapping time-frequency areas in each channel. This decomposition procedure is identical for different channels. For each Laplacian channel, 5th order Butterworth filters were employed to obtain 15

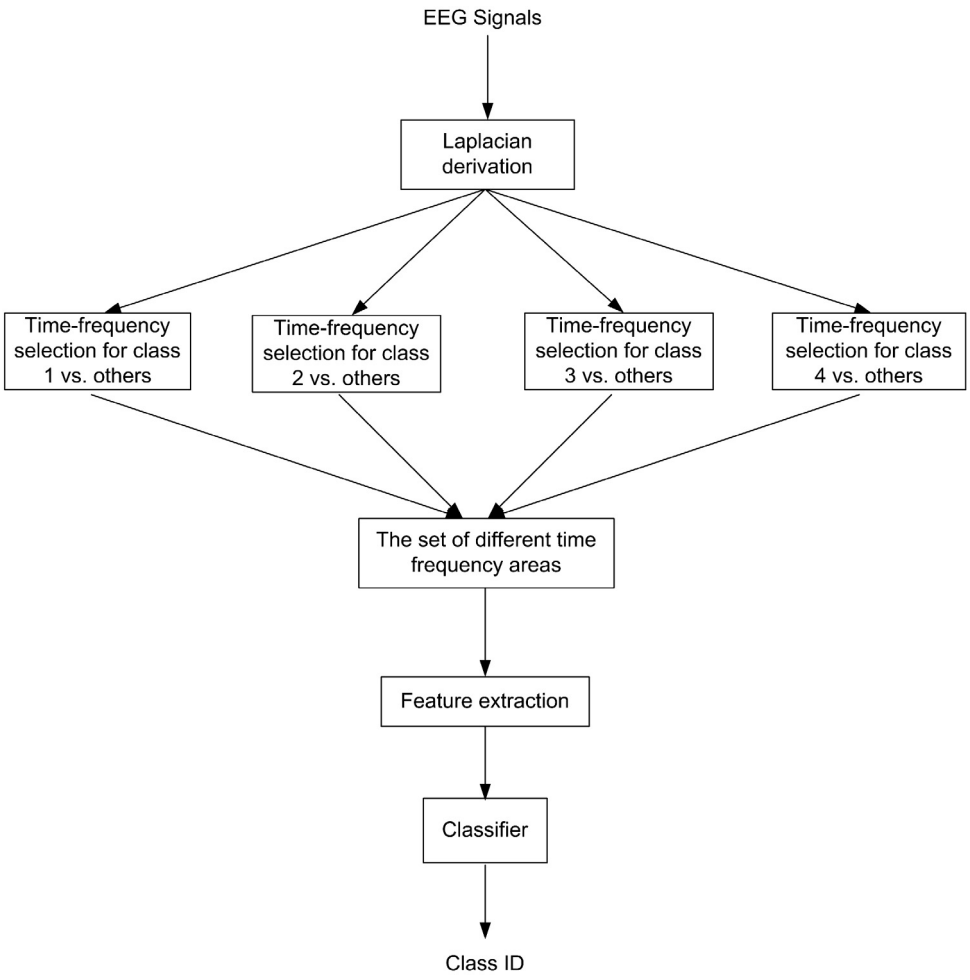

Fig. 2. Scheme of multi-class *F* score based time-frequency selection (MFTFS).

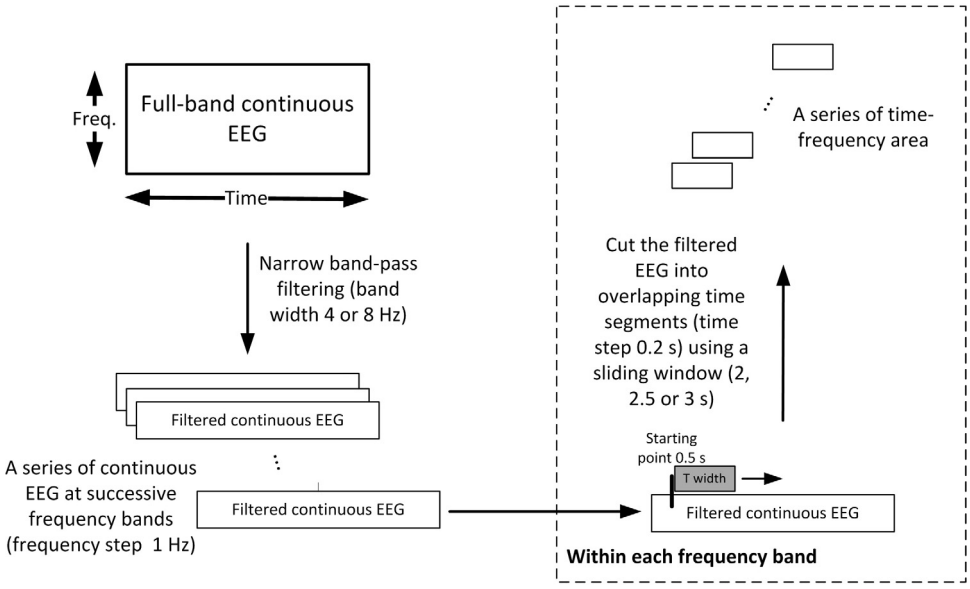

Fig. 3. Scheme of signal decomposition into a series of overlapping time-frequency areas.

successive 8 Hz-wide frequency bands (F = 8 Hz, F_s = 1 Hz): 8–16, 9–17, 10–18, . . ., 22–30 Hz, and 19 successive 4 Hz-wide frequency bands (F = 4 Hz, F_s = 1 Hz): 8–12, 9–13, 10–14 . . ., 26–30 Hz. Butterworth filter has flattest pass-band region among the commonly used filter (e.g. Chebyshev, Elliptic fliters), so it has the least attenuation over the desired frequency range. Thus, Butterworth filter is suitable for narrow band filtering. The order of Butterworth filter here was chosen to have a stable frequency response characteris-

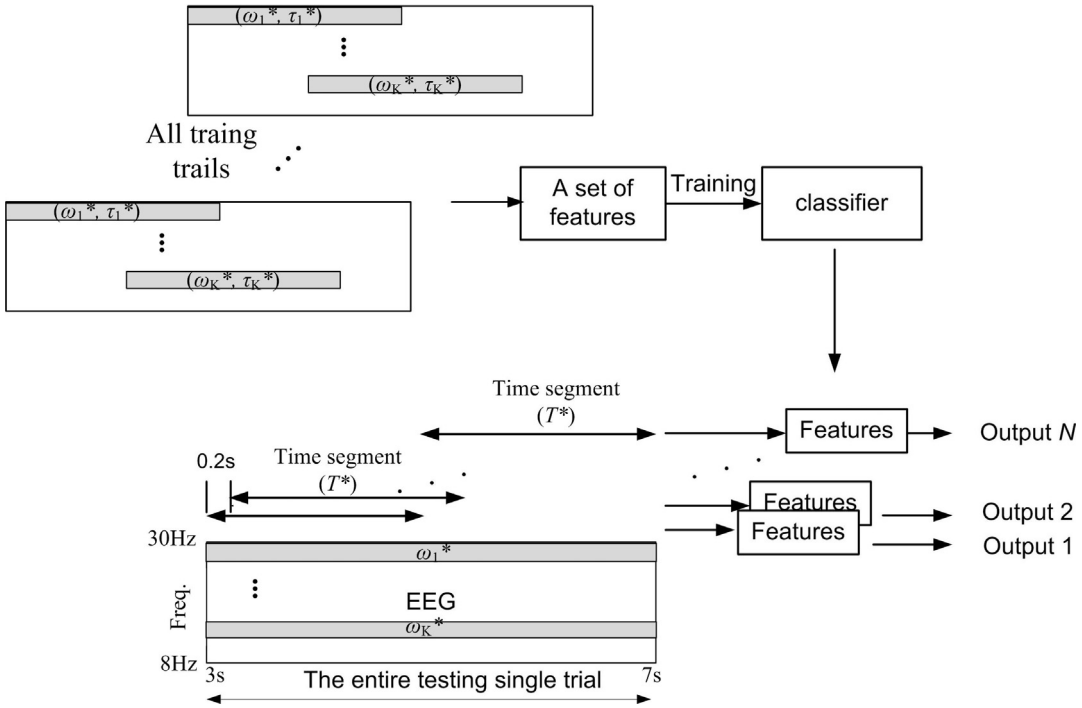

Fig. 4. Scheme of multi-class BCI based on subject-specific time-frequency features.

tic and a steep boundary. Shown in previous studies [29,48–50], the 5th order Butterworth filters work well with different feature extraction methods for various frequency bands including the frequency bands we used in this study.

Previous studies have shown that the event-related (de)synchronization typically occurs around 0.5 s after cue-on. Therefore, we used sliding windows in the period from 0.5 s after cue-on until the end of MI task to segment the band-pass filtered data. Different widths of time windows are used to find the optimal one. Specially, we used 2, 2.5 and 3 s wide (i.e. $T = 2$, 2.5 and 3 s, respectively) sliding windows (12 segments for each sliding window) with 0.2s-step (i.e. $T_s = 0.2$ s) moving from 0.5 s after the cue on-set until the end of MI task to get 36 overlapping time segments in each frequency band.

Thus, there were 34 frequency bands (i.e. fifteen 8 Hz-wide and nineteen 4 Hz-wide frequency bands) × 36 time segments (three different sizes of time windows and twelve segments for each size) = 1224 time-frequency areas in total. The F-score is calculated in each time-frequency area to find the optimal time-frequency area with maximum F-score using Eq. (6) for each class (i.e. one time-frequency area for one class).

When optimal time-frequency areas $\{(\omega^*, \tau^*)_i \mid i \in 1, \ldots, K, 1 \leq K \leq 4\}$ were selected for each subject, we extracted subject-specific BP features from the training trials to train the classifier. We used the multi-class Fisher's linear discriminant analysis (LDA) as the classifier, which was in line with the FDA-type F-score. The ω_i^*-bandpass ($i \in 1, \ldots, K, 1 \leq K \leq 4$) filtered EEG segments with the same time length as τ^* were generated from the whole single-trial of testing data via a 0.2-s step sliding window to obtain continuous classification results (see Fig. 4)

Firstly, we evaluated our method in the BCI competition III dataset IIIa [34] by comparing with other methods. To keep consistent with previous studies on this dataset, we used all training trials to seek for the optimal time-frequency areas and train the classifier, and then tested it with the independent testing trials. The results were compared with those obtained by data providers [34] and other recently developed methods applied to the same dataset, as well as using BP features extracted from the broad band (8–30 Hz) and full length (from the start to the end of motor imagery) EEG signals at the same three Laplacian channels. Since several recent studies used 10 fold cross-validations instead of independent testing trails to evaluate their methods, we also provided the results of 10 fold cross-validations. In the 10 fold cross-validations, the whole dataset is randomly split into 10 folds of equal size. At each iteration, 9 folds are used to train the classifier and test it with the rest one fold. We averaged over all folds to estimate the mean classification performance of cross-validation. Kappa coefficient and classification accuracy are two metrics commonly used for evaluating classification results. The relationship between kappa coefficient (κ) and classification accuracy (Acc) is $\kappa = (Acc - ch)/(1 - ch)$, where ch is the chance level for classification ($ch = 0.25$ for four-class classification). Kappa coefficient is generally thought to be a more robust measure than classification accuracy, since Kappa coefficient takes into account the possibility of the agreement occurring by chance. Thus, kappa coefficient is recommended in the BCI competitions [36]. However, many BCI studies provide classification accuracy as well, since classification accuracy directly indicates the agreement between classification results and truth labels. Here we provide results in both kappa coefficient and classification accuracy to compare our results with those obtained by other methods. This part of results and corresponding discussions are provided in Section 3.1

Secondly, we tested our method with different amounts of artifacts contaminated (AC) trials to evaluate its robustness to artifacts. We started with using only "clean" trials for time-frequency selection and classifier training, and test the classifier with all testing trials. Then, we ran several tests by randomly picking up certain amount of AC trials to add to training data to repeat the evaluation. In each test, we repeated 20 times for the same amount of AC trials to estimate the mean classification performance and its standard deviation. For each new test, we added more AC trials (the amount equal to 5% of total training data, so 180 × 5% = 9 trials for k3 and 120 × 5% = 6 trails for k6 and l1) than previous one until all AC trials were added, so as to get the curve of classification performance

Table 2
Comparisons between the MFTFS and other methods in BCI competition III using independent testing datasets. 'NC' is the number of channels used for feature extraction and classification. The best performances are highlighted in bold.

	Kappa coefficient					Classification accuracy					*NC*
	k3	k6	l1	Mean	Std.	k3	k6	l1	Mean	Std.	
MFTFS (our method)	0.64	**0.71**	**0.72**	**0.69**	**0.04**	0.73	**0.78**	**0.79**	**0.77**	**0.03**	**3**
Broad band BP	0.14	0.01	0.05	0.07	0.07	0.36	0.26	0.29	0.30	0.04	**3**
AAR [34]	0.70	0.37	0.39	0.49	0.19	0.78	0.53	0.54	0.62	0.11	60
ICA + PCA [36]	**0.95**	0.41	0.52	0.63	0.29	**0.96**	0.58	0.64	0.72	0.17	60
CSP [36]	0.90	0.43	0.71	0.68	0.23	0.93	0.58	0.78	0.76	0.14	60
JAD-CSP [37]	0.76	0.41	0.53	0.57	0.18	0.82	0.56	0.65	0.68	0.11	60

Table 3
Comparisons between the MFTFS and the state-of-the-art methods (published after 2012) using 10-fold cross-validation. 'NC' is the (average) number of channels used for feature extraction and classification. The best performances are highlighted in bold.

	Kappa coefficient					Classification accuracy					*NC*
	k3	k6	l1	Mean	Std.	k3	k6	l1	Mean	Std.	
MFTFS (our method)	0.71	**0.77**	**0.85**	**0.78**	**0.04**	0.79	**0.84**	**0.89**	**0.84**	**0.03**	**3**
STFSCSP [39]	0.84	0.66	0.82	0.77	0.08	0.88	0.75	0.86	0.83	0.06	16
ARR [40]	0.69	0.36	0.39	0.48	0.15	0.77	0.52	0.54	0.61	0.11	20
DCT [40]	0.17	0.29	0.25	0.24	0.06	0.38	0.47	0.44	0.43	0.04	20
KL-CSP [38]	0.78	0.49	0.56	0.61	0.15	0.84	0.62	0.67	0.71	0.09	60
KL-LTCSP [38]	0.79	0.50	0.54	0.61	0.16	0.84	0.63	0.66	0.71	0.10	60
LP-SVD + logistic model tree [51]	**0.87**	0.68	0.70	0.75	0.08	**0.90**	0.76	0.78	0.81	0.06	20
LP-SVD + AR + error variance [40,41]	0.69	0.56	0.45	0.57	0.12	0.77	0.67	0.59	0.68	0.07	20

over different amounts of AC trials. This part of results and corresponding discussions are provided in Section 3.2. The results are provided in kappa coefficient only.

3. Results and discussion

3.1. Improving classification performance based on few EEG channels

The classification performances obtained by using our method MFTFS and other methods are provided in Tables 2 and 3. The performance is evaluated with kappa coefficient (κ) and classification accuracy (Acc). Higher kappa coefficient and classification accuracy indicate better classification performance. Table 2 shows the results using independent testing dataset as BCI competition required. Table 3 provides the results of 10-fold cross-validation using all the available data.

Using BP features directly extracted from the broad band (8–30 Hz) and full length (from the start to the end of motor imagery) EEG signals at the three Laplacian channels (C3, Cz and C4) yields the poorest classification performance among all methods, which is just above the chance level (zero kappa). We also provide receiver operating characteristic (ROC) curves of four classes for our method MFTFS in comparison to using the broad band, full length data (Fig. 5). From the ROC curves, we can see that using our method MFTFS to extract BP features from the optimal time-frequency areas greatly improves classification performances for all classes. Thus, it is necessary to seek for the optimal time-frequency areas for BP feature extraction when using only three Laplacian channels for multi-class BCI.

We also compared our method with the methods applied to the same dataset in BCI competition including adaptive autoregressive (AAR) used by data providers [34],[1] independent common analysis (ICA), principal component analysis (PCA) and common spatial pattern (CSP) [36] and a previous study using joint approximate diagonalization based CSP (JAD-CSP) [37]. The results are summarized in Table 2. All these results were obtained on the dependent testing dataset.

Furthermore, we compared our method with the methods that were proposed in the last five years from 2012 to 2016, including sparse time-frequency segment CSP (STFSCSP) [39], Kullback-Leibler (KL) divergence based CSP (KL-CSP) [38], KL divergence based local temporal common spatial patterns (KL-LTCSP) [38], discrete cosine transform (DCT) [40] and linear prediction singular value decomposition (LP-SVD) [40,41,51]. Since all these recent works used 10-fold cross-validation to test their methods, we provide our results in 10-fold cross-validation as well to compare with them in Table 3.

Our method MFTFS yielded the best mean classification accuracy (0.77 for independent testing data, 0.84 for 10-fold cross validation) and kappa coefficient (0.69 for independent testing data and 0.78 for 10-fold cross validation) with smallest standard deviation among all methods in both comparisons (see Tables 2 and 3). Moreover, our method used only three Laplacian channels, which are far less than other methods in comparison. These results indicate our method is very effective in improving classification performance based on few EEG channels.

Motor imagery BCI classifies subject's motor intentions based on the features extracted from EEG signals. The underlying neurophysiological mechanism is that motor imagery of a specific body part induces EEG power changes (known as event-related desynchronization and synchronization) in the specific frequency band of EEG oscillation (i.e. sensorimotor rhythm) over the sensorimotor cortex [35]. Thus, we used band power features to identify the task-relevant band power change in the sensorimotor rhythm for classifying the motor imagery tasks. We noted that several recent studies used other features for classification in the same dataset. In comparison with methods using other features, i.e. AAR, ICA, DCT features (see Tables 2 and 3), we cannot conclude that using other features could be superior to using band power features; while more computational cost may be required for calculating other features, such as ICA features.

For using band power features, it is essential to extract the task-relevant band power change in the sensorimotor rhythm. As

[1] Using AAR as the feature extraction method, Schlögl and colleagues provided classification results obtained by four different classifiers, namely minimum distance analysis, linear discriminant analysis, k-nearest-neighbor and support vector machine [34]. Here we list their best results for comparison.

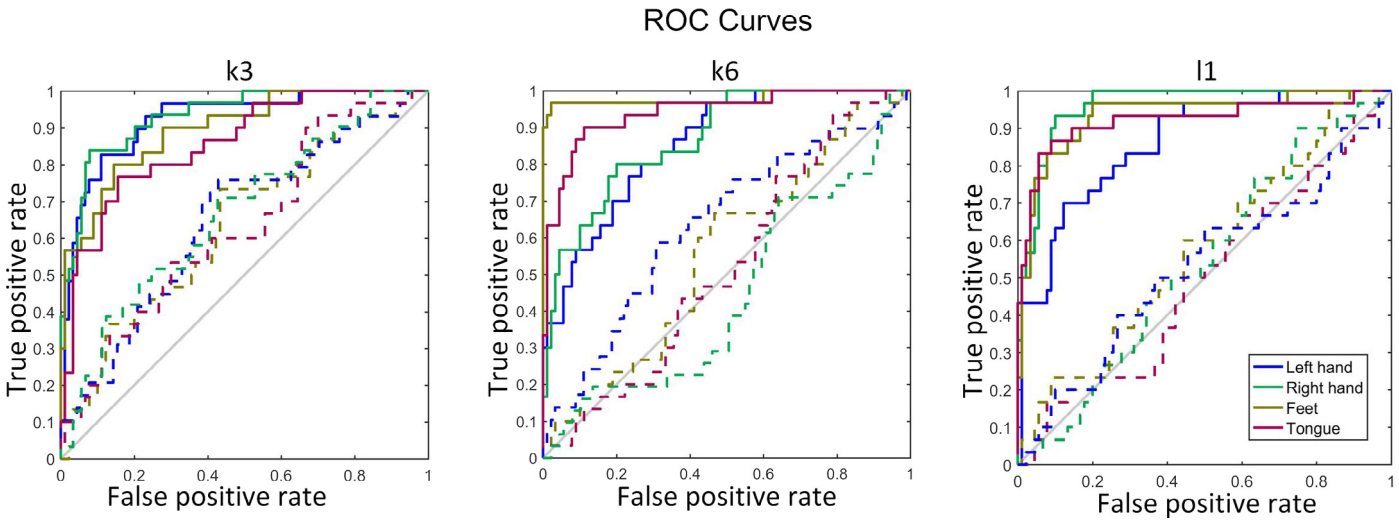

Fig. 5. ROC curves for our method (MFTFS, solid lines) in comparison to using the broad band, full length data (dashed lines).

indicated in Table 5, the exact frequency band of sensorimotor rhythm can varies from subject to subject. Individual differences in the frequency band of sensorimotor rhythm will deteriorate BCI performances when using a general parameter setting for all subjects (e.g. features from the broad frequency band 8–30 Hz), as shown in Fig. 5 and Table 2. Additionally, the delay between the cue onset and the starting of motor imagery varies with individuals [21]. Previous studies have demonstrated that estimating optimal time-frequency areas for each individual can greatly improve the classification performance [52,29]. Due to the volume conduction effect, spatial filtering is also needed to reduce the correlation of EEG signals and eliminate the artefacts [18]. Data-driven spatial filtering methods, such as common spatial pattern (CSP), usually need a large number of EEG channels. Alternatively, the bipolar or Laplacian derivation can be used when there are only a few electrodes placed around the sensorimotor cortex. This option has been successfully used in the previous studies for two-class cases, generating even better results than CSP [53,54,29]. The central channels C3, Cz and C4 are close to functional regions of the sensorimotor cortex for motor imageries of left vs. right hand, feet and tongue [10]. Moreover, the central electrodes are relatively free of muscle artefact compared to the electrodes in the boundary of EEG cap [55]. Our method selects the optimal time-frequency areas to extract band power features based on the Laplacian channels C3, Cz and C4, which combines the knowledge discussed above to improve classification results based on few channels. As a result, our method can yield better performances in comparison to other methods.

Noteworthy, our time-frequency selection method is not expensive in computational time (2.5 min in average for finding the characteristic time-frequency area for each class, so around 10 min in total for the four-class problem, using Matlab 7.10.0 on Windows 7 Professional 64bit, RAM 2.0G, CPU 2.66G Hz). For on-line BCI, this step could be performed off-line before on-line classification.

Table 4
Evaluation of the MFTFS sensitivity (evaluated with *kappa coefficient*) to artifacts on BCI competition III dataset IIIa.

	Subjects			
	k3	k6	l1	Mean
All	0.64	**0.71**	**0.72**	**0.69**
Clean	**0.69**	0.70	0.60	0.66

3.2. Robustness to artifacts

Table 4 lists the classification results (evaluated by *kappa coefficient* [56], κ) of using all training trials (All) v.s. using only the "clean" trials. We examined the results for each subject individually. For Subject *k*3, using only the clean trials ($\kappa = 0.69$) yields a better classification result than using all training trials ($\kappa = 0.63$). However, for Subjects *k*6 and *l*1, the classification results obtained by using only the clean trials (Subject *k*6: $\kappa = 0.70$, Subject *l*1: $\kappa = 0.60$) are worse than those obtained by using all training trials (Subject *k*6: $\kappa = 0.71$, Subject *l*1: $\kappa = 0.72$).

Generally speaking, artifacts should theoretically deteriorate the classification results, since artifacts reduce the signal-to-noise ratio. However, removing AC trials will definitely decrease the number of trials for training, where a limited amount of data might not be sufficient to train the classifier. Therefore, a trade-off should be made between rejecting AC trials and maintaining the amount

Table 5
Characteristic time-frequency areas for different classes on BCI competition III dataset IIIa, obtained by using all training trials (All) and only the "clean" trials, respectively.

Subject			Left hand	Right hand	Feet	Tongue
k3	All	Freq.(Hz)	12–20	13–21	13–21	12–20
		Time(s)	0.9–3.9	1.9–4.9	2.1–5.1	0.7–3.7
	Clean	Freq.(Hz)	12–20	12–20	13–21	12–20
		Time(s)	2.5–5.0	2.1–5.1	2.1–5.1	0.7–3.7
k6	All	Freq.(Hz)	22–30	26–30	22–30	19–27
		Time(s)	0.5–3.5	0.9–3.9	2.7–5.7	2.7–5.7
	Clean	Freq.(Hz)	22–30	26–30	22–30	18–26
		Time(s)	0.5–3.5	0.9–3.9	2.3–5.3	2.7–5.7
l1	All	Freq.(Hz)	20–28	12–20	22–30	12–20
		Time(s)	2.7–5.7	1.1–4.1	2.5–5.5	1.1–4.1
	Clean	Freq.(Hz)	22–30	13–17	22–30	12–20
		Time(s)	0.7–3.7	1.8–4.8	2.7–5.7	2.7–5.7

of training data. This trade-off, in some extent, also depends on the sensitivity of the method to noise. If the method is very sensitive to noise, then adding AC trials to the training dataset can only deteriorate the classification result. As a result, using only the clean trials will yield better results than adding AC trials. On the contrary, if a method is robust to artifacts, then adding AC trials may not decrease the classification results any more.

In Table 4, we can see that using all training trials ($\bar{\kappa} = 0.69$) generates a better mean classification result than using only clean trials ($\bar{\kappa} = 0.64$), indicating that MFTFS is robust to artifacts. In this dataset, subject *l*1 has the least clean training trials (84 trials, see Table 1). If only using clean trials, the classification result for *l*1 ($\kappa = 0.60$) is the worst among all the subjects.

Table 5 lists the characteristic time-frequency areas for different classes, obtained by using all training trials (All) and only the clean trials, respectively. From Table 5, we can see that the characteristic time-frequency areas shift for some classes for each subject between using all training trials and only the clean trials. Thus, MFTFS can adapt to the amount of training data and noise to find the optimal time-frequency areas for extracting the most discriminative features.

To further study the effect of adding AC trials on the performance of MFTFS, we add different amounts of AC data to training data, so as to get a curve of classification performance with respect to different numbers of training data with different amounts of noise. In this test, we randomly picked out certain amount of AC trials adding to training data and repeated the evaluation 20 times. Note that the repeated evaluation is not for the case using only "clean" trials (no AC trials at all) and the case using all trials (including all AC trials). Therefore, there are no error bars for these two cases. From Fig. 6, we can see that adding AC trials to the training dataset does not necessarily deteriorate classification performances, indicating that our method is tolerant to artifacts. For Subjects "k6" and "l1", who have the limited numbers of "clean" trials (92 trials for "k6" and 84 trials for "l1"), adding AC trials can generally improve the classification performance until the training data are more than hundred trials. The best performance ($\kappa = 0.77$) is achieved with 116 training trials (AC trials/training trials = 24/92) for Subject "k6" and 114 training trials (AC trials/training trials = 30/84) for Subject "l1". However, for Subject "k3", adding AC trials cannot improve the classification results. The best performance is achieved when using only clean trials for this subject. The reason is that this subject already has a large number of training trials (149 "clean" trials, see Table 1). Usually, a training dataset should have five to ten times as many trials as the dimensionality of features to obtain a good performance of a classifier [57,58]. Increasing the number of trials in this range usually will improve the classification performance. For a four-class problem, the dimensionality of MFTFS selected BP features are around $3 \times 4 = 12$, so that 120 trials is the upper boundary in this range, which is closed to the reported optimal number of trials for Subjects "k6" and "l1". For Subject "k3", the amount of "clean" trials (149 trials) are already above this boundary. In this case, adding AC trials deteriorates the classification performance, since it mainly introduces artifacts rather than providing more useful information for training.

To sum up, using MFTFS, when the number of clean training trials is less than ten times of the feature dimension, it is possible to improve classification results by adding AC trials. On the contrary, if the number of clean training trials is large enough, adding AC trials is not helpful any more.

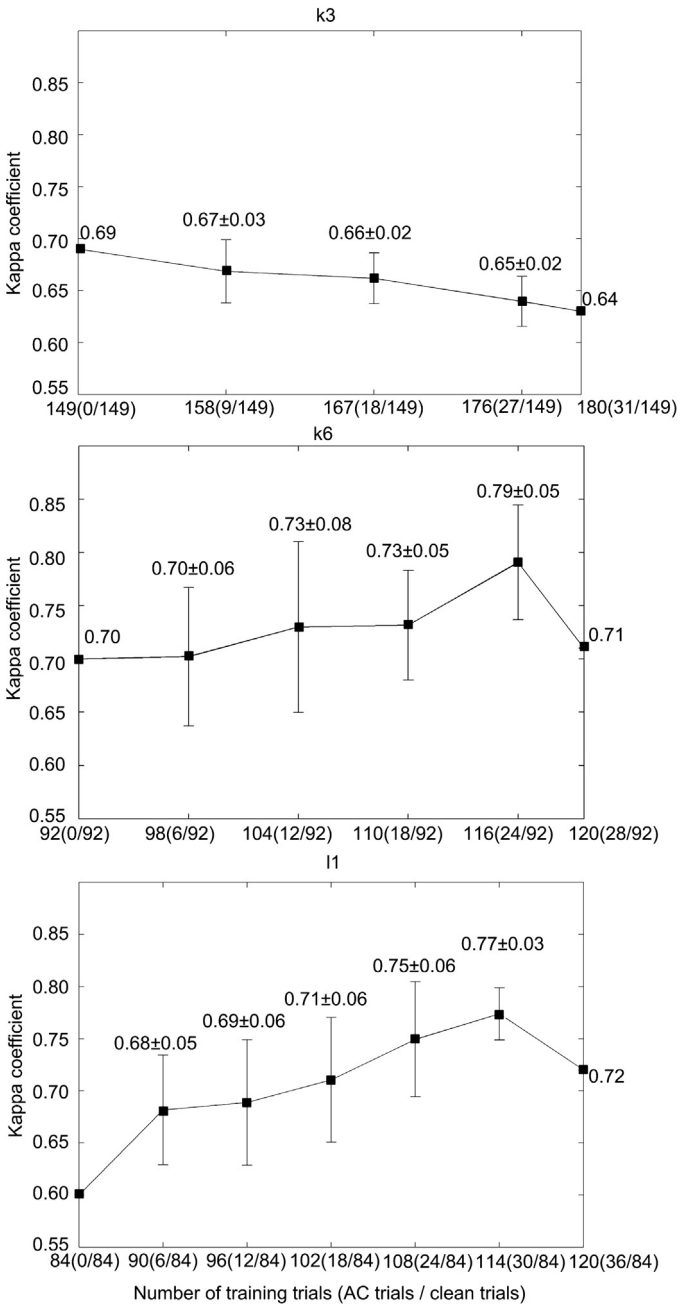

Fig. 6. Curve of classification performance (measured by κ values) with respect to different numbers of training data with different amounts of AC trials for different subjects. Results are averaged over 20 repetitions. We randomly pick out certain amount of AC trials and added to training data for each repetition. Error bars show standard deviations of κ values. We also provided the numerical values (mean ± std.).

4. Conclusion

Previous studies have demonstrated the importance of feature extraction and using few EEG channels to the widespread use of BCI. The optimal frequency band and time segment to extract motor-imagery features differ from subject to subject. Extracting the feature from a uniform time-frequency area cannot guarantee the best BCI performance for all subjects and therefore reduces the inter-subject robustness. To address this challenge, we proposed an effective method to seek optimal time-frequency areas for extracting subject-specific features, in order to improve the classification performance using few channels EEG. Different from our previous work, this study focused on the multi-class motor imagery BCI, which aims to provide the user with more freedom in the control. The method was evaluated on a standard multi-class BCI dataset (BCI competition III dataset IIIa). The experimental results show

that our method yields better classification performance than other methods, using fewer EEG channels. Moreover, the performance of our method is stable over subjects and robust to artifacts. This work could contribute to daily use multi-class BCIs based on few EEG channels. This BCI based on few channels can be used for patients with lock-in syndrome or spinal injury, whose cortical structure and function are similar to healthy subjects. Nevertheless, it could be a challenge for patients with brain injury such as a stroke, when brain functions have been affected by the lesion and the post-injury brain reorganization. The brain activity recorded from C3, Cz and C4 (around the sensorimotor cortex) may be too weak to perform any MI-based control. A few groups are aiming to solve this problem, e.g. using invasive electrocorticogram recording [11]. In the future, we will combine our proposed method with a subject-specific channel selection algorithm [21] to provide a non-invasive solution for non-severe chronic stroke patients.

Ethical statements

We validated our method by an open-access BCI dataset, i.e. the dataset IIIa [34] from BCI competition III (http://www.bbci.de/competition/iii/). Thus, our study did not involve any self-recorded datasets from human participants or animals. The authors declare that they have no conflict of interest.

Acknowledgements

Authors thank Dr. Teodoro Solis-Escalante and Dr. Olexiy Kyrgyzov for useful discussions about the method, and Dr. Alois Schlögl for providing the BCI dataset. Authors also thank Prof. Gert Kwakkel and Prof. Julius Dewald for useful discussions about BCI in stroke. This work was partially supported by funding from Orange Labs, France Télécom. Since November 2013, Dr. Yuan Yang has been funded by the European Research Council under the European Union's Seventh Framework Programme (FP/2007–2013)/ERC Grant Agreement No. 291339 (4D-EEG project) obtained by Prof. Dr. Frans C.T. van der Helm and Prof. Dr. Gert Kwakkel in 2012.

References

[1] A. Vallabhaneni, T. Wang, B. He, Brain–computer interface, Neural Eng. (2005) 85–121.
[2] E.A. Curran, M.J. Stokes, Learning to control brain activity: a review of the production and control of EEG components for driving brain–computer interface (BCI) systems, Brain Cogn. 51 (2003) 326–336.
[3] L.A. Farwell, E. Donchin, Talking off the top of your head: toward a mental prosthesis utilizing event-related brain potentials, Electroencephalogr. Clin. Neurophysiol. 70 (1988) 510–523.
[4] J. Jin, B.Z. Allison, E.W. Sellers, C. Brunner, P. Horki, X. Wang, C. Neuper, An adaptive p300-based control system, J. Neural Eng. 8 (2011) 036006.
[5] J.J. Vidal, Toward direct brain–computer communication, Annu. Rev. Biophys. Bioeng. 2 (1973) 157–180.
[6] X. Chen, Y. Wang, M. Nakanishi, X. Gao, T.-P. Jung, S. Gao, High-speed spelling with a noninvasive brain–computer interface, Proc. Natl. Acad. Sci. U. S. A. 112 (2015) E6058–E6067.
[7] Z. Qiu, B.Z. Allison, J. Jin, Y. Zhang, X. Wang, W. Li, A. Cichocki, Optimized motor imagery paradigm based on imagining Chinese characters writing movement, IEEE Trans. Neural Syst. Rehabil. Eng. (2017).
[8] G. Pfurtscheller, B.Z. Allison, C. Brunner, G. Bauernfeind, T. Solis-Escalante, R. Scherer, T.O. Zander, G. Mueller-Putz, C. Neuper, N. Birbaumer, The hybrid BCI, Front. Neurosci. 2 (2010) 1–12.
[9] M. Wang, I. Daly, B.Z. Allison, J. Jin, Y. Zhang, L. Chen, X. Wang, A new hybrid BCI paradigm based on p300 and SSVEP, J. Neurosci. Methods 244 (2015) 16–25.
[10] G. Pfurtscheller, C. Brunner, A. Schlögl, F.H. Lopes da Silva, Mu rhythm (de)synchronization and EEG single-trial classification of different motor imagery tasks, Neuroimage 31 (2006) 153–159.
[11] S. Silvoni, A. Ramos-Murguialday, M. Cavinato, C. Volpato, G. Cisotto, A. Turolla, F. Piccione, N. Birbaumer, Brain–computer interface in stroke: a review of progress, Clin. EEG Neurosci. 42 (2011) 245–252.
[12] R. Swaminathan, S. Prasad, Brain computer interface used in health care technologies, in: Next Generation DNA Led Technologies, Springer, 2016, pp. 49–58.
[13] A. Kübler, F. Nijboer, J. Mellinger, T.M. Vaughan, H. Pawelzik, G. Schalk, D.J. McFarland, N. Birbaumer, J.R. Wolpaw, Patients with ALS can use sensorimotor rhythms to operate a brain–computer interface, Neurology 64 (2005) 1775–1777.
[14] R. Scherer, A. Schlögl, F. Lee, H. Bischof, J. Janša, G. Pfurtscheller, The self-paced Graz brain–computer interface: methods and applications, Comput. Intell. Neurosci. 2007 (2007) 79826.
[15] Y. Yang, J. Wiart, I. Bloch, Towards next generation human-computer interaction-brain–computer interfaces: applications and challenges, 1st International Symposium of Chinese CHI (Chinese CHI 2013) (2013) 1–2.
[16] D virtual reality environments.
[17] S. Liang, K.-S. Choi, J. Qin, W.-M. Pang, Q. Wang, P.-A. Heng, Improving the discrimination of hand motor imagery via virtual reality based visual guidance, Comput. Methods Programs Biomed. 132 (2016) 63–74.
[18] B. Blankertz, R. Tomioka, S. Lemm, M. Kawanabe, K.R. Müller, Optimizing spatial filters for robust EEG single-trial analysis, IEEE Signal Process. Mag. 25 (2008) 41–56.
[19] Y. Yang, S. Chevallier, J. Wiart, I. Bloch, Automatic selection of the number of spatial filters for motor-imagery BCI, 20th European Symposium on Artificial Neural Networks, Computational Intelligence and Machine Learning (ESANN 2012) (2012) 109–114.
[20] S. Wang, C.J. James, Extracting rhythmic brain activity for brain–computer interfacing through constrained independent component analysis, Comput. Intell. Neurosci. 2007 (2007) 41468.
[21] Y. Yang, I. Bloch, S. Chevallier, J. Wiart, Subject-specific channel selection using time information for motor imagery brain–computer interfaces, Cogn. Comput. 8 (2016) 505–518.
[22] Y. Yang, O. Kyrgyzov, J. Wiart, I. Bloch, Subject-specific channel selection for classification of motor imagery electroencephalographic data, IEEE International Conference on Acoustics, Speech and Signal Processing (ICASSP 2013) (2013) 1277–1280.
[23] L. He, Y. Hu, Y. Li, D. Li, Channel selection by Rayleigh coefficient maximization based genetic algorithm for classifying single-trial motor imagery EEG, Neurocomputing 121 (2013) 423–433.
[24] M. Arvaneh, C. Guan, K.K. Ang, C. Quek, Optimizing the channel selection and classification accuracy in EEG-based BCI, IEEE Trans. Biomed. Eng. 58 (2011) 1865–1873.
[25] O. Kyrgyzov, I. Bloch, Y. Yang, J. Wiart, A. Souloumiac, Data ranking and clustering via normalized graph cut based on asymmetric affinity, in: Image Analysis and Processing-ICIAP 2013, Springer, 2013, pp. 562–571.
[26] H. Shan, H. Xu, S. Zhu, B. He, A novel channel selection method for optimal classification in different motor imagery BCI paradigms, Biomed. Eng. Online 14 (2015) 93.
[27] J. Wang, F. Xue, H. Li, Simultaneous channel and feature selection of fused EEG features based on Sparse Group Lasso, BioMed Res. Int. 2015 (2015) 703768.
[28] A. Barachant, S. Bonnet, Channel selection procedure using Riemannian distance for BCI applications, 5th International IEEE/EMBS Conference on Neural Engineering (NER 2011) (2011) 348–351.
[29] Y. Yang, S. Chevallier, J. Wiart, I. Bloch, Time-frequency optimization for discrimination between imagination of right and left hand movements based on two bipolar electroencephalography channels, EURASIP J. Adv. Signal Process. 2014 (2014) 38.
[30] Y. Yang, S. Chevallier, J. Wiart, I. Bloch, Time-frequency selection in two bipolar channels for improving the classification of motor imagery EEG, 34th IEEE Annual International Conference of Engineering in Medicine and Biology Society (EMBC 2012) (2012) 2744–2747.
[31] B. Yang, H. Li, Q. Wang, Y. Zhang, Subject-based feature extraction by using fisher WPD-CSP in brain–computer interfaces, Comput. Methods Programs Biomed. 129 (2016) 21–28.
[32] J. Luo, Z. Feng, J. Zhang, N. Lu, Dynamic frequency feature selection based approach for classification of motor imageries, Comput. Biol. Med. 75 (2016) 45–53.
[33] C. Ansuini, A. Cavallo, A. Koul, M. Jacono, Y. Yang, C. Becchio, Predicting object size from hand kinematics: a temporal perspective, PLoS ONE 10 (2015) e0120432.
[34] A. Schlögl, F. Lee, H. Bischof, G. Pfurtscheller, Characterization of four-class motor imagery EEG data for the BCI-competition 2005, J. Neural Eng. 2 (2005) L14.
[35] G. Pfurtscheller, F.H. Lopes da Silva, Event-related EEG/MEG synchronization and desynchronization: basic principles, Clin. Neurophysiol. 110 (1999) 1842–1857.
[36] B. Blankertz, K.R. Müller, D.J. Krusienski, G. Schalk, J.R. Wolpaw, A. Schlögl, G. Pfurtscheller, J.R. Millán, M. Schroder, N. Birbaumer, The BCI competition III: validating alternative approaches to actual BCI problems, IEEE Trans. Neural Syst. Rehabil. Eng. 14 (2006) 153–159.
[37] M. Grosse-Wentrup, M. Buss, Multiclass common spatial patterns and information theoretic feature extraction, IEEE Trans. Biomed. Eng. 55 (2008) 1991–2000.
[38] H. Wang, Harmonic mean of Kullback-Leibler divergences for optimizing multi-class EEG spatio-temporal filters, Neural Process. Lett. 36 (2012) 161–171.
[39] M. Miao, H. Zeng, A. Wang, C. Zhao, F. Liu, Discriminative spatial-frequency-temporal feature extraction and classification of motor imagery EEG: an sparse regression and weighted Naïve Bayesian classifier-based approach, J. Neurosci. Methods 278 (2017) 13–24.

[40] M. Mesbah, A. Khorshidtalab, H. Baali, A. Al-Ani, Motor imagery task classification using a signal-dependent orthogonal transform based feature extraction Neural Information Processing, vol. 9490, Springer, 2015, pp. 1–9.
[41] H. Baali, A. Khorshidtalab, M. Mesbah, M.J. Salami, A transform-based feature extraction approach for motor imagery tasks classification, IEEE J. Transl. Eng. Health Med. 3 (2015) 1–8.
[42] C. Ansuini, A. Cavallo, A. Koul, et al., Grasping others' movements: rapid discrimination of object size from observed hand movements, J. Exp. Psychol. Hum. Percept. Perform. 42 (7) (2016) 918.
[43] J. Deng, J. Yao, J.P. Dewald, Classification of the intention to generate a shoulder versus elbow torque by means of a time-frequency synthesized spatial patterns BCI algorithm, J. Neural Eng. 2 (2005) 131.
[44] D.M.J. Tax, R.P.W. Duin, Using two-class classifiers for multiclass classification International Conference on Pattern Recognition, vol. 2, IEEE, 2002, pp. 124–127.
[45] C. Vidaurre, N. Kramer, B. Blankertz, A. Schlögl, Time domain parameters as a feature for EEG-based brain–computer interfaces, Neural Netw. 22 (2009) 1313–1319.
[46] R.A. Johnson, D.W. Wichern, Applied Multivariate Statistical Analysis, Prentice Hall, Englewood Cliffs, NJ, 1992.
[47] K.V. Mardia, Measures of multivariate skewness and kurtosis with applications, Biometrika 57 (1970) 519–530.
[48] H.-I. Suk, S.-W. Lee, A novel Bayesian framework for discriminative feature extraction in brain–computer interfaces, IEEE Trans. Pattern Anal. Mach. Intell. 35 (2013) 286–299.
[49] F. Lotte, C. Guan, Regularizing common spatial patterns to improve BCI designs: unified theory and new algorithms, IEEE Trans. Biomed. Eng. 58 (2011) 355–362.
[50] C. Park, D. Looney, N. ur Rehman, A. Ahrabian, D.P. Mandic, Classification of motor imagery BCI using multivariate empirical mode decomposition, IEEE Trans. Neural Syst. Rehabil. Eng. 21 (2013) 10–22.
[51] A. Khorshidtalab, M.J. Salami, A. Rini, Motor imagery task classification using transformation based features, Biomed. Signal Process. Control 33 (2017) 213–219.
[52] K.K. Ang, Z.Y. Chin, C. Wang, C. Guan, H. Zhang, Filter bank common spatial pattern algorithm on BCI Competition IV datasets 2a and 2b, Front. Neurosci. 6 (2012) 39.
[53] B. Lou, B. Hong, X. Gao, S. Gao, Bipolar electrode selection for a motor imagery based brain–computer interface, J. Neural Eng. 5 (2008) 342–349.
[54] T. Solis-Escalante, G. Müller-Putz, G. Pfurtscheller, Overt foot movement detection in one single Laplacian EEG derivation, J. Neurosci. Methods 175 (2008) 148–153.
[55] S. Fitzgibbon, D. DeLosAngeles, T. Lewis, D. Powers, E. Whitham, J. Willoughby, K. Pope, Surface Laplacian of scalp electrical signals and independent component analysis resolve EMG contamination of electroencephalogram, Int. J. Psychophysiol. 97 (2015) 277–284.
[56] A. Schlögl, J. Kronegg, J.E. Huggins, S.G. Mason, Toward Brain-Computer Interfacing, MIT Press, 2007, pp. 327–360.
[57] A. Jain, D. Zongker, Feature selection: evaluation, application, and small sample performance, IEEE Trans. Pattern Anal. Mach. Intell. 19 (1997) 153–158.
[58] S.J. Raudys, A.K. Jain, Small sample size effects in statistical pattern recognition: recommendations for practitioners, IEEE Trans. Pattern Anal. Mach. Intell. 13 (1991) 252–264.
[59] B. Hjorth, An on-line transformation of EEG scalp potentials into orthogonal source derivations, Electroencephalogr. Clin. Neurophysiol. 39 (5) (1975) 526–530.

2018 26th European Signal Processing Conference (EUSIPCO)

Transfer Learning for SSVEP-based BCI using Riemannian similarities between users

Emmanuel K. Kalunga
VASTech
Stellenbosch, South Africa
emmanuelkalunga.k@gmail.com

Sylvain Chevallier
LISV
Université de Versailles St Quentin
Velizy, France
sylvain.chevallier@uvsq.fr

Quentin Barthélemy
Mensia Technologies SA
Paris, France
qb@mensiatech.com

***Abstract*—Brain-Computer Interfaces (BCI) face a great challenge: how to harness the wide variability of brain signals from a user to another. The most visible problem is the lack of a sound framework to capture the specificity of a user brain waves. A first attempt to leverage this issue is to design user-specific spatial filters, carefully adjusted with a lengthy calibration phase. A second, more recent, opening is the systematic study of brain signals through their covariance, in an appropriate space from a geometric point of view. Riemannian geometry allows to efficiently characterize the variability of inter-subject EEG, even with noisy or scarce data. This contribution is the first attempt for SSVEP-based BCI to make the most of the available data from a user, relying on Riemannian geometry to estimate the similarity with a multi-user dataset. The proposed method is built in the framework of transfer learning and borrows the notion of composite mean to partition the space. This method is evaluated on 12 subjects performing an SSVEP task for the control of an exoskeleton arm and the results show the contribution of Riemannian geometry and of the user-specific composite mean, whereas there is only a few data available for a subject.**

***Index Terms*—Brain-computer interface, transfer learning, Riemannian geometry, SSVEP.**

I. Introduction

Brain-computer interfaces (BCI) endow a user with the ability to interact with a system, such as a physical interface or an application, based on the brain activity [1]. These BCI are of prime interests for users with physical disabilities or with difficulties to interact physically with a system. Brain activity is decoded in real-time to control or to provide insight on the user intentions and decisions. To ensure the portability and a reduced cost for BCI system, a common choice is to rely on electroencephalography (EEG) for recording brain activity [2], or in a lesser extend functional near-infrared spectra [1]. The EEG is most appropriate to detect fast temporal variations or transient events, but is subject to the volume conduction effect [3], mixing cerebral sources and smoothing spatial information.

The strongest limitation for a wide adoption of BCI, and the emergence of out-of-the-lab applications, is known as the BCI deficiency problem [4]. This effect is visible for circa 15 to 30% of the BCI users, who achieve a deceptive near-chance performance, and is not yet correlated with a specific psychological or neurological traits. Some tentative solutions may lie in a better protocol design, which could benefit from advances in human-machine interfaces [5]. Still, one of the main sources of this problem is the important variations between users, and for a given user, the variation from day to day, and in some case from hour to hour. To mitigate this issue, most of the existing approaches rely on a calibration phase. During this calibration, the various preprocessing and filtering steps could be tailored to the specific brain waves of a user. Nonetheless, this calibration is a source of fatigue, frustration and could induce loss of performance for the real task to come [6], [7].

The calibration phase should be performed before each session and is common to all neurobiological signals used for BCI. Existing BCI protocols rely mostly on Event-Related Potentials (ERP), Event-Related Desynchronization and Synchronization (ERD/S) and Steady-State Visually Evoked Potentials (SSVEP) [1]. The ERP is a transient activation induced by an exogenous event, resulting often from the combination of several cognitive components being activated concurrently. Using the oddball paradigm, it is possible to induce a visible ERP component 300 ms after the apparition of an awaited stimulus, called P300 and notoriously employed for BCI spelling tasks. Following another paradigm, the ERD/S has been mostly employed in motor imagery tasks for BCI, where the (de)synchronization results in a change of amplitude in a given frequency band and is related with the movement preparation of a body part. The SSVEP is a brain wave exhibited as a response from a repetitive stimulation with a fixed frequency. The most common practice being to generate visual patterns that are "blinking", which induce a cortical activity in visual areas synchronized with the stimulation. This paper focus on the visual SSVEP for the experimental part, even if the general approach could be adapted to any type of BCI.

The most common approach for all the BCI paradigms is to rely on spatial filters to enhance the signal of interest and to remove bad and noisy electrodes. These spatial filters allow to project the sensor data in a surrogate sensor space, where a proper combination of electrodes augment the signal to noise ratio. The XDAWN spatial filter [8] focuses on maximizing the signal-to-signal plus noise ratio by finding components best correlated with the ERP timings. With ERD, the common spatial patterns [9] is a popular and efficient approach to find

ISBN 978-90-827970-1-5

spatial filters that maximize the variance change during the ERD. For SSVEP, the canonical correlation analysis [10], [11] has proven to be a good candidate to compute spatial filters that maximize the canonical correlation between EEG data and reference signals of known frequencies. In all those cases, the spatial filters are also exploited as a dimensionality reduction technique, by selecting only an appropriate subset of filters. The correct estimation of those filters requires nonetheless a large amount of data, both in terms of number of electrodes and of length of calibration period. The estimation of spatial filters is especially sensitive to noise and label error, and a significant part of the literature is focusing on the possibilities to reduce the adverse effects of noise.

An orthogonal approach of the signal processing behind BCI is to consider subspaces that include all possible surrogate sensor space, that is linear transformation of the input signal. In that case, there is no need to estimate session- and user-specific spatial filters as they are encompassed in the geometry of the considered space. One such approach is known as the Riemannian BCI [12], [13], where spatial covariance matrices are estimated from the EEG signal and classified in the space of symmetric and positive-definite matrices. This Riemannian point of view of the BCI has demonstrated its interests in several occasions, and is now systematically found in the top tier submissions in BCI and EEG competitions. The main challenge is to reformulate the classification problems in the adequate geometrical space [14], [15]. Even without the need of estimating spatial filters, a calibration phase is still required to parametrize the classifier. One possibility to reduce the calibration phase is to rely on a smart initialization, that is using previously acquired data to produce a fast and precise parameterization of the classifier.

The contribution of this paper is to propose such smart initialization, using Riemannian geometry tools in a transfer learning framework. This is the first contribution attempt for SSVEP-based BCI. Section II introduces the geometric formalization of the EEG signal processing and explains how the classification is achieved. In Section III, the reduction of the calibration phase is formulated from a transfer learning point of view and novel approaches are introduced. Section IV demonstrates the interest of the proposed approaches on a real SSVEP dataset. Section V concludes this paper.

II. Riemannian BCI

In the following, we will consider a differentiable manifold $\mathcal{M}$ characterized by a Riemannian metric, that is a collection of inner products on the tangent space $T_\Sigma\mathcal{M}$ varying smoothly at each point Σ of the manifold. Endowed with this inner product, it is possible to compute the length of any curve. The shortest curve between any two points of the manifold is called a geodesic $\gamma(t)$. The length of the geodesic curve between Σ_1 and Σ_2 is the Riemannian distance δ:

$$\delta(\Sigma_1,\Sigma_2) = \left\| \log(\Sigma_1^{-\frac{1}{2}}\Sigma_2\Sigma_1^{-\frac{1}{2}}) \right\|_F \ . \tag{1}$$

It is known as the affine-invariant Riemannian (AIR) distance [16].

The notion of mean (or center of mass) of a set of points Σ_i can be extended in the context of Riemannian manifold, called Karcher (or Fréchet) mean. In that case, the mean $\bar{\Sigma}$ is the point minimizing the dispersion on the manifold, captured by the square of the distances between $\bar{\Sigma}$ and Σ_i. This optimization problem does not have a closed form and is written as:

$$\bar{\Sigma} = \mu(\{\Sigma_i\}) = \arg\ \min_\Sigma \sum_{i=1}^{N} \delta^2(\Sigma_i,\Sigma) \ . \tag{2}$$

There is an exact solution for $N = 2$, but for $N > 2$ it should be estimated iteratively [17].

In this paper, we will consider the weighted mean μ_w, where a coefficient w_i is associated with each point Σ_i of the considered set, with $\sum_i w_i = 1$ [17]:

$$\bar{\Sigma} = \mu_w\left(\{w_i\};\{\Sigma_i\}\right) = \arg\ \min_\Sigma \sum_{i=1}^{N} w_i\ \delta^2(\Sigma_i,\Sigma) \ . \tag{3}$$

The classifier *Minimum Distance to Mean* (MDM), introduced in [14], is presented for multi-class classification in the manifold. The covariance matrices of EEG trials are classified based on their distance to the $k = 1 \dots K$ centers of the classes $\bar{\Sigma}^{(k)}$. The predicted class $\hat{k}$ of the current matrix Σ is defined as:

$$\hat{k} = \arg\min_k \delta(\Sigma,\bar{\Sigma}^{(k)}) \ . \tag{4}$$

It is a simple Bayesian classifier, under the hypotheses that classes have identical dispersion and that it is operating on a manageable space.

III. Proposed approach for transfer learning

A. Related works

In BCI the need to transfer learning is important due to *inter-subject* variability and *inter-session* variability. Inter-subject variability is expressed by the difference of brain signals recorded from different subjects despite them being involved in the similar mental activities. This difference is mostly attributed to anatomical differences among users. Inter-session variability is visible between distinct recording sessions of a unique subject. This variability is attributed to changes in the mental states of the user, such as fatigue, and changes in experimental settings, e.g. electrodes placement, environment, stimulation.

Exposed to the same stimuli, BCI users do not produce similar EEG response. On top of user-specific brain waves, changes induced by different environmental conditions should also be taken into account. These cross-session changes have a lesser impact in Riemannian framework, as congruence invariance allows to reduce the sensitivity to spatial filtering of EEG [13]. In this work, we focus on cross-subject transfer to mitigate inter-subject variability [18], [19]. These efforts are meant to shorten the calibration phase, thus reducing the user fatigue and discomfort. In a cross-subject transfer perspective, the source domain is the dataset of all subjects previously

ISBN 978-90-827970-1-5

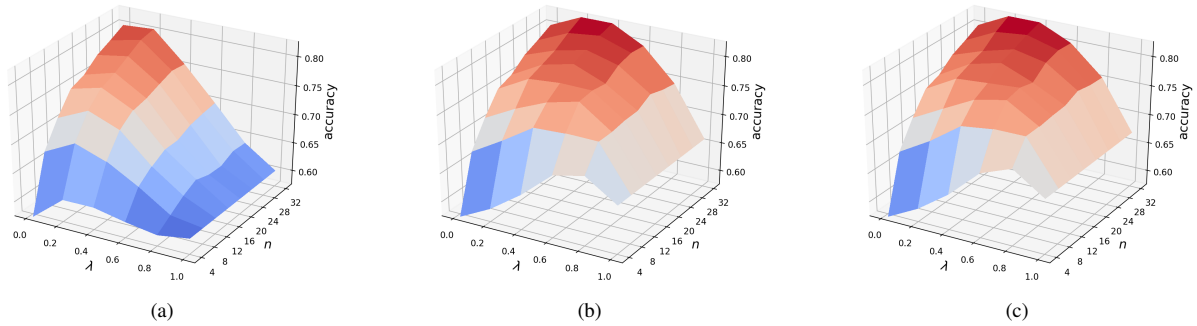

Fig. 1. Average accuracy value evaluated through grid search for λ and n, for minimum distance to E-MDPM 1(a), R-MDPM 1(b) and R-MDWM 1(c).

recorded, that is all the labeled covariance matrices for different users. The target domain is the covariance matrices that are acquired for a target subject. In the scope of this paper, we consider that only a few covariance matrices are available for the target subject.

Let $k = 1, \ldots, K$ be the number of classes and $j = 1, \ldots, J+1$ be the number of subjects. The resting-state class (no task) will be defined by $k = 0$. In order to estimate a model for a target user with few recordings, there are several possibilities at hand to make the most of source user models. In our case, the source models are described by the covariance matrices $\Sigma_j^{(k)}$ for a given user and a given class. Our first approach is to adapt composite mean [20], in the Euclidean space, to allow transfer from user-to-user. This approach could be adapted for the curved space of covariance matrices, relying on Riemannian geometry. The covariance matrices of different users could be averaged into a unique matrix, hypothesizing that each existing model contributes equally to estimate a user model. We called this approach Minimum Distance to Pooled Means (MDPM). We introduce a more advanced approach, called Minimum Distance to Weighted Means (MDWM), is to adjust the influence each model depending on the similarity between the EEG database and the newly observed EEG.

B. Composite Euclidean Mean

Composite Euclidean Mean is an *instance transfer* technique, *i.e.* re-weighting existing labeled data to be applied on newly recorded data, inspired from the composite common spatial patterns method proposed by [20]. It could be seen as a regularization of the newly observed data from user i, where the observed covariance matrices are modified to include information from existing models of users j:

$$\bar{\Sigma}_i^{(k)} = (1-\lambda)\Sigma_i^{(k)} + \lambda \sum_{j \neq i} \frac{1}{J} \Sigma_j^{(k)} \ . \tag{5}$$

The obtained $\bar{\Sigma}_i^{(k)}$ are then diagonalized in order to obtain transferred CSP filters [20], [21]. The hyperparameter $\lambda \in [0, 1]$ allows to choose if the centers of class rely more on the existing data, that is the source domain, or more on newly acquired data, that is the target domain. With $\lambda = 0$, there is no transfer, only the data acquired from a subject are used. With $\lambda = 1$, this is a calibration-free BCI system as no data are required from the subject.

C. Minimum Distance to Pooled Means (MDPM)

The former formulation does not take into account the specific geometry of covariance matrices. The rightmost term in Eq. (5) could be replaced with a Riemannian mean. The whole right-hand side could also be written as Riemannian mean. This geometric formulation could be written as:

$$\bar{\Sigma}_i^{(k)} = \mu_w \left(\{1-\lambda, \lambda\} ; \left\{ \Sigma_i^{(k)}, \bar{\Sigma}_{w,j}^{(k)} \right\} \right) \ , \tag{6}$$

with $\bar{\Sigma}_{w,j}^{(k)} = \mu \left(\left\{ \Sigma_j^{(k)} \right\}_{j \neq i} \right)$.

Even if Eq. (5) has never been used in a MDM based BCI, a MDM applied after it will be called E-MDPM (Euclidean-MDPM), and will be considered as the state-of-the-art. MDM applied with mean from Eq. (6) will be referred to as R-MDPM (Riemannnian-MDPM)

D. Minimum Distance to Weighted Means (MDWM)

The similarity between two subjects i and j is defined as the inverse of the AIR distance δ between their covariance matrices of the resting-state class $k = 0$:

$$s_{i,j} = \frac{1}{\bar{s}_i} \times \frac{1}{\delta(\Sigma_i^{(0)}, \Sigma_j^{(0)})} \ , \tag{7}$$

where $\bar{s}_i$ is a normalization factor integrating all distances to the subjects of the database:

$$\bar{s}_i = \sum_{j \neq i} \frac{1}{\delta(\Sigma_i^{(0)}, \Sigma_j^{(0)})} \ . \tag{8}$$

These weights are obtained in an unsupervised way; no labels are required to estimate this similarity, only a clean recording of 2min of resting-state.

Taking into account these similarities, it is possible to rewrite Eq. (6) as a weighted mean:

$$\bar{\Sigma}_i^{(k)} = \mu_w \left(\{(1-\lambda), \lambda\} ; \left\{ \Sigma_i^{(k)}, \bar{\Sigma}_{w,j}^{(k)} \right\} \right) \ , \tag{9}$$

with $\bar{\Sigma}_{w,j}^{(k)} = \mu_w \left(\left\{ s_{i,j}^{(k)} \right\}_{j \neq i} ; \left\{ \Sigma_j^{(k)} \right\}_{j \neq i} \right)$.

ISBN 978-90-827970-1-5

Eq. (5) can also be rewritten taking with similarity measures as:

$$\bar{\Sigma}_i^{(k)} = (1-\lambda)\Sigma_i^{(k)} + \lambda \sum_{j \neq i} s_{i,j}^{(k)} \Sigma_j^{(k)} \ . \tag{10}$$

Thus, an MDWM applied with means from Eq. (9) will be called R-MDWM (Riemannian-MDWM), and E-MDWM (Euclidean-MDWM) when applied with Eq. (10).

IV. Results

A. SSVEP experimental setup and data

The experimental study is conducted on multichannel EEG signals recorded during a SSVEP-based BCI experiment. There are 3 groups of 4 LEDs blinking at different frequencies: $F = 3$ visual target stimuli blinking respectively at 13, 21 and 17 Hz. A sequence of trials is proposed to the user. When he do not intend to activate any SSVEP command, this constitutes the reject class, *i.e.* reference state or no-SSVEP state. This, plus the 3 groups of LEDs make a 4-class BCI ($K = 4$). The EEG was recorded at a sampling rate of 256 Hz with $C = 8$ electrodes/channels (PO7, PO3, POz, PO4, PO8, O1, Oz, and O2).

In a session, 32 trials were recorded: 8 for each visual stimulus and 8 for the resting-state class. A trial is 4 seconds long. There were 12 subjects and the number of sessions recorded per subject varied from 2 to 5. The full description of the experiment and dataset can be found in [11].

The covariance matrices are estimated from a modified version of the input signal $X \in \mathbb{R}^{C \times T}$:

$$X \in \mathbb{R}^{C \times T} \rightarrow \begin{bmatrix} X_{\text{freq}_1} \\ \vdots \\ X_{\text{freq}_F} \end{bmatrix} \in \mathbb{R}^{FC \times T} \ , \tag{11}$$

where X_{freq_f} is the input signal X band pass filtered around frequency freq_f, $f = 1, \ldots, F$. The sample covariance matrix estimator $\tilde{\Sigma}_{\text{scm}} = \frac{1}{C} X X^\intercal$ is a possible choice, but a shrinkage estimator [22] could produced a better conditioned estimator $\tilde{\Sigma}_{\text{skrinkage}} = \kappa \text{tr}(\hat{\Sigma}_{\text{scm}}) \mathbf{I}_C + (1-\kappa)\hat{\Sigma}_{\text{scm}}$. In the rest of the document, we will write Σ to denote matrices estimated with the shrinkage estimator.

This dataset is accessible at https://github.com/sylvchev/dataset-ssvep-exoskeleton.

B. Experimental comparison

Four transfer learning approaches are compared: E-MDPM (Eq. 5) considered as the state-of-the-art, R-MDPM (Eq. 6), E-MDWM (Eq. 10), and R-MDWM (Eq. 9).

The four approaches are evaluated at different values of $\lambda \in \{0, 0.2, 0.4, 0.6, 0.8, 1\}$. The objective of our transfer learning approaches being to eliminate or reduce the number of training samples required for the target domain subjects by using data from source domain subjects, the approaches are also evaluated with various numbers of available training samples from the target subject $n \in \{4, 8, 12, 16, 20, 24, 28, 32\}$.

The target domain is made of a test subject, while the remaining data from other subjects are used as the source domain. The number of labeled samples in the target domain corresponds to n. The classifier is evaluated on unlabeled samples of the target domain (varying from 32 to 128). For statistical significance, bootstrapping is used. The classifier is implemented on 10 bootstraps of the target domain training data by re-sampling with replacement.

C. Results and discussion

1) E-MDPM *and* R-MDPM*:* The results obtained with the classifier trained as described in Eq. (5) and Eq. (6) over various λ and n are shown in Fig. 1. It can be seen that the accuracy is always better when the test subject or target domain has more label samples (*i.e.* higher values of n). Taking class means from the source domain ($\Sigma_j^{(k)}$) improves the results as λ grows from zero. Although this trend is observed on all values of n, it is significantly bigger for small values of n, indicating that, when a subject has very few training samples available, the composite Riemannian mean transfer learning approach is a good BCI initialization.

Comparing Fig. 1(a) to Fig. 1(b), it is visible that *R-MDPM*, which is consistent with the Riemannian approach, outperforms *E-MDPM*. A one way ANOVA analysis shows significance in this improvement with f-value of over 40 and corresponding p-value in the order of 10^{-10}. It is therefore important to consider the fully Riemannian approach of the composite Riemannian mean introduced in Eq. (6) rather than the one of Eq. (5).

2) R-MDPM *versus* R-MDWM*:* The composite Riemannian mean of Eq. (9) introduces a weight based of a similarity measure between subjects.

Table I compares the results of *R-MDPM* and *R-MDWM*. For illustration purposes, the value of n is fixed to 12 and on the value of λ that yields the highest classification accuracy is considered. To test the statistical significance of the results, a paired Student t-test is run on the results (across all λ and all n) of *R-MDPM* on one side, and *R-MDWM* on the other side. The p-values show that these two methods yield significantly different results, and *R-MDWM* improves the overall results.

3) Euclidean *versus* Riemannian*, and* pooled *versus* weighted*:* A two-way ANOVA is performed on the four methods, and the interaction between Euclidean/Riemannian mean and pooled/weighted mean is shown in Fig. 2. It shows that using remannian mean in transfer learning of class mean (*i.e* Eq. (6) and Eq. (9)) significantly improves the classification performance, with F-value of 103 and equivalent p-value in the orders of 10^{-23}. On a smaller scale, weighting the data in the source domain based on their similarity to the target domain shows a trend in the improvement the performance (F-value close to 1, and p-value in the order of 0.1).

V. Conclusion

This paper proposes a Riemannian transfer learning approach for SSVEP-based BCI, inspired from composite mean for instance transfer where a user's model is combined with with those of similar subjects. The Riemannian geometry offers a very robust framework for inter-subject transfer learning

ISBN 978-90-827970-1-5 © EURASIP 2018

	Sub. 1	Sub. 2	Sub. 3	Sub. 4	Sub. 5	Sub. 6	Sub. 7	Sub. 8	Sub. 9	Sub. 10	Sub. 11	Sub. 12
	Accuracy											
E-MDPM	0.619	0.875	0.925	0.756	0.756	0.844	0.808	0.869	**0.938**	0.641	0.619	**0.845**
R-MDPM	**0.625**	0.856	0.944	0.862	**0.794**	0.844	0.821	**0.875**	0.812	0.656	**0.788**	0.842
E-MDWM	0.619	**0.881**	0.925	0.756	0.762	0.838	0.808	0.869	0.875	0.647	0.625	**0.845**
R-MDWM	**0.625**	0.85	**0.950**	**0.881**	**0.794**	**0.856**	**0.829**	**0.875**	0.812	**0.659**	**0.788**	0.842
	Best λ											
E-MDPM	0.0	0.4	0.0	0.0	0.2	0.4	0.0	0.0	1.0	0.2	0.2	0.4
R-MDPM	0.2	0.2	0.8	0.8	0.6	0.6	0.2	0.4	0.6	0.4	0.8	0.2
E-MDWM	0.0	0.4	0.0	0.0	0.2	0.4	0.0	0.0	1.0	0.4	0.2	0.4
R-MDWM	0.2	0.2	0.6	0.6	0.6	0.4	0.2	0.4	1.0	0.4	0.8	0.2

TABLE I
SNAPSHOT OF *E-MDPM*, *R-MDPM*, *E-MDWM*, *R-MDWM* PERFORMANCES AT $n = 12$.

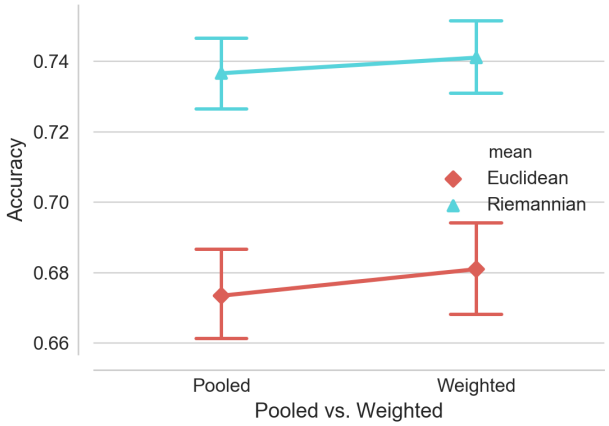

Fig. 2. Two-way ANOVA: interactions between Euclidean/Riemannian mean and pooled/weighted mean.

and we have shown that it outperforms the Euclidean formulation. We introduce two Riemannian approaches, the minimum distance to pooled means (R-MDPM) and the minimum distance to weighted means (R-MDWM). The results demonstrate that taking into account the similarities between subjects yields significantly better results for almost all considered subjects. This transfer learning has been applied to SSVEP, but could be easily used for MI or P300 paradigms.

REFERENCES

[1] C.S. Nam, A. Nijholt, and F. Lotte, *Brain–Computer Interfaces Handbook: Technological and Theoretical Advances*, CRC Press, 2018.

[2] E. Niedermeyer and F. H. Lopes da Silva, *Electroencephalography: Basic Principles, Clinical Applications, and Related Fields*, Lippincott Williams & Wilkins, 2005.

[3] P. L. Nunez, R. Srinivasan, A. F. Westdorp, R. S. Wijesinghe, D. M. Tucker, R. B. Silberstein, and P. J. Cadusch, "EEG coherency: I: Statistics, reference electrode, volume conduction, Laplacians, cortical imaging, and interpretation at multiple scales," *Electroencephalogr Clin Neurophysiol*, vol. 103, no. 5, pp. 499–515, 1997.

[4] C. Vidaurre and B. Blankertz, "Towards a cure for BCI illiteracy.," *Brain Topography*, vol. 23, no. 2, pp. 194–198, 2010.

[5] C Jeunet, E Jahanpour, and F Lotte, "Why standard brain-computer interface (BCI) trainingprotocols should be changed: An experimental study," *J Neural Eng*, vol. 13, 2016.

[6] J. Faller, C. Vidaurre, T. Solis-Escalante, C. Neuper, and R. Scherer, "Autocalibration and recurrent adaptation: Towards a plug and play online ERD-BCI," *IEEE Trans Neural Syst Rehabil Eng*, vol. 20, no. 3, pp. 313–319, 2012.

[7] F. Lotte, "Signal processing approaches to minimize or suppress calibration time in oscillatory activity-based brain–computer interfaces," *Proc IEEE*, vol. 103, no. 6, pp. 871–890, 2015.

[8] B. Rivet, A. Souloumiac, V. Attina, and G. Gibert, "xDAWN Algorithm to Enhance Evoked Potentials: Application to Brain-Computer Interface," *IEEE Trans Biomed Eng*, vol. 56, no. 8, pp. 2035–2043, 2009.

[9] B. Blankertz, R. Tomioka, S. Lemm, M. Kawanabe, and K. R. Muller, "Optimizing Spatial filters for Robust EEG Single-Trial Analysis," *IEEE Signal Process Mag*, vol. 25, no. 1, pp. 41–56, 2008.

[10] G. Bin, X. Gao, Z. Yan, B. Hong, and S. Gao, "An online multi-channel SSVEP-based brain-computer interface using a canonical correlation analysis method," *J Neural Eng*, vol. 6, no. 4, 2009.

[11] E. K. Kalunga, S. Chevallier, O. Rabreau, and E. Monacelli, "Hybrid interface: Integrating BCI in multimodal human-machine interfaces," in *Int Conf on Adv Int Mech (AIM)*, 2014, pp. 530–535.

[12] F. Yger, M. Berar, and F. Lotte, "Riemannian approaches in brain-computer interfaces: a review," *IEEE Trans Neural Syst Rehabil Eng*, vol. 25, no. 10, pp. 1753–1762, 2017.

[13] M. Congedo, A. Barachant, and R. Bhatia, "Riemannian geometry for EEG-based brain-computer interfaces; a primer and a review," *Brain-Computer Interfaces*, vol. 4, pp. 1–20, 2017.

[14] A. Barachant, S. Bonnet, M. Congedo, and C. Jutten, "Multiclass brain–computer interface classification by Riemannian geometry," *IEEE Trans Biomed Eng*, vol. 59, no. 4, pp. 920–928, 2012.

[15] E. K. Kalunga, S. Chevallier, Q. Barthélemy, K. Djouani, E. Monacelli, and Y. Hamam, "Online SSVEP-based BCI using Riemannian geometry," *Neurocomputing*, vol. 191, pp. 55–68, 2016.

[16] M. Moakher, "A differential geometric approach to the geometric mean of symmetric positive-definite matrices," *SIAM Journal on Matrix Analysis and Applications*, vol. 26, no. 3, pp. 735–747, 2005.

[17] P. T. Fletcher, C. Lu, S. M. Pizer, and S. Joshi, "Principal geodesic analysis for the study of nonlinear statistics of shape," *IEEE Trans Med Imaging*, vol. 23, no. 8, pp. 995–1005, 2004.

[18] H He and D Wu, "Transfer learning enhanced common spatial pattern filtering for brain computer interfaces (BCIs): Overview and a new approach," in *NIPS*, 2017, pp. 811–821.

[19] N R Waytowich, V J Lawhern, A W Bohannon, K R Ball, and B J Lance, "Spectral transfer learning using information geometry for a user-independent brain-computer interface," *Frontiers in Neuroscience*, vol. 10, pp. 430, 2016.

[20] H. Kang, Y. Nam, and S. Choi, "Composite common spatial pattern for subject-to-subject transfer," *IEEE Signal Process Lett*, vol. 16, no. 8, pp. 683–686, 2009.

[21] F. Lotte and C. Guan, "Regularizing common spatial patterns to improve BCI designs: Unified theory and new algorithms," *IEEE Trans Biomed Eng*, vol. 58, pp. 355–362, 2011.

[22] O. Ledoit and M. Wolf, "A well-conditioned estimator for large-dimensional covariance matrices," *Journal of Multivariate Analysis*, vol. 88, no. 2, pp. 365–411, 2004.

ISBN 978-90-827970-1-5